Eng. Mestr. Ricardo Henrique Buzolin

Microstructure Design of Titanium Alloys via Thermomechanical Treatments

DOCTORAL THESIS

to schieve the university degree of

Doktor der technischen Wissenschaften

Submitted to

Graz University of Technology

Supervisor

Assoc. Prof. Dr.techn. Maria Cecilia Poletti

Institute of Materials Science, Joining and Forming

Graz, Dezember 2020

AFFIDAVIT

I declare that I have authored this thesis independently, that I have not used other than the declared sources/resources, and that I have explicitly indicated all material which has been quoted either literally or by content from the sources used. The text document uploaded to TUGRAZonline is identical to the present doctoral thesis.

Date, Signature

Simplicity if the ultimate sophistication

Leonardo da Vinci

DEDICATION

To my parents, for the everlasting incentive.

Acknowledgements

Firstly, I would like to express my sincere gratitude to my supervisor Prof. Maria Cecilia Poletti, for the continuous support during my PhD work, for her never-ending patience, motivation, and immense knowledge. Her fascinating passion for science guided helped me in this valuable time of research and writing of this thesis. This document is the fruit of her persistent generosity, comprehension and trust. I really appreciate her systematic guidance and great effort, offering me this opportunity. I could not have imagined having a better supervisor. For all, I want to express to her my gratitude: Muchas gracias Cecilia!!

I am deeply acknowledged to Prof. Logé, who acceded to take part in the defence as the second examiner and took his valuable time to do a detailed review with exceptional comments. Thank you.

I would like to thank Dr. Fernando Warchomicka for the synchrotron radiation data and uncountable fruitful discussions, ideas and scientific insights.

I want to thank Dr. David Canelo-Yubero for helping me with the analysis, interpretation and discussion of the synchrotron radiation data.

I acknowledge my gratitude to Professor Shoichi Nambu to host me at The University of Tokyo and providing technical support during my stay at the Department of Materials Engineering.

This work was carried out in the framework of the CD Laboratory for Design of High-Performance Alloys by Thermomechanical Processing (D-1303000107). I am intensely beholden to the Christian Doppler Forschungsgesellschaft and voestalpine BÖHLER Aerospace GmbH & Co KG for financial support.

My cordial acknowledgement to Michael Lasnik, Dr. Alfred Krumphals, Dr. Flora Godor, and Dr. Aleksandar Stanojevic from voestalpine BÖHLER Aerospace for the helpful discussion during project meetings.

I would like to express my heartfelt gratitude to the Institute of Materials Science, Joining and Forming (IMAT) of the Graz University of Technology (TU Graz) for providing its research facilities and warm hospitality.

My honest gratitude to Manuela Prader and Sandra Wesener for the exceptional assistance in every administrative matter.

I thank my fellow officemates and lab mates in for the stimulating discussions, for all the fun we have had in during my stay in Graz. In particular, I thank René Wang, Kashyap Pradeep, Peng Wang, Franz M.B. Ferraz, Florian Pixner, Florian K. Riedlsperger, Rafael P.M. Guimaraes, Maximilian Stummer, Bernhard Krenmayr, Mateusz Skalon, Desirée Weiß, Arthur Fuchs, Christian Hoflehner, Siegfried Arneitz, Saham Sharifi, Dr. Rudolf Vallant, Fatemeh Iranshani, Mohammad Nasiri, Mariana Poliserpi, and many colleagues and friends for the friendship, support and the happy time we spent together.

Last but not least, I would like to thank my family for the never-ending incentive pushing me to achieve another dream: Ao meu pai e minha mãe, um imenso muito obrigado!!

Abstract

The production of typical structural components of Ti and Ti alloys can be described as complex thermo-mechanical treatments. The processing parameters window usually is small, and the mechanical properties of the final material rely on the control of these parameters. Therefore, the understanding and description of the material response to the processing parameters are necessary to design the thermo-mechanical processing route. The development of physical models to predict material behaviour enables the simulations of real-time production of complex - shape components.

This work comprises the description and modelling of the phase transformation, hot deformation, and static recrystallisation behaviours of alpha+beta and near beta titanium alloys. These phenomena are systematically investigated, and the microstructure characterised using light optical and scanning electron microscopy. The understanding of the material behaviour is translated into physically-based models developed based on the evolution of internal variables.

Diffusion equations coupled with classical nucleation are used to describe the α-phase formation during cooling. The primary α-phase is considered as spherical particles that grow into a β-matrix, while the secondary α and allotriomorphic α-phases nucleates and grows as semi-infinite plates. The phase fraction and morphological features evolution obtained from the simulated continuous cooling heat treatments are validated with the microstructure evolution observed by optical and electron microscopy for a Ti-6Al-4V.

The hot deformation behaviour is described as the formation of low angle grain boundaries due to dynamic recovery and their increase in misorientation to form new high angle grain boundaries via continuous dynamic recrystallisation. The microstructure is modelled as being composed by dislocations (mobile, immobile and wall), subgrains and grains. The dislocation reactions are described as the interrelated role of production, recovery and immobilisation.

The formation of misorientation spread within the β-phase as well as low and high angle grain boundaries in Ti-5553 and Ti-17 alloys are systematically investigated using electron backscattered diffraction. The formed low angle grain boundaries within a β-grain are more homogeneously distributed at lower strain rates. The developed model can predict the evolution of a deformed microstructure from an initially recrystallised one, as well as its subgrain and grain sizes. The developed model can estimate the microstructure evolution up to large strains.

The dynamic globularisation of the α phase is modelled to describe the formation of boundaries within the α-platelets and the migration of α/β interfaces to form globular α-particles. Lower strain rates lead to a more advanced stage of dynamic globularisation for a given strain. Additionally, the changes in the load partitioning between the α and the β-phases are interpreted to have a direct influence on the flow stress evolution in the α+β domain.

Finally, the hot deformation and the static recrystallisation behaviours in the Ti-17 alloy are coupled in a model based on strain-induced boundary migration, grain growth and static recovery. The formed microstructure during hot deformation is considered as the initial microstructure for static recrystallisation. Larger strain rates lead to higher stored energy within the β-grains.

The results obtained in this work enable a comprehensive understanding of the several thermomechanical processing steps of typical Ti alloys. The description of β→α phase transformation, hot deformation and static recrystallisation using the same internal variables allow the developed models to predict the entire thermomechanical processing route as well as to explain the role of each processing parameter on the developed microstructure at each step.

Kurzfassung

Die Herstellung typischer Strukturkomponenten aus Ti und Ti-Legierungen kann als komplexe thermomechanische Behandlung beschrieben werden. Die mechanischen Eigenschaften des fertig verarbeiteten Materials hängen stark von den Prozessparametern ab, welche nur in einem kleinen Bereich verändert werden können. Daher erfordert der Entwurf einer thermomechanischen Verarbeitungsroutine, ein Verständnis und eine profunde Beschreibung des Materialverhaltens auf sich ändernde Verarbeitungsparameter. Die Entwicklung physikalischer Modelle zur Vorhersage des Materialverhaltens, ermöglicht die Simulation von Produktionsabläufen komplexer Komponenten in Echtzeit.

Diese Arbeit umfasst die Beschreibung und Modellierung von Phasenumwandlungs-, Heißverformungs- und statischen Rekristallisationsverhalten in Alpha+Beta-, sowie metastabilen Beta-Titanlegierungen. Diese Phänomene werden systematisch untersucht und die Mikrostruktur mittels Licht- und Rasterelektronenmikroskopie charakterisiert. Das Verständnis des Materialverhaltens wird in physikalisch basierte Modelle übersetzt, die auf der Entwicklung interner Variablen basieren.

Diffusionsgleichungen gekoppelt mit klassischer Keimbildung werden verwendet, um die α-Phasenbildung während des Abkühlens zu beschreiben. Die primären α-Phasen werden als kugelförmige Teilchen betrachtet die in der β-Matrix wachsen, während die sekundären und allotriomorphen α-Phasen als semi-infinite Plättchen nukleieren und wachsen.. Der Phasenanteil und die Entwicklung der morphologischen Merkmale, die aus der Simulation einer kontinuierlichen Kühlung berechnet wurden, werden mit den gemessenen Mikrostrukturparametern aus optischer Mikroskopie und Elektronenmikroskope von Ti-6Al-4V validiert.

Die Ausbreitung von Fehlorientierungen innerhalb der β-Phase und Korngrenzen mit niedrigem und hohem Winkel in Ti-5553- und Ti-17-Legierungen werden systematisch unter Verwendung von Elektronenrückstreuungsbeugung untersucht.Die gebildeten Kleinkorngrenzen innerhalb eines β-Korns sind bei niedrigeren Dehnraten homogen verteilt..

Das entwickelte Modell kann die Veränderung einer deformierten Mikrostruktur aus einer anfänglich rekristallisierten Struktur, sowie deren Subkorn- und Korngrößen vorhersagen.Das entwickelte Modell kann die Mikrostrukturentwicklung bis zu großen Dehnungen abschätzen.

Die dynamische Globularisierung der α-Phase wird modelliert, um die Bildung von Grenzen innerhalb der α-Plättchen und die Migration von α / β-Grenzflächen zur Bildung globulärer α-Partikel zu beschreiben. Niedrige Dehnungsraten führen zu einem fortgeschrittenen Stadium der dynamischen Globularisierung für eine gegebene Dehnung. Zusätzlich wird die Änderungen in der Lastverteilung zwischen der α- und der β-Phase als ein direkter Einfluss auf die Entwicklung der Fließspannung in der α + β-Domäne interpretiert.

Schließlich werden das Heißverformungs- und das statische Rekristallisationsverhalten in der Ti-17-Legierung in einem Modell gekoppelt, welches auf spannungsinduzierter Grenzmigration, Kornwachstum und statischer Erholung basiert. Die während der Heißverformung gebildete Mikrostruktur wird als anfängliche Mikrostruktur für die statische Rekristallisation

angesehen. Größere Dehnungsraten führen zu einer höheren gespeicherten Energie in den β-Körnern.

Die in dieser Arbeit erzielten Ergebnisse ermöglichen ein umfassendes Verständnis der verschiedenen thermomechanischen Verarbeitungsschritte typischer Ti-Legierungen. Die Beschreibung der $\beta \rightarrow \alpha$-Phasentransformation, der Heißverformung und der statischen Rekristallisation unter Verwendung derselben internen Variablen, ermöglicht es den entwickelten Modellen den gesamten thermomechanischen Verarbeitungsprozess vorherzusagen und den Einfluss jedes Verarbeitungsparameters auf die entwickelte Mikrostruktur, bei jedem Schritt zu erklären.

List of symbols and abbreviations

$\mathbf{A_{GB}^{*}}$	Parameter for nucleation of the α_{GB}
$\mathbf{A_{glob}}$	The factor for the velocity of α/β interface grooving during dynamic globularisation of the α-phase
$\mathbf{A_{iso\text{-}stress}}$	Constant for the calculation of material deforming in iso-stress load partition regime
AR	Aspect ratio
$\mathbf{A_{REF}}$	Parameter for f_{CDRX}
$\mathbf{A_{SEC}^{*}}$	Parameter for nucleation of the secondary α-phase
$\mathbf{A_{SYM}}$	Parameter for sympathetic nucleation
$\mathbf{A_{SRX}}$	The factor for the set of dislocation in the wall dislocation density
$\mathbf{A_{YS}}$	Parameter for the Arrhenius equation that defines the yield stress
$\mathbf{A_{\alpha\beta}}$	Parameter for nucleation at the β-grain boundary
$\mathbf{a_1}$	Parameter for the glide velocity
$\mathbf{A_1}$	Fraction of Rayleigh surface density
b	Burgers vector
BCC	Body cubic centre
$\mathbf{B_{GB}}$	Thickness of the allotriomorphic α-phase platelet
$\mathbf{\bar{B}_{GB}}$	Mean thickness of the allotriomorphic α-phase platelet
$\mathbf{B_{GBcrit}}$	Critical thickness for a disk-like allotriomorphic α-phase to nucleate
$\mathbf{B_{glob}}$	Parameter for the velocity of growth during dynamic globularisation of the α-phase
$\mathbf{B_{SEC}}$	Thickness of a secondary α-phase platelet
$\mathbf{\bar{B}_{SEC}}$	Mean thickness of a secondary α-phase platelet
$\mathbf{B_{SECcrit}}$	Critical thickness for a disk-like secondary α-phase to nucleate
BSE	Backscattered electrons
$\mathbf{B_{SRX}}$	Factor for the set of dislocation in the wall dislocation density
CDRX	Continuous dynamic recrystallisation
$\mathbf{C_w}$	Specific heat
$\mathbf{C_I}$	Concentration of V β-interface chemical composition
$\mathbf{C_M}$	Concentration of V β-matrix chemical composition
$\mathbf{C_P}$	The concentration of V α-particle chemical composition
$\mathbf{C_P^{\alpha_{GB}}}$	Concentration of V in the allotriomorphic α-phase
$\mathbf{C_P^{\alpha_{SEC}}}$	Concentration of V in the secondary α-phase
$\mathbf{D_s}$	Self-diffusion coefficient
$\mathbf{D_V^{\beta}}$	Intrinsic diffusion coefficient of V in β titanium
CRSS	Critical resolved shear stress
DDRX	Discontinuous dynamic recrystallisation
DRV	Dynamic recovery
DRX	Dynamic recrystallisation
E	Young modulus
EBSD	Electron Backscattered diffraction

$\mathbf{E_{GG}}$	Stored energy for grain growth
$\mathbf{E_{MOB}}$	Driving force for movement of high angle grain boundaries during continuous dynamic recrystallisation
$\mathbf{E^0_{MOB}}$	Parameter for the driving force for movement of high angle grain boundaries during continuous dynamic recrystallisation
$\mathbf{E_{SIBM}}$	Stored energy for strain-induced boundary migration
$\mathbf{f_{BG}}$	Fraction of formed boundaries within the α-platelet contributing to movement of the α/β interface during dynamic globularisation
$\mathbf{f_{CDRX}}$	Factor for the contribution of recovery to continuous dynamic recrystallisation
$\mathbf{f^0_{CDRX}}$	Pre-factor for the f_{CDRX}
$\mathbf{f_{glob}}$	Fraction of dynamic globularisation of α-phase
$\mathbf{f_{iso\text{-}stress}}$	Fraction of material under iso-stress load partition regime
$\mathbf{f_{LAGB}}$	Fraction of low angle grain boundaries
$\mathbf{f_{LAGB_{cells}}}$	Fraction of cell boundaries
$\mathbf{f_R}$	Fraction of boundary surface corresponding to a Rayleigh distribution of misorientation angle
$\mathbf{F_w}$	Factor of strengthening of the wall dislocation density
$\mathbf{F^0_w}$	Pre-factor of strengthening of the wall dislocation density
$\mathbf{f_\alpha}$	Fraction of α-phase
$\mathbf{f_{\alpha GB}}$	Fraction of allotriomorphic α-phase
$\mathbf{f_{\alpha p}}$	Fraction of primary α-phase
$\mathbf{f_{\alpha SEC}}$	Fraction of secondary α-phase
G	Shear modulus
GOS	Grain orientation spread
GS	Grain size
$\mathbf{\bar{G}_s}$	Mean grain size
$\mathbf{G^0_s}$	Initial grain size
$\mathbf{GS^{ref}_0}$	Reference grain size
GRDX	Geometric dynamic recrystallisation
$\mathbf{G_{SIBM}}$	Recrystallised grain size formed by strain-induced boundary migration
HAGB	High angle grain boundary
HCP	Hexagonal closed-packed
$\mathbf{h_1}$	Factor for production of immobile dislocations
$\mathbf{h^0_1}$	Pre-factor for production of immobile dislocations
$\mathbf{h_2}$	Factor for recovery of immobile dislocations
$\mathbf{h^0_2}$	Pre factor for recovery of immobile dislocations
KAM	Kernel average misorientation
$\mathbf{k_B}$	Boltzmann constant
$\mathbf{K_{nuc}}$	Constant for subgrain nucleation
$\mathbf{K_w}$	Thermal conductivity
LAGB	Low angle grain boundary
LOM	Light optical microscopy

$L_{\alpha_{CLIMB}}$	Length governing the elastic interaction between the dislocation and the defects
IPF	Inverse pole figure
JMAK	Johnson-Mehl-Avrami-Kolmogorov
M	Taylor factor
m_{GB}	Ledge coefficient for the growth of allotriomorphic α-phase
M_{HAGB}	Mobility of high angle grain boundaries
M_{LAGB}	Mobility of low angle grain boundaries
m_{SEC}	Ledge coefficient for the growth of secondary α-phase
M_0	Pre-factor for the mobility of high angle grain boundaries
m_1	Exponent for the production of immobile dislocations
m_2	Exponent for the recovery of immobile dislocations
n	Set of dislocations forming the wall dislocation density
N_A	Avogadro constant
N_{GB}	Number of α_{GB} particles
n_{glob}	Number of α-particles formed from an α-platelet during dynamic globularisation
n_{HAGB}	Exponent for the driving force of high angle grain boundaries
n_{max}	Factor for the set of dislocation in the wall dislocation density
n_s	Exponent for the fraction of material deforming in iso-stress load partition regime
N_{SIBM}	Number of nuclei formed by strain-induced boundary migration
$\dot{N}_{SIBM}$	Nucleation rate due to strain-induced boundary migration
$\bar{N}_{SIBM}$	Nucleation frequency during strain-induced boundary migration
n_v	Particle number density
N_{SEC}	Number of α_{SEC} particles
n_{YS}	Exponent for the Arrhenius equation that defines the yield stress
N_{0GB}	Pre-exponent term for the nucleation of α_{GB}
N_{0SEC}	Pre-exponent term for the nucleation of α_{SEC}
OPS	Oxide polishing solution
P_{LAGB}	Pressure for subgrain growth
p_{SG}	Rayleigh distribution of subgrain size
P_{Zener}	Zener back pressure
Q_{DIFF}	Activation energy for self-diffusion along the grain boundary
Q_{eq}	Equivalent activation energy for the velocity of high angle grain boundaries
Q_{HAGB}	Activation energy for the movement of a high angle grain boundary
Q_{SIBM}	Activation energy for nucleation via strain-induced boundary migration
Q_{YS}	Equivalent activation energy for the Arrhenius equation that defines the yield stress
Q_α	Activation energy for atomic migration across the α/β interface
Q_1	Equivalent activation energy for the production of immobile dislocations
Q_2	Equivalent activation energy for the recovery of immobile dislocations
R	Universal constant of gases

$\mathbf{R_\alpha}$	Radius of an α-particle
SE	Secondary electrons
SEM	Scanning electron microscopy
$\mathbf{S_{glob}}$	α/β surface density during dynamic globularisation
$\mathbf{SG_s}$	Subgrain size
$\mathbf{\overline{SG_s}}$	Mean subgrain size
$\mathbf{SG_s^*}$	Critical subgrain size
SIBM	Strain-induced boundary migration
SRV	Static recovery
SRX	Static recrystallisation
$\mathbf{S_v}$	Volumetric boundary density
$\mathbf{S_{v_{CDRX}}}$	volumetric boundary density formed by CDRX
$\mathbf{S_{v_{interface}}}$	α/β boundary interface density
$\mathbf{S_v^{REF}}$	Reference boundary interface density
$\mathbf{S_{v_{HAB}}^0}$	Initial surface density
$\mathbf{S_{TOTAL}}$	Total surface density within the α-platelet
$\mathbf{S(\theta)}$	Shape factor
T	Temperature
$\mathbf{t_{HAGB}}$	Thickness of a high angle grain boundary
$\mathbf{t_\alpha}$	Thickness of an α-platelet
$\mathbf{v_c}$	Climb velocity
$\mathbf{v_g}$	Glide velocity
$\mathbf{v_{glob}}$	Velocity of α/β interface movement due to grooving during dynamic globularisation
$\mathbf{v_{growth}}$	Velocity of α/β interface promoting the growth of α-grains during dynamic globularisation
$\mathbf{v_{HAGB}}$	Velocity of a high angle grain boundary during continuous dynamic recrystallisation
$\mathbf{v_0}$	Pre-factor for the velocity of high angle grain boundaries
$\mathbf{v_{SIBM}}$	Velocity of high angle grain boundaries during strain-induced boundary migration
$\mathbf{X_{def}}$	Heterogeneity factor
$\mathbf{X_{SRX}}$	Static recrystallisation fraction
$\mathbf{X_0}$	Recrystallisation fraction achieved when $X_{def} = 0$
$\mathbf{W_g}$	Glide activation energy
$\mathbf{w_\alpha}$	Width of an α-platelet
α	Taylor constant
α'	Martensite
$\mathbf{\alpha_{CDRX}}$	Probability of formation of new low angle grain boundaries during continuous dynamic recrystallisation
$\mathbf{\alpha_{GB}}$	Allotriomorphic α-phase
$\mathbf{\alpha_P}$	Globular primary α-phase

α_{SEC}	Lamellar secondary α-phase
α_{YS}	Factor for the Arrhenius equation that defines the yield stress
δ_{DRV}	Distance for dynamic recovery
δ_{SG}	Parameter for the production of mobile dislocations at the subgrain boundary
ΔG^{*}_{NucGB}	Energy barrier for heterogeneous nucleation of α_{GB}
ΔG^{*}_{NucSEC}	Energy barrier for heterogeneous nucleation of α_{SEC}
ΔG_{VGB}	Chemical free energy of phase transformation of α_{GB}
ΔG_{VSEC}	Chemical free energy of phase transformation of α_{SEC}
Δt	Incremental time step
$\Delta \rho_{cDRX}$	Dislocation density that takes place on continuous dynamic recrystallisation in an iteration
ε	Strain
ε_e	Elastic strain
ε_p	Plastic strain
$\dot{\varepsilon}$	Elastic strain rate
$\dot{\varepsilon}_p$	Plastic strain rate
$\dot{\varepsilon}_{ref}$	Reference strain rate
$\dot{\varepsilon}_{\alpha}^{\varepsilon}$	Strain rate in the α-phase in iso-strain load partition regime
$\dot{\varepsilon}_{\alpha}^{W}$	Strain rate in the α-phase in iso-power load partition regime
$\dot{\varepsilon}_{\alpha}^{\sigma}$	Strain rate in the α-phase in iso-stress load partition regime
$\dot{\varepsilon}_{\beta}^{\varepsilon}$	Strain rate in the β-phase in iso-strain load partition regime
$\dot{\varepsilon}_{\beta}^{W}$	Strain rate in the β-phase in iso-power load partition regime
$\dot{\varepsilon}_{\beta}^{\sigma}$	Strain rate in the β-phase in iso-stress load partition regime
γ_{HAGB}	High angle grain boundary energy
γ_{LAGB}	Low angle grain boundary energy
$\gamma_{\alpha\alpha}$	Interface energy of α/α phase
$\gamma_{\alpha\beta}$	Interface energy between α/β phases
λ	Wavelength
$\lambda_{interspace}$	Mean particle interspace
Λ	Growth rate parameter
λ_i	Immobile dislocation inter-distance
λ_m	Mobile dislocation inter-distance
Λ_{GB}	Growth rate parameter for the allotriomorphic α-phase
Λ_{SEC}	Growth rate parameter for the secondary α-phase
θ	Boundary misorientation angle
$\bar{\theta}$	Mean boundary misorientation angle
θ_c	Transition misorientation angle for the definition of a high angle grain boundary
θ_{cells}	Transition misorientation angle for the definition of a cell boundary
$\bar{\theta}_{LAGB}$	Average low angle grain boundary misorientation angle
θ_{glob}	Critical misorientation angle for the definition of the boundary within an α-platelet to start grooving during dynamic globularisation

$\overline{\theta_R}$	Average misorientation of the Rayleigh distribution
θ_0	Boundary misorientation angle of the formed boundaries by continuous dynamic recrystallisation
Θ	Boundary misorientation angle distribution
Θ_R	Rayleigh misorientation angle distribution
Θ_M	Mackenzie misorientation angle distribution
η	Parameter for transfer of defect into jogs on the dislocation
ρ_i	Immobile dislocation density
ρ_m	Mobile dislocation density
ρ_w	Wall dislocation density
ν	Poisson ratio
σ	Stress
σ_{ath}	Athermal stress
σ_{climb}	Stress for the climb of a dislocation dipole
σ_{th}	Thermal stress
σ_{ath}^0	Initial athermal stress
σ_{YS}	Yield stress
σ_α	Stress in the α-phase
σ_β	Stress in the β-phase
ϕ_α	α-particles of a particle size
Ψ	Supersaturation
$\Psi_{\alpha GB}$	Supersaturation for the formation of allotriomorphic α-phase
$\Psi_{\alpha SEC}$	Supersaturation for the formation of secondary α-phase
χ	Normalised subgrain size
Ω	Atomic volume

Table of contents

1. Introduction

The processing route of typical structural components of Ti and Ti alloys comprises a systematic series of heat treatments and deformation steps. The desired mechanical properties of the final product, especially toughness, fatigue, strength and ductility, are strictly related to the final microstructure. Among the main microstructural features, it can be highlighted: grain and subgrain sizes, dislocation density, phase content, morphology and size of α-phase and α-colony size. Therefore, the prediction of the microstructure evolution during a complex thermo-mechanical treatment enables the design and control of the final properties. A typical processing route for Ti and Ti-alloys can be divided into four main parts [1], as schematically shown in Figure 1. The pre-annealing treatment aims to break the dendritic structure of the cast ingots. During deformation II, the dynamic phenomena depend on the temperature of deformation, total deformation, and strain rate. The cooling after forging leads to the occurrence of static phenomena, such as static recrystallisation and phase transformation. The recrystallisation treatment III aims to form a homogeneous recrystallised microstructure and to control the size and morphology of α-phase.

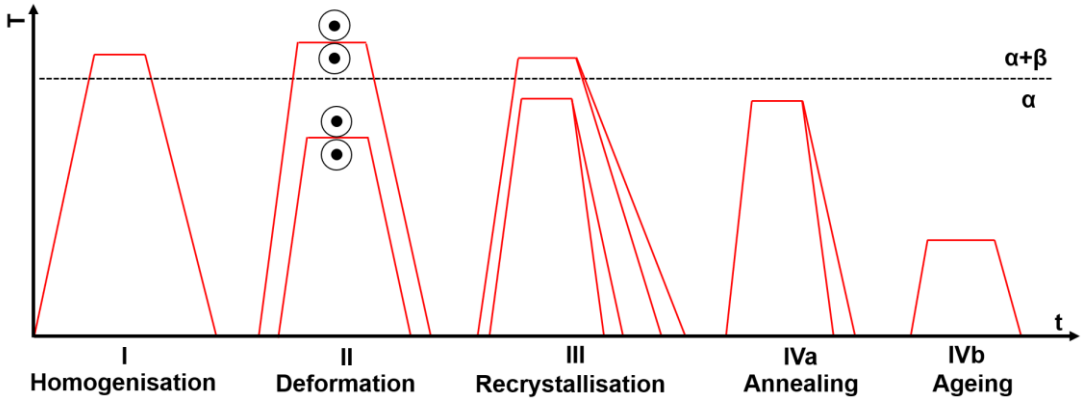

Figure 1: Schematic representation of the main thermo-mechanical cycles for Ti and Ti alloys.

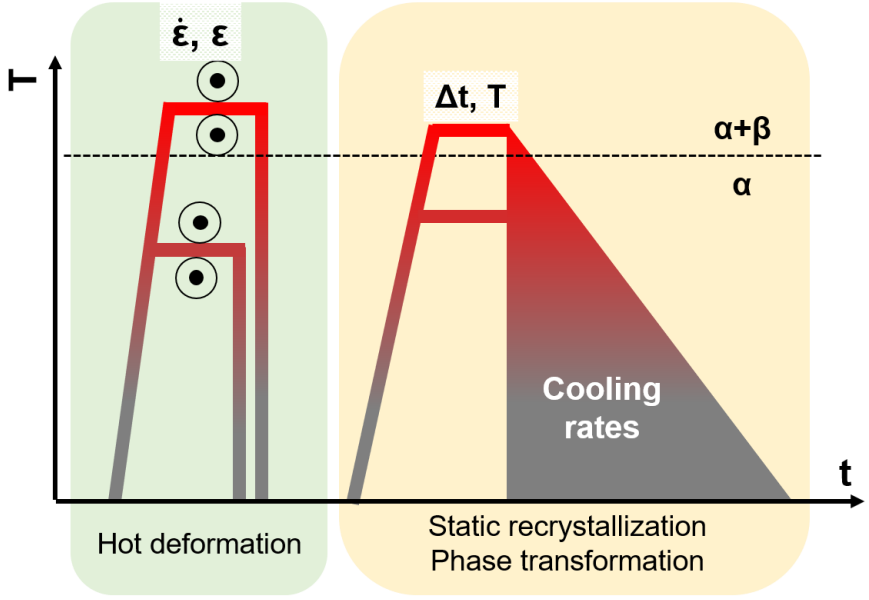

Figure 2: Schematic representation of the two performed thermo-mechanical cycles.

In this research, the steps of deformation, recrystallisation, and annealing are investigated. The schematic representation of the performed experiments is shown in Figure 2.

The typical thermo-mechanical treatments of Ti and Ti alloys can be separated into homogenisation, forging, and recrystallisation treatments. Depending on the material, further ageing can also be performed. The phenomena occurring during forging and recrystallisation treatments can be separated into dynamic and static. Post-dynamic recrystallisation as in low stacking fault energy materials was not reported and not investigated in this work. Recovery, recrystallisation and phase transformation can occur dynamically if a load is applied, or statically.

Several modelling approaches have been developed to predict the microstructure evolution due to hot deformation, recrystallisation, or phase transformation. Among them, mesoscale models are of great interest due to the possibility of being implemented as subroutines into finite element for simulation of complex components without demanding great computational effort. Moreover, the mesoscale models are also able to predict the evolution of several microstructural features as well as of the flow stress during hot deformation. Physically-based models are developed in this work, allowing the predictability of several internal variables even beyond the conditions of the experiments.

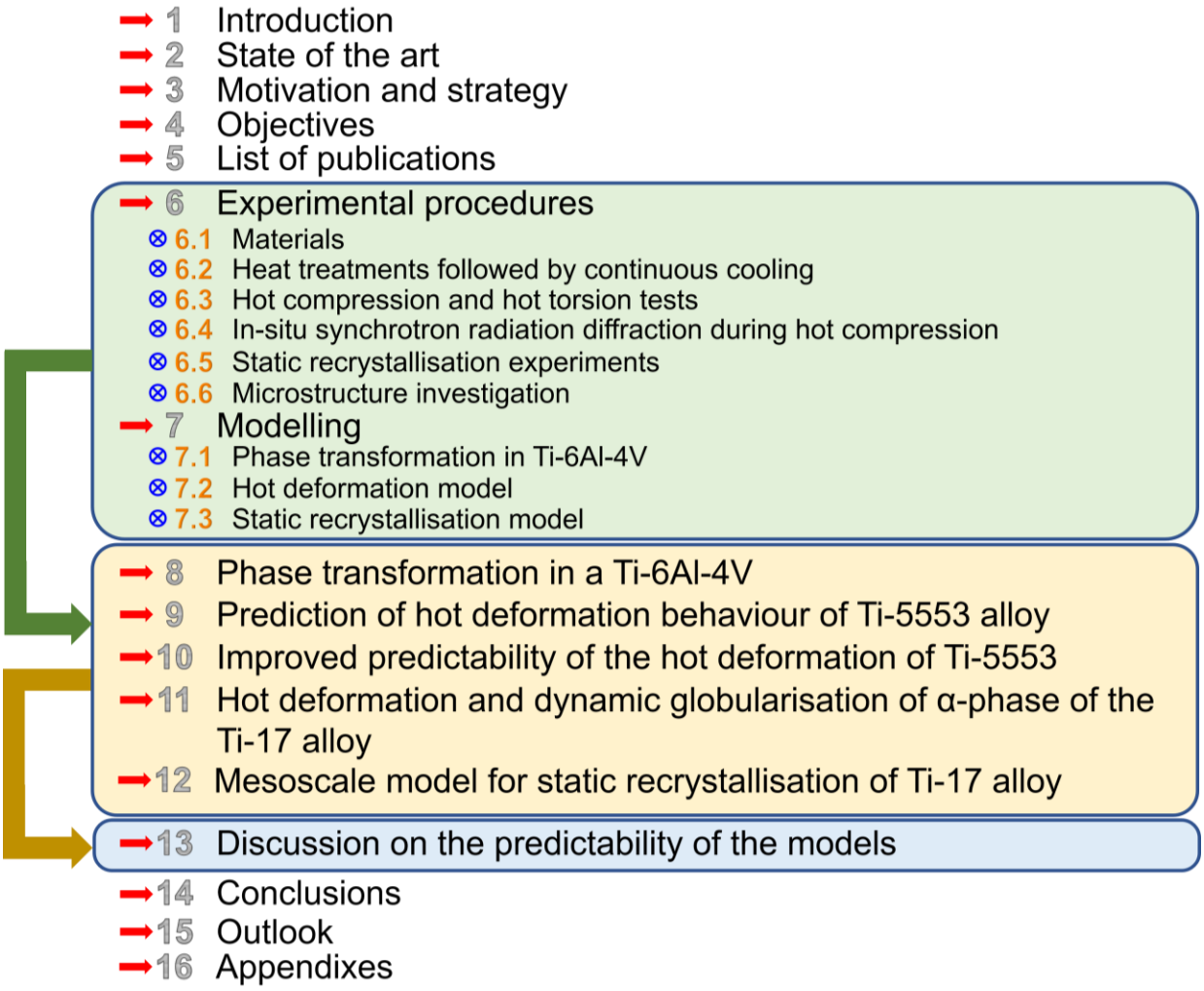

Figure 3: Organisation of the chapters of this thesis.

The organisation of the thesis can be seen in Figure 3. Chapter 2 discusses the state of the art relevant literature that supports the developed models in this thesis. The motivation of this work and the adopted strategy are presented in chapter 3. Chapter 4 describes the principal and specific objectives of this work. The already published or in press papers that are used in the following chapters are given in chapter 5. Several experiments were performed to investigate phase transformation, hot deformation behaviour, as well as static recrystallisation of different Ti alloys following the methods discussed in chapter 6.

In this work, three Ti alloys were investigated: Ti-6Al-4V, Ti-5553, and Ti-17. They are described in section 6.1. Sections 6.2 details the experimental procedures for the continuous cooling treatment carried out for the Ti-6Al-4V. The parameters and procedures for the hot compression tests performed for the Ti-5553 and Ti-17 and hot torsion tests performed for the Ti-5553 are described in section 6.3. Complementary data is obtained from synchrotron radiation diffraction measurements carried out during in-situ hot compression, and the procedures are described in section 6.4. The experimental methods for the static recrystallisation experiments performed at the Gleeble® 3800 device are given in section 6.5. Finally, the procedure and parameters adopted for the microstructure characterisation of the tested materials are detailed in section 6.6.

The thermomechanical behaviour of Ti alloys is modelled in the mesoscale, i.e. a mean value is considered to represent the material properties. Chapter 7 details the modelling strategy, subdivided into phase transformation, hot deformation and static recrystallisation. The phase transformation model is developed for the Ti-6Al-V and is described in section 7.1. The phase transformation sequence and kinetics are modelled using the exact solution of diffusion equations for the growth of spheres and platelets of α-phase immersed in a β-matrix. The hot deformation behaviour is modelled using two different approaches for dislocation density reactions and is coupled with a model of continuous dynamic recrystallisation. The coupled model predicts the evolution of subgrain and grain boundary densities as well as boundary misorientation angle. The complex load transfer between α and β-phases is considered to describe the flow softening in the two-phase domain. The change of load partitioning is correlated to the evolution of dynamic globularisation of the α-phase. The assumptions and fundamental equations of the developed coupled model for hot deformation are explained in section 7.2. The modelling ends with section 7.3 to describe static recrystallisation. The assumptions and fundamental equations of the model of static recrystallisation with the developed hot deformation model are detailed. During heat treatment, the simultaneous phenomena of static recovery, static recrystallisation, and grain growth are coupled in a mesoscale model. The static recrystallisation model is coupled with the hot deformation model, demonstrating the integration of the proposed models to predict microstructure evolution during a typical thermo-mechanical processing route for Ti and Ti alloys.

The results are discussed separately in chapters 8 to 12. Summary and conclusions of every chapter are presented separately. The kinetics and sequence of α-formation and growth are discussed in chapter 8 for the Ti-6Al-4V. The prediction of the hot deformation behaviour of Ti-5553 is separated into two chapters. In chapter 9, a simpler model for dislocation reactions is used for the simulations. Chapter 10 discusses the comparison of the microstructure formation and the simulated results using the simple model and the comprehensive model for dislocation reactions. Chapter 11 discusses a novel and fully coupled model to predict the dynamic α-globularisation,

change in load partitioning, and continuous dynamic recrystallisation using the same comprehensive model for dislocation reactions of chapter 10 but applied to the Ti-17 alloy. Finally, the measured and simulated static recrystallisation behaviour of the Ti-17 is discussed in Chapter 12.

The developed models being presented and discussed in different chapters use the same internal variables, allowing their integration in case of complex thermomechanical cycles. The main inputs and outputs of all developed models are highlighted in Figure 4. The initial microstructure is defined and depending on the active phenomenon (phase transformation, hot deformation or static recrystallisation), different outputs are obtained. A more in-depth discussion on the predictability of the developed models is presented in chapter 13.

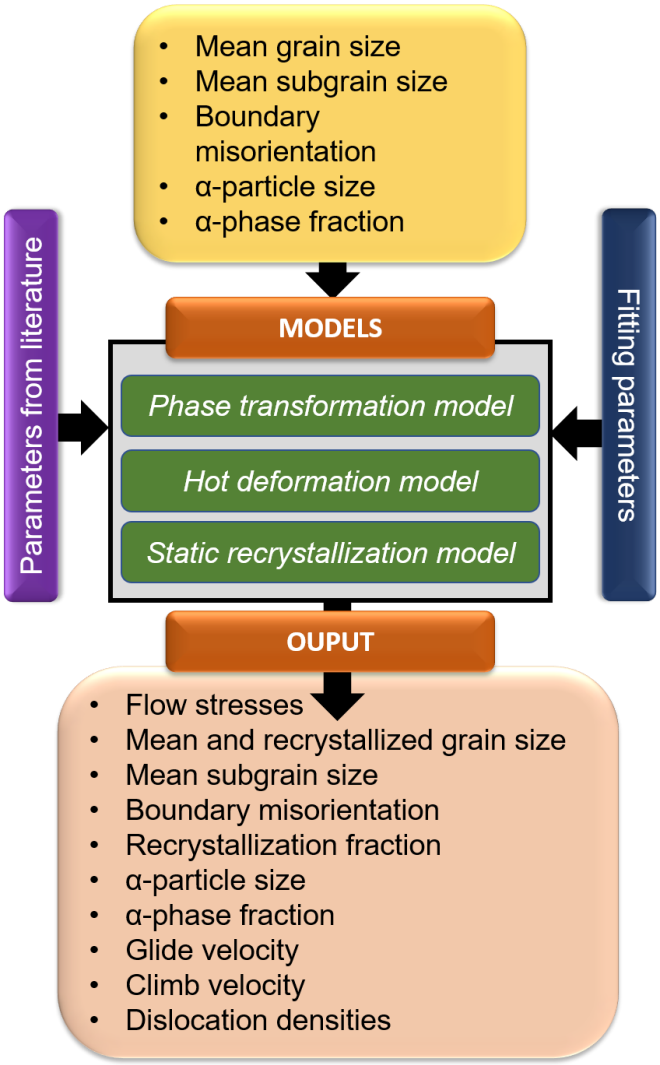

Figure 4: Schematic representation of the developed models with the main inputs and outputs.

The thesis ends with general conclusions of this work in chapter 14 separated for three major topics of this work: phase transformation, hot deformation and static recrystallisation. A short outlook with suggestions for further research is given in chapter 15. The procedure for the fitting of the constants and parameters used in the developed models as well as the obtained values are given in the Appendixes. The parameters are either obtained directly from the measurements, from established values obtained in the literature or purely by fitting.

2. State of the art

2.1. Ti and Ti alloys production and their applications

Pure titanium has a density of 4.51 g·cm^{-3}, is the heaviest light metal and stands out due to the high specific strength and excellent corrosion resistance [2]. Due to the elevated price for processing, Ti, and Ti alloys are majorly applied in the aerospace sector, the chemical industry, medical engineering, and the leisure sector [2]. The high specific strength of Ti alloys makes them attractive for structural applications up to 500°C [2].

Ti sponge is the base material for the production of all Ti-based semi-finished products [3]. Forming processes, such as forging, rolling, extrusion, and pulling, is the typical route for the production of semi-finished Ti products [3]. A tailored thermomechanical treatment concerning its requirements for application is necessary to produce high quality forged Ti products [4]. The typical processing route consists of mixing forging stock, Ti sponge, and master alloys, pressing to briquettes, vacuum arc re-melting until the production of a cast ingot [4]. The ingot is processed to billets or bars using radial forging and/or hand forging [4]. This stage aims to break up the cast structure and to produce a homogenous microstructure. The latest step is the hand or die forging up to the required dimensions before the following heat treatments and final machining [4].

2.2. Alloy classification

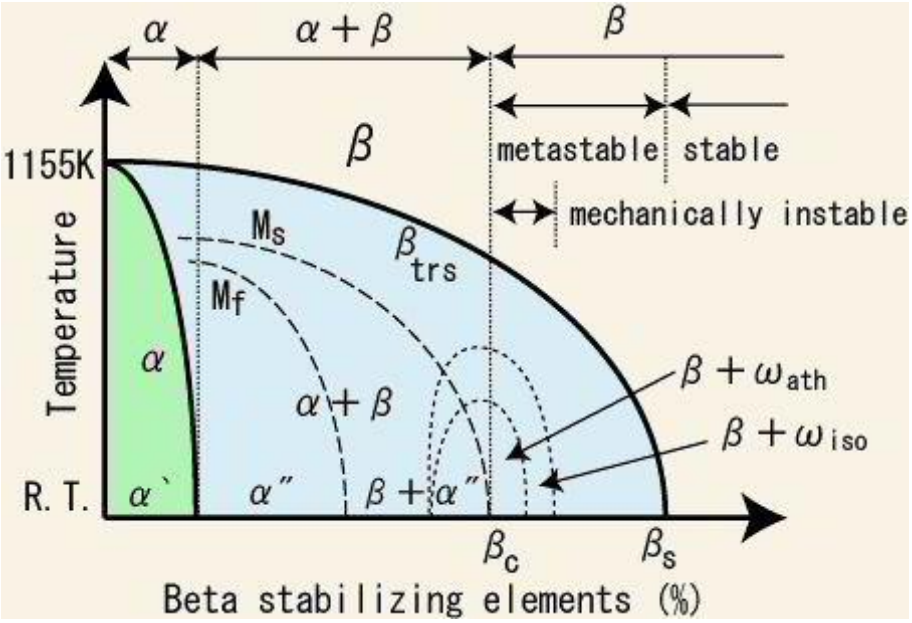

Figure 5: Schematic phase diagram for Ti alloys with the different alloys types and possible phases. [5]

Like several other metals (Ca, Fe, Co, Zr, Sn, Ce, Hf), Ti occurs in various crystals structures. Pure Ti crystallises at low temperatures in a modified, ideally hexagonal closed packed (hcp) structure, α-phase [2]. A body-centred cubic (bcc) structure is formed at high temperatures, β-phase. During cooling from the β-domain, the most densely packed planes of the β-phase {110} transform to the basal planes {0001} of the α-phase [2]. The β/α transformation causes a slight atomic distortion, leading to a slight contraction of the c-axis relative to an ideally hcp structure [2].

Different alloying elements can be added to Ti, and they are classified as neutral, α-stabilizers, or β-stabilizers. The α-stabilizers extended the α-phase field to higher temperatures. Al, O, N, and C belong to this category. The β-stabilizers shift the β-phase field to lower temperatures, and Mo, V, Ta, Fe, Mn, Cr, Co, Ni, Cu, Si, and H are the main elements. Sn and Zr are considered neutral elements due to minor influences on the β-transus temperature [2]. Commercial Ti alloys can be classified into three different categories: α, α+β, and β alloys. This classification takes into account the position in the pseudo-binary section of a β isomorphous phase diagram, Figure 5 [5].

2.3. Phase transformation in Ti alloys

Martensitic or diffusion-controlled nucleation and growth process are the types of transformation of the β-phase to the α-phase in CP Ti and Ti alloys, and it depends on cooling rate and alloy composition [1].

2.3.1. Martensitic transformation

The mechanism for martensite transformation is a cooperative movement of atoms by a shear-type process resulting in a microscopically homogeneous transformation of the β-phase into the hexagonal crystal lattice over a given volume. The martensite volume is normally plate-shaped or disk-shaped for most Ti alloys. This hexagonal martensite is termed as α' and is observed in two morphologies: massive martensite (lath or packet martensite) and acicular martensite [6]. Massive martensite occurs only in pure Ti, very dilute alloys, and in alloys with a high martensitic transformation temperature. The lower martensitic transformation temperature is favourable for the occurrence of acicular martensite with higher solute content [1].

The higher the solute content, the higher the distortion in the hexagonal structure of the martensite. The crystal structure loses its hexagonal symmetry and must be described as orthorhombic [6]. This orthorhombic martensite is designated α''. In many alloys in which the martensitic reaction is suppressed, the β-phase decomposes upon quenching in an athermal process leading to the formation of the athermal ω phase of extremely fine particles (size 2-4 nm). The ω particles have a diffuse, coherent interface, and the structure is an elastically distorted bcc lattice [1].

2.3.2. Nucleation and diffusion growth

If the cooling rates from the β-domain into the α+β domain are sufficiently low, the α-phase first nucleates preferentially at β-grain boundaries forming a continuous α-layer. The α phase is incoherent with respect to the β-phase. The α-plates nucleate either at the interface of the continuous α-layer or at the β grain boundary itself during continued cooling and grow into the β-grain as parallel plates belonging to the same variant of the Burgers relationship and are called α-colony. The crystallographic relationship between α and β plates within a colony is schematically shown in Figure 7b: $(110)_\beta || (0002)_\alpha$ and $[1\bar{1}1]_\beta || [11\bar{2}0]_\alpha$ [1]. The flat surface of the α-phase is parallel to the $(\bar{1}100)$ plane of the α-phase and parallel to the $(\bar{1}12)$ plane of the β-phase [1]. They continue to grow into the β-grain interior until they meet other α-colonies nucleated at other grain boundary areas of the β-grain and belonging to other variants of the Burgers relationship. This process is often called sympathetic nucleation and growth. The individual α-plates are separated

within the α-colonies by the retained β-matrix, forming the often called α and β lamellae, and the resulting microstructure is then designated as lamellar [1].

2.3.3. Types of formed microstructure in α+β and near-β alloys

The processing parameters of the industrial thermo-mechanical treatments of Ti alloys depend on the alloy and desired microstructure because the mechanical properties of Ti alloys, especially fatigue resistance, toughness and ductility, are strictly correlated with its microstructure [1]. Three types of microstructures are typically found in α+β and near-β Ti alloys: globular, lamellar, and bimodal. The typical microstructure is shown in Figure 6. Near-α alloys and commercially pure Ti exhibits a typical one-phase microstructure at room temperature since β-phase transforms completely into α or α'.

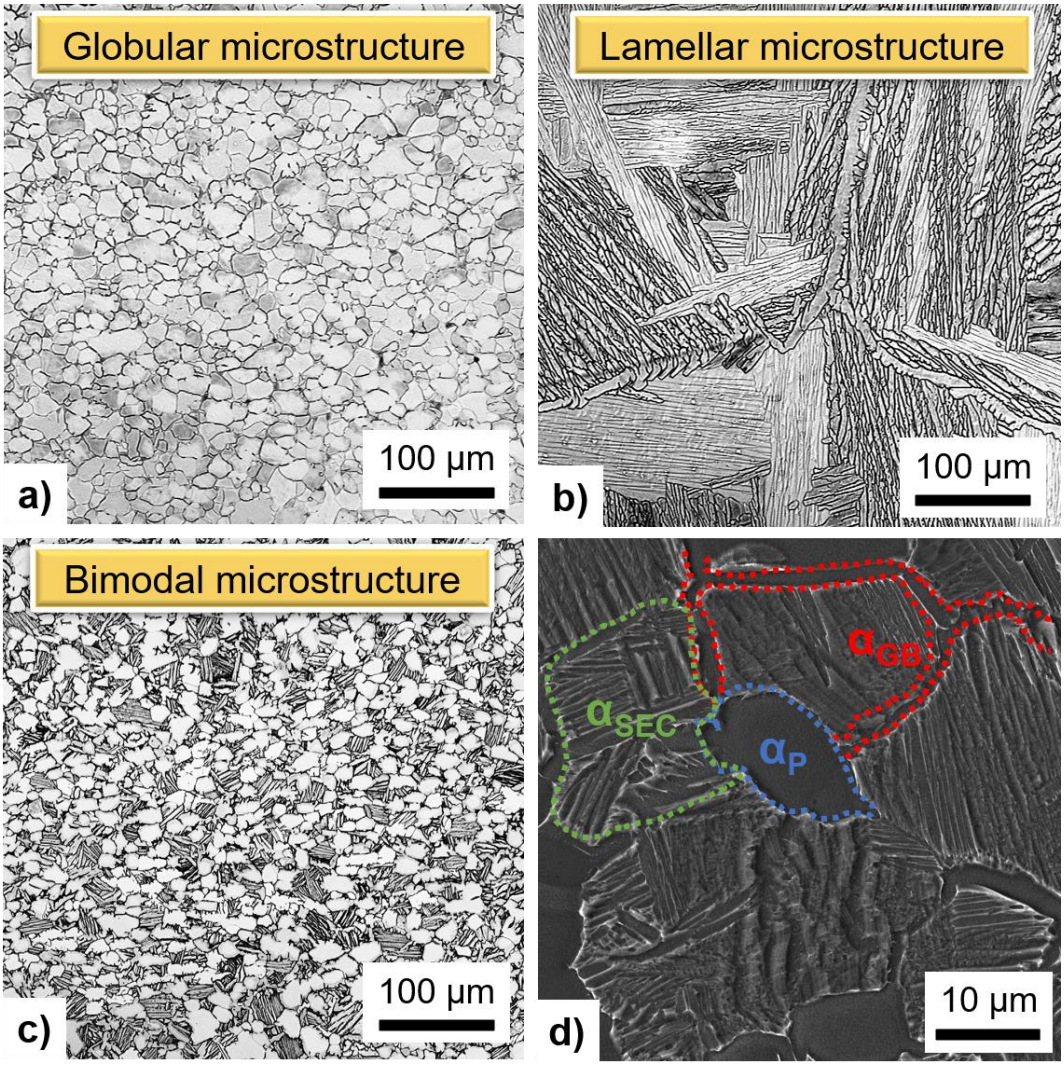

Figure 6: Possible formed microstructures in α+β or near-β alloys and illustrated for a Ti-6Al-4V: a) Globular; b) lamellar; c) bimodal; d) a detailed view of the bimodal microstructure with the α_P, α_{GB} and α_{SEC}.

A bimodal microstructure consists of lamellar α or secondary α (α_{SEC}) and globular primary α (α_p) and offers the combination of high ductility and high toughness [1]. Figure 7a shows the formation of the bimodal microstructure during cooling. The globular α_p phase grows during cooling, while lamellar or secondary α (α_{SEC}) nucleates and grows at the prior β grain boundaries

and α_p. Moreover, the third morphology of α-phase, named allotriomorphic α (α_{GB}), forms as platelets along the grain boundaries during cooling.

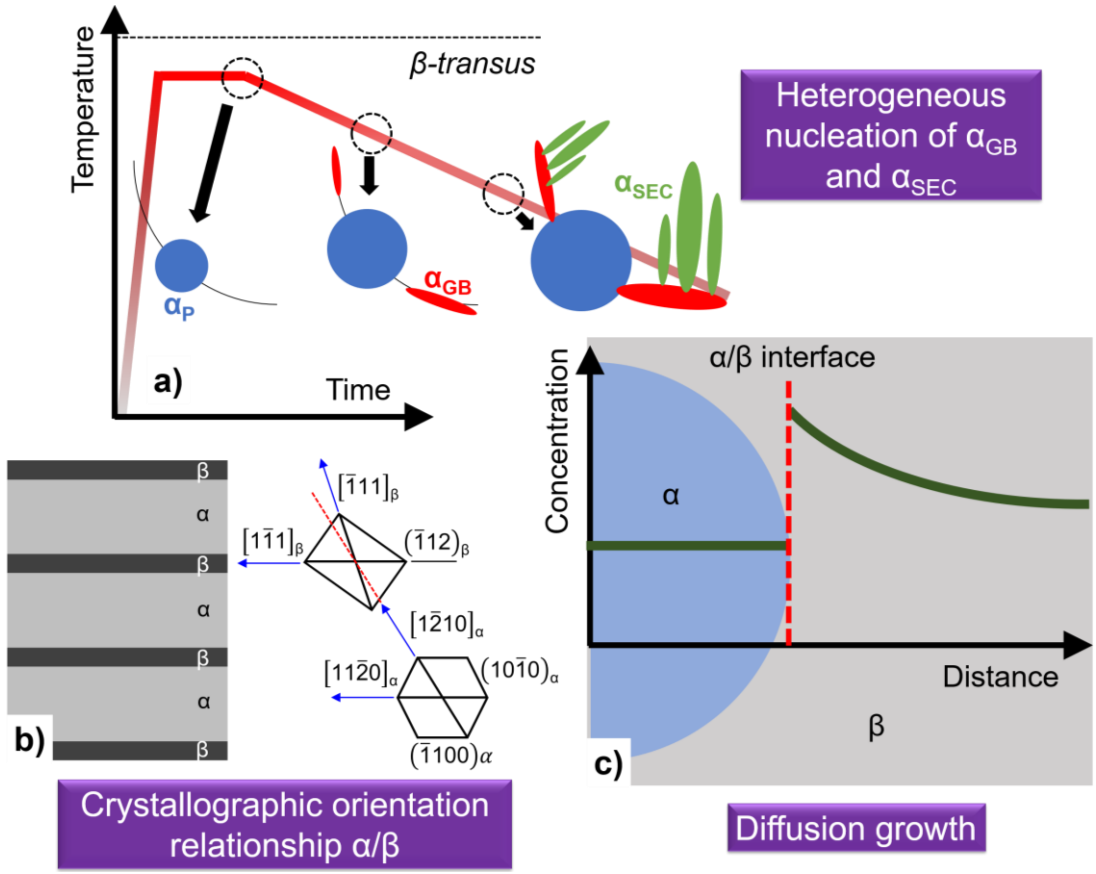

Figure 7: a) Schematical representation of the formation of bimodal microstructure during cooling with the growth of α_P, as well as heterogeneous nucleation and growth of α_{SEC} and α_{GB}; b) Schematical representation of the crystallographic relationship between α-plates and β-matrix in α-colonies [1]; c) Schematical representation of the formation of supersaturation of slow diffusing β-stabilizing elements at the α/β interface.

The growth of α_p, α_{GB} and α_{SEC} phase is diffusion-controlled. Supersaturation of slow diffusing β-stabilizing elements at the α/β interface is formed during cooling and is the driving force for growth, as schematically shown in Figure 7c. The inter-diffusion coefficient of the slowest diffusing element controls the growth kinetics. For very slow cooling rates, the β-phase transforms mainly into α_p. Thus, the resulting microstructure consists of almost only large equiaxed α_p with small amounts of retained β-phase [7]. The amount of α_p decreases for increasing cooling rates, when other morphologies of α-phase are formed [8]. Semiatin et al. [9] observed that α_p exhibits epitaxial growth for Ti-6Al-4V controlled by the diffusion of V in the β-phase. The growth of α_P competes with the formation of α_{SEC} and α_{GB} for intermediate cooling rates (between 5 to 300°Cmin^{-1}) [9,10]. The retardation and finally the end of α_p growth with decreasing temperature during cooling can be attributed to two simultaneous effects related to the formation of α_{SEC} and α_{GB}: 1) a geometric restriction for growth (pinning effect), and 2) a decrement of the supersaturation of elements in the β matrix. Formation of α_{SEC} occurs in colonies (Figure 7b). They nucleate at β-grain boundaries, but if they cannot fill the whole grain interior, then nucleation on boundaries of other colonies also occurs [1]. The new α-plates tends to nucleate nearly perpendicular to the parent one to minimise the overall elastic strains, leading to the formation of

a characteristic microstructure called “basket wave” or Widmanstätten [1]. For a given cooling rate, the “basket wave” structure is more pronounced in alloys with higher contents of slow diffusing β-stabilizing elements [1].

The nucleation rate and growth of α_{GB} depend on the cooling rate and follows a platelet-like formation [7,9]. However, extensions from α_p with the same crystallographic orientation were observed preferentially along the β/β boundary, suggesting that the formation of α_{GB} can also occur from α_p [8]. Sun et al. [11] observed for a near-α alloy TA15 (Ti-6Al-2Zr-1Mo-1V) cooled from the β-domain preferential nucleation of α_{GB} at triple junctions of the β-grains, followed by growth to one side of the grain boundary forming a flat plate. The α_{GB} can also nucleate from the middle of one β/β grain boundary due to high levels of local supersaturation, forming an unconnected layer of α_{GB}. The formation of α_{GB} depends on the available energy and time for growth. Therefore, different morphologies of α_{GB} were observed: flat, zig-zag, and a mix of both.

2.3.4. Modelling phase transformation in Ti alloys

Different modelling approaches were proposed for the β→α phase transformation [12–20]. The classical Johnson-Mehl-Avrami-Kolmogorov (JMAK) equation was applied to predict the phase transformation kinetics in Ti-6Al-4V [12]. The growth of α_{GB} was modelled using the diffusion solution for the growth of plate-like particles [13], ellipsoid particles [13,14], and via ledge growth [13,15,16]. A cellular automaton model based on diffusion, mixed, and interface phase transformation was proposed by Song et al. [17] for phase transformation in titanium alloys. Phase-field models were also developed [18–20] and showed notably accuracy to predict the growth of particles in the case of complex supersaturation fields in the particle growth front [19].

Semiatin et al. [9] proposed a model for the growth of α_p using the exact solutions of diffusion equations with the following considerations: a) the diffusion coefficients were corrected with a thermodynamic factor for the specific composition of the material, and b) the supersaturation degree reached during cooling is the driving force for the diffusion process [9]. Meng et al. [21] complemented the model proposed by Semiatin et al. [9] by considering the effect of thermal history on the diffusion field around the α_p and the overlap of diffusion fields of growing phases [22].

Extensive modelling of the formation of α_{SEC} was performed by Katzarov et al. [23]. The morphology, distribution, and geometry of the α_{SEC} were simulated using finite element modelling implemented to solve the diffusion equation on the domain occupied by the β-phase. A random nucleation model as a function of the supersaturation of V in the matrix was implemented for 1-D and 2-D simulations of the formation of α_{SEC} without considering the presence of α_P. It was observed that lower cooling rates lead to a faster transformation of $\beta \rightarrow \alpha_{SEC}$, considering the same temperature. Additionally, the thickness dependency of the α_{SEC} on temperature during isothermal treatment was also measured and simulated. Despite the broad capability of prediction of the model proposed by Katzarov et al. [23], the model was developed only for β→α transformation from the β-field, and not from the α+β field. Using a similar approach, the formation of α_{SEC} in competition with the epitaxial growth of α_p was modelled and simulated for a TA15 alloy [10] using the diffusion of Mo in β-phase as the controlling mechanisms. The growth of α_{SEC} was proposed to be a competition between direct interference from interface stability, the no misorientation

between the nucleating plate and the substrate, and sympathetic nucleation, where low angle boundaries exist between the nucleating plate and the pre-existing matrix.

2.4. Hot deformation behaviour of Ti-alloys

The hot deformation mechanisms are intrinsically related to the stacking fault energy of a material [24]. Low and high stacking fault energy alloys deformed at high temperatures typically undergoes a complex microstructure evolution attributed to the distinct role of dynamic recovery (DRV) and dynamic recrystallisation (DRX) [25]. Recovery is a phenomenon generally described as the reorganisation of dislocations with the formation of subgrains or cells [26]. Furthermore, several types of mechanisms of DRX have been proposed, such as discontinuous dynamic recrystallisation (DDRX) [27,28], geometric dynamic recrystallisation (GDRX) [29], and continuous dynamic recrystallisation (CDRX) [25]. They have in common the phenomena of movement of high angle grain boundary (HAGB) and the formation of new grains. The DDRX takes place through the nucleation of new grains and their growth, consuming the deformed material [30]. On the other hand, the impingement of HAGBs due to refining the grains is the fundamental concept of GDRX. CDRX [31] and GDRX can occur at large strains [32]. CDRX is characterised by the progressive and continuous process of formation of subgrain boundaries, the increment of their misorientation due to lattice rotation, and the progressive transformation into HAGBs [33]. On the other hand, during GDRX, HAGB gets closer during deformation until the serrated boundaries come into contact, splitting the grain into grains with sizes in the order of the subgrain size.

In low stacking fault alloys, the formation of a defined substructure is limited due to the formation of partial dislocations or stacking faults limiting the movement of dislocations and then, the role of DRV [34]. High stacking fault alloys exhibit accelerated recovery, and a well-defined substructure is formed at high-temperature deformations [35].

In this chapter, the hot deformation behaviour of α and β-phases is presented.

2.4.1. α-phase

The deformed microstructure results from the DRV and consists of subgrains, sharp LAGBs, and dislocation networks between subgrains. Slip occurs on the {0001} basal, $\{10\bar{1}0\}$ prismatic, as well as on the $\{10\bar{1}1\}$ pyramidal planes. Thus, the critical resolved shear stress values in all slip planes are comparable at temperatures above 600 K [36]. Planar slip is predominant below 500 K, changing to wavy slip at temperatures between 500 and 800 K, and above 800 K slip is random and equally probable in all slip planes [36]. Intense cross-slip-assisted DRV plays a role at temperatures above this threshold, leading to marginal strain hardening [36]. Al plays a major role in defining the slip behaviour due to solid solution hardening [36].

Globularisation of the α-phase occurs during hot compression in the α+β field, as is shown in Figure 8. It decreases its activity with an increase in temperature [37]. Figure 8a shows a typical micrograph where the grooving of the α/β interfaces are indicated by the dashed red curves and pointed by the violet arrows. Formation of subgrain boundaries within α-platelet is Figure 8c [38], and the wedge of the β-phase into the α-phase leading to their separating is shown in Figure 8e [38]. According to Jackson et al. [39], two possible mechanisms can describe for the transformation of lamellar α-phase into shorter segments during hot deformation. One mechanism suggests that both low and high angle grain boundaries are formed across α-phases and that the β-phase can

penetrate into the lamellar α-phase along these boundaries. If the α-lamella width is small, the separation of α-phase will occur faster. The diffusion of alloying elements through the bulk or along the interfaces would control the penetration rate. This mechanism is illustrated in Figure 8d, considering the diffusion of Al and V for the α and β-phase, respectively. The second mechanism is related to the localised shear and rotation of the α-lamella during hot deformation. The penetration of β-phase into the α-phase along shear lines may also occur, separating the α-lamella into shorter segments [40]. Yu et al. [38] proposed that the globularisation process should occur in four stages: 1) subgrains form in the α-plates due to DRV; 2) migration of subgrains due to α/β interfacial instability and thermal grooving; 3) an interface migration occurs promoting the β-phase to wedge into the α-phase; 4) the α-laths disintegrate due to diffusion and grain boundary sliding.

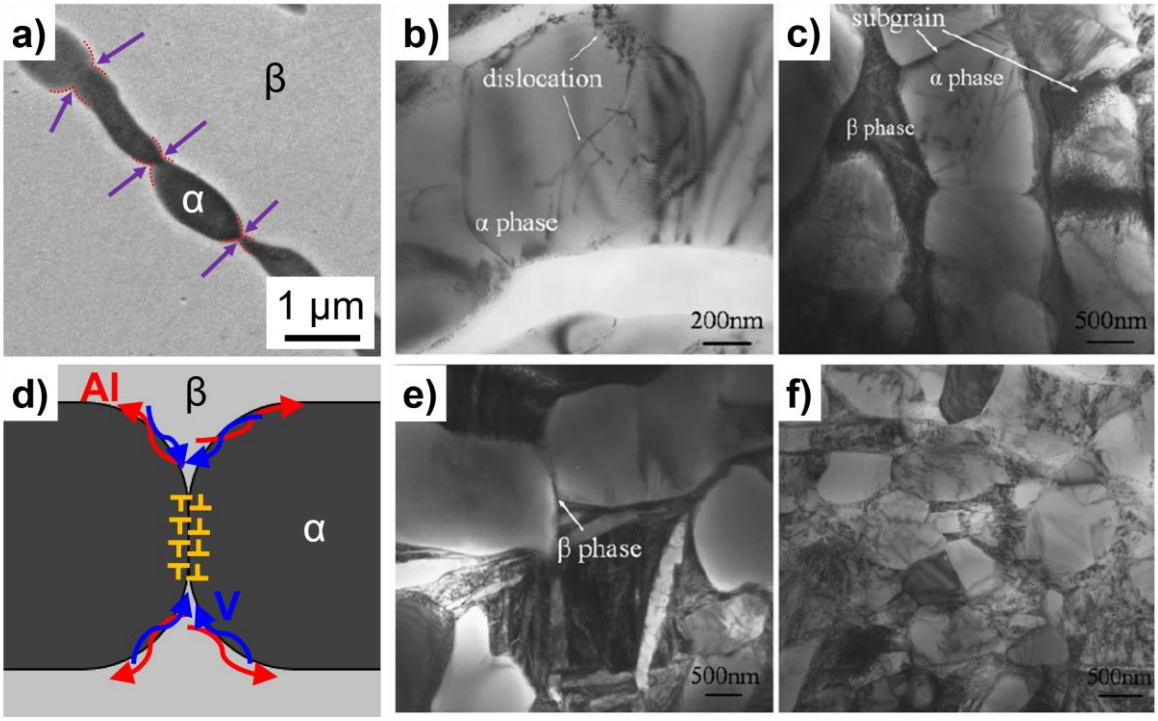

Figure 8: Typical micrographs for the dynamic α-globularisation: a) Grooving of α/β interface for a Ti-17; (b,c,e,f) [38] micrographs from transmission electron microscopy (TEM) showing b) accumulation of dislocations in α-phase, c) formation of subgrains in α-platelets, e) wedge of β-phase into α-phase, f) formation of globular α-phase; d) schematical illustration of the thermal grooving at boundaries within α-phase with the diffusion of α (Al) and β (V) stabilising elements.

Finally, efficiency in the separation of the α-phase is increased by decreasing the deformation rates. It is suggested that if the strain rate is relatively low, dynamic globularisation has sufficient time to occur [41]. Similar findings were observed for the globularisation of the α-phase for Ti-17 (Ti-5Al-2Sn-2Zr-4Mo-4Cr, wt.%) alloy [42–45]. Sun et al. [42] explain the dynamic globularisation of the α-phase as the result of rotational recrystallisation and GDRX.

2.4.2. β-phase

It is reported in the literature that the restoration mechanisms that can dominate during the hot deformation of the β-phase are related to temperature, strain rate, and phase volume fraction [46]. Furuhara et al. [47] showed that the presence of α-phase enhances the DRX of the β-phase. No detail or statement was addressed to the type of DRX (continuous, discontinuous, or

geometric). Moreover, DRX of the β-grains was previously proposed to be the main deformation mechanism in the β-field [48]. Furthermore, the deformation mechanisms of the β-phase were studied by Li et al. [49] for a series of heat-treated Ti-17 alloy. A high misorientation spread within the β grains, accompanied by local texture, was observed in regions of globularised α-platelets. Moreover, advanced stage of CDRX in the β-phase with the formation of new HAGB is observed in areas where the α-platelets were kinked, while only subgrain formation via DRV was observed in the other regions [49].

Other investigations suggest DDRX as the active recrystallisation mechanism in Ti alloys [28,50–60] and that the applied strain rate controls the occurrence of DDRX or CDRX. They propose that at low strain rates promote strain-induced boundary migration (SIMB) [61], leading to the formation of new DDRX grains formed at triple junctions, while CDRX can occur by increasing the strain rate.

Finally, Poletti et al. [62] proposed a unified description of the softening behaviour of a β-metastable and a Ti-6Al-4V alloy. The combination of fast cooling rates and reconstruction of the parent beta phase from electron backscattered diffraction (EBSD) measurements enabled the conclusion that DRV is the restoration mechanism for the β-phase during hot deformation. At large strains, the β-phase undergoes DRV [62] followed by CDRX [63] or GDRX [64,65].

2.4.3. Investigated alloys: Ti-5553 and Ti-17

Ti-5553 (Ti–5Al–5Mo–5V–3Cr, wt.%) is a near β-Ti alloy with excellent workability and a good combination of strength and ductility [66]. The usual processing route includes plastic deformation at high temperatures, mainly aiming to tune the microstructure to adjust the performance of the product during service. Ti-17 (Ti-5Al-2Sn-2Zr-4Mo-4Cr, wt.%) is a 'beta-rich' α+β Ti alloy that was designed to achieve 25% higher strength compared to Ti-6Al-4V, fracture toughness of 65 MPa.$m^{1/2}$, and uniform hardening behaviour in sections as big as 150 mm^3. Its applications correspond to gas turbine engine components, such as disks for fan and compressor stages [67]. Like many Ti alloys, forging followed by heat treatments is the typical processing route of this alloy.

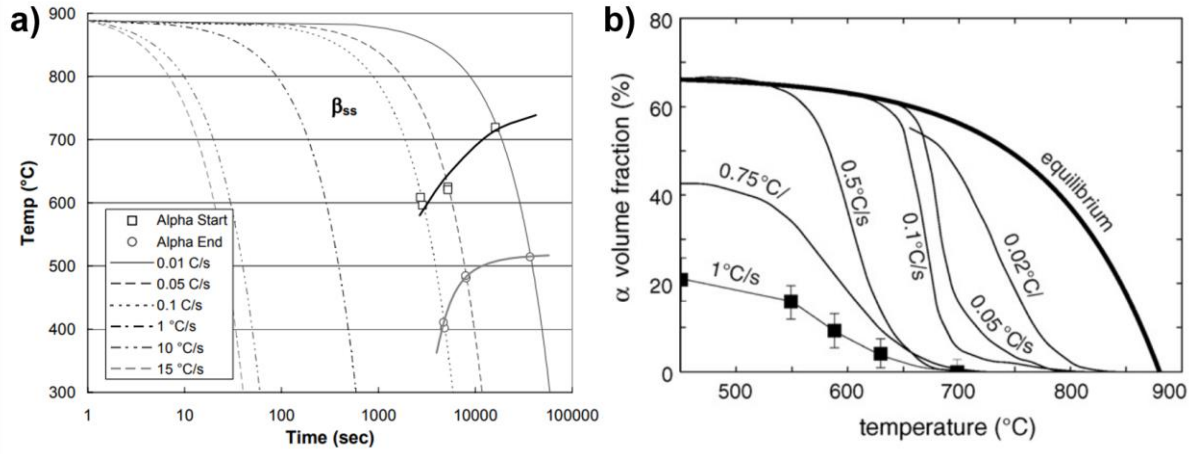

Figure 9: Continuous cooling transformation (CCT) diagrams for the: a) Ti-5553 [68]; b) Ti-17 [69].

Figure 9(a,b) shows the continuous cooling transformation (CCT) diagram for the Ti-5553 and Ti-17, respectively. The formation of α-phase for cooling from the β-domain starts at temperatures as low as 700°C for both alloys and comparing the same cooling rate, occurs first for the Ti-17 compared to the Ti-5553. Moreover, for cooling rates higher than 30°C/min (0.5°C/s), retained β-phase will be retained for the Ti-17. For cooling rates higher than 60°C/min (1°C/s), β-phase is totally retained for the Ti-5553 at room temperature.

The microstructure modification during hot deformation was investigated [41,42,44,49,70], and dynamic globularisation of the α-phase [42–45] is responsible for the flow softening observed during deformation in the α+β domain. The hot deformation behaviour of Ti-17 with different initial primary α-phase morphologies was investigated in [70]. Higher values of stresses at the peak stress were observed for the material with lamellar microstructure. The initial microstructure did not influence the flow stress at a steady state.

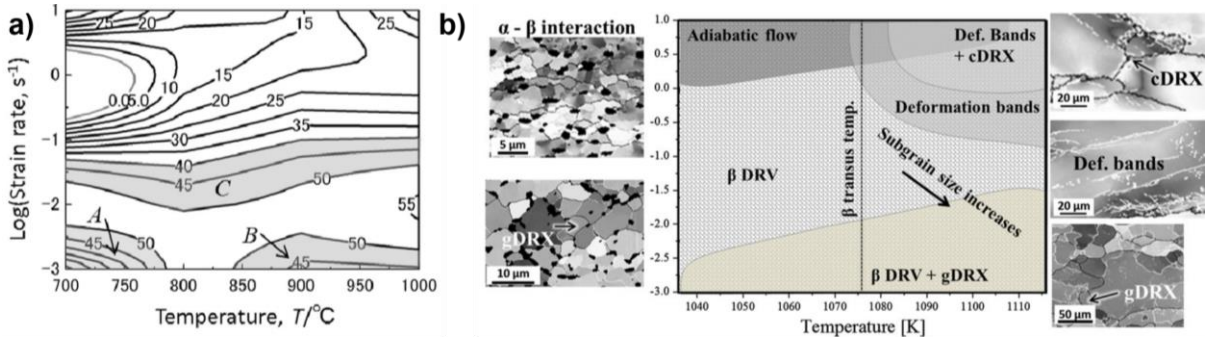

Figure 10: a) power dissipation map for a Ti-5553 alloy [63]. A, B, and C indicate regions where grain boundary sliding, DRV, and CDRX are proposed as deformation mechanisms; b) summary of deformation mechanisms found in a Ti-55531 up lo a local strain of 0.7 [64].

A power dissipation map obtained for the hot deformation of a Ti-5553 alloy [63] is shown in Figure 10. The regions A, B and C indicate domains of stable flow. A is associated with grain boundary sliding and superplasticity, B with a dominant effect of DRV and C with CDRX due to intensive formation of LAGBs [63]. Overall, any deformation below 0.1 s^{-1} seems to lead to stable flow for the Ti-5553. A summary of proposed deformation mechanisms as well as typical microstructures of a Ti-55531 alloy is shown in Figure 10b [64]. DRV, gDRX and cDRX are observed for different temperatures and strain rate regimes, while adiabatic flow and deformation bands occur at high strain rates.

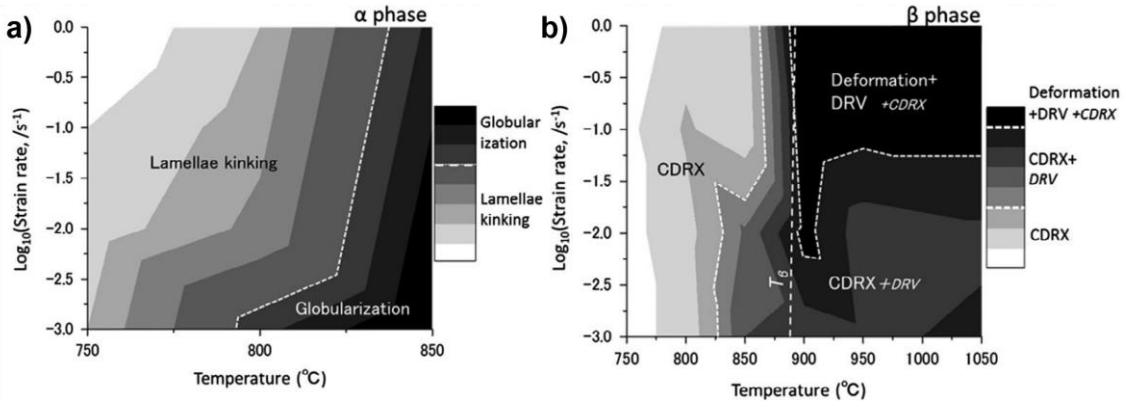

Figure 11: Proposed mechanisms of deformation for a Ti-17 [71] for the: a) α-phase; b) β-phase.

The deformation mechanisms related to the energy dissipation are shown in Figure 11 for the processing maps for a Ti-17 [71]. Two different mechanisms of deformation in the α-phase are identified: lamellae kinking and globularisation. High strain rates and low temperature promote lamellae kinking, while high temperature and low strain rate promote dynamic globularisation of α-phase. Three different mechanisms are proposed for the β-phase: DRV, CDRX and "deformation" [71]. The last one is associated with the formation of a deformed microstructure without a notable formation of LAGBs nor HAGBs. CDRX occurs in the α+β domain, while CDRX and DRV are indicated as main mechanisms in the β-domain for low strain rates. The increase in train rate leads to the formation of deformation within the β-phase, associated with the formation of misorientation spread without the formation of LAGBs nor HAGBs.

2.5. Mesoscale modelling of the hot deformation behaviour

Physical models based on internal variables such as the dislocation density evolution have been developed to predict the stress relaxation [72,73], anisotropic yield behaviour [74,75], cyclic strain-strain behaviour [76], adiabatic shear banding [77], work hardening [62,78,79], up to extremely high strain rates [80], and DRV and DRX of different materials: general and multiscale DDRX description [27], plain carbon steels [81], high grade steel [82,83], Ni superalloy [84,85], Cu alloys [86,87], Ti-6Al-4V [57] and Ti-Nb-Al alloys [88].

From discrete dislocation dynamics [89] to phenomenological approaches [90,91], the hot deformation behaviour of metallic alloys has been modelled and predicted. Among the methods that showed considerable predictability power when implemented for simulations of complex parts, the mesoscale models are of great interest [71]. Initial attempts to develop dislocation density-based models for metal plasticity were made by Kocks [92], Bergström [93], Bergström and Roberts [94], Roberts and Bergström [95] and Mecking and Estrin [96]. These initial attempts to model fundamental material physics were later developed to include more detailed and complex mechanisms. Bergström [97] partitioned dislocation density into mobile and immobile. Another approach followed by Estrin et al. [98] was to split dislocations into low dislocation density channels and high dislocation density walls with separate evolution equations. Feaugas [99], Feaugas and Gaudin [100] extended this to account for kinematic hardening by separating the immobile dislocation density to walls and channels. Barlat et al. [101] used a similar framework with forest and reverse dislocation densities to describe the Bauschinger effect. Statistically Stored Dislocations and Geometrically Necessary Dislocations used by Arsenlis et al. [102] and Cheong et al. [103] are fundamentally similar to Estrin's model (Estrin et al. [98]). Ghoniem et al. [104] proposed a dislocation-based model to describe the creep behaviour of steels, comprising of comprehensive rate equations to account for the several dislocation density reactions that can occur in a mesoscopic scale. The hot deformation behaviour of Ti and Ti alloys was also simulated using dislocation density-based models [105], [106],[107]. The prediction of the deformation behaviour of a Ti-6Al-4V over a wide temperature range was achieved [107], while constitutive equations applied to room temperature deformation were developed to describe the complex deformation mechanism [105]. The influence of the chemical composition on the deformation behaviour of a Ti-6Al-4V is considered in the constitutive equations proposed by Picu and Majorell [106].

2.6. Load partitioning in two-phase Ti-alloys

Among the proposed models for Ti-alloys, either only the deformation of one phase for the α+β domain is considered [52,60] or the distinction each phase is neglected [50,55–57]. Self-consistent models have been successfully applied to predict the hot deformation behaviour of two-phase materials [51,108–110]. The anisotropic deformation behaviour between α and β-phase is related to the strain partitioning as well as Hall-Petch strengthening between α and β-phases [111,112]. The deformation of hard platelets of α-phase immersed in a softer β-matrix occurs differently for both phases. As explained in [113–115], iso-strain, iso-stress, and iso-power conditions have to be taken into account. The change in load transfer mechanism between both phases explains the observed flow softening in the α+β domain.

2.6.1. Initial α-lamellar structure

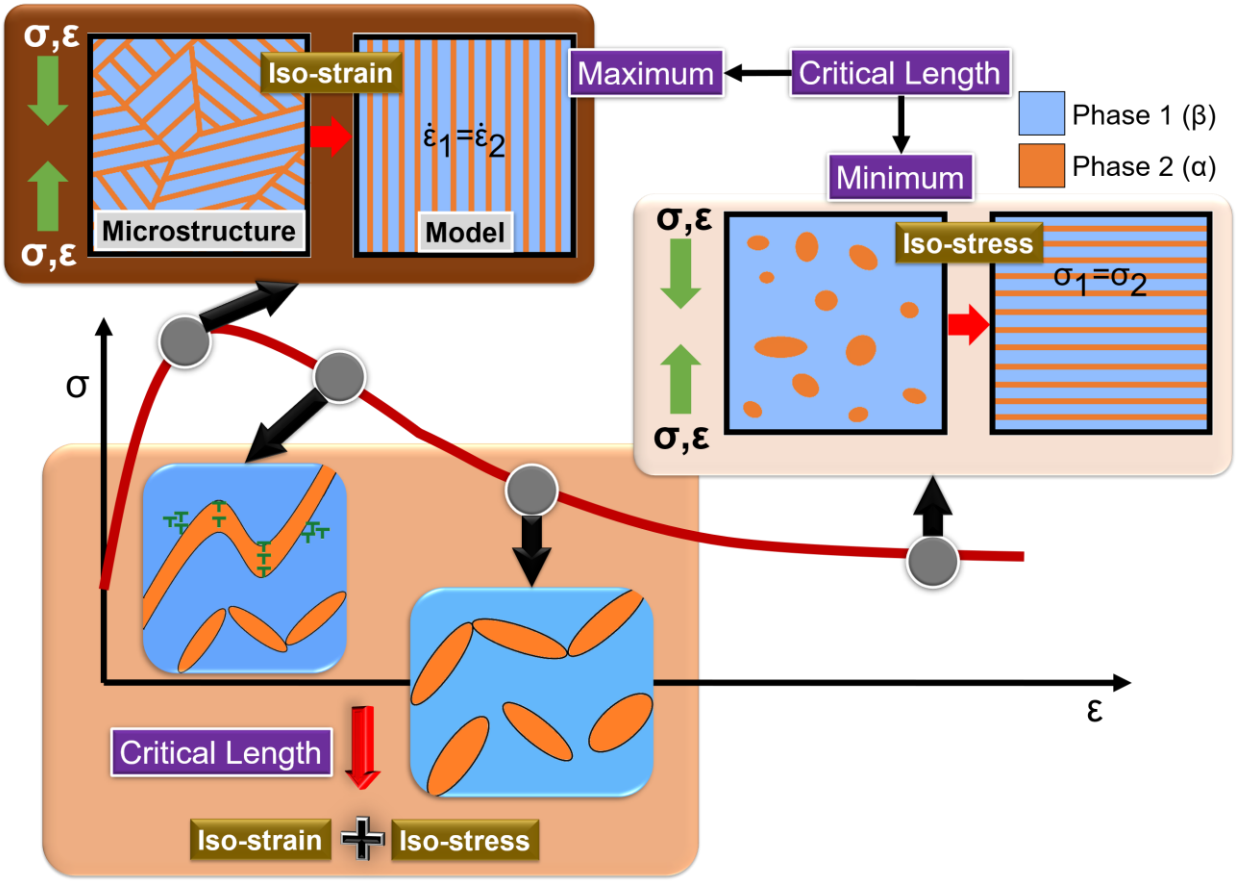

Figure 12: Schematical representation of the evolution of the load partitioning between α and β-phases from iso-strain to iso-stress regime

The flow softening in the α+β domain from a starting α-lamellar structure is attributed to the process of dynamic α-globularisation [44,116,117]. It was proposed that dynamic α-globularisation is a type of DDRX [52] that consume a notable large dislocation density formed within the α-phase. However, the process of globularisation consists of a progressive formation of boundaries within the α-platelets and grooving of the α/β interfaces until the complete separation of the formed α-particles is achieved [42,44]. The flow softening must be related to the transformation of a platelet of an initial aspect ratio into smaller grains of α-phase, and, therefore, for a change in the load partition model.

Canelo-Yubero et al. [118] observed that β-phase is majorly a load transfer agent during hot deformation for a Ti-6Al-6V-2Sn alloy, while the α-lamellae deform by rotation with respect to the crystal orientation of the β-matrix until the yield stress of α-phase corresponds to the flow stress of β-phase. Therefore, the geometric modification of the α-phase via dynamic globularisation and the stress evolution are correlated. Additionally, Canelo-Yubero et al. [118] show that the crystallographic texture an effect in the softening has, although this change is not enough to account for the whole softening. This effect is indirectly considered as a new load partition regime of overall lower stress. The change in flow partition is shown in Figure 12 and describes the combined effects that lead to a flow softening during deformation in the α+β domain without pointing at the physical phenomena.

2.6.2. Initial α-globular structure

The flow softening in the α+β domain from a starting α-lamellar structure is interpreted as a consequence of the rotation of the globular α-phase with respect to the β-matrix, leading to different plastic strain rates between α and β phases. It leads to back-stresses [99,119,120] that can be understood as internal stress built in the soft phase that can cause a local decrease of the stress withstood by the hard phase [119]. At the beginning of deformation, both phases dissipate the same energy, i.e. so-power [115] regime. Once the α-phase accommodates the plastic deformation by rotation, the iso-stress regime is reached.

2.7. Static recrystallisation phenomenon

Static recrystallisation (SRX) occurs when deformed materials are held at temperatures higher than the homologous temperature. In this case, the stored energy that is built in the material due to plastic deformation is the driving force to produce new dislocation-free grains [121]. The kinetics is temperature and stored energy-dependent and can be divided into two simultaneous processes of nucleation and growth. Nucleation consists of a crystallite of low internal energy that grows into a deformed or recovered material from which it is separated by a HAGB [121]. The number of nuclei per unit volume can either remain constant during SRX or increase. The first case is consists of saturated nucleation, and the number of nuclei is a critical parameter to describe SRX, while in the second case, the nucleation rate is the critical parameter to describe the nucleation process [121]. The nucleation sites in SRX are non-randomly distributed, and prior grain boundaries, shear bands, and transition bands are potential sites [121]. The ratio between the number of nuclei to the number of potential sites defined the overall inhomogeneous distribution of nuclei.

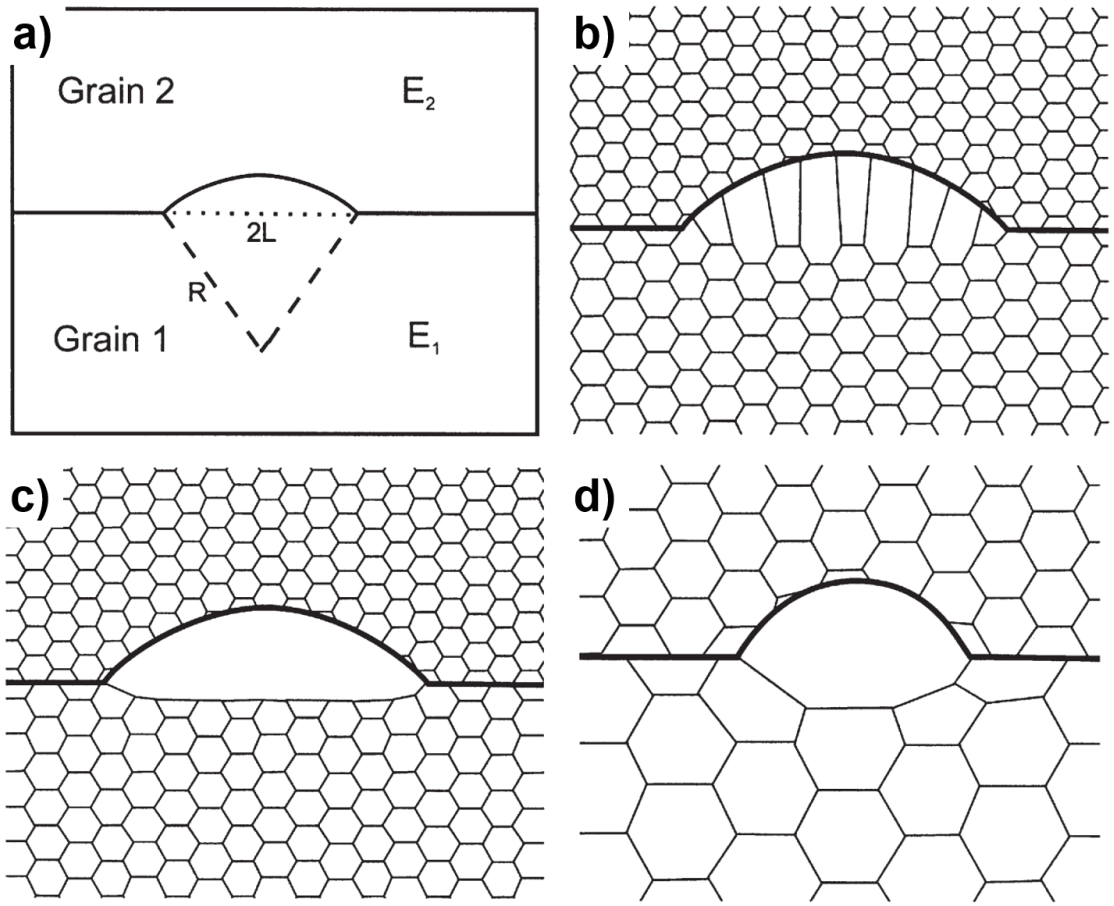

Figure 13: Schematic representation of the SIBM [121]: a) SIBM of a HAGB separating a grain of low stored energy (E_1) from one of higher energy (E_2), (b) movement of HAGB via dragging of the substructure behind the migrating HAGB, (c) the migrating HAGB is not dragged from the dislocation structure, (d) SIBM of a HAGB originating at a single large subgrain.

Among the investigated mechanisms of nucleation and growth, strain-induced boundary migration (SIBM) has been observed in several metallic materials [121]. It consists of the bulging of a part of the pre-existing grain boundary that moves towards a region of lower stored energy. Two types of SIBM can occur depending on the driving force: multiple subgrain SIBM or single subgrain SIBM. In the first case, the bulging boundary is joined to the lower grain with higher dislocation density by an array of dislocations of LAGBs. Moreover, the separation of regions of high or low stored energy is not straightforward at the stage where the bulged boundary becomes hemispherical [121]. The schematic representation of SIBM is shown in Figure 13. The cases b, c, and d represent: a) a boundary separates regions of high stored energy; c) a boundary separates a region of high stored energy and a perfect crystal; d) SIBM occurs at a large and single subgrain.

On the other hand, single subgrain SIBM occurs in a material with a well-recovered subgrain structure [121]. A single large subgrain is originated from the subgrain structure. An energy difference between the two grains is not required for single subgrain SIBM. However, higher stored energy difference across the boundary decreases the critical subgrain size for SIBM. Therefore, multiple subgrain SIBM occurs under most conditions, while for low stored energy difference between the grains, single subgrain SIBM can play a role.

2.8. SRX of the β-phase in Ti-alloys

The SRX of Ti-alloys has been investigated [122–131], and the kinetics of SRX of Ti-64 during β-annealing following hot deformation in the β-domain was established [128]. Moreover, heterogeneities in SRX in the β-domain following β hot deformation for Ti-64 and Ti-5Sn-0.5Mo [129,130] were associated with variations in the local deformation inside grain and between grains. On the other hand, hot deformation below the β-transus temperature followed by β-annealing is a common practice to obtain a uniform, refined grain size, and the thermo-mechanical processing parameters have been systematically investigated for various Ti-alloys [125–127]. The SRX behaviour of Ti-17 was investigated by Semblanet et al. [126], and grain-size refinement was only achieved for relatively short times ($\leq$30 min) while β-grain sizes comparable to or greater than the starting size are produced due to static grain growth for longer soaking times.

Several mesoscopic SRX approaches have been proposed [132–136], and they differ from assuming a nucleation rate of recrystallised grains [133,136] or merely assuming the growth of organised cellular structures [134,135]. The development of a deformation model based on the crystal plasticity finite element method enabled the prediction of the spatial distribution of stored deformation energy in the material [133]. Despite the accuracy and power of predictability of those models, this method cannot be applied for simulation of a typical thermo-mechanical process in industrial components due to the substantial computational effort.

3. Motivation

The technological motivations are:

- The need for a simple but robust physically-based model for phase transformation considering all α fractions and morphologies as well as the β-starting condition motivate the development of this work.
- Robust, accurate, and simple computational models to simulate the β→α transformation, hot deformation and static phenomena are necessary to predict and control the evolution of the microstructure in components with complex shapes produced by thermo-mechanical processing. The models must be able to predict not only the microstructure after the thermo-mechanical process but also to be able to account for the influence of the starting microstructure.

The open scientific questions are:

- The understanding and identification of the restoration mechanisms are necessary to develop a physically-based model for the hot deformation behaviour of Ti alloys. Although CDRX or GDRX are observed as restoration mechanisms for high stacking fault energy materials, most existing models still consider DDRX as the deformation mechanism [28,50–60].
- The difference in strength between the α and β-phases leads to a load transfer during deformation. The harder phase deforms with a lower plastic strain rate in comparison to the softer phase. However, a relationship between the plastic strain rates is not straightforward. Depending on the morphology, distribution, and interconnectivity of the phases, different behaviours can be observed [70]. The dynamic globularisation of the α-phase and associated with flow softening observed during deformation in the α+β domain [52] need to be physically modelled

The following questions are meant to be answered in this work:

- How can the whole thermomechanical processing route of Ti alloys be described using physical models using the same set of internal variables?
- Can CDRX of the β-phase be described in a mesoscale model that also couples other metallurgical phenomena, such as dynamic globularisation of the α-phase?
- How is the stored energy predicted after hot deformation coupled to an SRX model for annealing treatment?

4. Objectives and innovative aspects

The main objective of this work is the establishment of the relationships between the processing parameters, the chemical composition, and the measured properties through the whole processing route of Ti and Ti alloys is.

The specific objectives are:

- Describe and model the phase transformation sequence during continuous cooling for a Ti-6Al-4V
- Describe and model the hot deformation behaviour of Ti alloys in α+β and β domains
- Quantify the microstructural features and their evolution during hot deformation and establish the relationships to the measured flow stress
- Describe and model the SRX phenomena
- Couple the hot deformation model with the model for SRX using the same internal variables and microstructure description

The innovative technological aspects are:

- The development of a mesoscale model to predict the combined formation of primary, secondary and allotriomorphic α-phase during cooling
- The development of a novel and unified mesoscale model that can predict the microstructure evolution of Ti alloys during deformation followed by SRX

The innovative scientific aspects are:

- Several dislocation reactions are coupled with CDRX to account for different phenomena and used to predict the flow stress and microstructure evolution during hot deformation
- The misorientation distribution of formed boundaries during deformation is described as a weighted sum of Rayleigh and Mackenzie distributions
- The plastic deformation behaviour of a biphasic alloy is described, and the change in load partitioning regime is used to describe the flow softening

5. List of Publications

Six papers were published and are referenced in this thesis:

- R.H. Buzolin, F.M. Branco Ferraz, M. Lasnik, A. Krumphals, M.C. Poletti, Improved predictability of microstructure evolution during hot deformation of titanium alloys, Materials (2020) In Press:

Author Contributions: Conceptualization, Ricardo Henrique Buzolin, Franz Miller Branco Ferraz, Michael Lasnik, Alfred Krumphals and Maria Cecilia Poletti; Data curation, Maria Cecilia Poletti; Investigation, Ricardo Henrique Buzolin; Methodology, Ricardo Henrique Buzolin, Franz Miller Branco Ferraz and Maria Cecilia Poletti; Project administration, Michael Lasnik, Alfred Krumphals and Maria Cecilia Poletti; Resources, Michael Lasnik, Alfred Krumphals and Maria Cecilia Poletti; Software, Ricardo Henrique Buzolin; Supervision, Maria Cecilia Poletti; Validation, Ricardo Henrique Buzolin; Visualization, Ricardo Henrique Buzolin; Writing – original draft, Ricardo Henrique Buzolin; Writing – review & editing, Franz Miller Branco Ferraz, Michael Lasnik, Alfred Krumphals and Maria Cecilia Poletti.

The experimental procedures described in this paper are also partially described in sections 6.3 and 6.6. The modelling strategy described in section 7.2 corresponds to an expanded version of the modelling strategy shown in the paper. The discussions and conclusions of the paper are partially used in chapter 10.

- R.H. Buzolin, M. Lasnik, A. Krumphals, M.C. Poletti, Hot deformation and dynamic α-globularization of a Ti-17 alloy: Consistent physical model, Mater. Des. 197 (2021) 109266. https://doi.org/https://doi.org/10.1016/j.matdes.2020.109266:

Author Contributions: Conceptualization, Ricardo Henrique Buzolin, Michael Lasnik, Alfred Krumphals and Maria Cecilia Poletti; Data curation, Maria Cecilia Poletti; Investigation, Ricardo Henrique Buzolin; Methodology, Ricardo Henrique Buzolin, and Maria Cecilia Poletti; Project administration, Michael Lasnik, Alfred Krumphals and Maria Cecilia Poletti; Resources, Michael Lasnik, Alfred Krumphals and Maria Cecilia Poletti; Software, Ricardo Henrique Buzolin; Supervision, Maria Cecilia Poletti; Validation, Ricardo Henrique Buzolin; Visualization, Ricardo Henrique Buzolin; Writing – original draft, Ricardo Henrique Buzolin; Writing – review & editing, Michael Lasnik, Alfred Krumphals and Maria Cecilia Poletti.

The experimental procedures described in this paper are also partially described in sections 6.3 and 6.6. The modelling strategy described in the paper is used in section 7.2, especially section 7.2.9. The results shown in the paper are used in sections 11.2.1, 11.2.2, 11.2.3, 11.2.6, and 11.2.7. The discussions and conclusions shown in the paper are partially used in sections 11.3 and 11.4, respectively.

- R.H. Buzolin, M. Lasnik, A. Krumphals, M.C. Poletti, A dislocation-based model for the microstructure evolution and the flow stress of a Ti5553 alloy, Int. J. Plast. 136 (2021). https://doi.org/10.1016/j.ijplas.2020.102862:

Author Contributions: Conceptualization, Ricardo Henrique Buzolin, Michael Lasnik, Alfred Krumphals and Maria Cecilia Poletti; Data curation, Maria Cecilia Poletti; Investigation, Ricardo Henrique Buzolin; Methodology, Ricardo Henrique Buzolin, and Maria Cecilia Poletti; Project

administration, Michael Lasnik, Alfred Krumphals and Maria Cecilia Poletti; Resources, Michael Lasnik, Alfred Krumphals and Maria Cecilia Poletti; Software, Ricardo Henrique Buzolin; Supervision, Maria Cecilia Poletti; Validation, Ricardo Henrique Buzolin; Visualization, Ricardo Henrique Buzolin; Writing – original draft, Ricardo Henrique Buzolin; Writing – review & editing, Michael Lasnik, Alfred Krumphals and Maria Cecilia Poletti.

The experimental procedures described in this paper are also partially described in sections 6.3 and 6.6. The modelling strategy described in the paper is partially used in section 7.2. The results, discussion and conclusions are partially used in chapter 9.

- R.H. Buzolin, D. Canelo-Yubero, F. Warchomicka, M. Lasnik, A. Krumphals, M.C. Poletti, Refinement of the Ti-17 microstructure after hot deformation: Coupled mesoscale model, Mater. Sci. Eng. A. (2020) 140268. https://doi.org/https://doi.org/10.1016/j.msea.2020.140268:

Author Contributions: Conceptualization, Ricardo Henrique Buzolin, David Canelo-Yubero, Fernando Warchomicka, Michael Lasnik, Alfred Krumphals and Maria Cecilia Poletti; Data curation, Maria Cecilia Poletti; Investigation, Ricardo Henrique Buzolin; Methodology, Ricardo Henrique Buzolin, David Canelo-Yubero, Fernando Warchomicka and Maria Cecilia Poletti; Project administration, Michael Lasnik, Alfred Krumphals and Maria Cecilia Poletti; Resources, Michael Lasnik, Alfred Krumphals and Maria Cecilia Poletti; Software, Ricardo Henrique Buzolin; Supervision, Maria Cecilia Poletti; Validation, Ricardo Henrique Buzolin; Visualization, Ricardo Henrique Buzolin; Writing – original draft, Ricardo Henrique Buzolin; Writing – review & editing, David Canelo-Yubero, Fernando Warchomicka, Michael Lasnik, Alfred Krumphals and Maria Cecilia Poletti.

The experimental procedures described in this paper are also partially described in sections 6.3, 6.5 and 6.6. The modelling strategy described in the paper is partially used in section 7.2 and used in section 7.3. The results, discussions and conclusions shown in the paper are partially used in chapter 12.

- R.H. Buzolin, D. Weiß, A. Krumphals, M. Lasnik, M.C. Poletti, Modelling the Competitive Growth of Primary, Allotriomorphic, and Secondary Alpha in Ti-6Al-4V, Metall. Mater. Trans. A. (2020). https://doi.org/10.1007/s11661-020-05810-4:

Author Contributions: Conceptualization, Desirée Weiß, Ricardo Henrique Buzolin, Michael Lasnik, Alfred Krumphals and Maria Cecilia Poletti; Data curation, Desirée Weiß, Maria Cecilia Poletti; Investigation, Ricardo Henrique Buzolin, Desirée Weiß; Methodology, Ricardo Henrique Buzolin, Desirée Weiß, and Maria Cecilia Poletti; Project administration, Michael Lasnik, Alfred Krumphals and Maria Cecilia Poletti; Resources, Michael Lasnik, Alfred Krumphals and Maria Cecilia Poletti; Software, Ricardo Henrique Buzolin; Supervision, Maria Cecilia Poletti; Validation, Ricardo Henrique Buzolin, Desirée Weiß; Visualization, Ricardo Henrique Buzolin; Writing – original draft, Ricardo Henrique Buzolin; Writing – review & editing, Desirée Weiß, Michael Lasnik, Alfred Krumphals and Maria Cecilia Poletti.

The experimental procedures described in this paper are also partially described in sections 6.2 and 6.6. The modelling strategy described in the paper is used in section 7.1. The results, discussion and conclusions shown in the paper are used in chapter 8.

- R.H. Buzolin, F. Krumphals, M. Lasnik, A. Krumphals, M.C. Poletti, A continuous dynamic recrystallization model to describe the hot deformation behaviour of a Ti5553 alloy, J. Phys. Conf. Ser. 1270 (2019) 12048. https://doi.org/10.1088/1742-6596/1270/1/012048.

Author Contributions: Conceptualization, Ricardo Henrique Buzolin, Friedrich Krumphals, Michael Lasnik, Alfred Krumphals and Maria Cecilia Poletti; Data curation, Maria Cecilia Poletti; Investigation, Ricardo Henrique Buzolin; Methodology, Ricardo Henrique Buzolin, and Maria Cecilia Poletti; Project administration, Michael Lasnik, Alfred Krumphals and Maria Cecilia Poletti; Resources, Michael Lasnik, Alfred Krumphals and Maria Cecilia Poletti; Software, Ricardo Henrique Buzolin; Supervision, Maria Cecilia Poletti; Validation, Ricardo Henrique Buzolin; Visualization, Ricardo Henrique Buzolin; Writing – original draft, Ricardo Henrique Buzolin; Writing – review & editing, Friedrich Krumphals, Michael Lasnik, Alfred Krumphals and Maria Cecilia Poletti.

The experimental procedures described in this paper are also partially described in sections 6.3 and 6.6. The modelling strategy described in the paper is partially used in section 7.2. The results shown in the paper are partially used in sections 9.1.1, 9.1.3, and 9.1.4.

6. Experimental procedures

Three Ti alloys were used in this work. A Ti-6Al-4V was used for phase transformation investigations, and a Ti-5553 and a Ti-17 were used for the investigation of the hot deformation behaviour. The SRX behaviour of the Ti-17 was also investigated.

6.1. Materials

6.1.1. Ti-6Al-4V

The Ti-6Al-4V used in this investigation was cogged in the β and α+β-domains, annealed at 730°C for 1h and air-cooled. The β-transus calculated using JMatPro® v.10 is 995°C, and the chemical composition is listed in Table 1 [137].

Table 1: Chemical composition of the investigated Ti-6Al-4V [wt.%].

Al	V	Fe	O	C	N	H	Y
6.54	4.21	0.20	0.185	0.028	0.023	0.000335	<0.001

6.1.2. Ti-5553

A disk 127 mm of a commercial Ti-5553 (Ti-5Al-5V-5Mo-3Cr) alloy was delivered after cogging in the α+β domain. The alloy presents a β-transus temperature of ~860°C, calculated using JMatPro® v.10 for the standard chemical composition as listed in Table 2, in agreement with the literature [138,139].

Table 2: Chemical composition of the investigated Ti-5553 alloy [wt.%].

Al	V	Mo	Cr	Fe	O	N	C	Ti
5	**5**	**5**	**3**	**0.46**	**0.13**	**0.005**	**0.1**	**Bal.**

6.1.3. Ti-17

A disk of 256 mm of Ti-17 alloy was delivered after cogging in the β-domain. The calculated β-transus temperature using JMatPro® v.10 is 865°C, and the chemical composition is listed in Table 3.

Table 3: Chemical composition of the investigated Ti-17 [wt.%].

Al	Mo	Sn	Zr	Cr	V	Fe	O	C	N	H
4.96	3.91	1.95	1.91	3.68	0.01	0.08	0.112	0.07	0.05	0.0043

6.2. Heat treatments followed by continuous cooling

The procedures shown here were already published in [140] for the Ti-6Al-4V. Cylindrical samples with a diameter of 5.5 mm and a length of 10 mm were used for heat treatments. A dilatometer DIL 805A/D (TA Instruments, Hüllhorst, Germany) was used to perform the continuous cooling treatments for the Ti-6Al-4V alloy. The tests were carried out in a protective atmosphere of Argon. After heating with a rate of 30°Cmin^{-1}, the samples were held for 1h at two different holding temperatures ('T_H') in the α+β field, 930 and 960°C, and then continuously cooled down to room temperature. The cooling was conducted using five different cooling rates: 10, 30, 40, 100, and 300°Cmin^{-1}, and the thermo-cycle is schematically shown in Figure 14a.

Interrupted continuous cooling heat treatments were carried out in order to elucidate the mechanisms governing the β→α transformation during cooling. The samples were heated at 30°Cmin^{-1}, held for 1h at a constant temperature of 960°C, and cooled with 10 and 100°Cmin^{-1}. The samples were quenched using argon flow for four different temperatures ('T_i'), 900, 875, 850, and 800°C, and the thermocycle is schematically shown in Figure 14b.

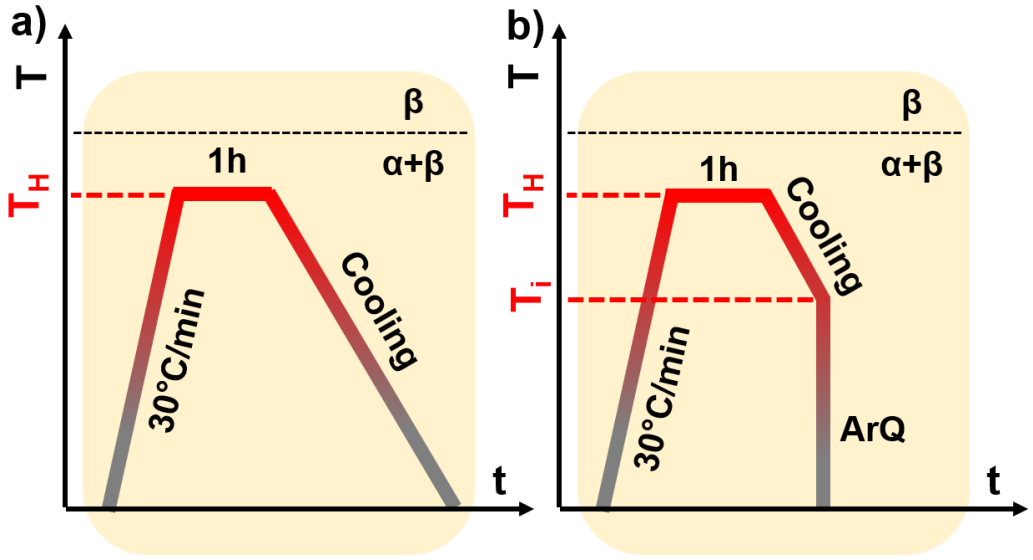

Figure 14: Cooling treatments for the Ti-6Al-4V: a) continuous cooling; b) continuous cooling interrupted by Ar quenching (ArQ). T_H and T_i are the holding temperature and the temperature of interruption, respectively.

6.3. Hot compression and hot torsion tests

The procedures shown here were already published in [141] for the Ti-5553 and in [142] for the Ti-17. Cylindrical samples with 10 mm in diameter and 15 mm in length were wire cut with the length perpendicular to the forging direction and parallel to the cogging direction for both Ti-5553 and Ti-17. The samples were hot compressed using a Gleeble® 3800. The hot deformation tests were performed for the Ti-5553 in the α+β phase domain at 800°C, 820°C and 840°C and in the single β-phase domain at 880°C, 900°C and 920°C. The tests were performed for the Ti-17 in the α+β phase field at 810°C, 830°C and 850°C and in the single β-phase field at 930°C, 950°C and 970°C. Five different strain rates from 0.001 s^{-1} to 10 s^{-1} were tested. The specimens were heated up at 300°Cmin^{-1}. Test samples were soaked for 5 min before compression in the β-domain for the Ti-5553, and for the other conditions and both Ti-5553 and Ti17 alloys, they were soaked at the testing temperature for 15 min before deformation. The temperature was measured with a thermocouple type K welded at the surface of the sample, and Ar was used as a protective atmosphere. Carbon and Ta foils were used to reduce the friction between the sample and the anvils. The samples were in-situ water quenched immediately after hot deformation to preserve the microstructure. The microstructure before deformation was also investigated by soaking for the same holding time before compression at the tested temperatures followed by in-situ water quenching. In the case of the Ti-17 alloy, interrupted tests at 0.25 strain were performed in both α+β and β-domain, as well as at 0.50 strain in the α+β domain, to address the microstructure evolution and to compare with the results obtained using in-situ synchrotron radiation diffraction.

The stress-strain data were corrected for adiabatic heating [143] [144], using a material density of 4300 kgm^{-3} [145], a specific heat (C_p) [$JK^{-1}kg^{-1}$] and thermal conductivity (K_w) [$Wm^{-1}K^{-1}$] given in Equation 1 and Equation 2, respectively. Thermal conductivity of 10 $Wm^{-1}K^{-1}$ [144] was considered for a die of TiC.

$$C_p=5.82\cdot10^{-9}\cdot T^2-1.12\cdot10^{-6}\cdot T+6.18\cdot10^{-3} \quad \textit{Equation 1}$$

$$K_w = - 0.0109\cdot T + 34.22 \quad \textit{Equation 2}$$

Cylindrical samples of the Ti-5553 with a gauge of 10 mm diameter and 20 mm length were deformed using the torsion module of a Gleeble 3800®. Experiments were performed in the single β-phase field at selected conditions. The tests were conducted up to effective strains of 7.3 (8 revolutions). The specimens were heated up with a rate of $5°Cs^{-1}$ and held at the testing temperature for 5 min before the deformation started. The temperature was measured and regulated using S-thermocouples on the side of the sample. A second thermocouple on the sample's shoulder served as a reference. After hot deformation, in situ water quenching was used.

6.4. In-situ synchrotron radiation diffraction during hot compression

The procedures shown here were already published in [146] for the Ti-17. In-situ hot compression tests in the β-domain were performed using synchrotron radiation diffraction experiments at the P07 beamline of Harwi-II, DESY (Deutsches Elektronen-Synchrotron) in 2011. A monochromatic beam with the energy of 100 keV (λ = 0.0124 nm) and slit dimensions of 1.0 x 1.0 mm^2 was used. Cylindrical specimens of Ti-17 with a diameter of 5 mm and a length of 10 mm were used for the in-situ compression experiments. The diffraction patterns were recorded with a Mar555 flat panel detector with a pixel size of 139 x 139 μm^2, which was placed at a sample-to-detector distance of 1528 mm from the specimen (distance calibrated with a LaB_6 standard powder sample). The acquisition time for each image was 3 s. The specimens were placed in the chamber of a DIL 805A/ D dilatometer (TA Instruments, Hüllhorst, Germany), combined with a modified heating induction coil so that the beam passes only through the sample [147]. The specimens were heated up to the deformation temperature at a rate of $300°Cmin^{-1}$ and held at this temperature for 5 min before the deformation to ensure temperature homogeneity. The incident beam was fixed at 3.5 mm from one side of the sample, and a maximum change in the diffracted volume at the end of the deformation was estimated at ~ 28% [148]. The matrix of experiments with the deformation conditions and holding time after deformation is shown in Table 4. The "SD1", "SD2" and "SD5" were used to investigate in detail the hot deformation behaviour of the Ti-17, while "SD1", "SD3" and "SD4" were used for the investigation of the SRX behaviour of the Ti-17.

Two types of analysis were performed:

- The two-dimensional diffraction patterns were converted into azimuthal angle–time/strain (AT) plots to study the evolution of the microstructure, according to the methodology explained in [149] which is briefly summarised following: i) stacking of the recorded 2D images, ii) selection of the diffraction ring and conversion into cartesian coordinates with a final 3D volume of axis 2θ, t (or strain ε), and φ (azimuthal angle), and iii) projection over the t (or ε)-φ plane. These plots are generated for the chosen crystallographic planes. The

starting point for the time was right after the deformation stage, i.e. at the beginning of the isothermal heat treatment.

- The Debye-Scherrer rings were also azimuthally integrated to generate the diffraction patterns and study individually the diffraction peaks β-110, β-200, and β-211. The full-width-at-half-maximum (FWHM) and the normalised interplanar distance for each plane (i.e. divided by the interplanar distance at the beginning of the isothermal treatment) were calculated.

Table 4: Matrix of the performed hot compression tests followed by annealing treatments during in-situ synchrotron radiation diffraction measurements.

ID	Temperature [°C]	Strain [-]	Strain rate [s^{-1}]	Annealing time [min]
SD1	930	0.5	0.001	10
SD2	930	0.7	0.01	2
SD3	930	0.5	0.1	10
SD4	930	0.5	5	10
SD5	970	0.5	0.001	-

6.5. Static recrystallisation experiments

The procedures shown here were already published in [146]. The SRX behaviour of Ti-17 was assessed by performing hot compression tests followed by isothermal heat treatments (Figure 15a) at the deformation temperatures for specific holding times of 1 min, 5 min, 20 min and 60 min for the deformation at 0.001 s^{-1}, and 15 s, 1 min, 5 min and 20 min for the deformation at 0.1 s^{-1} and immediately water quenched after the holding time. Continuous cooling heat treatments after deformation (Figure 15b) were also performed after deformation at 930°C for 0.001 s^{-1} and 0.1 s^{-1} followed by cooling at 2°Cmin^{-1}, 5°Cmin^{-1} and 30°Cmin^{-1} and interrupted at 810°C by water quenching the specimens.

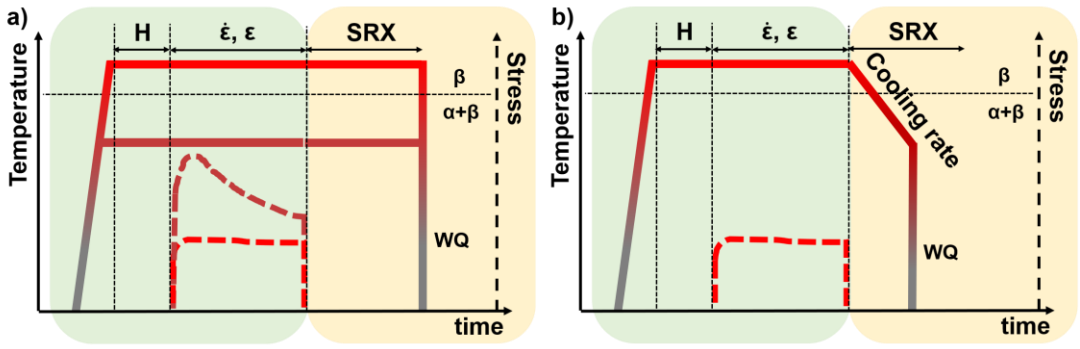

Figure 15: SRX experiments performed at the Gleeble® device: a) isothermal holding after hot compression; b) interrupted continuous cooling after hot compression. H stands for the holding time prior to hot compression experiments. ε, ε̇ and WQ correspond to the strain, strain rate, and water quenching, respectively. SRX is the static recrystallisation treatment.

6.6. Microstructure investigation

6.6.1. Metallographic preparation

The samples were cold mounted and ground using SiC paper, polished using oxide polishing solution (OPS), and vibro-polished before the microstructure investigation. For light optical microscopy (LOM) analysis and EBSD investigations in α+β domain where only β-phase is measured, samples were etched for 15 s with the Kroll's reagent: 91 ml water, 6 ml HNO_3 (69 vol.%), and 3 ml HF (40 vol.%). The samples were etched for 2 min before the EBSD investigations in the β-domain using a modified Kroll's reagent: 75 ml water, 15 ml HNO_3, and 10 mL HF. Preparation using a cross-section polisher JEOL SM-09010 was used instead of chemical etching before the EBSD investigations in the α+β domain of Ti-17.

6.6.2. Microscopy and Electron-backscatter diffraction

The scanning electron microscopy (SEM) analyses were conducted using a Tescan Mira3 microscope equipped with a Hikari EBSD camera and a JEOL JSM7001F microscope. Secondary electron (SE) and backscattered electrons (BSE) images were acquired using an acceleration voltage of 10 kV and a working distance of 10 to15 mm. An acceleration voltage between 15 to 30 kV, a working distance of 15 to 25 mm, and a spot size between 5 to 100 nm were used for the EBSD measurements acquired using a TSL-OIM Data Collector® software package. The data treatment was performed using the software OIM DataAnalysis® v.8. A confidence index standardisation was performed considering a minimum grain size of 5 points and a minimum boundary misorientation angle of 12°. Finally, the neighbour confidence index correlation was used to re-index the data-points with a confidence index lower than 0.5.

The kernel average misorientation (KAM) was calculated with respect to the first neighbour. The recrystallisation grade of the SRX samples was evaluated using grain orientation spread (GOS) analysis, and grains with misorientation spread lower than 2° were considered statically recrystallised. The Taylor factor was calculated according to the deformation gradient matrix of uniaxial compression (Table 5) and considering the possible slip systems for a bcc system for the β-phase: {110}⟨$\bar{1}$11⟩, {211}⟨$\bar{1}$11⟩, and {321}⟨$\bar{1}$11⟩.

Table 5: Deformation gradient matrix for the calculation of the Taylor factor maps.

Deformation gradient		
0.5	0	0
0	0.5	0
0	0	-1

6.6.3. Image analysis

For the Ti-6Al-4V, a minimum of five representatives LOM micrographs were analysed for each cooling rate and holding temperature for the quantification of the globular α_p. The procedure is shown in Figure 16. For each micrograph (Figure 16a), the particles of α_p were manually marked using the software GIMP (GNU Image Manipulation Program) [150] (Figure 16b) and analysed using ImageJ® software [151], Figure 16d

The aspect ratio of the globular α_p was calculated by fitting an ellipse to each of the globular particles using ImageJ® software and calculated as the major axis divided by the minor axis, Figure

16c. This procedure was adopted to compare the obtained data with an ideal circle, minimizing the influence of the presence of protuberances in the measured aspect ratio for the different α-morphologies. The circularity was measured according to Equation 3.

$$\text{Circularity} = \frac{4\pi \text{AREA}}{\text{PERIMETER}^2} \qquad \textit{Equation 3}$$

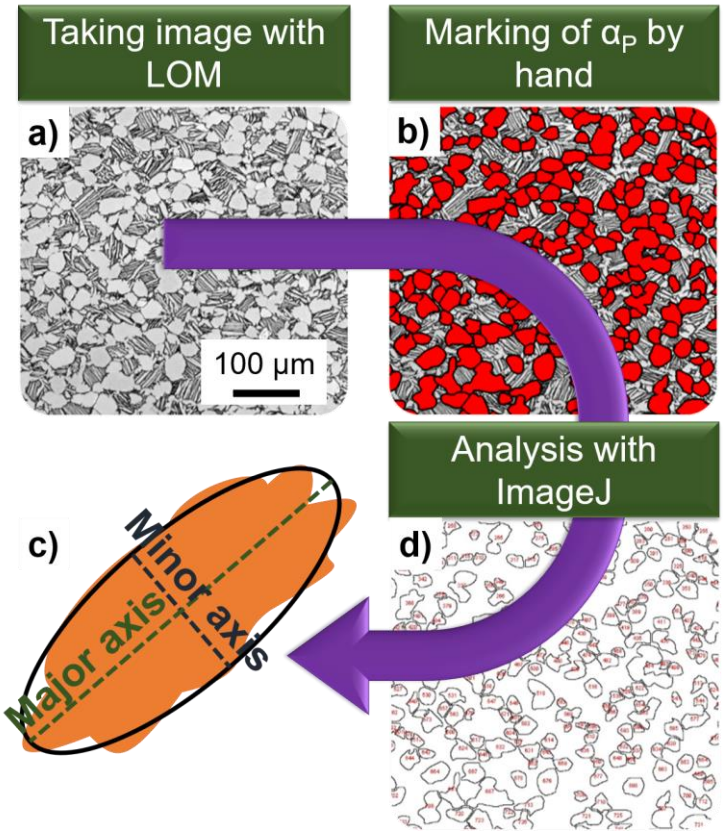

Figure 16: Procedure for the measurement of the shape descriptors of the α_P: a) LOM micrograph; b) α_P marked by hand; c) fitted ellipse; d) analysis with ImageJ.

A minimum of five representative SE-micrographs was acquired to measure the thickness of α_{GB} and α_{SEC}. Two procedures were adopted and are schematically shown in Figure 17.

- **Method I:** a mean value of the thickness of α_{GB} as well as of α_{SEC} were measured based on the stereology procedures for quantification described by Tiley et al. [152], Figure 17(a,b).
- **Method II:** the interspace distance between the lamellas of α_{SEC} and the thickness of α_{GB} were manually measured to obtain a thickness distribution, Figure 17(c,d).

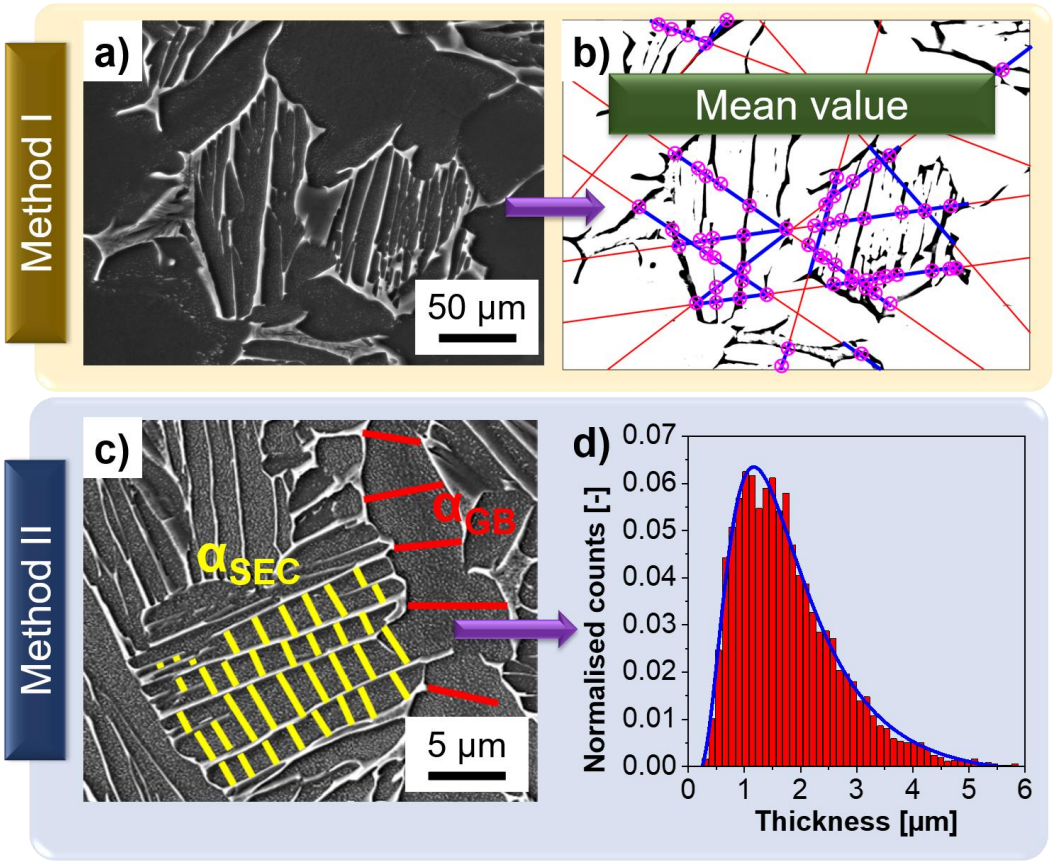

Figure 17: Procedure for the measurement of the thickness of α_{GB} and α_{SEC}: Method I (a,b) and Method II (c,d). A SE-micrograph (a) is measured using the line-intercept method (b), while interspace distance between the lamellas of α_{SEC} and the thickness of α_{GB} are manually marked (c) and measured using ImageJ to obtain a thickness distribution (d)

For the Ti-17 alloy, BSE micrographs were acquired to measure the shape descriptors of the α-phase. The procedure is shown in Figure 18. The micrographs were analysed using the software ImageJ® [151]. The particles of α-phase were fitted using ellipses, and the aspect ratio and minor axis were calculated. The aspect ratio is calculated as the ratio between the major and the minor axis of the fitted ellipse. The thickness of the α-particles is considered as the minor axis of the ellipse.

Figure 18: Procedure to obtain the shape factors in α-phase for the Ti-17.

7. Modelling

The developed models comprise three significant phenomena: phase transformation, hot deformation and SRX. Phase transformation was developed as a separated model, while the hot deformation and SRX models are coupled.

7.1. Phase transformation in Ti-6Al-4V

The model strategy shown here was already published in [140]. The modelled microstructure consists of three significant α-phase morphologies, Figure 19a: α_p, α_{SEC}, and α_{GB}, all embedded in a β-phase matrix with chemical composition C_M, Figure 19b. In the proposed model, the formation of α_{SEC}, α_{GB}, and α_p is computed simultaneously and is separated on nucleation kinetics (does not apply for the α_p) and growth kinetics. The growth of spherical α_p during cooling in heat treatments conducted below the β-transus temperature was modelled based on [9]. Mean diameter of spherical α_p instead of a distribution of sizes is considered. The formations of α_{GB} and α_{SEC} were modelled based on the classical model of nucleation and diffusion equation for the growth of platelets [10].

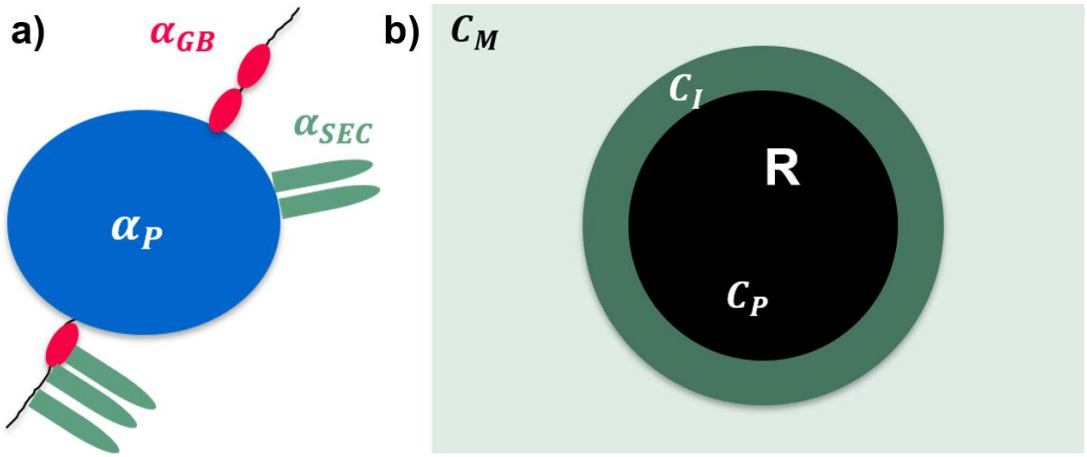

Figure 19: a) Different morphologies of α-phase: primary (α_p), secondary (α_{SEC}) and allotriomorphic (α_{GB}), formed during cooling for a typical Ti-6Al-4V alloy; b) growth of a spherical particle of radius R and particle composition C_P embedded in an infinite matrix of composition C_M, in which C_I is the chemical composition of the matrix at the interface.

7.1.1. Growth of primary alpha (α_P)

Semiatin et al. [9] showed that for Ti-6Al-4V the growth of spherical α_p phase during cooling is governed by V diffusion from α-phase into β-phase and that the supersaturation of V in the β-phase is the driving force for the growth of α_p. The intrinsic diffusion coefficient of V in β Ti (D_V^β) as a function of temperature T (in K) is calculated from [153] and also adopted in [9] and [154] (Equation 4) [140].

$$D_V^\beta(\mu m^2/s) = 1x10^5 e^{-\frac{17460}{T}} \qquad \textit{Equation 4}$$

The growth of a spherical particle embedded in an infinite matrix of the composition C_M is given according to Equation 5 [9].

$$\frac{dR_\alpha}{dt} = 2\Lambda^2 \frac{D_V^\beta}{R}$$ ***Equation 5***

R is the radius of the α_p particle, and Λ is a growth rate parameter calculated according to Equation 6 [9].

$$\left\{\Lambda^2 e^{\Lambda^2}\right\}\left[e^{-\Lambda^2} - \Lambda\pi^{1/2}\mathrm{erfc}(\Lambda)\right] = \frac{\Psi}{2}$$ ***Equation 6***

The parameter Ψ corresponds to the supersaturation of V. It is calculated according to Equation 7 and related to Figure 19b [9].

$$\Psi = \frac{(C_M - C_I)}{(C_P - C_I)}$$ ***Equation 7***

C_I is the composition of V in the β-matrix at the α-phase interface, and C_P is the composition of V in the α_p phase. C_I and C_P are considered as the equilibrium phase compositions of the β-phase and α-phase, respectively, obtained from the phase diagram [140]. They are regarded as constant values with respect to the temperature [9]. Following this assumption, α_p, α_{SEC}, and α_{GB} have the same C_P. The compositions are given in wt.%.

The supersaturation is the driving force for the growth of α_p. The α-phase fraction at equilibrium as well as the chemical composition of the β-phase (C_I) was calculated using the software JMatPro® v.10 in wt.% and are shown in Figure 20 a and b, respectively [140]. To account for the soft impingement on the "far-field" matrix composition, C_M is calculated using a usual mass balance between the total fraction of α (f_α) phase, as given by Equation 8 [9].

$$C_M = \frac{(C_0 - f_\alpha C_P)}{(1 - f_\alpha)}$$ ***Equation 8***

C_0 is the nominal concentration of V in the material (Table 1).

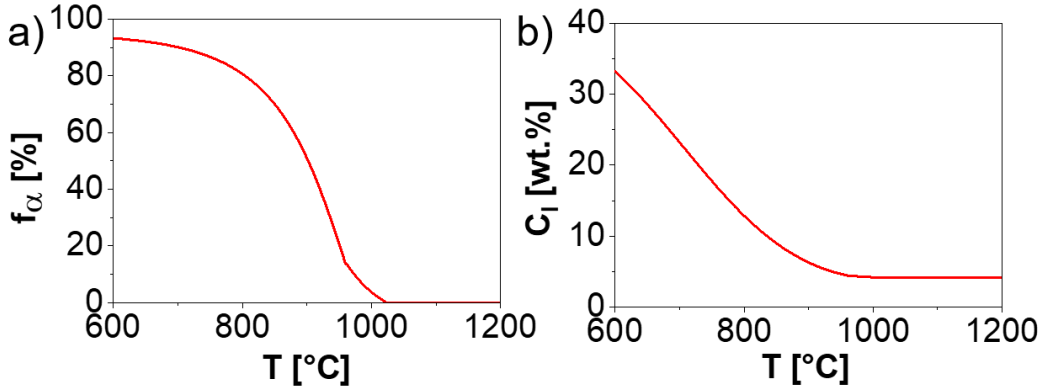

Figure 20: Simulated data using JMatPro® v.10: a) equilibrium α-phase fraction; b) equilibrium V concentration for the β-matrix obtained from the phase diagram.

The evolution of the fraction of the spherical α_p ($f_{\alpha p}$) is calculated according to Equation 9 considering isotropic growth [9].

$$f_{\alpha p} = f_{\alpha p}^0 \left(\frac{R_\alpha}{R_\alpha^0}\right)^3$$ ***Equation 9***

$f_{\alpha p}^{0}$ and R_{α}^{0} are the initial volume fraction of α_p and the initial radius of the α_p, respectively.

7.1.2. Formation of allotriomorphic alpha (α_{GB})

Due to the high anisotropy in the interfacial energy, a plate-like morphology of the α-phase is observed of both α_{SEC} and α_{GB} [140]. In the present model, the lengthening is considered notably higher in comparison to the thickening as also suggested by phase-field simulation [155]. Therefore, the volume fraction of α_{SEC} and α_{GB} increases mainly due to the increase in the number density and their thickness [10]. The nucleation, growth, and overall transformation kinetics of grain boundary allotriomorphic platelets were proposed for steels [13] and titanium alloys [14]. Following a similar approach, the nucleation rate of precipitates is given according to Equation 10 [10].

$$\frac{dN_{GB}}{dt} = N_{0GB}\left(1 - f_{\alpha p} - f_{\alpha GB} - f_{\alpha SEC}\right) \exp\left(-\frac{Q_{\alpha}}{RT}\right) \exp\left(-\frac{\Delta G^{*}_{NucGB}}{RT}\right) \qquad \textit{Equation 10}$$

N_{0GB} is a constant corresponding to the number of incubation sites multiplied by a constant [23]. Q_{α} is the activation energy for atomic migration across the interface and assumed to be half of the activation energy for diffusion [156,157]. ΔG^{*}_{NucGB} is the activation energy for heterogeneous nucleation, R the molar gas constant and T the absolute temperature. $f_{\alpha p}$, $f_{\alpha GB}$ and $f_{\alpha SEC}$ are the calculated volume fraction of α_p, α_{GB} and α_{SEC}, respectively, and their sum is the total fraction of alpha phase (f_{α}) [140]. The activation energy for the heterogeneous nucleation of α_{GB} is calculated according to Equation 11 [10]. Here, no effect of activation energy due to stored energy by deformation is considered.

$$\Delta G^{*}_{NucGB} = -\frac{\left(A^{*}_{GB}\right)^{3}}{(RT)^{2}\left[\ln\left(\frac{C_M}{C_I}\right)\right]^{2}} \qquad \textit{Equation 11}$$

A^{*}_{GB} is a parameter to account for nucleation at grain boundary ($A_{\alpha\beta}$), and sympathetic nucleation (A_{SYM}) [10], Equation 12.

$$A^{*}_{GB} = 0.12A_{SYM} + 0.88A_{\alpha\beta} \qquad \textit{Equation 12}$$

Where:

$$A_{SYM} = \left(4\pi N_A \gamma_{\alpha\beta}^{2} \gamma_{\alpha\alpha} \Omega^{2}\right)^{1/3} \qquad \textit{Equation 13}$$

$$A_{\alpha\beta} = \left(\frac{16\pi N_A \gamma_{\alpha\beta}^{3} S(\theta) \Omega^{2}}{3}\right)^{1/3} \qquad \textit{Equation 14}$$

N_A is the Avogadro constant ($N_A = 6.02214076 \cdot 10^{23}$ mol^{-1}), $\gamma_{\alpha\beta}$ is the interface energy between α/β phases $\gamma_{\alpha\beta} = 0.10$ J/m^2 [23]. $\gamma_{\alpha\alpha}$ is the interface energy of α/α phase equals 0.30 J/m^2 [10]. Ω is the atomic volume of Ti ($\Omega = 1.0896 \cdot 10^{-5}$ m^{3}mol^{-1}) and S(θ) is a shape factor given as a function of the wetting angle of the optimum nucleus shape [23]. $\gamma_{\alpha\beta}\left(S(\theta)\right)^{1/3} = 0.012$ Jm^{-2} [23]. A small variation in the interface energies ($\gamma_{\alpha\beta}$ or $\gamma_{\alpha\alpha}$) notable impacts the nucleation rate. The

parameters representing sympathetic nucleation (A_{SYM}) is a function of both, $\gamma_{\alpha\beta}$ (second-order) and $\gamma_{\alpha\alpha}$ (first-order). The parameter $A_{\alpha\beta}$ is a function of only $\gamma_{\alpha\beta}$ (third-order). Finally, the activation energy for heterogeneous nucleation is adjusted with respect to the measured data as shown in Equation 12 considering a weighted sum of both A_{SYM} and $A_{\alpha\beta}$ [140].

The critical thickness (B_{GBcrit}) for a disk-like α_{GB} to nucleate is calculated according to Equation 15 [10].

$$B_{GBcrit} = -\frac{4\gamma_{\alpha\beta}}{\Delta G_{VGB}} \qquad \textit{Equation 15}$$

ΔG_{VGB} is the chemical Gibbs free-energy for the formation of α-phase obtained for a polymorphous transformation from the parent β-phase, Equation 16 [158].

$$\Delta G_{VGB} = \frac{C_I - C_P^{\alpha_{GB}}}{1 - C_I} \frac{RT}{\left(1 + \frac{\partial V}{\partial C_I}\frac{C_I}{V}\right)} \ln\left(\frac{C_I}{C_M}\right) \qquad \textit{Equation 16}$$

$C_P^{\alpha_{GB}}$ is the concentration of V in the α_{GB} assumed equal to the V concentration in the α_p ($C_P^{\alpha_{GB}} = C_P$).

If the misfit strain energy is ignored, the nucleus of α_{GB} grows by the diffusion process by the thickening of a planar disordered boundary via a ledge growth mechanism. The evolution in the volume fraction of α_{GB} only depends on the variation of the number density of α_{GB} and its thickness [140]. The variation in number density is related to the number of nuclei and calculated according to Equation 10 [10]. The thickening of the α_{GB} is modelled according to Equation 17.

$$\frac{dB_{GB}}{dt} = \frac{2m_{GB}\Lambda_{GB}^2 D_V^{\beta}}{B_{GB}} \qquad \textit{Equation 17}$$

B_{GB} is the thickness of the α_{GB}, m_{GB} is a ledge coefficient to account for the planar disordered growth [10], and Λ_{GB} is a growth rate parameter related to the interface α_{SEC}/β and is calculated according to Equation 18 [10].

$$\pi^{1/2} \exp(\lambda_{GB}^2) \operatorname{erfc}(\Lambda_{GB}) = \Psi_{\alpha GB} \qquad \textit{Equation 18}$$

$\Psi_{\alpha GB} = (C_I - C_M)/\left(C_I - C_P^{\alpha_{GB}}\right)$ is a dimensionless supersaturation parameter, and considered equal to Ω because $C_P^{\alpha_{GB}} = C_P^{\alpha_p}$. The mean thickness of the platelets is calculated according to Equation 19 [159].

$$\frac{d\bar{B}_{GB}}{dt} = \frac{dB_{GB}}{dt} + \frac{1}{N_{GB}}\frac{dN_{GB}}{dt}\left(B_{GBcrit} - \bar{B}_{GB}\right) \qquad \textit{Equation 19}$$

The first term corresponds to the growth of the existing platelets of α_{GB}, while the second one represents the contribution of new nuclei of critical size calculated according to Equation 15. The overall fraction of α_{GB} is calculated according to Equation 20 [10].

$$f_{\alpha GB} = N_{GB}\bar{B}_{GB} \qquad \textit{Equation 20}$$

The fitting procedure is shown in Appendix A and parameters used for the simulation of the formation of α_{GB} are listed Table A. 1 (see Appendix A).

7.1.3. Formation of secondary alpha (α_{SEC})

The formation of α_{SEC} is modelled similarly to the formation of α_{GB}, i.e., nucleation and growth of disk platelets. The thickness and number density of the formed α_{SEC} platelets are obtained. The lengthening is neglected since it is considered notably faster in comparison to the thickening of the α_{SEC}. Differently from the growth of α_{GB} that is along the β/β grain boundaries, the growth of α_{SEC} occurs from the grain boundary towards the centre of the prior β grain as well as from the α_p [140]. The rate of nucleation of α_{SEC} is given according to Equation 21 [10].

$$\frac{dN_{SEC}}{dt} = N_{0SEC}\left(1 - f_{\alpha p} - f_{\alpha GB} - f_{\alpha SEC}\right)\exp\left(-\frac{Q_\alpha}{RT}\right)\exp\left(-\frac{\Delta G^*_{NucSEC}}{RT}\right) \qquad \textit{Equation 21}$$

N_{0SEC} is a pre-exponent term similar to N_{0GB}. ΔG^*_{NucSEC} is the activation energy for heterogeneous nucleation of the α_{SEC} and calculated according to Equation 22 [10].

$$\Delta G^*_{NucSEC} = -\frac{\left(A^*_{SEC}\right)^3}{(RT)^2\left[\ln\left(\frac{C_M}{C_I}\right)\right]^2} \qquad \textit{Equation 22}$$

A^*_{SEC} is fitted and calculated according to Equation 23.

$$A^*_{SEC} = 0.56A_{SYM} + 0.44A_{\alpha\beta} \qquad \textit{Equation 23}$$

The pre-factors 0.56 and 0.44 for the activation energy for heterogeneous nucleation are adjusted as shown in Figure A. 1 in Appendix A. The critical thickness ($B_{SECcrit}$) for a disk-like α_{SEC} to nucleate is calculated according to Equation 24 [10].

$$B_{SECcrit} = -\frac{4\gamma_{\alpha\beta}}{\Delta G_{VSEC}} \qquad \textit{Equation 24}$$

$\gamma_{\alpha\beta}$ is the interface energy between α and β phases, ΔG_{VSEC} is the chemical Gibbs free-energy for the formation of α_{SEC} obtained for a polymorphous transformation from the parent β-phase, Equation 25 [158].

$$\Delta G_{VSEC} = \frac{C_I - C_P^{\alpha_{SEC}}}{1 - C_I}\frac{RT}{\left(1 + \frac{\partial V}{\partial C_I}\frac{C_I}{V}\right)}\ln\left(\frac{C_I}{C_M}\right) \qquad \textit{Equation 25}$$

$C_P^{\alpha_{SEC}}$ is the concentration of V in the α_{SEC}, considered to be equal to the V concentration in the α_p and α_{GB} ($C_P^{\alpha_{SEC}} = C_P^{\alpha_{GB}} = C_P$) [140].

The growth of the nucleus of α_{SEC} is modelled as the growth of the α_{GB}. The thickening of the α_{SEC} is given according to Equation 26 [10].

$$\frac{dB_{SEC}}{dt} = \frac{2m_{SEC}\Lambda^2_{SEC}D^\beta_V}{B_{SEC}} \qquad \textit{Equation 26}$$

B_{SEC} is the thickness of the α_{SEC}, m_{SEC} is a ledge coefficient, and Λ_{SEC} is a parameter denoting the interface α_{SEC}/β that is calculated according to Equation 27 [10].

$$\pi^{1/2}\exp\left(\Lambda^2_{SEC}\right)\mathrm{erfc}\left(\Lambda_{SEC}\right) = \Psi_{\alpha SEC} \qquad \textit{Equation 27}$$

$\Psi_{\alpha SEC} = (C_I - C_M)/(C_I - C_P^{\alpha_{SEC}})$ is a dimensionless supersaturation parameter. The mean thickness of the α_{SEC} is calculated according to Equation 28 [159].

$$\frac{d\bar{B}_{SEC}}{dt} = \frac{dB_{SEC}}{dt} + \frac{1}{N_{SEC}}\frac{dN_{SEC}}{dt}\left(B_{SECcrit} - \bar{B}_{SEC}\right) \qquad \textit{Equation 28}$$

The first term corresponds to the growth of the existing platelets of α_{SEC}, while the second represents the contribution of new nuclei of critical size calculated according to Equation 24. The overall fraction of α_{SEC} is calculated according to Equation 29 [10].

$$f_{\alpha SEC} = N_{SEC}\bar{B}_{SEC} \qquad \textit{Equation 29}$$

The parameters used for the simulation of the formation of α_{SEC} are listed Table A. 1 (see Appendix A).

7.2. Hot deformation model

The developed hot deformation model consists of five main elements: microstructure modelling, microstructure initialisation, constitutive equations, plastic strain rate partitioning, and rate equations. Two models for rate equations are proposed: a) based on Kock-Mecking formalism and b) based on the work of Ghoniem et al. [104]. The modelling strategy adopted in a) was already published in [146], where the hot deformation model is shortly described. The model strategy for b) was already published in [141] for the Ti-5553, where the microstructure model, the initialisation of the microstructure, the rate equations, and the Boundary density and misorientation distribution evolutions are described and discussed. The modelling strategy b) is complemented by the work already published in [142], where the model of dynamic α-globularisation is described for the Ti-17. Finally, the load partitioning results in the combined approaches already published in [141,142]. The procedure to obtain the fitting parameters is schematically discussed in Figure B. 1 (see Appendix B) and Figure D. 1 (see Appendix D) for the Ti-5553, as well as in Figure E. 1 (see Appendix E) and Figure F. 1 (see Appendix F) for the Ti-17. The fitting parameters of the model are listed in Appendix B, D, E and F.

7.2.1. Microstructure model

The microstructure is represented by mean values of internal variables, such as subgrain and grain sizes, dislocation densities, and boundary misorientation distribution [141]. The dislocation densities are separated into three populations to account for the different roles in the plastic deformation. The mobile dislocations slide along the active slip systems [160] contributing to the plastic deformation of the material. Its volumetric density is expressed by ρ_m. The immobile dislocations are blocked by obstacles, such as other dislocations, boundaries, or phase interfaces [161], do not contribute directly to plastic deformation [162], and are responsible for the hardening [162]. Its volumetric density expressed by ρ_i. A third population named wall dislocation density (ρ_w) accounts for the dislocations forming subgrain or wall boundaries. The dislocations form either cells at low temperatures or sharp subgrain boundaries at high temperatures [76,163,164]. The proposed model considers the formation of a sharp low angle grain boundary (LAGB). Figure 21 shows schematically the modelled microstructure composed by high angle grain boundaries (HAGBs), LAGBs, ρ_i and ρ_m. In Figure 21a, an initial fully recrystallised microstructure is assumed. At early stages, dislocations multiply while a substructure is formed due to the

reorganisation of dislocation into LAGBs via DRV, Figure 21(b,c). The subgrains progressively increase their misorientation due to lattice rotation and/or accumulation of dislocations, forming new HAGBs via CDRX [25,33], Figure 21d. A steady-state is eventually achieved when reaching a dynamic equilibrium of production of new LAGBs, and its consumption by the movement of existing HAGBs, Figure 21e.

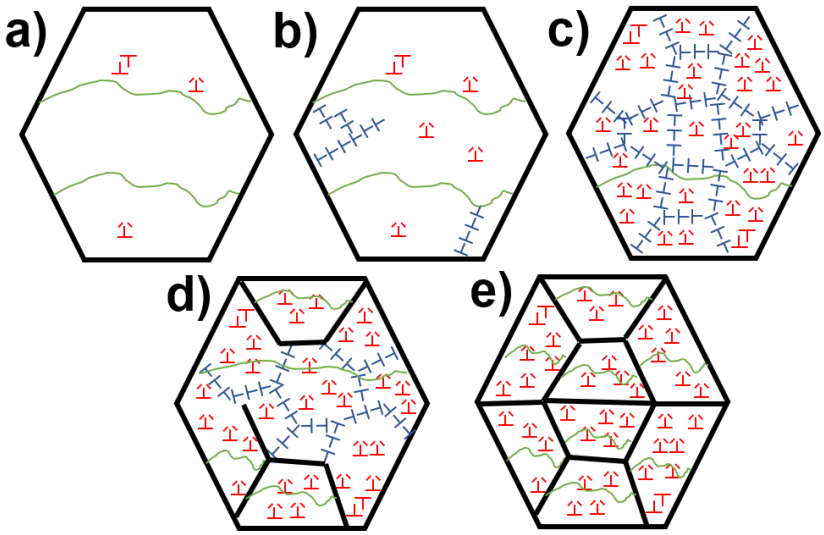

Figure 21: Schematic representation of the microstructure consisted of HAGBs (black lines), LAGBs (blue arrangement of wall dislocations), immobile dislocations (red) and mobile dislocations (green lines): a) Initial stages of deformation; b) formation of the substructure; c) initial stage of the CDRX; d) fully recrystallised state.

The misorientation distribution is modelled as a sum of Rayleigh and Mackenzie distributions [141]. The Rayleigh distribution ($\Theta_R(\theta)$, Equation 30 and Equation 31) accounts for the misorientation caused by the LAGB formed during deformation. The Mackenzie distribution ($\Theta_M(\theta)$) considers a fully recrystallised material with random texture.

$$\Theta_R(\theta) = \frac{\theta}{\Pi^2}\exp\left(-\frac{\theta^2}{2\Pi^2}\right) \qquad \textit{Equation 30}$$

$$\Pi = \overline{\theta_R}\sqrt{\frac{2}{\pi}} \qquad \textit{Equation 31}$$

θ is the misorientation angle, Π is a scale parameter and $\overline{\theta_R}$ is the average misorientation of the Rayleigh distribution. $\overline{\theta_R}$ also corresponds to the average misorientation angle of the formed boundaries during deformation [141]. The Mackenzie distribution ($\Theta_M(\theta)$) is described in [165]. It is given according to Equation 32 to Equation 34.

$$\Theta_M(\theta) = \frac{24}{\pi}(1-\cos(\theta)) \quad [0 < \theta \leq \pi/4] \qquad \textit{Equation 32}$$

$$\Theta_M(\theta) = \frac{24}{\pi}(1-\cos(\theta))\left[3(\sqrt{2}-1)\cot\left(\frac{\theta}{2}\right)-2\right] \quad [\pi/4 < \theta \leq \pi/3] \qquad \textit{Equation 33}$$

$$\Theta_M(\theta) = \frac{24}{\pi}(1-\cos(\theta))\left\{\left[3(\sqrt{2}-1)+\frac{4}{\sqrt{3}}\right]\cot\left(\frac{\theta}{2}\right)-6\right\} \quad [\pi/3 < \theta \leq 1.06] \qquad \textit{Equation 34}$$

7.2.2. Microstructure initialisation

The initial microstructure is defined by its initial subgrain (SG_s^0) and grain (G_s^0) sizes, as well as by the average boundary misorientation angle and dislocation densities [141]. The maximum boundary surface density (S_v) in each phase is given by the total surface of boundaries (HAGB + LAGB) over the total volume. Its initial value is expressed by S_v^0 and is calculated by Equation 35 [33] assuming spherical-like subgrain shape.

$$S_v = \frac{2}{SG_s} \quad \text{at } t \;\Big|\; S_v^0 = \frac{2}{SG_s^0} \quad \text{at } t = 0 \qquad \textit{Equation 35}$$

SG_s is the mean subgrain diameter. The HAGBs are separated into two distinct categories:

- HAGBs existing before the deformation
- HAGBs formed during the hot deformation via CDRX

To separate the evolution of these two categories of HAGBs the volumetric density of prior HAGBs ($S_{v_{HAB}}^0$) [141] are calculated assuming an initial spherical-like shaped grain size (G_s^0), Equation 36 [33].

$$S_{v_{HAB}}^0 = \frac{2}{G_s^0} \qquad \textit{Equation 36}$$

The volumetric boundary density formed by CDRX ($S_{v_{CDRX}}$) is calculated using Equation 37.

$$S_{v_{CDRX}} = S_v - S_{v_{HAGB}}^0 \quad \text{at } t \;\big|\; S_{v_{CDRX}}^0 = S_v^0 - S_{v_{HAGB}}^0 \quad \text{at } t = 0 \qquad \textit{Equation 37}$$

$S_{v_{CDRX}}^0$ is negligible for an initial fully recrystallised microstructure ($S_v^0 \cong S_{v_{HAGB}}^0$). In the case of a partially recrystallised microstructure, the different initial subgrain and grain sizes will define the $S_{v_{CDRX}}^0$. Finally, a multiplicative factor (A_1) is calculated, Equation 38.

$$A_1 = \frac{S_{v_{CDRX}}}{S_v} \quad \text{at } t \;\Big|\; A_1^0 = \frac{S_{v_{CDRX}}^0}{S_v^0} \quad \text{at } t = 0 \qquad \textit{Equation 38}$$

Since the Mackenzie distribution is limited by the misorientation angle range only the fraction (f_R) of the Rayleigh distribution that belongs to [$0 < \theta \leq 1.06$] is considered in the calculations, Equation 39.

$$f_R = \int_0^{1.06} \Theta_R(\theta)d\theta \quad \text{at } t \;\Big|\; f_R^0 = \int_0^{1.06} \Theta_R^0(\theta)d\theta \quad \text{at } t = 0 \qquad \textit{Equation 39}$$

$\Theta_R^0(\theta)$ is defined by the initial Rayleigh boundary average misorientation angle, $\overline{\theta_R}^0$. The boundary misorientation distribution ($\Theta(\theta)$) of each phase is calculated according to Equation 40 [141]. This description allows considering not only the evolution of boundaries formed during deformation as in [33] but also to predict a steady-state recrystallised boundary misorientation distribution that is physically-based.

$$\Theta(\theta) = A_1 f_R \Theta_R(\theta) - (1 - A_1 f_R)\Theta_M(\theta) \quad \text{at } t \,|\Theta^0(\theta) = A_1^0 f_R^0 \Theta_R^0(\theta) - \left(1 - A_1^0 f_R^0\right)\Theta_M(\theta) \quad \text{at } t = 0 \qquad \textit{Equation 40}$$

The assumptions considered from Equation 35 to Equation 40 enable the simulation of any starting microstructure since any initial subgrain, grain sizes and average boundary misorientation defines the necessary parameters and functions for the microstructure evolution completely.

Finally, the ρ_w is considered as n sets of aligned dislocation walls forming a LAGB with an average misorientation ($\bar{\theta}_{LAGB}$) and are calculated according to Equation 41 [33]. The generally accepted transition angle between LAGB and HAGB is 15° in the case of an ideal arrangement of dislocations [166]. Transition angles as low as 8.6° was reported in the literature [167]. A value of 12° is chosen as the transition angle.

$$\rho_w = \frac{nS_v\bar{\theta}_{LAGB}f_{LAGB}}{b} \quad \text{at } t \,\Big|\, \rho_w^0 = \frac{nS_v^0\bar{\theta}_{LAGB}^0 f_{LAGB}^0}{b} \quad \text{at } t = 0 \qquad \textit{Equation 41}$$

f_{LAGB} is the fraction of LAGBs and calculated according to Equation 42.

$$f_{LAGB} = \int_0^{\theta_c} \Theta(\theta)d\theta \quad \text{at } t \,\Big|\, f_{LAGB}^0 = \int_0^{\theta_c} \Theta^0(\theta)d\theta \quad \text{at } t = 0 \qquad \textit{Equation 42}$$

7.2.3. Yield stress

A simple Arrhenius-type approach [168] is considered to calculate the yield stress for each phase, Equation 43.

$$\sigma_{YS_x} = \frac{1}{\alpha_{YS_x}} \ln\left\{\left(\frac{\dot{\varepsilon}_x \exp\left(\frac{Q_{YS_x}}{RT}\right)}{A_{YS_x}}\right)^{\frac{1}{n_{YS_x}}} + \left[\left(\frac{\dot{\varepsilon}_x \exp\left(\frac{Q_{YS_x}}{RT}\right)}{A_{YS_x}}\right)^{\frac{1}{2n_{YS_x}}} + 1\right]^{1/2}\right\} \quad x = \alpha, \beta \qquad \textit{Equation 43}$$

$\dot{\varepsilon}$ is the strain rate. The activation energy (Q_{YS}), and the values α_{YS}, A_{YS}, and n_{YS} define the yield stress of the α and β-phases. A detailed procedure on the parameter calculation was published elsewhere [168] and described in Figure 22 for the Ti-17. The yield stress of the β-phase is obtained in the β-domain, Figure 22a. Using a simple law of mixtures in the α+β domain ($\sigma_{YS} = \sigma_{YS_\alpha} f_\alpha + \sigma_{YS_\beta} f_\beta$), the yield stress of the α-phase is calculated (Figure 22c), where the yield stress of the β-phase is extrapolated using Equation 43 for the obtained values of α_{YS}, Q_{YS}, A_{YS}, and n_{YS} obtained in the β-domain [141], Figure 22b. Figure 22d shows the calculated values of yield stress for the σ-phase. Figure 22e shows the calculated yield stress values at 810°C as a function of strain rate, while Figure 22f shows the overall stress as a function of temperature and strain rate.

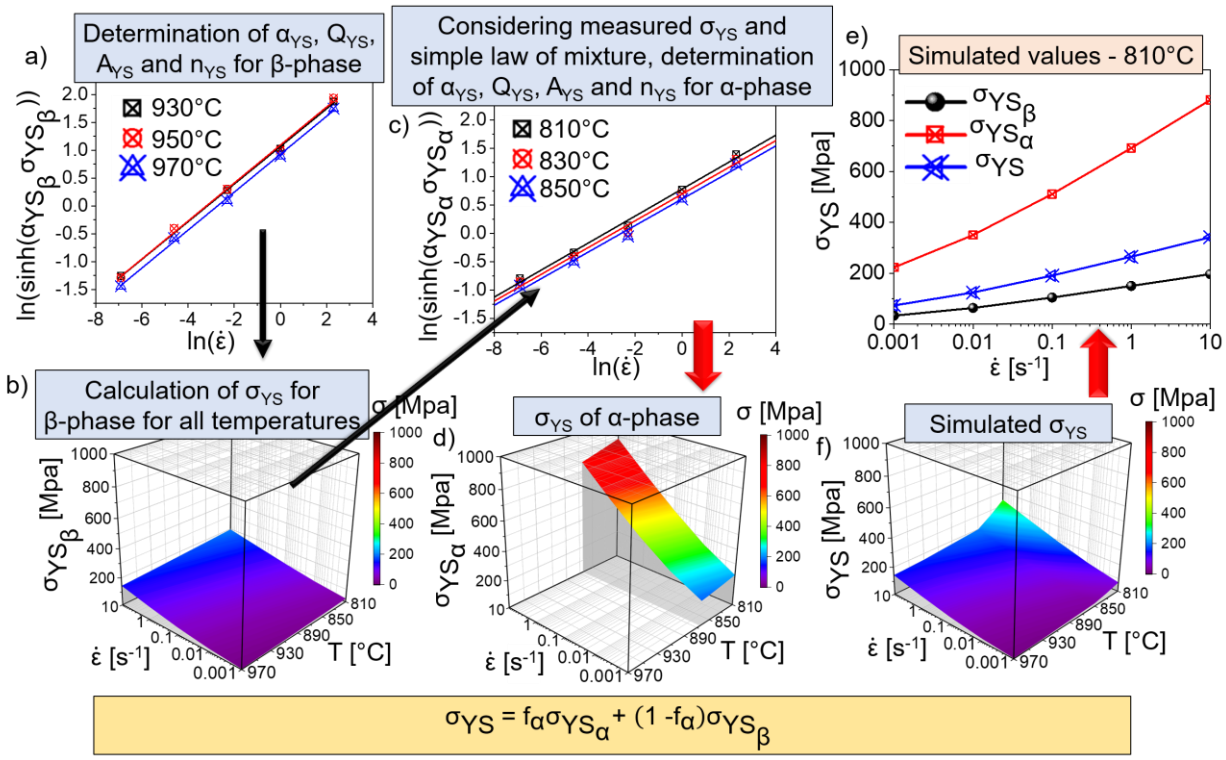

Figure 22: procedure for calculation of yield stress for the α and β phases for the Ti-17: a) Using procedure described in [168]***, α_{YS}, Q_{YS}, A_{YS}, and n_{YS} are obtained for the β-phase; b) calculated yield stress of β-phase using Equation 43 as a function of temperature and strain rates; c) calculation of yield stress in the α-phase considering $\sigma_{YS} = \sigma_{YS_\alpha} f_\alpha + \sigma_{YS_\beta} f_\beta$ and determination of α_{YS}, Q_{YS}, A_{YS}, and n_{YS} for the α-phase; d) calculated yield stress of the α-phase; e) yield stress of the α, β, and overall at 810°C; f) Simulated overall yield stress.***

7.2.4. Constitutive equations

Constitutive equations are required to couple the microstructure with the flow stress models. The thermal (σ_{th}), and athermal (σ_{ath}), stresses are the constituents of the flow stress, Equation 44. Any effect of dislocation pile-up along the grain boundary (Hall-Petch effect) is considered negligible [51,169]. All equations are applied for each phase.

$$\sigma_x = \sigma_{ath_x} + \sigma_{th_x} \quad x = \alpha, \beta \qquad \textit{Equation 44}$$

The athermal stress is expressed according to Equation 45.

$$\sigma_{ath_x} = \alpha_x M_x G_x b_x \sqrt{\rho_{i_x} + \rho_{m_x} + F_{w_x}\rho_{w_x}} \quad x = \alpha, \beta \qquad \textit{Equation 45}$$

α is the Taylor constant and considered 0.1 for both phases; M is the Taylor factor, and G is the shear modulus at the deformation temperature and calculated using JMatPro® v.10 for the chemical composition of the alloy. In the initial stages of deformation, cells of dislocations can be present and further evolve to typical subgrain boundaries due to the simultaneous increase in lattice rotation, consumption of dislocations at LAGB, and the onset of DRV. The internal stress caused for subgrain boundaries is negligible [104]. However, an empirical factor (F_w) is proposed to describe the contribution of the strain field size caused by dislocation cells on the σ_{ath} and

calculated according to Equation 46. F_w is a fraction of the ρ_w that causes a strain field factor of F_w^0 ($0 \leq F_w^0 \leq 1$) in comparison to ρ_i or ρ_m.

$$F_{w_x} = F_{w_x}^0 f_{LAGB_{cells_x}} \quad x = \alpha, \beta \qquad \textit{Equation 46}$$

$f_{LAGB_{cells}}$ is the fraction of LAGBs that behave like dislocation cells and calculated according to Equation 47.

$$f_{LAGB_{cells_x}} = \int_0^{\theta_{cells}} \Theta_x(\theta) d\theta \quad x = \alpha, \beta \qquad \textit{Equation 47}$$

θ_{cells} is a transition angle between cell and subgrain boundaries and considered equal to 3°. At the initial stages of deformation ($\overline{\theta_R} < 3°$) the contribution of the dislocation cells to stress is high and F_w decreases asymptotically to a minimum value with higher average boundary misorientations [141].

The thermal stress is assumed to have a dependency with the yield stress, σ_{YS}, as expressed in Equation 48.

$$\sigma_{th_x} = \sigma_{YS_x} - \sigma_{ath_x}^0 \quad x = \alpha, \beta \qquad \textit{Equation 48}$$

σ_{ath}^0 is calculated considering initial dislocation densities at each phase. Therefore, the thermal stress is assumed constant for a specific strain rate and temperature. The definition of the initial microstructure is the major limitation of this approach since it affects the calculation of the initial athermal stress [141].

7.2.5. Implementation of the plastic strain partitioning

Both phases are considered to evolve separately for simplification. The difference in strength between α and β phases leads to different plastic strain rates between both phases. Moreover, different initial morphologies of α-phase lead to different load transfer regimes between the phases, as discussed in section 2.6. It is proposed:

- **Ti-5553 (globular α initial microstructure):** the rotation and accommodation of plastic deformation in the α-particles up to a steady-state condition lead to the change from iso-power to iso-stress regimes.
- **Ti-17 (lamellar α initial microstructure):** the process of dynamic α-globularisation leads to a change from iso-strain to iso-stress regimes.

The eventual formation of texture is not considered in the model. However, its effect will indirectly affect the flow partition in the α+β domain. The eventual texture development in the β-phase does not seem to affect the flow stress in the β-domain.

7.2.5.1. Iso-strain

Lamellar α-phase acts as a reinforcement of the soft β-matrix, and that the material withstands an iso-strain regime of deformation. In the iso-strain regime, Equation 49 is fulfilled.

$$\dot{\varepsilon} = \dot{\varepsilon}_\alpha^\varepsilon = \dot{\varepsilon}_\beta^\varepsilon \qquad \textit{Equation 49}$$

Where $\dot{\varepsilon}$, $\dot{\varepsilon}_{\alpha}^{\varepsilon}$ and $\dot{\varepsilon}_{\beta}^{\varepsilon}$ are the applied strain rate, the strain rate in α-phase, and strain rate in the β-phase in iso-strain regime, respectively.

7.2.5.2. Iso-power

Globularised α-phases acts as reinforcement until they accommodates the plastic deformation. This is assumed to obey the iso-power law [115], i.e. α and β phases dissipate the same amount of energy during plastic deformation. The iso-power model is described according to Equation 50 and Equation 51 [115].

$$\dot{\varepsilon} = f_{\alpha}\dot{\varepsilon}_{\alpha}^{W} + (1 - f_{\alpha})\dot{\varepsilon}_{\beta}^{W} \qquad \textit{Equation 50}$$

$$\sigma_{\alpha}\dot{\varepsilon}_{\alpha}^{W} = \sigma_{\beta}\dot{\varepsilon}_{\beta}^{W} \qquad \textit{Equation 51}$$

$\dot{\varepsilon}_{\alpha}^{W}$ and $\dot{\varepsilon}_{\beta}^{W}$ are the strain rates of α and β, respectively, deforming in the iso-power regime and $\dot{\varepsilon}$ is the applied strain rate. σ_{α} and σ_{β} are the stresses in the α and β, respectively. f_{α} is the fraction of α-phase.

7.2.5.3. Iso-stress

The iso-stress regime occurs when α-phase accommodates the plastic deformation either by rotation of the α-phase (Ti-5553) or by consumption of formed boundaries within α-phase during dynamic globularisation (Ti-17). The flow stress of the β-phase equals the yield stress of α-phase. The strain rate in the α-phase ($\dot{\varepsilon}_{\alpha}^{\sigma}$) in the iso-stress regime is calculated by reorganizing the Arrhenius equation (Equation 43), Equation 52. The strain rate in the β-phase ($\dot{\varepsilon}_{\beta}^{\sigma}$) is calculated assuming that the applied strain rate follows a simple law of microstructure ($\dot{\varepsilon} = f_{\alpha}\dot{\varepsilon}_{\alpha}^{\sigma} + (1 - f_{\alpha})\dot{\varepsilon}_{\beta}^{\sigma}$), Equation 53.

$$\dot{\varepsilon}_{\alpha}^{\sigma} = \exp\left(n_{YS_{\alpha}} \ln\left(\sinh\left(\alpha_{YS_{\alpha}}\sigma_{\beta}\right)\right) - \frac{Q_{YS_{\alpha}}}{RT} + \ln\left(A_{YS_{\alpha}}\right)\right) \qquad \textit{Equation 52}$$

$$\dot{\varepsilon}_{\beta}^{\sigma} = \frac{f_{\alpha}\dot{\varepsilon}_{\alpha}^{\sigma} - \dot{\varepsilon}}{(1 - f_{\alpha})} \qquad \textit{Equation 53}$$

7.2.5.4. The fraction of material in iso-stress regime

During deformation, a volumetric fraction of the material deformed in the iso-stress condition ($f_{iso\text{-}\sigma}$), while a complementary fraction ($1 - f_{iso\text{-}\sigma}$) deforms either in the iso-strain (in the case of Ti-17) or iso-power regime (in the case of Ti-5553).

In the case of the Ti-5553, the evolution of $f_{iso\text{-}\sigma}$ is given empirically by an Avrami-like expression dependent on the strain (ε), Equation 54. The coefficient $A_{iso\text{-}\sigma}$ and the exponent n_s express the dependency of the accommodation of plastic strain in α-phase and are fitting parameters of the model.

$$f_{iso\text{-}\sigma} = 1 - \exp\left(-A_{iso\text{-}\sigma}\left(\frac{\dot{\varepsilon}}{\dot{\varepsilon}_{ref}}\right)^{n_s}\varepsilon^{n_s}\right) \qquad \textit{Equation 54}$$

In the case of the Ti-17, the $f_{iso\text{-}\sigma}$ is considered to be the same as the fraction of α-globularisation (f_{glob}). The evolution of f_{glob} is described in section 7.2.9. Finally, the overall strain

rate for each phase ($\dot{\varepsilon}_x$, x = α or β) is calculated as a simple rule of mixtures of both iso-strain and iso-stress contributions, Equation 55.

$$\dot{\varepsilon}_x = \begin{cases} (1\text{-}f_{iso\text{-}\sigma})\dot{\varepsilon}_x^W + f_{iso\text{-}\sigma}\dot{\varepsilon}_x^\sigma & \text{Ti-5553} \\ (1\text{-}f_{iso\text{-}\sigma})\dot{\varepsilon}_x^\varepsilon + f_{iso\text{-}\sigma}\dot{\varepsilon}_x^\sigma & \text{Ti17} \end{cases}, \; x = \alpha, \beta \qquad \textit{Equation 55}$$

7.2.5.5. Overall stress calculation

The overall or total stress is calculated as a simple law of mixtures of the volume fractions of α (f_α) and β ($1\text{-}f_\alpha$) phases, Equation 56.

$$\sigma = f_\alpha\sigma_\alpha + (1 - f_\alpha)\sigma_\beta \qquad \textit{Equation 56}$$

The stress in each phase is calculated based on Equation 44. The athermal stress is calculated using the dislocation densities in each phase. The thermal stress is a sum of the iso-stress and iso-power (for the Ti-5553) or iso-strain (for the Ti-17) components, Equation 57. Each thermal stress component ($\sigma_{th_x}^z$) is calculated according to Equation 58 for the yield stress obtained using the respective strain rate for each load partitioning regime. The yield stress values are calculated according to Equation 43.

$$\sigma_x = \begin{cases} \sigma_{ath_x} + f_{iso\text{-}\sigma}\sigma_{th_x}^\sigma + (1 - f_{iso\text{-}\sigma})\sigma_{th_x}^W & \text{Ti-5553} \\ \sigma_{ath_x} + f_{iso\text{-}\sigma}\sigma_{th_x}^\sigma + (1 - f_{iso\text{-}\sigma})\sigma_{th_x}^\varepsilon & \text{Ti-17} \end{cases}, \; x = \alpha, \beta \qquad \textit{Equation 57}$$

$$\sigma_{th_x} = \begin{cases} \sigma_{YS_x}\left(\dot{\varepsilon}_x^\varepsilon\right) - \sigma_{ath_x}^0 & \text{Iso-strain} \\ \sigma_{YS_x}\left(\dot{\varepsilon}_x^W\right) - \sigma_{ath_x}^0 & \text{Iso-power}, \; x = \alpha, \beta \\ \sigma_{YS_x}\left(\dot{\varepsilon}_x^\sigma\right) - \sigma_{ath_x}^0 & \text{Iso-stress} \end{cases} \qquad \textit{Equation 58}$$

7.2.5.6. Calculation of evolution of strain rate dependent variables

In this work, the evolution of the variables that are strain rate dependent is calculated according to Equation 59 in the α+β domain.

$$v_x^{i+1} = v_x^i + f_{iso\text{-}\sigma}\left(\frac{dv_x^{(\text{iso-stress})}}{dt}\right)\Delta t + (1\text{-}f_{iso\text{-}\sigma})\left(\frac{dv_x^{(\text{iso-strain or iso-W})}}{dt}\right)\Delta t \qquad \textit{Equation 59}$$

v_x^{i+1} is the updated value of a variable v_x at the step i+1, v_x^i is the last value, $dv_x^{(\text{iso-stress})}/dt$ is the variation of a variable calculated using the iso-stress strain rate, $dv_x^{(\text{iso-strain or iso-W})}/dt$ is the variation of a variable calculated using the iso-strain or iso-power strain rate, and Δt is the time step for the calculation.

7.2.6. Dislocation densities rate equations

Two models are developed for the dislocations rate equations. The first model accounts for a simplified physical description of the dislocation production and annihilation and is based on the Kocks-Mecking approach [170]. A second model is developed with comprehensive rate equations for separated phenomena involving the dislocations interactions and is based on the work of Ghoniem et al. [104].

7.2.6.1. Kocks-Mecking-based rate equations

The mobile dislocation density is assumed invariable with respect to strain rate and strain, while the glide velocity (v_g) is invariable with strain and can be calculated according to Orowan's equation, Equation 60. The plastic strain rate is considered equal to the experimental strain rate ($\dot{\varepsilon} = \dot{\varepsilon}_p$) in each phase.

$$v_{g_x} = \frac{M_x \dot{\varepsilon}_x}{b_x \rho_{m_x}} \quad x = \alpha, \beta \qquad \textit{Equation 60}$$

The evolution of internal variables is expressed as differential equations and solved using numerical incremental steps. The evolution of the immobile dislocation density for α and β phases are expressed in Equation 61.

$$\left.\frac{d\rho_y}{dt}\right|_x = \left.\frac{d\rho_{i_x}}{dt}\right|_{production} + \left.\frac{d\rho_{i_x}}{dt}\right|_{reduction} \quad x = \alpha, \beta \qquad \textit{Equation 61}$$

A modified expression from Kocks and Mecking [170] and Montheillet et al. [33] is proposed to describe the production rate of new immobile dislocations, Equation 62.

$$\left.\frac{d\rho_{i_x}}{dt}\right|_{production} = \left(1 + \frac{S_{v_{interface}}}{S_v^{REF}}\right) h_{1_x}\, \dot{\varepsilon}_x \quad x = \alpha, \beta \qquad \textit{Equation 62}$$

h_{1_x} is the hardening coefficient of either α or β phase, S_v^{REF} is a constant related for all conditions and fitting parameter of the model. The surface fraction of α/β interface ($S_{v_{interface}}$) is calculated depending on its morphology prior to deformation and considered constant during deformation. In the case of the Ti-5553, $S_{v_{interface}}$ is calculated according to Equation 63 assuming spherical α-particles of radius R_α^0 homogeneously distributed in the β-phase. In the case of the Ti-17, $S_{v_{interface}}$ is simplified assuming infinite and parallel α-plates of a thickness prior to the deformation t_α^0 where $S_{v_{interface}}$ is calculated according to Equation 64.

$$S_{v_{interface}} = \frac{3f_\alpha}{4\pi R_\alpha^0}, \text{ Ti-5553} \qquad \textit{Equation 63}$$

$$S_{v_{interface}} = \frac{2f_\alpha}{t_\alpha^0}, \text{ Ti-17} \qquad \textit{Equation 64}$$

Similarly, reduction of immobile dislocations is calculated using Equation 65.

$$\left.\frac{d\rho_{i_x}}{dt}\right|_{reduction} = -\left(1 + \frac{S_{v_{interface}}}{S_v^{REF}}\right) h_{2_x}\, \rho_{i_x}\, \dot{\varepsilon}_x \quad x = \alpha, \beta \qquad \textit{Equation 65}$$

h_{2_x} is the reduction coefficient of either α or β phase. The hardening (h_{1_x}) and reduction (h_{2_x}) coefficients are calculated according to Equation 66 and Equation 67 [33].

$$h_{1_x} = h_{1_x}^0 \left(\frac{\dot{\varepsilon}_x}{\dot{\varepsilon}_{ref}}\right)^{m_{1_x}} \exp\left(\frac{Q_{1_x}}{RT}\right) \quad x = \alpha, \beta \qquad \textit{Equation 66}$$

$$h_{2_x} = h_{2_x}^0 \left(\frac{\dot{\varepsilon}_x}{\dot{\varepsilon}_{ref}}\right)^{-m_{2_x}} \exp\left(-\frac{Q_{2_x}}{RT}\right) \quad x = \alpha, \beta \qquad \textit{Equation 67}$$

h_{1x}^0 and h_{2x}^0 are constants that account for the production of dislocations and reduction, respectively, m_1 and m_2 are exponents related to the strain hardening coefficient; and Q_{1x} and Q_{2x} are activation energies for the production of dislocations and reduction, respectively.

The immobile dislocations that are related to the recovery term ($d\rho_{ix}/dt\big|_{reduction}$) either migrate to existing LAGBs or form new LAGBs, Equation 68.

$$\Delta\rho_{CDRX_x} = \left(\frac{d\rho_{ix}}{dt}\bigg|_{reduction}\right)\Delta t \quad x = \alpha, \beta \qquad \textit{Equation 68}$$

Where $\Delta\rho_{CDRX_x}$ is the amount of dislocations forming LAGBs or migrating to existing ones for an incremental time step Δt for each phase.

7.2.6.2. Rate equations based on dislocation density reactions (Ghoniem)

A second approach with a detailed description of dislocation reactions that is developed based on [104] is presented in this section. The experimental strain (ε) is considered as a sum of the plastic strain (ε_p) with the elastic strain (ε_e) for each phase, Equation 69.

$$\varepsilon_x = \varepsilon_{e_x} + \varepsilon_{p_x} \quad x = \alpha, \beta \qquad \textit{Equation 69}$$

The variation in the flow stress at each iteration is expressed according to the derivative of the Hook's law, Equation 70.

$$\dot{\sigma}_x = E_x\left(\dot{\varepsilon}_x - \dot{\varepsilon}_{p_x}\right) \quad x = \alpha, \beta \qquad \textit{Equation 70}$$

For each phase, E is the Young modulus, $\dot{\varepsilon}$ is the experimental strain rate and $\dot{\varepsilon}_p$ is the calculated plastic strain rate. The plastic strain rate is calculated according to Orowan's relationship (Equation 60), and the glide velocity calculated as Equation 71 [104].

$$v_{g_x} = a_{1_x}\exp\left(-\frac{W_{g_x}}{k_B T}\right)\frac{\sigma_{th_x}\Omega}{k_B T} \quad x = \alpha, \beta \qquad \textit{Equation 71}$$

a_1 is a pre-factor, W_g corresponds to an activation energy for glide, k_B is the Boltzmann constant, and Ω is the atomic volume of Ti. The σ_{th} is an output in this second approach since the variation in stress is calculated by Equation 70. Thus, Equation 44 is reorganised as Equation 72.

$$\sigma_{th_x} = \sigma_x - \sigma_{ath_x} \quad x = \alpha, \beta \qquad \textit{Equation 72}$$

However, σ_{th} is assumed to be constant for a constant $\dot{\varepsilon}$ and temperature, and is calculated according to Equation 48 in the β-domain and according to Equation 58 in the α+β domain. An algorithm to limit the value of σ_{th} in this second approach is implemented and described in Appendix C.

Equation 73 describes the rate for mobile dislocation density [104].

$$\frac{d\rho_{m_x}}{dt} = \rho_{m_x}^{3/2} v_{g_x} + \frac{\delta_{SG_x}\rho_{m_x}\Phi_{sg_x}v_{g_x}}{\lambda_{m_x}^2} - \frac{\rho_{m_x}v_{g_x}}{\Phi_{sg_x}} - 8\frac{\rho_{m_x}v_{c_{m_x}}}{\lambda_{m_x}} - \delta_{DRV_x}\rho_{m_x}\left(\rho_{m_x}+\rho_{i_x}\right)v_{g_x} \qquad \textit{Equation 73}$$
$$x = \alpha, \beta$$

The production of mobile dislocations due to Read's source and at subgrain boundaries correspond to the first and second terms, respectively [142]. The third, fourth and fifth terms correspond to the immobilisation of mobile dislocations at subgrain boundaries, the static recovery due to climb, and the dynamic recovery, respectively. v_g is the glide velocity, λ_m and λ_i are the inter-dislocation distance for the mobile and immobile dislocations, respectively, v_{c_m} and v_{c_i} are the climb velocities for the mobile and immobile dislocations, respectively, and δ_{DRV} is the critical distance of dislocation annihilation via DRV [142]. If the production of mobile dislocations at subgrain boundaries is neglected, the immobilisation at subgrain boundaries can lead to the annihilation of all mobile dislocation. The expression is modified from [104] and, for simplification, δ_{SG} is an internal variable adjusted at each step to maintain a constant glide velocity during plastic deformation at a given strain rate and temperature. Consequently, the mobile dislocation density is also kept constant during plastic deformation at a given strain rate and temperature due to Orowan's relationship.

Equation 74 describes the rate equations for immobile dislocation density [104].

$$\frac{d\rho_{i_x}}{dt} = \frac{\rho_{m_x} v_{g_x}}{\Phi_{sg_x}} - 8\frac{\rho_{i_x} v_{c_{i_x}}}{\lambda_{i_x}} - \delta_{DRV_x}\rho_{m_x}\rho_{i_x} \quad x = \alpha, \beta \qquad \textit{Equation 74}$$

The production of immobile dislocations occurs by immobilisation of mobile dislocations (first term), while SRV and DRV are responsible for the annihilation of immobile dislocations (second and third terms, respectively) [142].

λ_m and λ_i are the dislocation interspacing, calculated according to Equation 75.

$$\lambda_y = \frac{1}{\sqrt{\rho_y}} \quad y = m, i \qquad \textit{Equation 75}$$

The SRV of mobile, as well as of immobile dislocations, is modelled as a process of formation and annihilation of dislocation dipoles by climbing [104]. The climb dislocation velocity (v_{c_y}) is calculated using Equation 76 [104].

$$v_{c_y} = \frac{2\pi\eta D_s \sigma_{climb} \Omega}{k_B T b\left(1 - \eta \ln\left(L_{\alpha_{CLIMB}}/\lambda_y\right)\right)} \quad y = m,i \qquad \textit{Equation 76}$$

The climb stress (σ_{climb}) is calculated according to Equation 77 [104].

$$\sigma_{climb} = \frac{Gb}{2\pi(1 - \nu)\lambda_y} \quad y = m,i \qquad \textit{Equation 77}$$

ν is the Poisson ratio. D_s is the self-diffusion coefficient given according to Equation 78 [171], η is a fitting parameter for transfer of defect into jogs on the dislocation, and $L_{\alpha_{CLIMB}}$ is the length governing the elastic interaction between the dislocation and the defects, Equation 79 [104].

$$D_s = 1.0\cdot10^{-4} \exp\left(-\frac{2.5\cdot10^5}{RT}\right) \qquad \textit{Equation 78}$$

$$L_{\alpha_{CLIMB}} = \frac{(1 + \nu)G\Omega}{6\pi(1 - \nu)k_B T} \qquad \textit{Equation 79}$$

A fraction (f_{CDRX}) of the mobile and immobile dislocations are statically or dynamically recovered either migrate to existing LAGBs or form new LAGBs, Equation 80 [141]. The complement fraction ($1 - f_{CDRX}$) corresponds to the fraction of dislocations that are annihilated [141].

$$\Delta\rho_{CDRX} = f_{CDRX}\left(\left.\frac{d\rho_m}{dt}\right|_{SRV} + \left.\frac{d\rho_i}{dt}\right|_{SRV} + \left.\frac{d\rho_m}{dt}\right|_{DRV} + \left.\frac{d\rho_i}{dt}\right|_{DRV}\right)\Delta t \qquad \textit{Equation 80}$$

$\Delta\rho_{CDRX}$ is the amount of dislocations forming LAGBs or migrating to existing ones for an incremental time step Δt.

The presence of phase interfaces and the role of α-phase on increasing lattice rotation of the β-phase or increase in misorientation promoting the formation of new LAGBs [49] is incorporated in the proposed model by assuming a value of f_{CDRX} that is correlated to the α-fraction and its size, Equation 81.

$$f_{CDRX} = f^0_{CDRX} + \frac{f^{interface}_{gloular} S_{v_{interface}}}{\lambda_{interspace}},\ \text{Ti-5553} \qquad \textit{Equation 81}$$

$$f_{CDRX} = f^0_{CDRX} + f^{interface}_{plates} S_{v_{interface}},\ \text{Ti-17} \qquad \textit{Equation 82}$$

f^0_{CDRX}, $f^{interface}_{gloular}$ and $f^{interface}_{plates}$ are constants. $S_{v_{interface}}$ is calculated according to Equation 63 for the Ti-5553 and according to Equation 64 for the Ti-17. $\lambda_{interspace}$ is the particle interspace and calculated according to Equation 83 [172] assuming a random distribution of spherical α-phase for the Ti-5553.

$$\lambda_{interspace} = \sqrt{\frac{\ln(3)}{2\pi n_d R^0_\alpha} + \frac{8R^{0^2}_\alpha}{3}} - \sqrt{\frac{8}{3}}R^0_\alpha, \qquad n_d = \frac{3f_\alpha}{4\pi\left(R^0_\alpha\right)^3} \qquad \textit{Equation 83}$$

7.2.7. Boundary density and misorientation distribution evolutions

The evolution of the boundary density and misorientation distribution is a result of SRV and DRV phenomena for both α and β phases. The recovered dislocations ($\Delta\rho_{CDRX}$) that are the source for either the formation of new LAGBs or for the increase of their misorientation [33]. A fraction α_{CDRX} for the formation of new LAGBs of an average misorientation (θ_0) is considered. Assuming that a dislocation wall is formed by (n) sets of dislocations, the production rate of new boundaries ($dS^+_{v_x}/dt$) is calculated according to Equation 84 [33].

$$\frac{dS^+_{v_x}}{dt} = \alpha_{CDRX_x}\frac{b_x}{n_x\theta_{0_x}}\Delta\rho_{CDRX_x}\dot{\varepsilon}_{p_x} \quad x = \alpha, \beta \qquad \textit{Equation 84}$$

The complementary fraction ($1 - \alpha_{CDRX}$) accounts for the increase of the average misorientation of existing LAGBs, Equation 85 [33].

$$\frac{d\overline{\theta_{R_x}}}{dt} = \left(1 - \alpha_{CDRX_x}\right)\frac{b_x}{n_x S_{v_x}}\Delta\rho_{CDRX_x}\dot{\varepsilon}_{p_x} \quad x = \alpha, \beta \qquad \textit{Equation 85}$$

The movement of HAGBs sweeps part of the immobile dislocations (Equation 86) as well as the existing and formed boundaries (Equation 87).

$$\left.\frac{d\rho_{y_x}}{dt}\right|_{\text{HAGB movement}} = \begin{cases} -\rho_{y_x} S_{v_x} f_{HAGB_x} v_{HAGB_x} & x = \alpha, \beta \quad y = i \quad \text{Kocks-Mecking} \\ -\rho_{y_x} S_{v_x} f_{HAGB_x} v_{HAGB_x} & x = \alpha, \beta \quad y = m, i \quad \text{Ghoniem} \end{cases} \qquad \textit{Equation 86}$$

$$\frac{dS_{v_x}^{-}}{dt} = -S_{v_x}{}^2 f_{HAGB_x} v_{HAGB_x} \quad x = \alpha, \beta \qquad \textit{Equation 87}$$

The overall surface fraction rate is given according to Equation 88.

$$\frac{dS_{v_x}}{dt} = \frac{dS_{v_x}^{+}}{dt} + \frac{dS_{v_x}^{-}}{dt} \quad x = \alpha, \beta \qquad \textit{Equation 88}$$

The mobility of the HAGBs [33] (M_{HAGB}) is given by Equation 89 [173]. The mobility of the LAGBs is considered negligible

$$M_{HAGB_x} = M_{0_x} \exp\left(-\frac{Q_{HAGB_x}}{RT}\right) \quad x = \alpha, \beta \qquad \textit{Equation 89}$$

Q_{HAGB} is the activation energy for HAGB movement, and M_0 is calculated according to Equation 90 [173].

$$M_{0_x} = \frac{b_x t_{HAGB_x}}{k_B T} \exp\left(-\frac{Q_{DIFF_x}}{RT}\right) \quad x = \alpha, \beta \qquad \textit{Equation 90}$$

With t_{HAGB} being the thickness of the HAGB, and Q_{DIFF} is the activation energy for self-diffusion along the grain boundary. The velocity of the HAGBs (v_{HAGB}) corresponds to the product of its mobility and a driving force (E_{MOB}), Equation 91.

$$v_{HAGB_x} = M_{HAGB_x} E_{MOB_x} \quad x = \alpha, \beta \qquad \textit{Equation 91}$$

The driving force for HAGB movement can be related to: a) the dislocation density difference between neighbour grains; b) the grain curvature. The role of both in CDRX is combined in a phenomenological expression given by Equation 92 [33].

$$E_{MOB_x} = E^0_{MOB_x} \left(\frac{\dot{\varepsilon}_{p_x}}{\dot{\varepsilon}_{ref}}\right)^{n_{HAGB_x}} \quad x = \alpha, \beta \qquad \textit{Equation 92}$$

E^0_{MOB} and n_{HAGB} are material fitting parameters. The final expression can be expressed according to Equation 93 [33].

$$v_{HAGB_x} = v_{0_x} \left(\frac{\dot{\varepsilon}_x}{\dot{\varepsilon}_{ref}}\right)^{n_{HAGB_x}} \exp\left(-\frac{Q_{eq_x}}{RT}\right) \quad x = \alpha, \beta \qquad \textit{Equation 93}$$

$v_0 = E^0_{MOB} b t_{HAGB} / k_B T$ is a velocity coefficient and $Q_{eq} = Q_{DIFF} - Q_{HAGB}$.

7.2.8. Wall dislocation density, grain and subgrain size evolutions

The grain size (G_s) and the subgrain size (SG_s) are calculated according to Equation 94 and Equation 95 [33], respectively.

$$G_s = \frac{2 f_{HAGB}}{S_v} \qquad \textit{Equation 94}$$

$$SG_s = \frac{2}{S_v} \qquad \textit{Equation 95}$$

Finally, the wall dislocation density (ρ_w) is updated according to Equation 41 at each iteration.

7.2.9. Dynamic globularisation of the α-phase

The stages of dynamic globularisation of the α-phase are modelled as schematically shown in Figure 23, where a platelet is considered as a block with a mean aspect ratio (AR), a mean thickness (t_α) and mean width ($w_\alpha = t_\alpha \cdot AR$) [142].

The dynamic globularisation consists of the formation of boundaries within the platelet due to plastic deformation ($dS^+_{v_\alpha}$, Equation 84) and further formation or migration of new α/β interfaces [142]. In this case, the evolution of the boundaries formed within the α due to plastic deformation via CDRX (Equation 84 and Equation 85) promote further α/β interface migration once HAGBs are formed within the α-platelet. The production of new α/β interfaces during dynamic globularisation of the α-phase can be calculated according to Equation 96 [142].

$$\frac{dS^+_{glob}}{dt} = \frac{f_{BG} S_{v_\alpha} v_{glob}}{t_\alpha} \qquad \textit{Equation 96}$$

S_{glob} is the α/β interfaces density formed, f_{BG} is the fraction of formed boundaries within the α-platelet that leads to grooving and movement of the α/β interface, and v_{glob} is the velocity of movement of α/β interfaces [142]. The interface movement kinetics during dynamic globularisation is expected to be related to the static globularisation kinetics [174], with the difference that the penetration of β-phase occurs through HAGBs. Thus, v_{glob} should be related to the diffusion at grain boundaries or pipe diffusion, and it would vary according to the degree of organisation of the formed HAGB. The calculation is simplified considering $v_{glob}$is the glide velocity of the mobile dislocation in the β-phase multiplied by a constant (A_{glob}), Equation 97 [142].

$$v_{glob} = A_{glob} v_{glide} \qquad \textit{Equation 97}$$

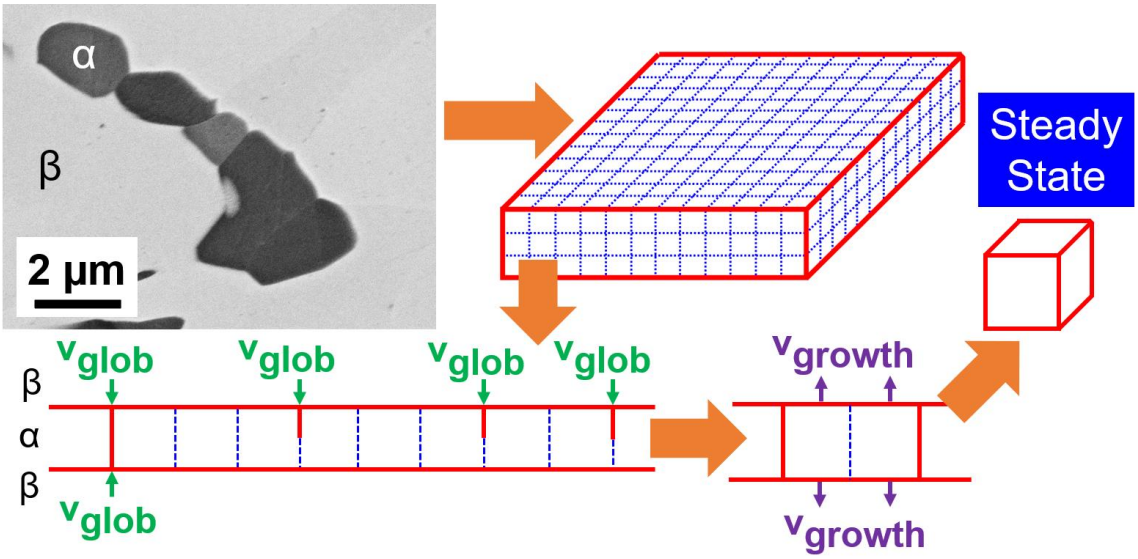

Figure 23: Schematic representation of the dynamic globularisation of the α-phase, illustrated by a backscattered electron micrograph after deformation at 810°C up to 0.85 strain for 0.001 s^{-1}: the formation of boundaries that leads to the division of the α-platelet with a mean α/β interface velocity v_{glob} accompanied by growth with a velocity v_{growth}.

The formation of an α/β interface leads to consumption of a fraction of the formed LAGBs and HAGBs within α-phase [142]. Therefore, the boundary density of LAGB and HAGB (S_{V_α}) can be calculated according to Equation 98.

$$\frac{dS_{V_\alpha}}{dt} = \frac{dS^{+}_{V_\alpha}}{dt} - \frac{dS^{+}_{glob}}{dt} \qquad \textit{Equation 98}$$

The total boundary density summing the α/β interface, and the LAGBs and HAGBs formed within the α-platelet is calculated according to Equation 99 [142].

$$S_{TOTAL_\alpha} = S_{V_\alpha} + S_{glob} \qquad \textit{Equation 99}$$

Fully globularisation of an α-platelet occurs when $S_{V_\alpha} = 0$. All the boundaries produced inside the platelet of α-phase during plastic deformation via CDRX are converted in α/β interface [142]. The globularisation fraction can be calculated according to Equation 100 [142].

$$f_{glob} = \frac{S_{glob}}{S_{TOTAL_\alpha}} \qquad \textit{Equation 100}$$

The consequence of this approach is that, even if $f_{glob} = 1$, it does not mean that the α-particles have an aspect ratio of 1. Depending on the initial thickness, temperature and strain rate, it is possible that the consumption of the formed boundaries is fast, and the globularisation finishes before achieving an aspect ratio of one [142]. This situation is illustrated in Figure 24(a,c,e). On the other hand, it can also occur that the aspect ratio is one while the globularisation fraction is smaller than one, Figure 24d.

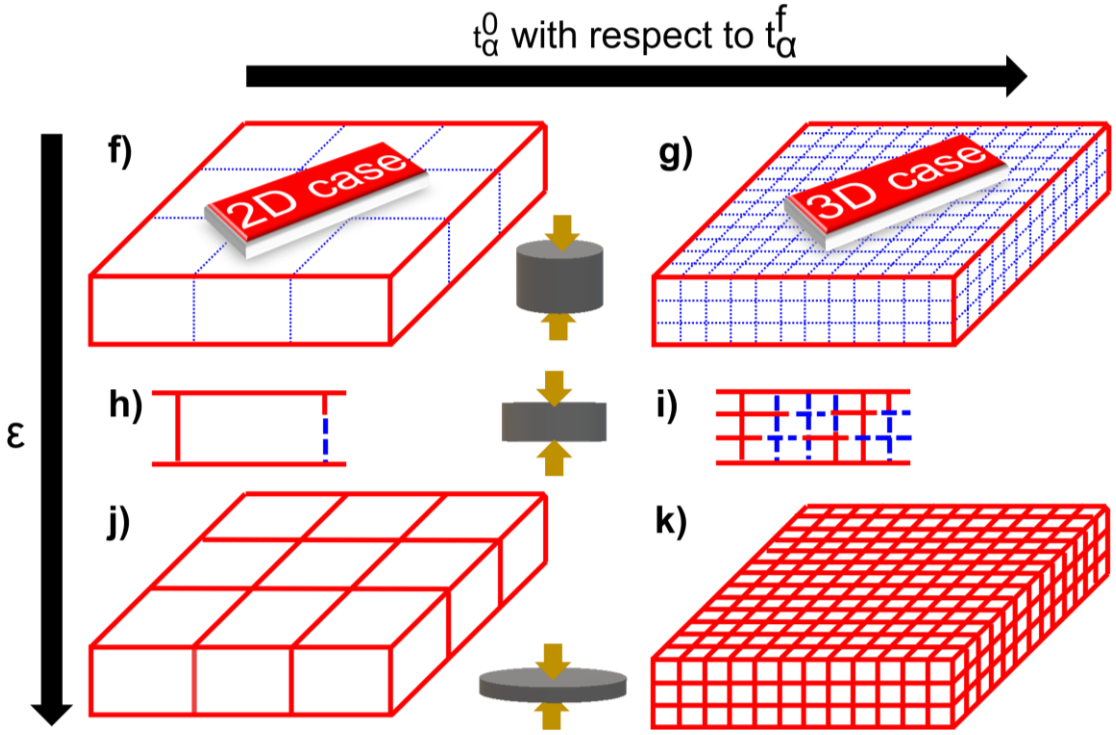

Figure 24: Illustration of the globularisation of an α-platelet for the 2D-case (a,c,e), and 3D-case (b,d,f). a) the formation of an insufficient amount of boundaries within α-platelet and c) the separation of the globularised particles, lead to e) formation particles with an aspect ratio higher than 1. In the 3D-case, b) the formation of boundaries leads to d,f) division of the platelet in particles smaller than its thickness.

The formed α/β interfaces divide the α-platelets into n_{glob} α-particles of a particle size ϕ_α, thus incorporating the three-dimensional aspect of the problem. In the two-dimensional case (2D-case), the particle size is larger than the thickness of the α-platelet. The formed boundaries within the platelet (Figure 24a) are rapidly consumed (Figure 24c) and the formed particles after the completion of α/β interface formation do not exhibit an aspect ratio of 1. The thickness of the formed α-phase increases with a velocity v_{growth} until reaching an aspect ratio of 1. Thus, the final thickness in the steady-state that can be notably larger than the initial thickness.

On the other hand, the division of the α-platelet into "layers" in the three-dimensional case (3D case) as schematically shown in Figure 24(b,d,f) leads to a progressive decrease of the lamellar thickness. All boundaries within the α-platelet are consumed, and the final thickness at the steady-state can be notably smaller than the initial thickness.

Therefore, the globularisation of α-phase starts in the "2D-case" (aspect ratio larger than one), and once the aspect ratio reaches one, the evolution occurs in the "3D-case".

Semiatin et al. [175] proved that the growth of the spherical particles during dynamic globularisation is an Ostwald-Ripening process with an accelerated diffusion due to pipe diffusion. Here, the shape of the α-particles varies during the process, and the growth is simplified adopting a mean velocity of thickening, v_{growth}. The growth of the α-platelets is calculated according to Equation 101 [142].

$$\frac{dt_\alpha}{dt} = 2f_{glob}v_{growth} \qquad \textit{Equation 101}$$

The thickening is a diffusion-related process, where the α/β movement during growth with v_{growth} is related to the transport of matter of α and β-phases to minimise the surface energy of the formed α-phase. In fact, during Ostwald-Ripening of non-spherical particles [176], complex solutions are necessary. Here the v_{growth} is simplified and related to the climb velocity of the mobile dislocation density in the β-phase, Equation 102. The v_{growth} is dependent on the mobile dislocation density in the β-phase, inter-diffusion coefficient and other material properties, Equation 76 [142].

$$v_{growth} = B_{glob}v_{climb} \qquad \textit{Equation 102}$$

- **"2D-case"** (AR > 1)

The particle size (ϕ_α) is calculated according to the formed S_{glob} during dynamic globularisation, Equation 103.

$$\phi_\alpha = \frac{2w_\alpha^2}{S_{glob}w_\alpha^2 + 2w_\alpha} \qquad \textit{Equation 103}$$

Furthermore, the width is calculated according to Equation 104 [142].

$$\frac{dw_\alpha}{dt} = -AR^2t_\alpha^3\frac{dt_\alpha}{dt} \qquad \textit{Equation 104}$$

Finally, the aspect ratio of the α-particles is calculated using Equation 105 [142].

$$AR = \frac{\phi_\alpha}{t_\alpha} \qquad \textit{Equation 105}$$

- **"3D-case"** (AR = 1)

The updated thickness is calculated for the iteration i+1 (t_α^{i+1}) as a function of the density of the α/β interface formed during dynamic globularisation of the α-phase (S_{glob}) and the thickness from the iteration i (t_α^i), Equation 106 [142].

$$t_\alpha^{i+1} = \phi_\alpha = \frac{4t_\alpha^i}{S_{glob}t_\alpha^i + 4t_\alpha^i} \qquad \textit{Equation 106}$$

Although the aspect ratio and thickness evolutions can be predicted, the model cannot predict the decrease in thickness due to plastic deformation nor the interspace between the formed α-grains.

7.3. Static recrystallisation model

The model comprises the simultaneous phenomena of SRV, subgrain evolution and grain growth of the deformed β-phase. The modelling strategy shown here was already published in [146] for the Ti-17. The model is based on strain induced boundary migration (SIBM) and is separated into nucleation and growth. Static grain growth independent on the recrystallisation grade is considered. The procedure to obtain the fitting parameters is schematically discussed in Figure F. 1 (see Appendix F).

7.3.1. Static recovery

The SRV of mobile as well as of immobile dislocations is modelled according to corresponding terms in Equation 73 and Equation 74, respectively.

7.3.2. Subgrain evolution

The proposed model is based on the simultaneous role of subgrain coarsening and subgrain nucleation from the reorganisation of dislocations within the subgrain [146], as proposed by Ghoniem et al. [104]. The rate of growth of subgrains is considered as the product of driving pressure and mobility. The smallest subgrains can collapse their boundaries, coalescing and joining adjacent boundaries during subgrain growth [104]. The pressure for subgrain growth is given according to Equation 107 [104].

$$P_{LAGB} = \frac{4}{3}Gb^2\rho_w \qquad \textit{Equation 107}$$

The mobility of a subgrain is described as a form of the climb due to lattice diffusion [104], Equation 108.

$$M_{LAGB} = \frac{2\pi\eta D_s\Omega}{bk_BT} \qquad \textit{Equation 108}$$

The presence of α-phase in the α+β domain is considered as a Zener back pressure opposing the motion of the LAGBs [177]. Therefore, the pressure for subgrain growth must satisfy Equation 109.

$$P_{LAGB} \geq P_{Zener} \qquad \textit{Equation 109}$$

The Zener pressure is given according to Equation 110 [178].

$$P_{Zener} = \frac{3f_{\alpha}AR^{0.47}}{2t_{\alpha}} \qquad \textit{Equation 110}$$

If Equation 109 is satisfied, the subgrain growth can be calculated according to Equation 111.

$$\left.\frac{dSG_s}{dt}\right|_{growth} = M_{LAGB}(P_{LAGB} - P_{Zener}) \qquad \textit{Equation 111}$$

The nucleation of subgrains is the result of the tendency of dislocations for self-organisation, and it is assumed to be dominated by the dislocation climb [104]. The time for nucleation (τ_{nuc}) is given according to Equation 112 [104].

$$\tau_{nuc} = \frac{k_B T\Omega}{G\eta K_{nuc}\sqrt{\rho_m + \rho_i}D_s}\left(\sqrt{\rho_m + \rho_i} - \frac{K_{nuc}}{SG_s}\right) \qquad \textit{Equation 112}$$

K_{nuc} is a constant with a value of around 10 [179,180]. The change of the mean subgrain size due to nucleation is then $SG_s - \left(K_{nuc}/\sqrt{\rho_m + \rho_i}\right)$. Therefore, the subgrain size refinement due to nucleation is given according to Equation 113 [104].

$$\left.\frac{dSG_s}{dt}\right|_{nucleation} = -\frac{G\eta K_{nuc}SG_s\left[\sqrt{\rho_m + \rho_i} - \left(\frac{K_{nuc}}{SG_s}\right)\right]\Omega D_s}{k_B T} \qquad \textit{Equation 113}$$

The overall subgrain size evolution is given according to Equation 114.

$$\frac{dSG_s}{dt} = \left.\frac{dSG_s}{dt}\right|_{nucleation} + \left.\frac{dSG_s}{dt}\right|_{growth} \qquad \textit{Equation 114}$$

7.3.3. Strain induced boundary migration

SRX is assumed to occur via SIBM. The bulging of a subgrain occurs by the movement of the HAGB that forms the subgrain. Original grain boundaries, transition bands and shear bands are favourite sites for nucleation [121]. Inhomogeneous distribution of recrystallisation nuclei can also happen due to variations in stored energy withing the grain [121]. A modified SIBM model is proposed to account for the non-randomly distributed nucleation due to the large prior β-grain size [146].

The nucleation model is adapted from the work of Kashif Rehman and Zurob [136], while the definition of recrystallised volume fraction is modelled according to the classical Mehl, Avrami, and Kolmogorov (JMAK) model [178].

7.3.3.1. Nucleation

The subgrain size of the deformed microstructure has a Rayleigh distribution, $p_{SG}(\chi)$, Equation 115 [136].

$$p_{SG}(\chi) = \frac{\pi}{2}\chi\exp\left(-\frac{\pi\chi^2}{4}\right) \qquad \textit{Equation 115}$$

χ is the normalised subgrain size by its mean value. A critical subgrain size (SG_s^*) is necessary to overcome the capillary forces for a nucleus to grow, Equation 116 [136].

$$SG_s^* = \frac{4\gamma_{HAGB}}{E_{SIBM}} \qquad \textit{Equation 116}$$

E_{SIBM} is the stored energy for the spherical cap of diameter SG_s^*, with specific boundary energy, γ_{HAGB}. The E_{SIBM} is the stored energy due to the difference in the dislocation density between the bulging subgrain and the adjacent subgrain minus the capillarity energy of the opposite subgrain boundary, Equation 117 [146].

$$E_{SIBM} = \frac{Gb^2(\rho_m + \rho_i + \rho_w)}{2} - \frac{4\gamma_{LAGB}}{SG_s} \qquad \textit{Equation 117}$$

γ_{LAGB} is the LAGB energy and given according to Equation 118 [181,182].

$$\gamma_{LAGB} = \frac{Gb\bar{\theta}_{LAGB}}{4\pi(1-\nu)}\left(0.23 - \ln\left(\bar{\theta}_{LAGB}\right)\right) \qquad \textit{Equation 118}$$

The model predicts an incubation time until the critical subgrain size for nucleation is reached. The largest subgrain is 2.5 times the average subgrain size assuming a Rayleigh distribution for the subgrain size, Equation 115. Therefore, incubation is over if the largest subgrain ($2.5 \cdot SG_s$) is larger than the critical subgrain size (SG_s^*), Equation 119.

$$SG_s > \frac{SG_s^*}{2.5} \qquad \textit{Equation 119}$$

Equation 120 [136] is proposed to incorporate the heterogeneity of deformation into the nucleation kinetics. A heterogeneity factor (X_{def}) is calculated as a function of the subgrain size (SG_s), the mean deformed grain size (G_s), the mean diameter of the bulging grains (hereon named recrystallised grain size) (G_{SIBM}) and the number of nuclei (N_{SIBM}). X_{def} describes the localisation of formation of subgrain boundaries and higher dislocation density in the vicinity of the prior β-HAGBs [146].

$$X_{def} = 1 - N_{SIBM}\left[\frac{\pi G_{SIBM}^3 G_s}{12 SG_s}\right] \qquad \textit{Equation 120}$$

Nucleation will only occur if $X_{def} > 0$. Additionally, the sets (n) of aligned dislocation walls forming a LAGB with an average misorientation ($\bar{\theta}_{LAGB}$) that is used to calculate the wall dislocation density (Equation 41) is recalculated phenomenologically in the SRX model according to Equation 121 to describe the heterogeneity of the deformation within the β-grains [146]. Thus, a difference in dislocation density between the region that promotes nucleation and the remaining portion of the material is predicted [146]. The update of n only occurs after the recrystallised grains consumes the region in the vicinity of the prior β-HAGBs ($X_{def} \leq 0$).

$$n = 2 + (n_{max} - 2)\exp\left(-\frac{1}{1 - \frac{X_{SRX} - X_0}{1 - X_0}}\right) \qquad \textit{Equation 121}$$

X_0 is the recrystallisation fraction achieved when $X_{def} = 0$. n_{max} is the initial sets of aligned dislocation walls forming a LAGB, and varies according to the applied strain rate, Equation 122. In the α+β domain, the effect of α-phase is taken into account in a simple way given in Equation 123 and Equation 124. Figure 25 illustrates the evolution of n decreasing asymptotically to 2 as well as ρ_w for a deformed grain.

$$n_{max} = \exp(A_{SRX}) + \dot{\varepsilon}^{B_{SRX}} \qquad \textit{Equation 122}$$

$$A_{SRX} = 4 - 5f_\alpha \qquad \textit{Equation 123}$$

$$B_{SRX} = \begin{cases} 0.3 - 2f_\alpha & \text{if } (0.3 - 2f_\alpha) > 0 \\ 0 & \text{if } (0.3 - 2f_\alpha) \le 0 \end{cases} \qquad \textit{Equation 124}$$

Finally, the nucleation rate can be calculated according to Equation 125 [136].

$$\dot{N}_{SIBM} = \frac{8\bar{N}_{SIBM} X_{def} \exp\left(-\frac{\pi\left(SG_s^*\right)^2}{4SG_s^2}\right) \exp\left(-\frac{Q_{SIBM}}{RT}\right)}{\pi G_s \left(SG_s^*\right)^2} \qquad \textit{Equation 125}$$

$\bar{N}_{SIBM}$ is the nucleation frequency and fitting parameter, the fraction of subgrains that are larger than the critical subgrain size is represented by $\exp\left(-\pi\left(SG_s^*\right)^2/4SG_s^2\right)$ and Q_{SIBM} is the activation energy for nucleation or bulging.

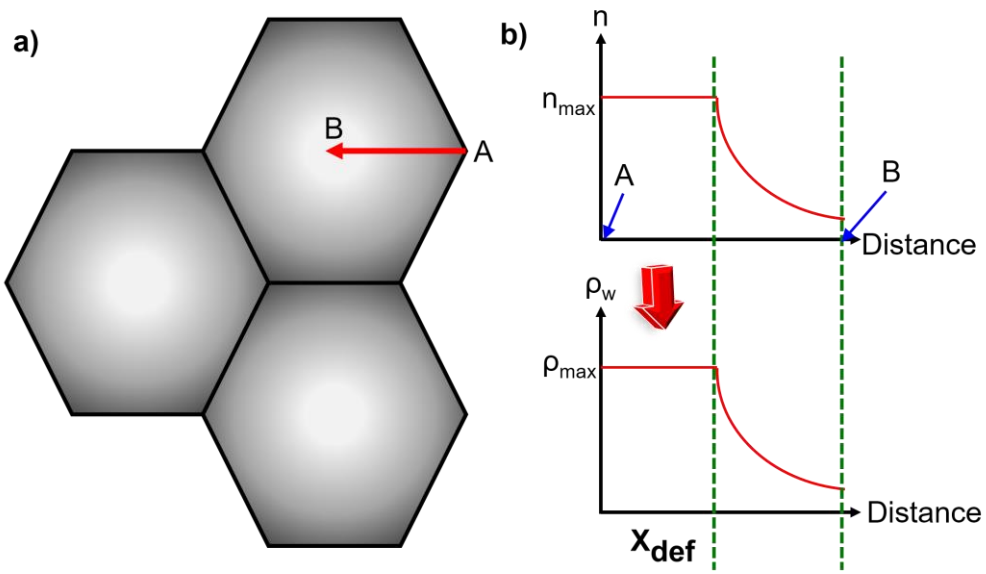

Figure 25: Schematic representation of the distribution of n and ρ_w for a typical microstructure: a) gradient of grey indicates the regions with higher wall dislocation density (darker) and with low wall dislocation density (lighter), b) evolution of the set of dislocations forming the dislocation walls as well as the evolution of the wall dislocation density from the grain boundary towards the centre of the grain.

7.3.3.2. Growth

The growth of the recrystallised grains (dG_{SIBM}/dt) is modelled analogue to precipitate growth [159], Equation 126. The formed recrystallised grains grow with a velocity v_{SIBM} (Equation 127) while the new recrystallised grains of a diameter of $2.5 \cdot SG_s$ formed at a rate $\dot{N}_{SIBM}$

are taken into account normalising their contribution to the average grain size by the total number of recrystallised grains ($N_{SIBM}= \int_0^t \dot{N}_{SIBM}\, dt$).

$$\frac{dG_{SIBM}}{dt} = v_{SIBM} + \frac{\dot{N}_{SIBM}}{N_{SIBM}}(2.5 \cdot SG_s - G_{SIBM}) \qquad \textit{Equation 126}$$

$$v_{SIBM} = M_{HAGB}(E_{SIBM} - P_{Zener}) \qquad \textit{Equation 127}$$

M_{HAGB} is the mobility of the HAGBs given according to Equation 89. The recrystallised fraction is given by Equation 128 using the classing JMAK approach [121].

$$X_{SRX} = 1 - \exp\left(-\frac{4\pi N_{SIBM}(G_{SIBM})^3}{3}\right) \qquad \textit{Equation 128}$$

7.3.4. Static grain growth

The static grain growth is modelled for the static recrystallised grains as well as for the deformed ones. The main reason for the assumption of HAGB movement for deformed grains aims to consider the growth of formed grains by CDRX and the movement of prior β-grains boundaries. Especially after deformation at low strain rates, it is not clear if a subgrain is bulging and promoting the formation of a dislocation-free grain or if it is a formed grain via CDRX and is moving due to capillary [146]. Therefore, all existing HAGBs apart from the ones taking part in SIBM are considered to have a typical curvature radius, and static grain growth occurs due to capillary, Equation 129 [183].

$$E_{GG} = \begin{cases} \frac{4\gamma_{HAGB}}{G_S} & \text{Deformed grains} \\ \frac{4\gamma_{HAGB}}{G_{SIBM}} & \text{Recrystallised grains} \end{cases} \qquad \textit{Equation 129}$$

The static grain growth of the deformed (G_s) or recrystallised grains (G_{SIBM}), are given according to Equation 130 and Equation 131 [183], respectively.

$$\frac{dG_s}{dt} = M_{HAGB}(E_{GG} - P_{Zener}) \qquad \textit{Equation 130}$$

$$\frac{dG_{SIBM}}{dt} = M_{HAGB}(E_{GG} - P_{Zener}) \qquad \textit{Equation 131}$$

An average subgrain ($\overline{SG}_s$) and grain sizes ($\bar{G}_s$) are calculated as representative for the whole material (deformed plus recrystallised fractions) and are expressed in Equation 132 and Equation 133, respectively (see Appendix G).

$$\overline{SG}_s = \frac{G_{SIBM} SG_s}{X_{SRX} SG_s + (1 - X_{SRX}) G_{SIBM}} \qquad \textit{Equation 132}$$

$$\bar{G}_s = \frac{G_{SIBM} G_s}{X_{SRX} G_s + (1 - X_{SRX}) G_{SIBM}} \qquad \textit{Equation 133}$$

8. Phase transformation in a Ti-6Al-4V

This chapter comprises the investigations about the competitive formation of α_{GB}, α_{SEC} and the growth of α_P for the Ti-6Al-4V alloy during continuous cooling. The formation kinetics of the different morphologies of the α-phase is related to the nucleation rate of α_{GB} and α_{SEC} as well as with the V supersaturation at the β matrix. The described mesoscale physical model in section 7.1 for the formation of α_{GB} and α_{SEC} as well as the growth of the α_P primary α is implemented. Continuous cooling tests are performed at two different holding temperatures in the α+β field, 930°C and 960°C, and five different cooling rates, 10, 30, 40, 100 and 300°C/min. Additionally, interrupted tests are conducted at different temperatures to determine the progress of growth of α_P and formation of α_{GB} and α_{SEC} during cooling. The results and discussions shown here were already published in [140].

8.1. Methodology

The performed dilatometry experiments are summarised in section 6.2, and the model is described in 7.1. The microstructural data is used for the investigation of the phase formation sequence as well as for the model validation. The constants and parameters used in the model are given in Appendix A.

8.2. Results and interpretation

Figure 26a and b show representative microstructures of the Ti-6Al-4V argon quenched after holding at 930°C and 960°C for 1h, respectively. The measured area fractions of α_p are 38.6 ± 2.8 % and 18.2 ± 3.3% for the heat treatment at 930°C and 960°C, respectively [140]. Sparsely and nearly separated α_p particles are found in a matrix of martensite (α'), originally a matrix of β-phase [140]. The agglomeration of α_p, defined as the fraction of the α-grains that are visibly connected, is higher for the heat treatment at 930°C, Figure 26a. No trace of α_{SEC} is observed. However, the α_p particles slightly deviate from an ideal spherical shape particle.

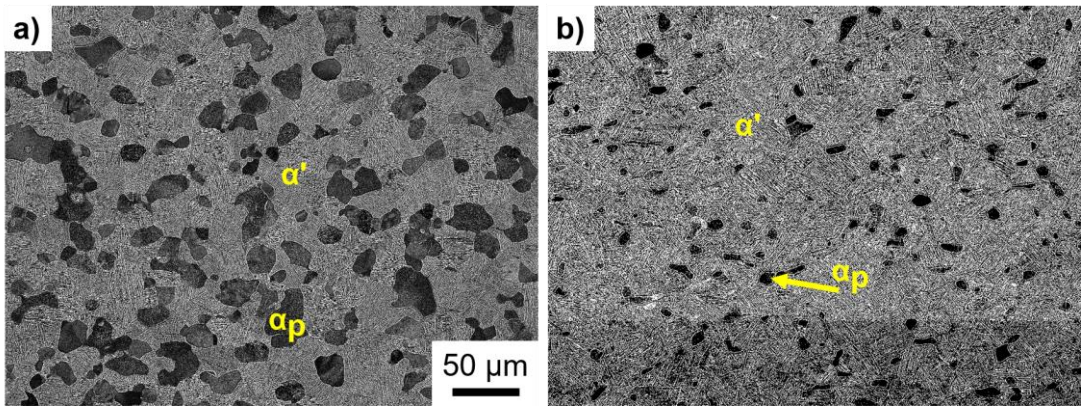

Figure 26: Representative BSE micrographs of the investigated Ti-6Al-4V after 1h at: a) 930°C followed by argon quenching; b) 960°C followed by argon quenching.

8.2.1. Experimental results

8.2.1.1. Influence of the cooling rate

Representative micrographs of the continuously cooled microstructure after holding for 1 h at 930°C and 960°C are shown in Figure 27. The cooling rate of 10°C/min leads to a nearly entirely

equiaxed microstructure in both cases. The shape of the α_p exhibits lower circularity at 960°C due to the formation of bumps [140]. It is difficult to distinguish the lamellas of α_{SEC} or α_{GB} from the globular α_p for samples cooled down at 10°C/min. A growth of α_p is also observed for the cooling rate of 30°C/min. The formation of α_{SEC}, as well as of α_{GB} phase, is promoted at higher cooling rates. The α_{GB} exhibit bulges at the interface by cooling at 300°C/min, as well as the α_p phase. Higher cooling rates lead to less pronounced growth of α_p.

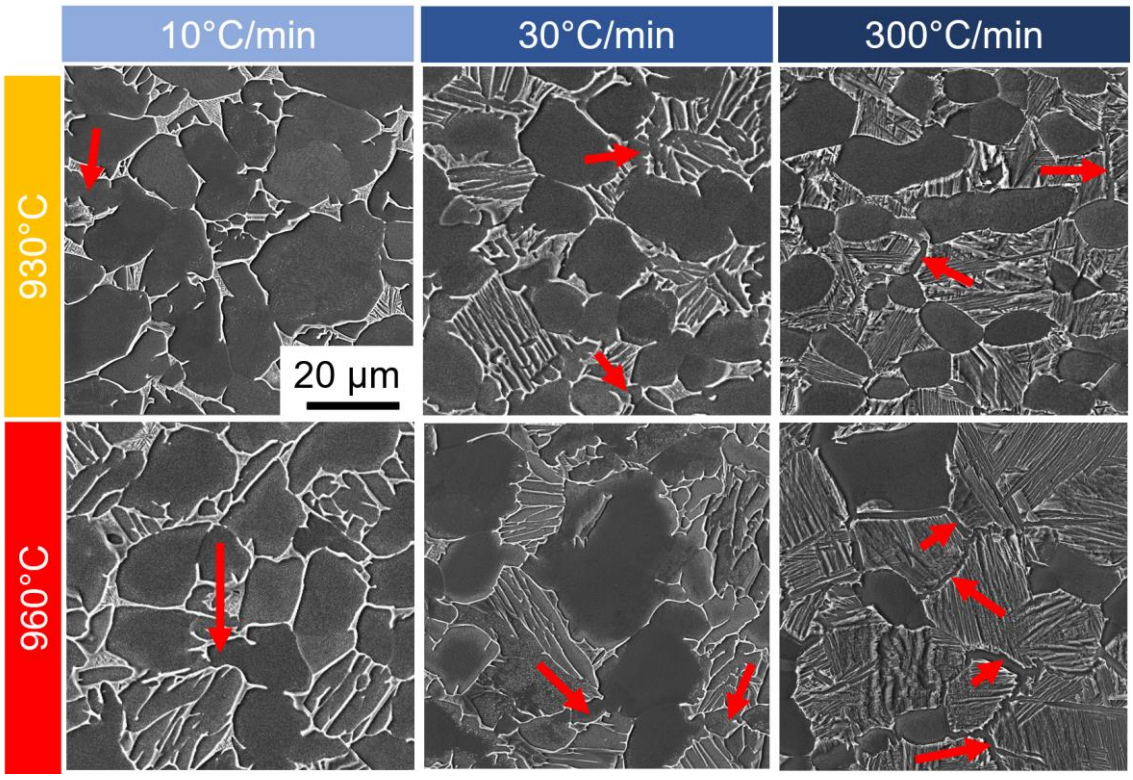

Figure 27: Representative SE micrographs of the investigated Ti-6Al-4V after holding at 930°C and 960°C for 1h followed by continuous cooling at: 10, 30 and 300°C/min. The red arrows highlight the α_{GB}.

The microstructure is shown in detail in Figure 28 after continuous cooling from 930°C and 960°C. The α_{GB} and α_{SEC} are highlighted with dashed red and green lines, respectively. Fine acicular-like martensite (α') is marked in yellow. Plate-like α_{SEC} is observed in the vicinity of α'. The morphology of α_{SEC} deviates slightly from a typical flat plate-like morphology. Irregular and discontinuous interlamellar β-phase is observed, especially for the cooling rate of 30°C/min. Moreover, the above-mentioned irregularities of the shape of α_P and α_{GB} are observed [140]. The serrations at the interfaces of α_P are related to the surface instability due to competitive growth of α_{GB}, α_{SEC} and α_P [8]. When the α_{SEC} or α_{GB} are formed in the vicinity of an α_P particle, it either hinders the local movement of the interface of the α_P and/or changes the local supersaturation of V needed for its growth. Comparably, if α_{SEC} nucleates from α_{GB} it also changes its interface movement kinetics and supersaturation field for growth. The serrations are more pronounced at 30°C/min than 300°C/min due to higher time for diffusion. A nearly flat plate-like α_{GB} is observed for the cooling rate of 300°C/min.

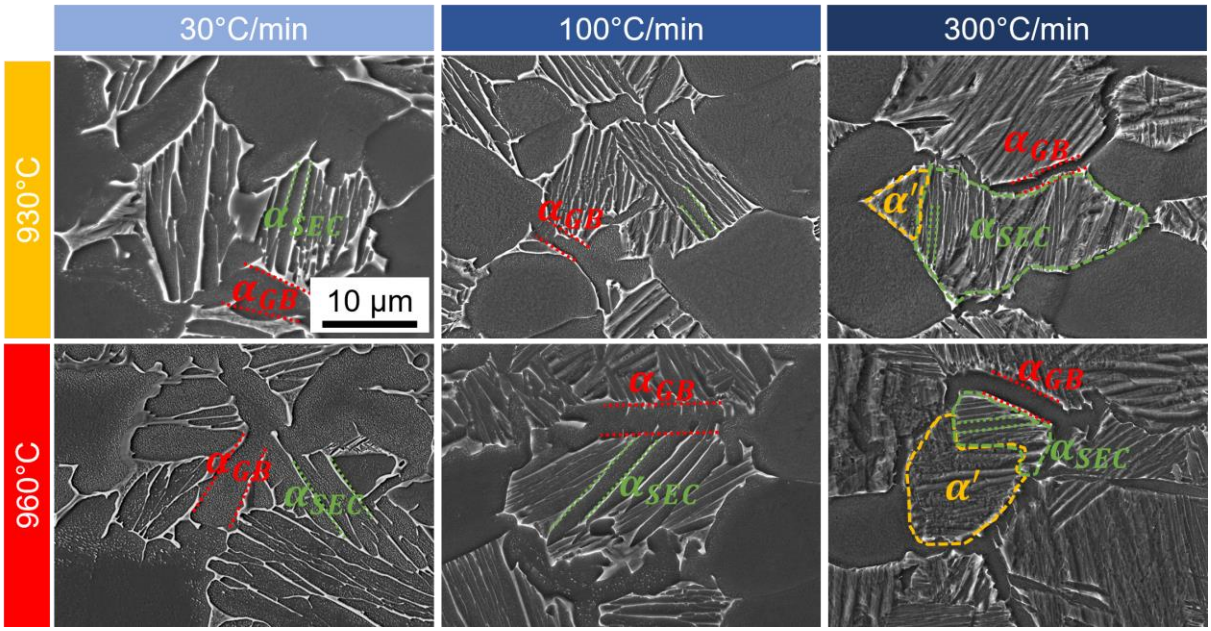

Figure 28: Representative SE-SEM micrographs of the investigated Ti-6Al-4V after holding at 930°C and 960°C for 1h followed by continuous cooling at 30°C/min, 100°C/min and 300°C/min.

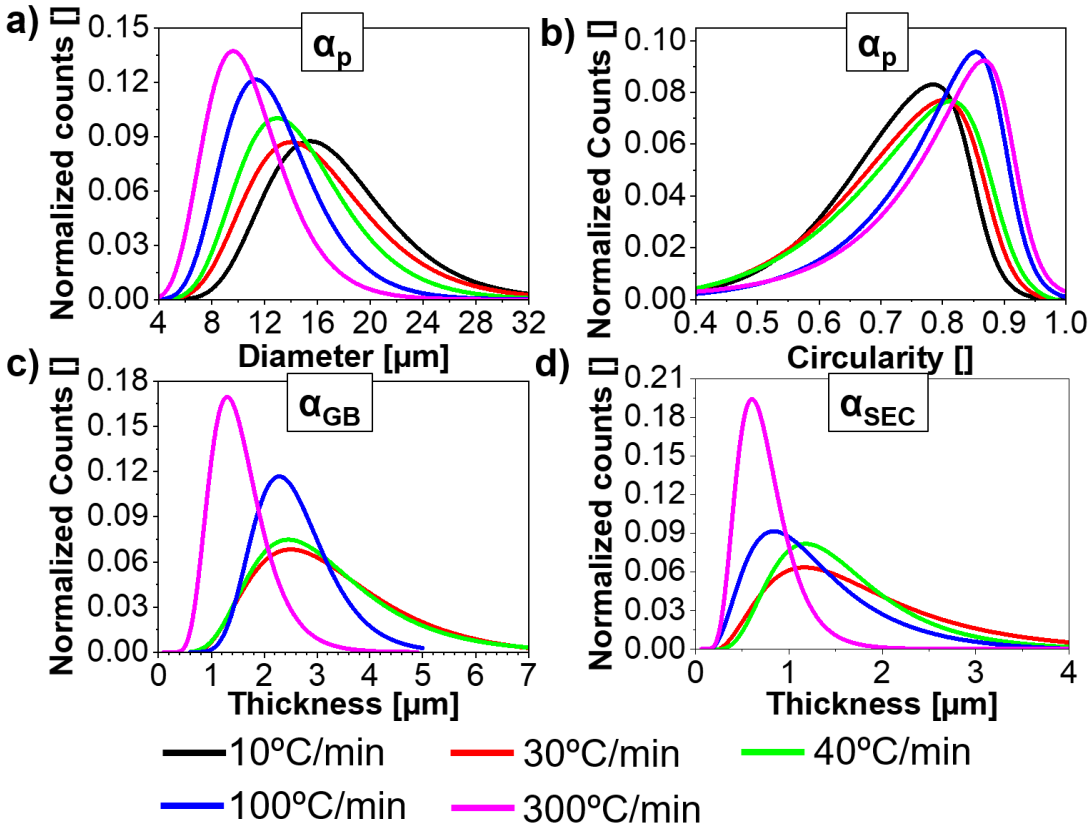

Figure 29: Normalised distributions of the measured: a) diameter of α_P; b) circularity of α_P; c) thickness of α_{GB}; and d) thickness of α_{SEC}.

Figure 29 illustrates the effect of the cooling rate on the distributions of the diameter of α_P (Figure 29a), the circularity of α_P (Figure 29b), and the thicknesses of α_{GB} (Figure 29 c) and α_{SEC} (Figure 29d). The distributions were normalised to the sum of counts and fitted using a lognormal distribution. The diameter of α_P increases with the decrease in cooling rate, and The circularity of

α_P decreases with decreasing cooling rate due to the formation of bumps and bulges. The thickness of α_{GB} or α_{SEC} is smaller with narrower distribution for higher cooling rate. The distributions for the cooling rate of 10°C/min are not shown due to the difficulty to distinguish α_P from α_{GB} or α_{SEC}. [140]

8.2.1.2. The sequence of phase formation

Figure 30 exhibits the typical micrographs after interrupted heat treatments. The α_P, α_{GB} and α_{SEC} are highlighted in blue dashed line, red dashed line and green dashed line, respectively. The α_{GB} forms from the globular α_p as well as from triple points of the β grains. The fraction of the grain boundary that is occupied by α_{GB} is very low for 900°C. At 850°C, the grain boundaries are nearly completely decorated with α_{GB}. Irregular growth of α_{GB} seems to occur at 800°C, being this effect more pronounced for 10°C/min. Nucleation and growth of α_{GB} do not seem to be significant at temperatures higher than 900°C for the two investigated cooling rates, leading to comparable evolution behaviour of the α_{GB} after holding at temperatures of 930°C and 960°C. The α_{SEC} formation is not pronounced before 850°C. Although Figure 30 shows the presence of α_{SEC} for 10°C/min, its area fraction is notably smaller in comparison to cooling at 100°C/min.

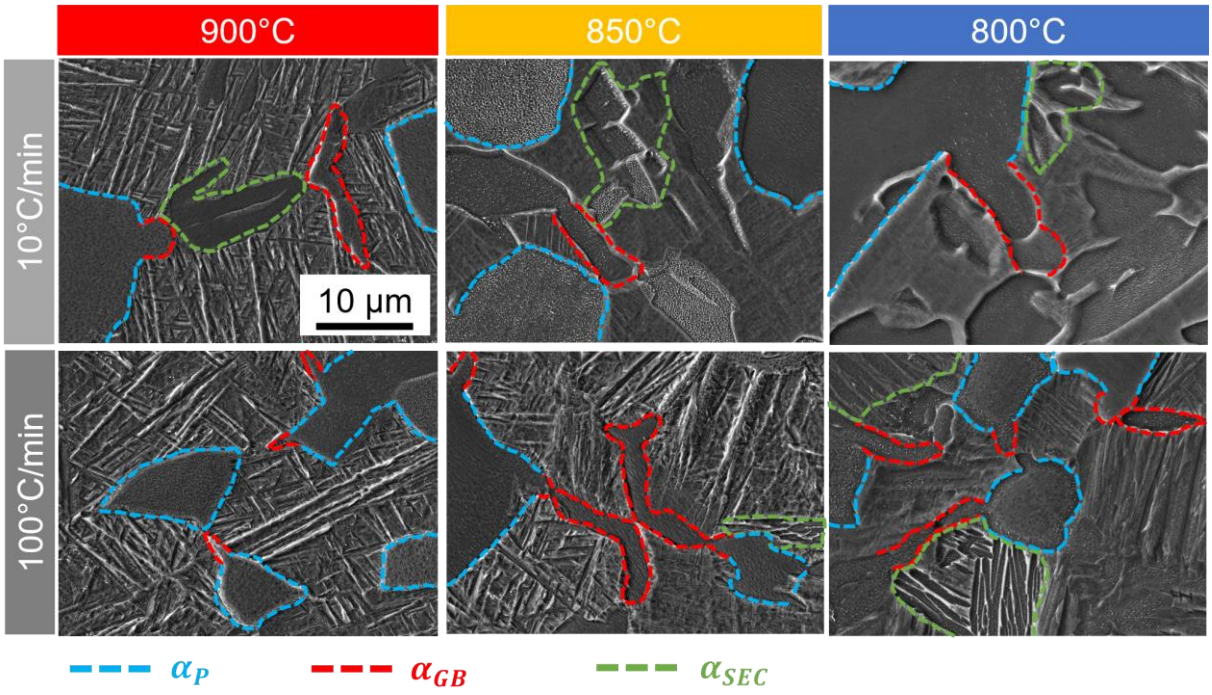

Figure 30: Representative SE-SEM micrographs of the interrupted heat treatments after holding at 960°C for 1h, followed by continuous cooling at 10°C/min, and 100°C/min. The tests were interrupted at: 900°C, 850°C and 800°C.

Figure 31 shows the inverse pole figure maps (IPF) of the EBSD measurements for four interrupted heat treatments. The presence of α_{GB} formed from the α_P is highlighted by a dashed white circle. In this case, none or very small (below 2°) misorientation angle is observed between the α_P and the formed α_{GB}. The presence of HAGBs is highlighted with white lines. Two nucleation sites were identified for α_{GB} [140] a) a bulge from the α_P, and b) at β triple boundaries and flat β-grain boundaries. It seems that the local supersaturation and surface energy determine the different nucleation sites. At β triple points, the high surface energy can promote the nucleation of

α_{GB}, while the nucleation of α_{GB} at the flat β grain boundaries is promoted by a high local supersaturation due to large interspacing between the α_P.

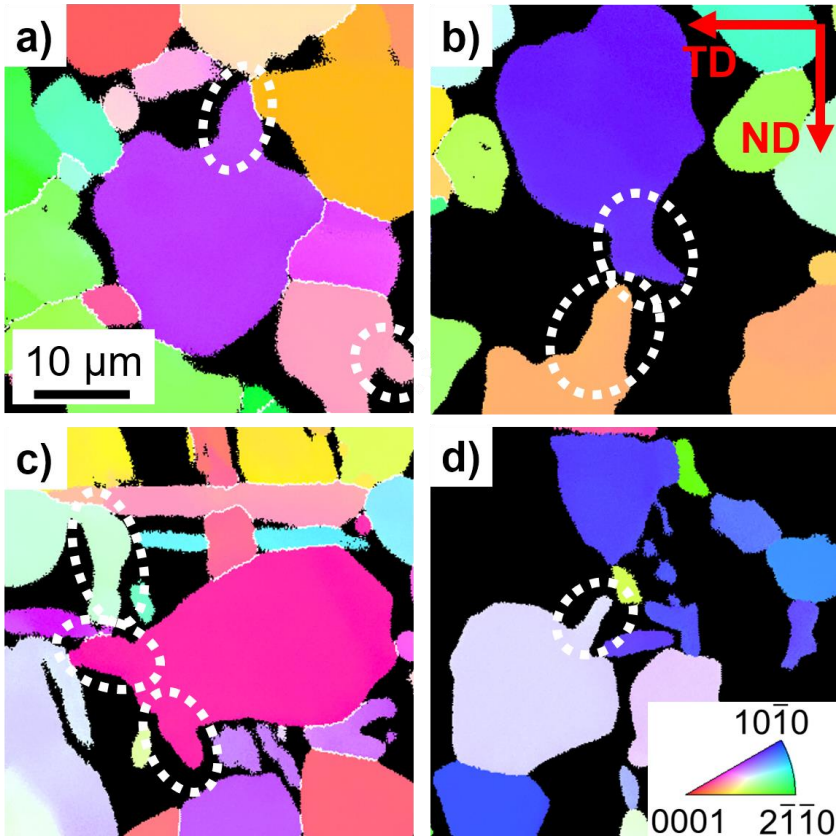

Figure 31: EBSD-IPF maps with α_P and α_{GB}. Dashed white circles indicate the bulged α_{GB} from α_P. The heat treatments correspond to an isothermal for 1h at 960°C followed by continuous cooling at: a) 10°C/min interrupted at 800°C b); 100°C/min interrupted at 800°C; c) 10°C/min interrupted at 875°C; d) 100°C/min interrupted at 875°C. The martensitic phase was erased for easier visualisation. The TD and ND correspond to cogging and normal direction, respectively.

8.2.2. Model performance

The fitting parameters shown in Appendix A are in the same range as reported in other investigations [10,23]. The results corroborate the work of Semiatin et al. [9] for the growth of α_P and Meng at al. [10] for the formation of α_{SEC}. This work adds the competitive growth of α_P, α_{GB} and α_{SEC} [140]. Despite not considering the thermo-history included in the model proposed by Meng et al. [10] and despite not accounting for complex supersaturation fields that are possible to predict when using phase-field models [19], the adoption of a ledge constant to the exact solution showed to be sufficient to achieve notably accuracy in a simple coupled model.

8.2.2.1. Influence of the cooling rate

The mean diameter and area fraction of α_p, mean thickness and area fraction of α_{GB} and mean thickness and area fraction of α_{GB} are plotted in Figure 32 for the holding temperature of 960°C. The growth of the α-phase morphologies for temperatures lower than 600°C is negligible. The formation of α_{GB} starts close to 920°C. Figure 32(b,e) shows a high growth rate for α_{GB} at around 900°C down to 800°C. These evolutions are in good agreement with the experimental observations depicted in Figure 30. The α_{SEC} formation starts at 875°C, with a significant growth

until 700°C, explaining the micrographs in Figure 30. Figure 32f shows that the fraction of α_{SEC} abruptly decreases when the cooling rate increases from 100°C/min to 300°C/min. The low nucleation rate and low time for diffusion explain this behaviour and are confirmed by the presence of martensite in the microstructure after cooling down at 300°C/min. Rae [184] proposed a time-temperature-transformation diagram for Ti-6Al-4V where the martensitic starting temperature is ~850°C [185] and martensite is formed if this temperature is achieved within ~5 s. In order to obtain a fully martensitic microstructure, the temperature of ~700°C should be achieved within ~1s from the holding temperature [184]. The lower formation of α_{SEC} for cooling at 300°C/min yields a significant remaining ("retained") β-fraction, interpreted here as the formation of martensite in Ti-6Al-4V.

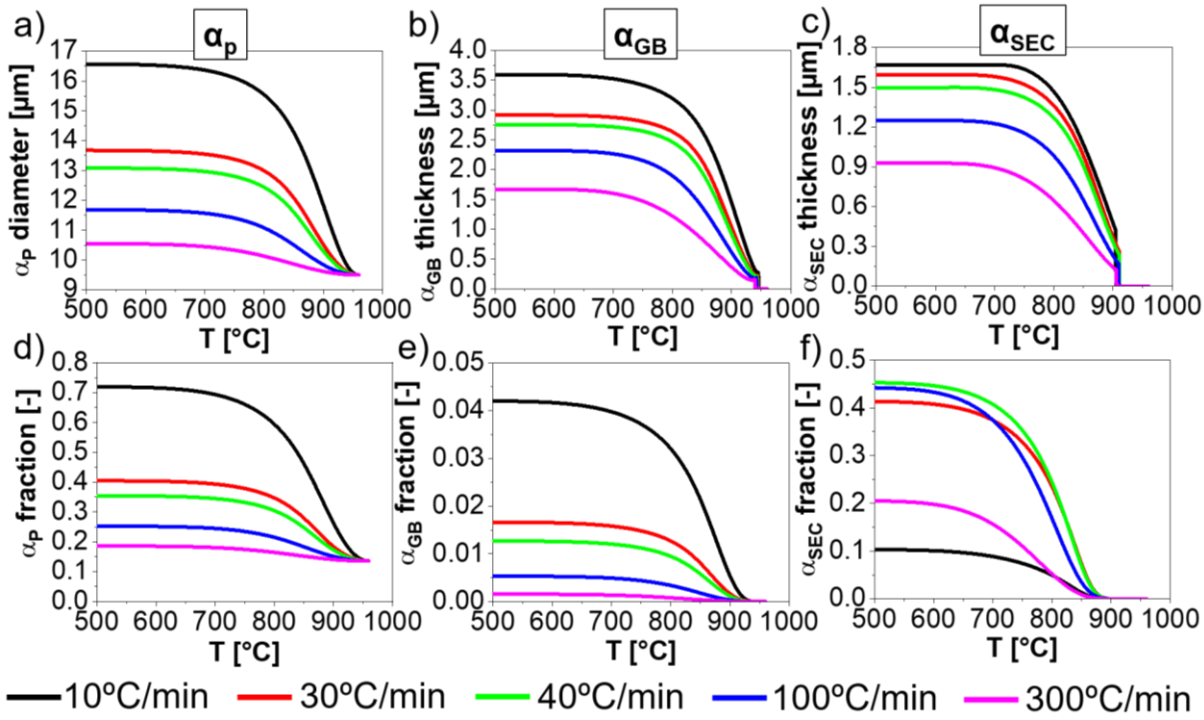

Figure 32: Simulation results for the holding temperature of 960°C during continuous cooling: a) mean α_P phase diameter; b) mean thickness of α_{GB}; c) mean thickness of α_{SEC}; d) phase fraction of α_P; e) phase fraction of α_{GB}; f) phase fraction of α_{SEC}.

The simulated area fraction of α_p, mean α_p diameter, mean thickness of α_{GB} and mean thickness of α_{SEC} are in good agreement to the experimental results. The differences between measured and simulated data are dependent on measurement limitations and model assumptions [140]. The stereological procedures adopted for phase quantification have an inherent error. For instance, the α_{SEC} that exhibit a disc-shape or irregular morphology leads to an error on the assumption that all α_{SEC} are semi-infinite platelets neglects. The assumption of α_p as isolated spherical particles directly impacts the prediction of α_p growth. The α_p particles are slightly elongated due to initial cogging process and have a certain degree of interconnectivity. Those differences can explain the deviations and relatively large standard deviation observed in Figure 33.

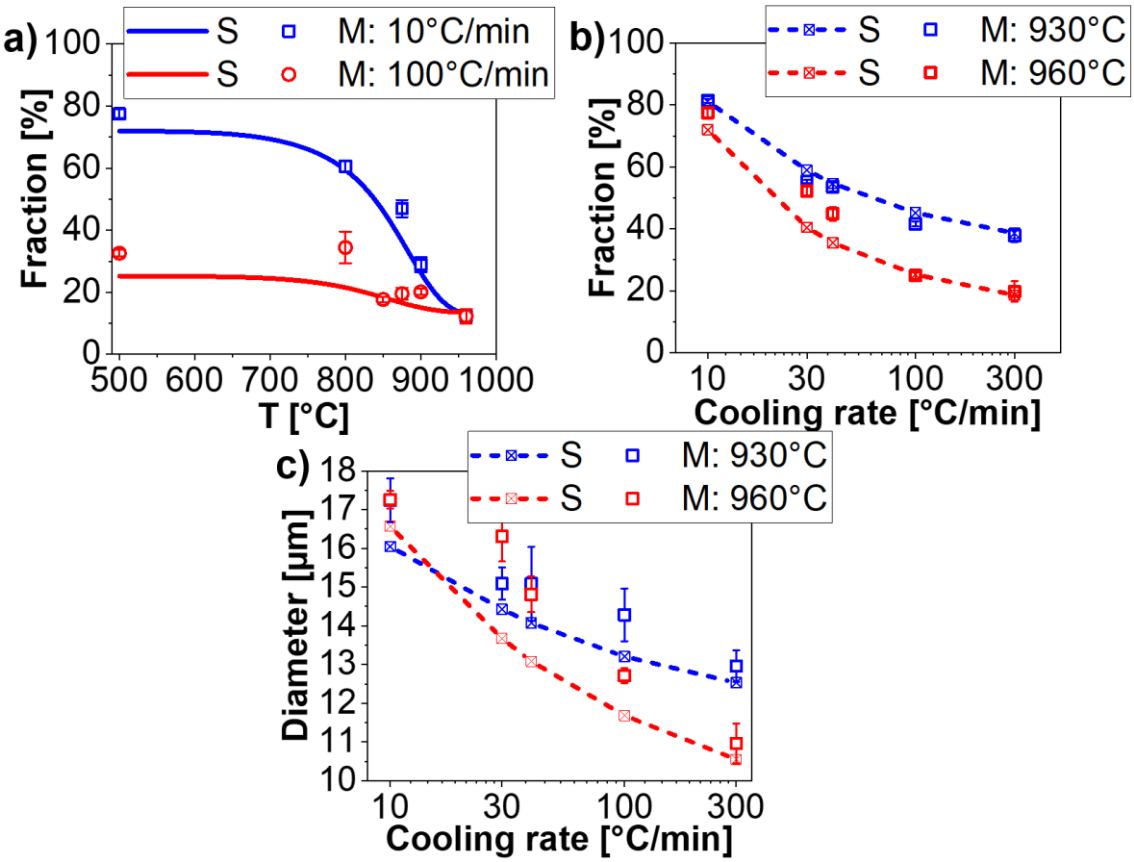

Figure 33: Measured (M) and simulated (S) microstructural features of α_P during continuous cooling and after holding at 930°C and 960°C: a) average phase fraction at 10 and 100°C/min (holding temperature of 960°C); b) average phase fraction; c) mean diameter.

The cooling rate plays a vital role in the formation of the different morphologies of α-phase. The following statements can be inferred [140]:

- During continuous cooling, the fraction of α_p increases rapidly until 800°C is reached (Figure 33a and Figure 32d). The area fraction of α_p increases for decreasing cooling rate. The model describes the area fraction evolution accurately apart from 30 and 40°C/min for the holding temperature of 960°C (Figure 33b).
- The mean diameter of α_p increases with decreasing cooling rate (Figure 33c and Figure 32a).
- The thickness of the α_{GB} are in the range of 1-4 µm and increases with decreasing cooling rate (Figure 34a and Figure 32b). Slightly thicker α_{GB} is observed for the holding temperature of 960°C. The higher supersaturation grade of the matrix at 960°C compared to 930°C, in addition to the faster growth after nucleation during the initial stages at high temperatures, can explain this difference with respect to the sample cooled from 930°C.

The thickness of α_{SEC} was in the range of 0.5-2 µm, and it increases with decreasing cooling rate (Figure 34b and Figure 32c). The different holding temperatures less influence its formation since α_{SEC} is formed at temperatures where the supersaturation of V in β-phase is comparable despite the different holding temperatures [140].

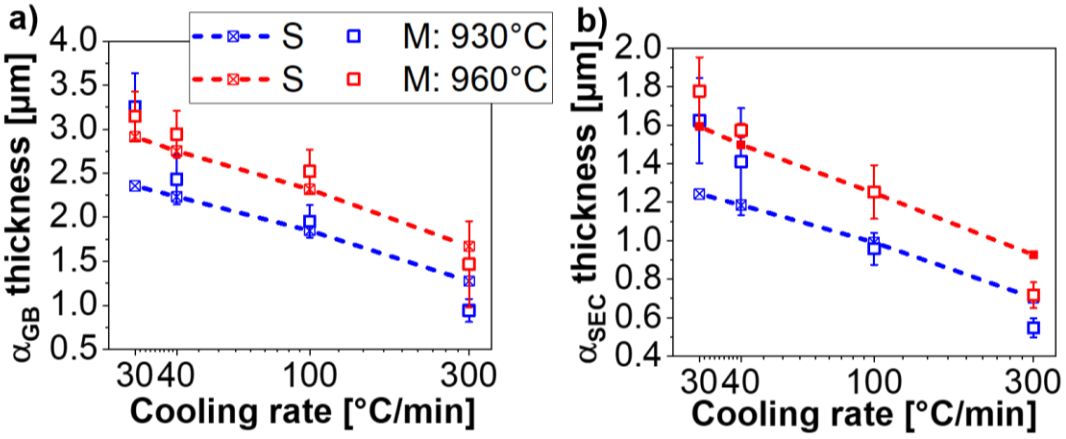

Figure 34: Measured (M) and simulated (S) microstructural features during continuous cooling after holding at 930°C and 960°C: a) mean thickness of α_{GB}; b) mean thickness of α_{SEC}.

8.2.2.2. Additional physical features

Figure 35 shows the nucleation rate of α_{GB} (Figure 35a) and α_{SEC} (Figure 35b) for the holding temperature of 960°C. The supersaturation of V within the β-phase matrix is shown in Figure 35c. The predicted nucleation rate of α_{GB} is significantly lower compared to α_{SEC} because only the grain boundaries are sites for nucleation and α_{GB} [140]. The estimated prior β grain size is 35 µm. Therefore, the number density number of for α_{GB} is notably smaller compared to α_{SEC}.

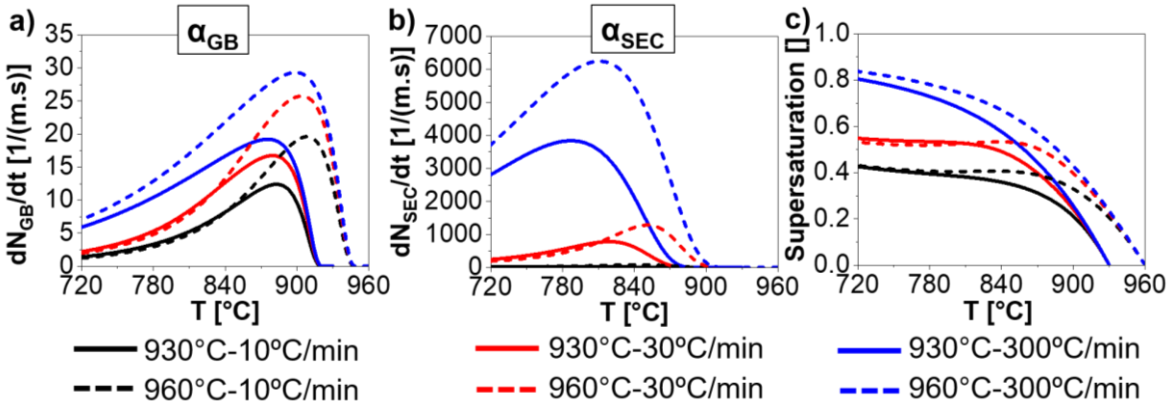

Figure 35: Simulated results for the holding temperature of 930°C and 960°C for the cooling rates of 10, 30 and 300°C/min: a) nucleation rate of α_{GB}; b) nucleation rate of α_{SEC}; and c) supersaturation of V in the β-matrix.

A summary with the temperature for the beginning of nucleation and for the maximum nucleation rate is shown in Figure 36. The α_{GB} nucleates and then α_{SEC} is formed when there are no changes in α_{GB}. The temperature for the onset of nucleation tends to increase with decrease cooling rate. An exception is calculated for the 10°C/min cooling rate. In this case, the predominant growth of α_P leaves no supersaturation to activate earlier nucleation of α_{GB}. A similar tendency is observed for the α_{SEC}. The slightly lower temperatures for nucleation in the case of 10°C/min is more pronounced, as expected due to the higher free energy for nucleation (Equation 12, in comparison to Equation 23). The dependency on the cooling rate in the case of the nucleation rate follows similar behaviour compared to the beginning of nucleation. The incomplete formation of α_{SEC} for high cooling rates (Figure 28 and Figure 32) is also predicted in the current model since the temperature for maximum nucleation rate of α_{SEC} lies close to 800°C. Furthermore, the notable

low amount of α_{SEC} formed during low cooling rates is also observed (Figure 27) and agrees with the model prediction.

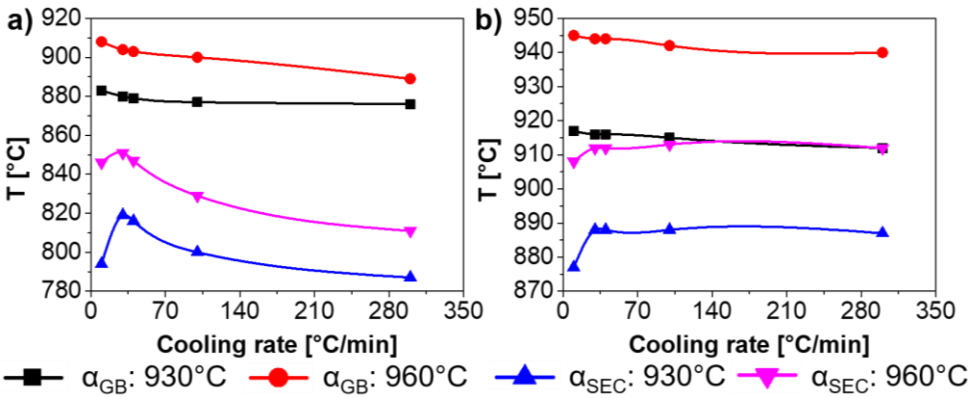

Figure 36: Simulated nucleation temperatures for the cooling rates of 10, 30, 40,100 and 300°C/min at isothermal treatments at 930°C and 960°C: a) temperature for the beginning of nucleation, b) temperature for maximum nucleation rate.

8.3. Summary

The sequence of formation and growth of the different morphologies of α-phase (primary, secondary and allotriomorphic) in Ti-6Al-4V were fully described during cooling from isothermal treatments below the β-transus temperature. A mesoscale physical model to account for the competitive growth of the different morphologies was developed. Nucleation and growth of α_{GB} as well as of α_{SEC} are modelled based on the nucleation and growth of platelets. The growth of α_P is modelled as the growth of a spherical particle. The conclusions are shown below. Innovative aspects with respect to the literature are highlighted in bold:

a) Conclusions from the simulation:

- The growth rate of α_P is more pronounced for slow cooling and until 800°C.
- **The nucleation rate dependency with respect to the cooling rate is more pronounced for the α_{SEC} than for α_{GB}.**
- A sharp increase of V supersaturation in the β matrix is predicted between 830 and 850°C, which is attributed to contributing to the formation of α_{SEC}, especially for cooling rates higher than 10°C/min.

b) Conclusions from the experiments:

- **Regular (planar) interface shape of α_{GB} is observed decorating the prior β-grain boundaries for high cooling rates. For low cooling rates, irregular α_{GB}/β interfaces are observed.**
- α_{GB} nucleates preferentially from existing α_p phase at low cooling rates. For higher cooling rates, nucleation occurs preferentially at triple β-boundaries and β/β grain boundary.
- α_{SEC} nucleates from the already existing α_{GB}, and it nucleates at the interface with the α_P.

c) General conclusions:

- Formation of αGB occurs first followed by the formation of α_{SEC}.

9. Prediction of hot deformation behaviour of Ti-5553

This chapter presents the results of the physical based on Kocks-Mecking formalism [170] described in section 7.2. The rate equations for the dislocation reactions are shown in section 7.2.6.1. Mean subgrain size, grain size, dislocation densities and boundary misorientation are calculated. The model is validated with hot compression experiments of a Ti-5553 alloy at temperatures between 800°C to 920°C and strain rates between 0.001 s^{-1} and 10 s^{-1} (see section 6.3). The microstructure results and their interpretation that are shown here were already published in [141]. The simulated results shown here are interpreted using the work published in [141]. The constants and parameters used in the model are given in Appendix B.

9.1. Results and interpretation

9.1.1. Microstructure before deformation

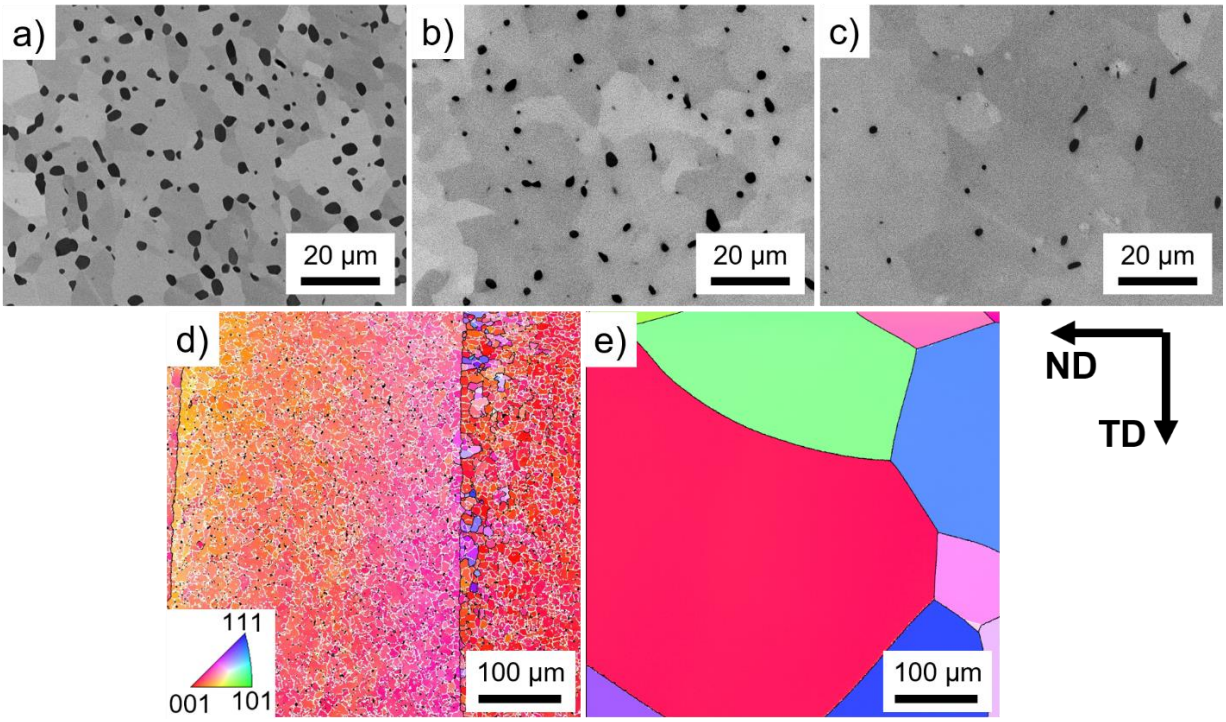

Figure 37: Typical microstructures of the Ti-5553 obtained by backscattered electron (BSE) after 15 min annealing at: a) 800°C; b) 820°C; c) 840°C. The globular α-phase appears dark grey. Inverse pole figure (IPF) maps after 15 min annealing at: d) 820°C; and e) 920°C. Black lines indicate HAGBs, while LAGBs are indicated by white lines; ND and TD correspond to the normal and cogging directions, respectively.

The microstructure of the investigated Ti-5553 prior to deformation is shown in Figure 37. Globular α-phase is observed embedded in a recovered β-matrix after 15 min annealing below the β-transus temperature (Figure 37(a-d)). The subgrain size of the β-phase in the α+β domain is assumed to have a similar size than the interparticle distance among α phases, $\lambda_{interspace}$ Equation 83.

Once achieved the β-transus temperature, the globular α-phase that hinders the movement of the boundaries of the β-phase dissolves. Besides, the mobility of boundaries increases due to

higher temperatures. Both effects lead to a fully recrystallised β-microstructure, as shown in Figure 37e.

9.1.2. Flow stress evolution

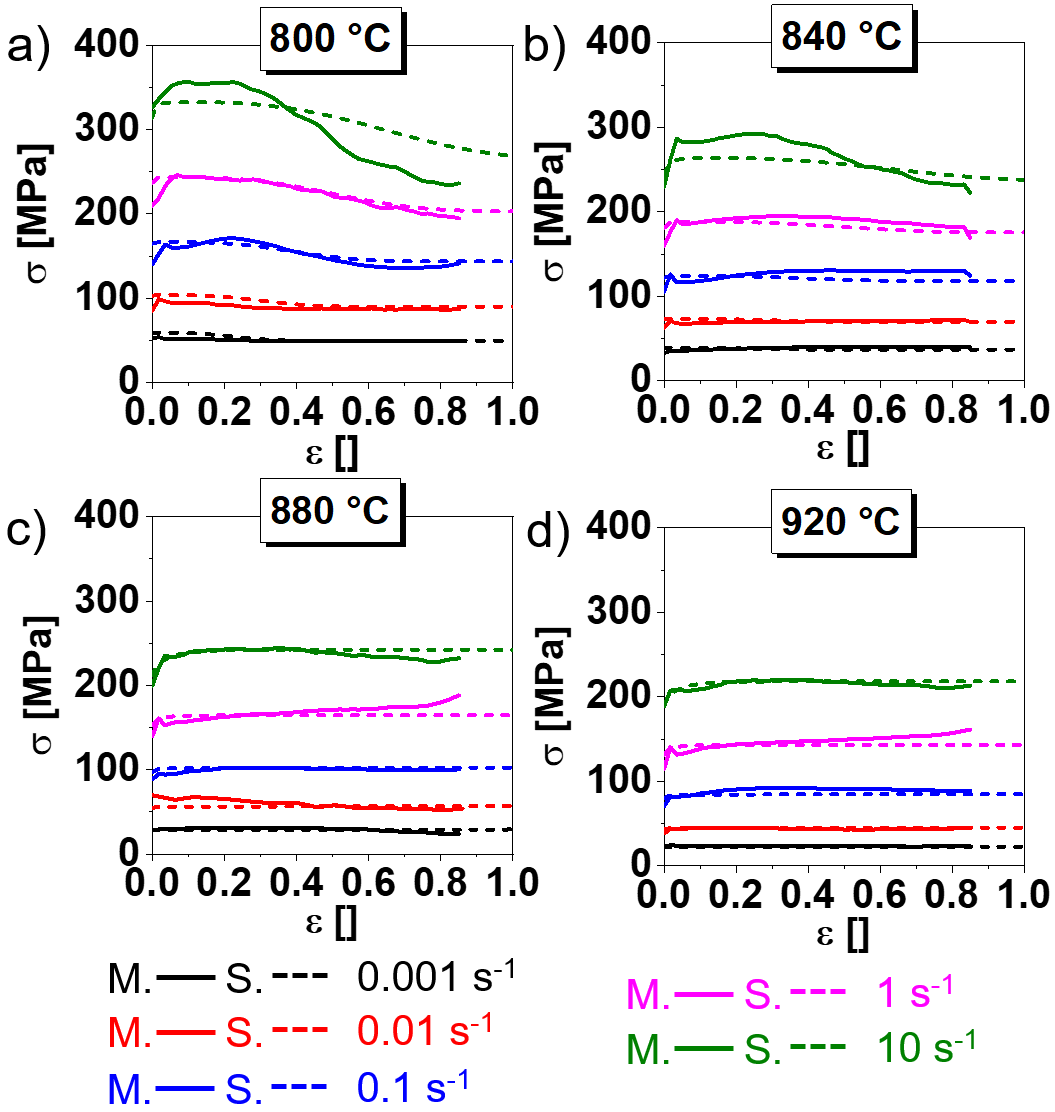

Figure 38: Measured (M.) and simulated (S.) flow curves: a) 800°C, b) 840°C, c) 880°C, and d) 920°C.

Figure 38 shows that the simulated and the measured flow curves are in good agreement. The measured flow curves are corrected for the adiabatic heating. The model can predict the nearly constant flow stress in the β-domain and the flow softening in the α+β domain [141]. Deviations for the high strain rate results must be related to local behaviours of the material that cannot be described with the mesoscale model a) local increment of the temperature and phase transformation, b) local softening and c) local misorientation accumulation.

The evolution of the stress components is exemplarily shown for the deformation at 800°C and 10 s^{-1} in Figure 39. According to the constitutive equation (Equation 44), the flow stress is a sum of σ_{th} and σ_{ath}. The thermal stress of the is considered constant for a given strain rate and temperature. However, due to the change in load partitioning in the α+β domain, the strain rate of the α-phase decreases and the β-phase increases, thus varying the yield stress (Equation 43) and consequently σ_{th} (Equation 48). The variation of thermal and overall stresses in the β-phase is

near negligible (Figure 39a) since the small increase in strain rate for that phase leads to a small increment in yield stress in β-phase, Figure 39c. However, the reduction of strain rate due to change in load partitioning leads to a notable decrease in the yield stress in α-phase (Figure 39d), thus decreasing the thermal stress (Equation 48), and consequently overall one (Figure 39b).

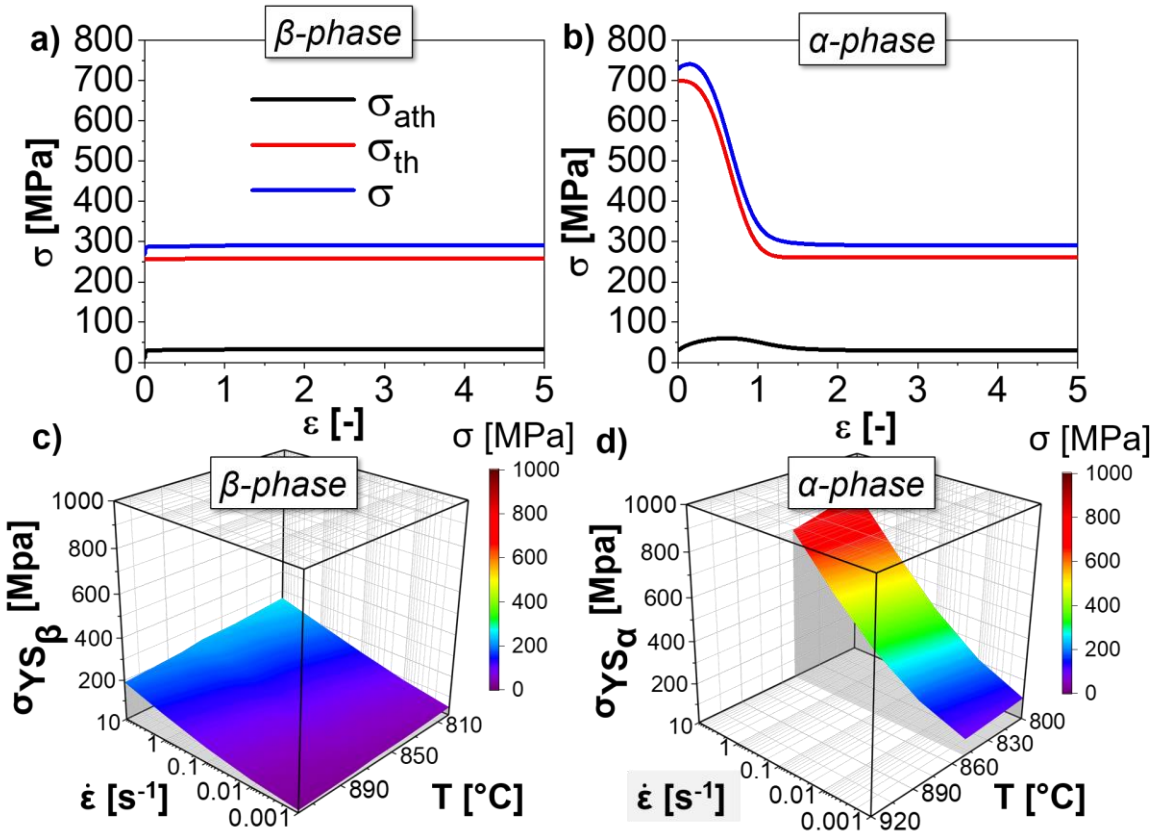

Figure 39: Stress components evolution for the temperature of 800°C and strain rate of 10 s^{-1} for both: a) β-phase, b) α-phase; calculated yield stresses for both: c) β-phase, d) α-phase

9.1.3. Microstructure after deformation in the α+β domain

BSE-micrographs of Ti-5553 deformed below the β-transus temperature are shown in Figure 40. The globular primary α phase is slightly elongated compared to the microstructure prior to deformation. From an aspect ratio of 1.6 ± 0.5, 1.6 ± 0.7, and 1.8 ± 0.9 for the heat-treated samples at 800°C, 820°C, and 840°C, respectively, the values increased after deformation at 0.001 s^{-1} to 2.3 ± 1.2, 2.0 ± 1.2, and 1.9 ± 1.4 for the respective deformation temperatures [141]. The aspect ratio measured for the deformed α-phase for the strain rate of 1 s^{-1} for 800°C, 820°C, and 840°C are 1.8 ± 0.8, 1.7 ± 0.6 and 2.1 ± 1.1, respectively [141]. The dissolution of α-phase was not considered in the model.

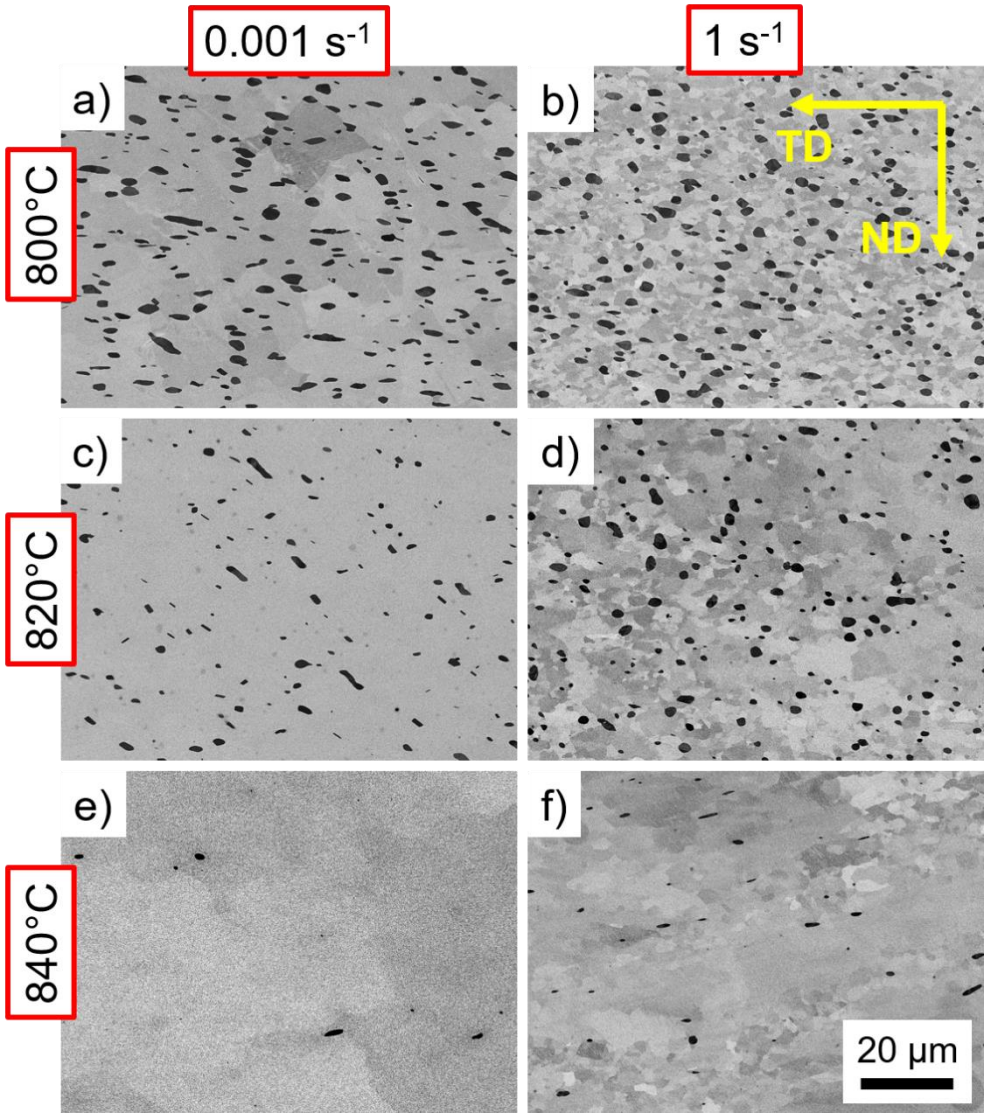

Figure 40: Typical BSE micrographs for Ti-5553 deformed in the α+β phase domain: a,b) 800°C; c,d) 820°C; e,f) 840°C; (a,c,e) strain rate of 0.001 s^{-1}; and (b,d,f) strain rate of 1 s^{-1}. ND and TD corresponding to the compression and transversal directions, respectively.

Figure 41 shows the EBSD-IPF maps of the indexed β-phase deformed in the α+β domain for the strain rates of 0.001 s^{-1} (a-c), 0.01 s^{-1} (d-f) and 1 s^{-1} (g-i) for the temperatures of 800°C (a,d,g), 820°C (b,e,h) and 840°C (c,f,i). A larger fraction of HAGBs is observed for 1 s^{-1}, and 800°C (Figure 41g) compared to 840°C (Figure 41i). However, the difference is less evident at 0.001 s^{-1}. The size and morphology of the formed substructure differ between the different deformation conditions. Higher slip activity, DRV and lower α-phase fraction, as well as the higher velocity of the HAGBs, are characteristic of the higher temperature. The subgrain size decreases with increasing strain rate and decreases temperature. The globular α-phase has a notable impact on the microstructure evolution of the β-phase in the α+β domain. The fraction of globular α-phase influences directly the pinning pressure at both low and high angle grain boundaries. Nearly flat prior β-grain boundaries are observed (Figure 41 a and d) and indicated by the white arrows.

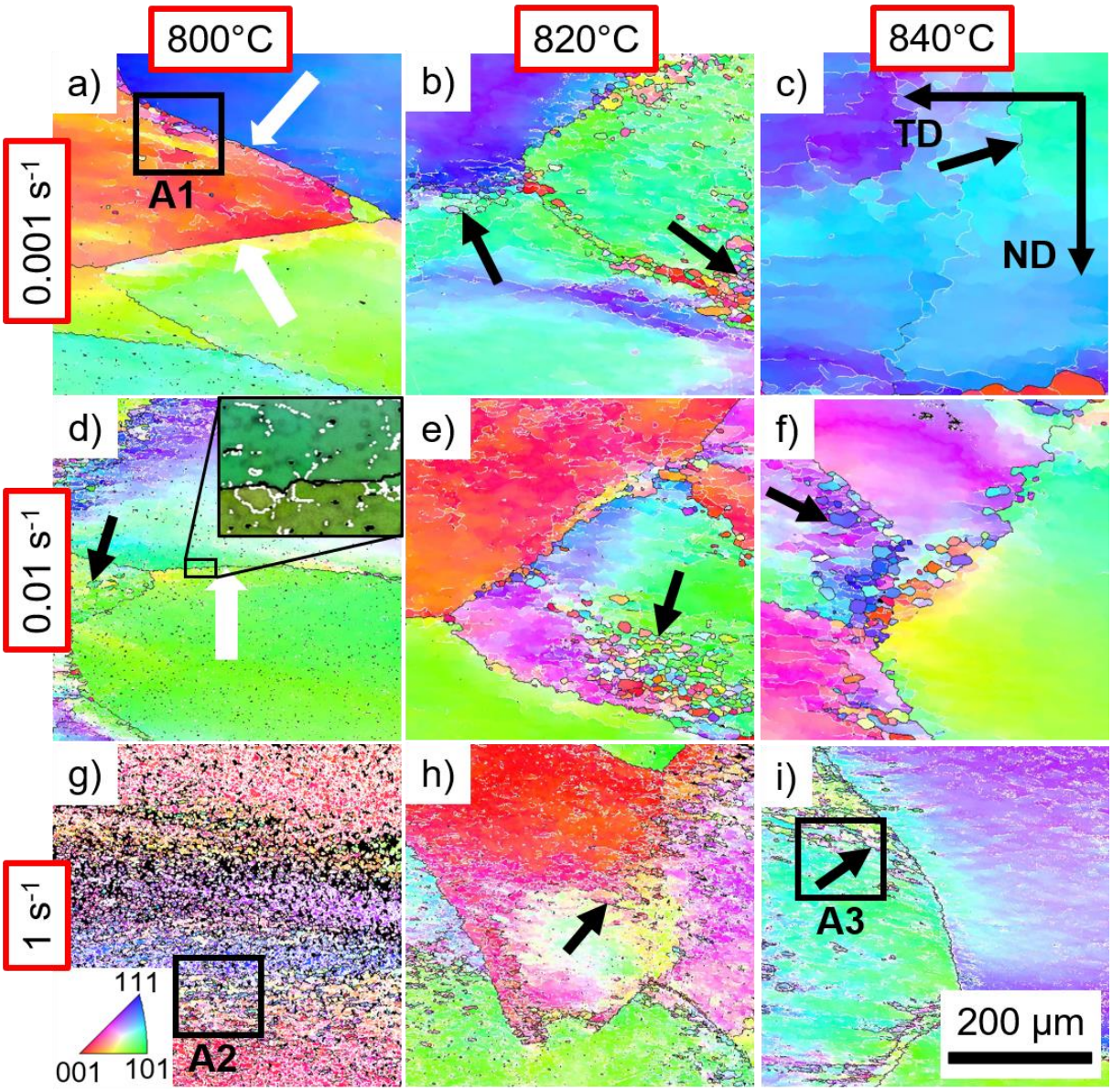

Figure 41: Electron backscattered diffraction (EBSD) inverse pole figure (IPF) maps of typical microstructures of Ti-5553 samples deformed in the α+β-phase domain at: (a-c) 0.001 s^{-1}; (d-f) 0.01 s^{-1}; (g-i) 1 s^{-1}; at the temperature of: (a,d,g) 800°C; (b,e,h) 820°C and (c,f,i) 840°C. Black lines indicate HAGBs and white lines indicate LAGBs; ND is the compression direction, and TD is the transversal direction. Black arrows indicate new HAGBs, and the white ones the prior β-HAGBs.

Several microstructural parameters can be obtained using the developed microstructure model. The evolution of grain and subgrain sizes as well as fraction of HAGB during deformation at 800°C and 840°C is shown in Figure 42 for the strain rates of 0.001 s^{-1} and 1 s^{-1} for the β-phase (Figure 42(a,b)) and the α-phase (Figure 42(c,d)). The mean α-grain size (G_s) is assumed to be constant and equal to the particle size (3 µm). The β subgrain size (SG_s) decreases slightly at the beginning of deformation. The lower temperatures result in a larger volumetric fraction of interface boundaries, increasing the production of immobile dislocation densities (Equation 62, Equation 65) and promoting the formation of smaller subgrains (Equation 84).

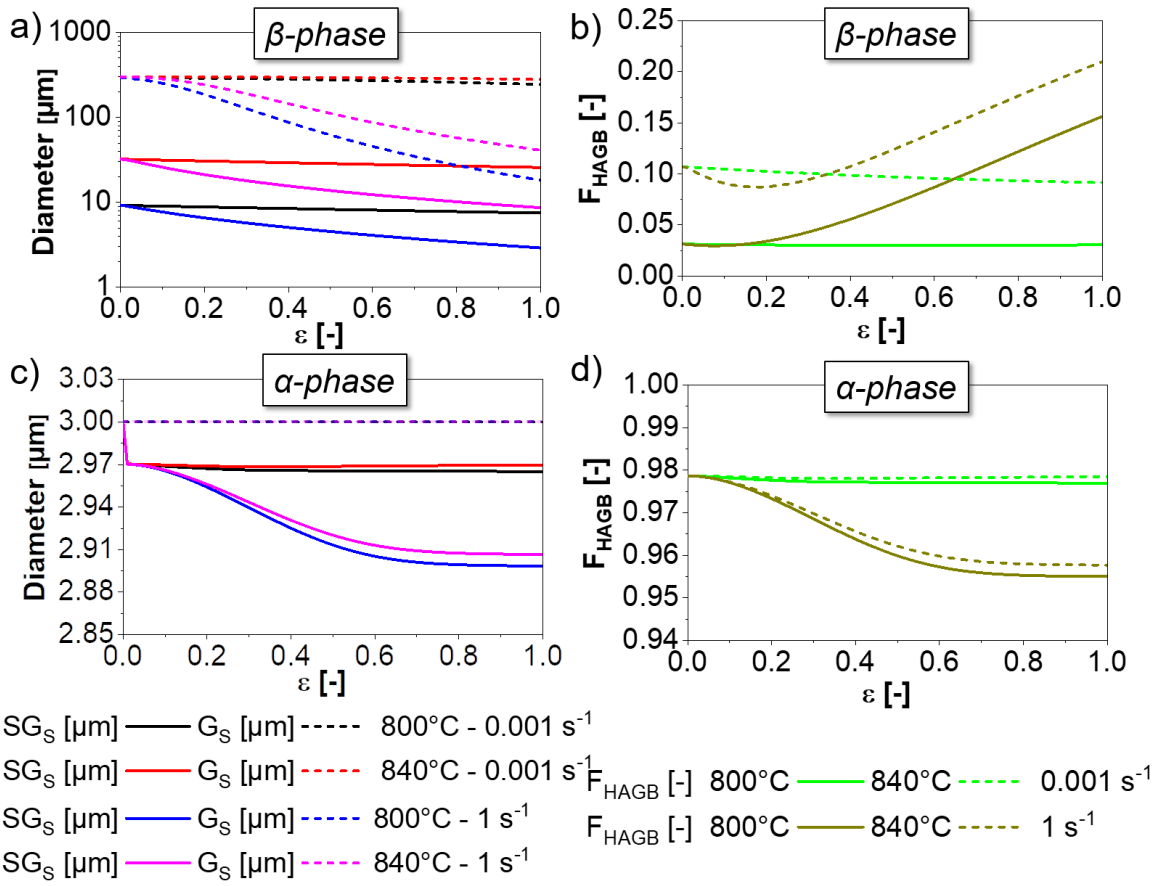

Figure 42: Simulation results of the developed model. Evolution of SG_s and G_s for both β (a) and α phases (c) as well as the fraction of HAGB for β (b) and α (d) for the temperature of 800°C and 840°C and the strain rates of 0.001 s^{-1} and 1 s^{-1} up to a true strain of 1.

The fraction of HAGBs is interpreted as the recrystallisation fraction. The initial strongly recovered microstructure of the β-phase exhibits an increase in boundary surface density at the early stages of deformation due to DVR. Consequently, subgrain size decreases. The progressive increase in the misorientation angle at boundaries leads to a progressive increase in the HAGB fraction. Higher strain rates result in lower recrystallisation grade at the same strain. The α-phase shows the scarce formation of LAGBs by a fraction of ~0.05.

9.1.4. Microstructure after deformation in the β domain

Figure 43 shows the EBSD-IPF maps of the β-phase deformed above the β-transus temperature. Similar to the α+β domain, a well-established, equiaxed-like substructure is observed for the strain rates of 0.001 s^{-1} (Figure 43(a-c)) and 0.01 s^{-1} (Figure 43(d-f)). Isolated HAGBs located within the β grains are also formed by CDRX, as indicated by the black arrows. Due to intensive DRV, the fraction of newly formed HAGB is notably low for 0.85 true strain for the strain rates of 0.001 s^{-1} and 0.01 s^{-1}. The subgrain size is ~10 times smaller for 1 s^{-1} compared to 0.001 s^{-1}. Furthermore, regions with large misorientation spread as well as low amplitude serration of the HAGB are observed for 1 s^{-1}, as well as deformation bands. The fast increase in dislocation density at high strain rates due to the short time for DRV results in the formation of misorientation spread and LAGBs localised close to the prior β-HAGBs indicated in Figure 43(e,f) by the black rectangles. Similar findings are reported in the literature [64,65,186–188]. The band-like

substructures are observed preferentially parallel to the β-grain boundaries or perpendicular to the compression axis and are also reported as ribbon-like grain structure [61,189].

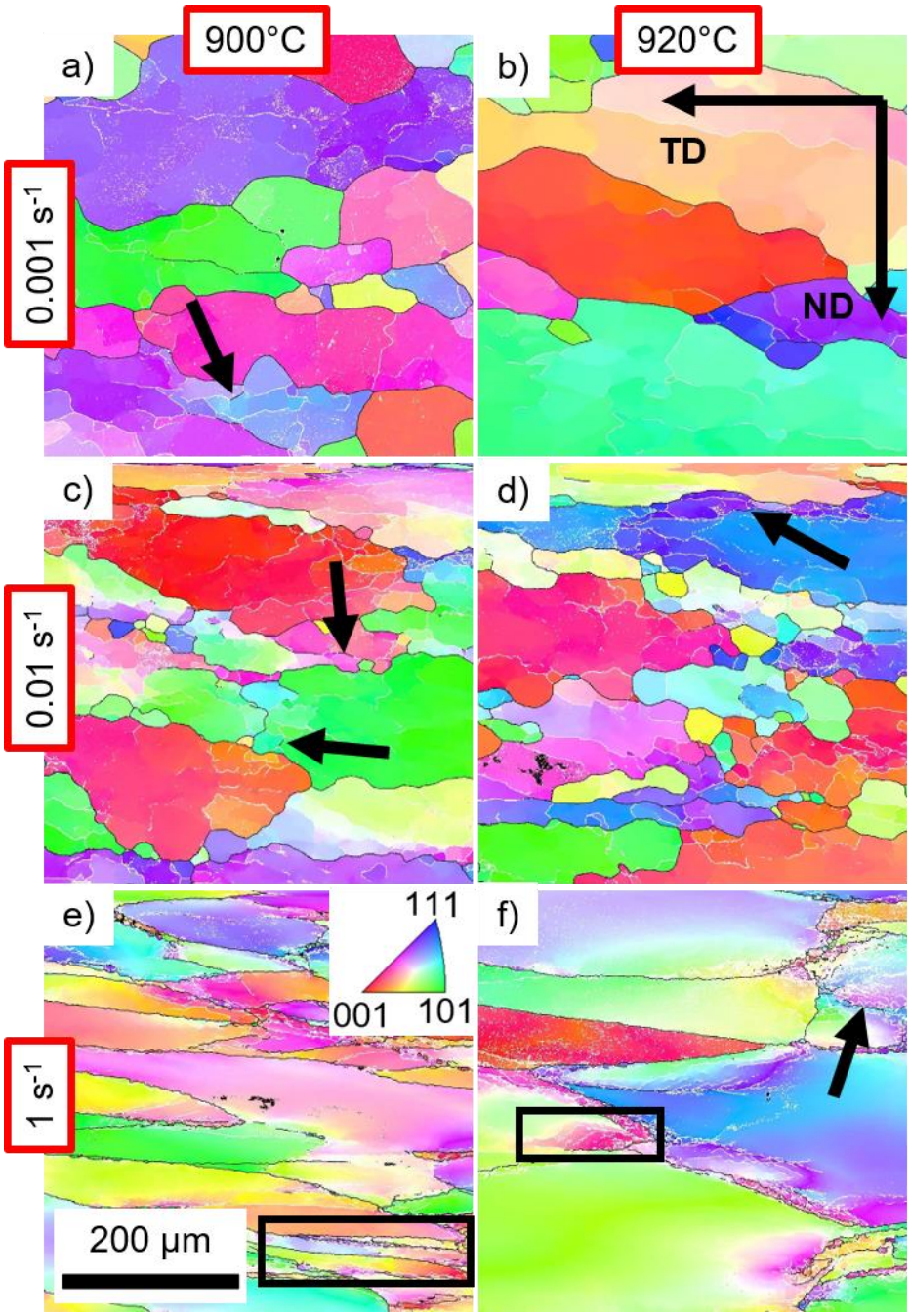

Figure 43: Electron backscattered diffraction (EBSD) inverse pole figure (IPF) maps of typical microstructures samples deformed in the β-phase domain at: (a,b) 0.001 s^{-1}; (c,d) 0.01 s^{-1}; (e,f) 1 s^{-1}; at the temperature of: (a,c,e) 900°C and (b,d,f) 920°C. Black lines indicate HAGBs and white lines indicate LAGBs.

The IPF maps of the hot torsion tests up to 7.3 of strain are shown in Figure 44. A more refined microstructure is observed compared to the hot compression tests up to 0.85 strain (Figure 43). The microstructure after torsion exhibits equiaxed-like subgrains surrounded by both LAGBs and HAGBs. The intensive DRV that lead to the formation of a substructure composed by LAGBs at lower strains (Figure 43) is combined with the local lattice rotation that leads to increase in boundary misorientation forming a dynamically recrystallised microstructure at larger strains

(Figure 44). However, a fully recrystallised microstructure formed by CDRX was not reached. LAGBs and misorientation spread within the subgrains are still observed in the samples after hot torsion, Figure 44.

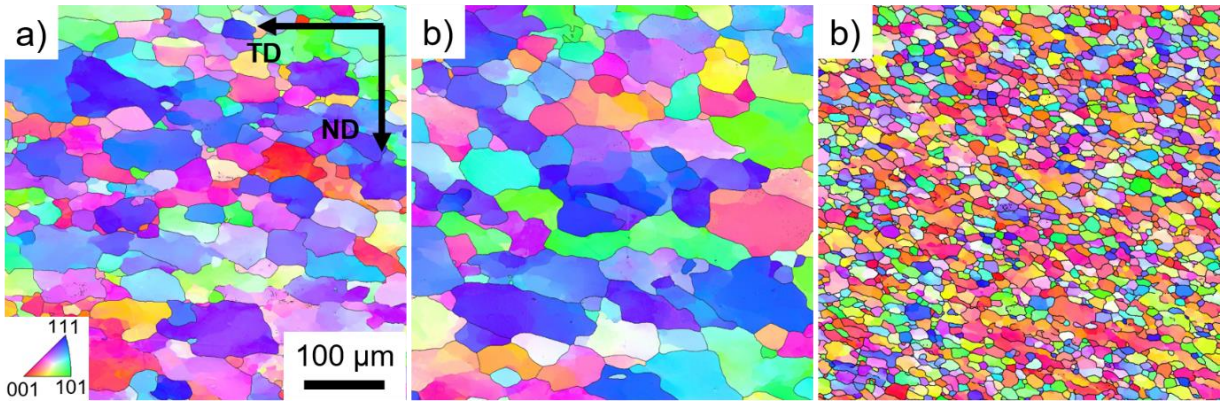

Figure 44: Electron backscattered diffraction (EBSD) inverse pole figure (IPF) maps of typical microstructures samples after hot torsion in the β-phase domain at: a) 0.01 s^{-1} and 880°C; b) 0.01 s^{-1} and 920°C; c) 1 s^{-1} and 920°C. Black lines indicate HAGBs. ND is the radial direction of the hot torsion sample, and TD is the longitudinal direction

The evolution of β grain and subgrain sizes during deformation above the β-transus temperature is shown in Figure 45. Figure 45a shows a substructure evolution starting with a fully recrystallised microstructure with fractions of HAGBs obtained from a Mackenzie distribution. Once the β-phase begins to deform plastically, LAGBs are rapidly formed, explaining the sharp decrease in subgrain size in Figure 45a. The HAGBs fraction of the β-phase deformed in the β-domain shows a minimum value at the early stages of deformation, while a steady-state is reached at large strains, Figure 45b. [141]

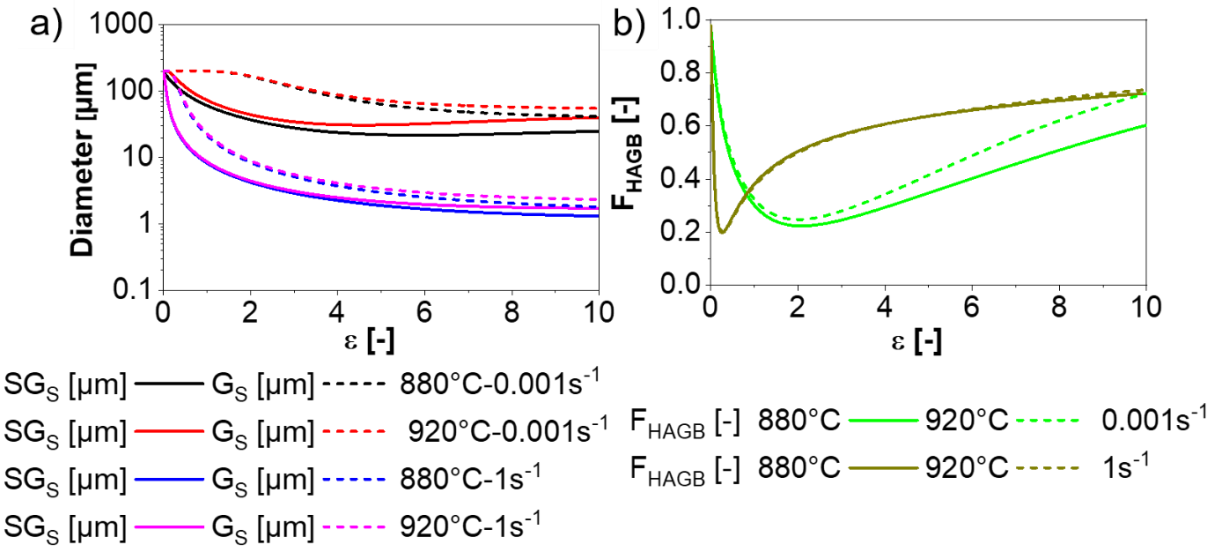

Figure 45: Evolution of subgrain and grain sizes in the β-domain (a) as well as fraction of HAGB for both β (b) for the temperatures of 880°C and 920°C and the strain rates of 0.001 s^{-1} and 1 s^{-1} up to a true strain of 10.

Figure 46 shows the predicted dislocation density for the β-phase deformed at 920°C. The mobile dislocation density is considered constant for all conditions. The immobile dislocation

density saturates at around 0.2 of strain after a sharp increase. The saturated value of immobile dislocation density increases with increasing strain rate and decreasing temperature as a result of a higher ratio between the production and consumption of dislocations. The rates of dislocation densities are affected by the size and fraction of α-phase. With the evolution of the deformation, the substructure will either coarsen or refined depending on the applied strain rate. Higher strain rates decrease the initial subgrain size, increasing the boundary density.

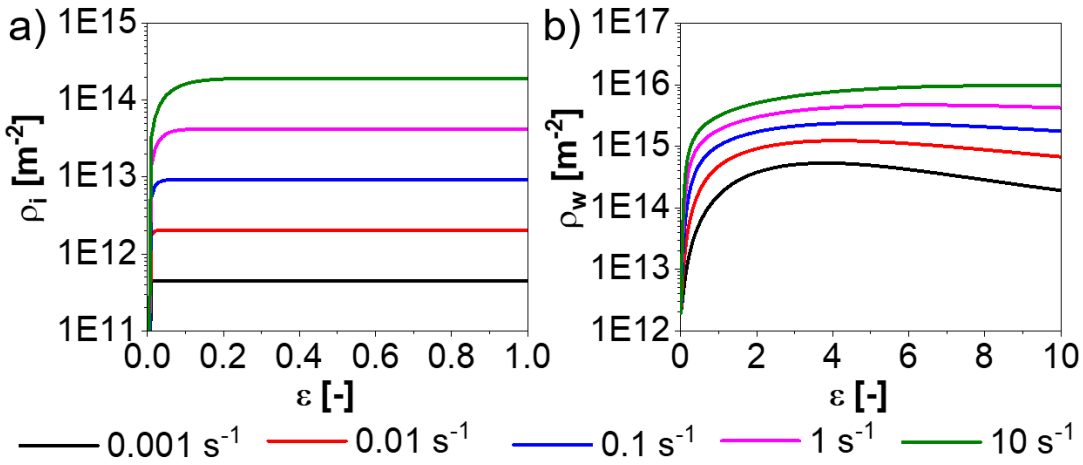

Figure 46: Dislocation densities evolution for the β-phase during the deformation at 920°C: a) immobile dislocation density and b) wall dislocation density.

9.1.5. Microstructure validation

Figure 47 and Figure 48 show the simulated and measured microstructural values for the β-phase after deformation at a local strain of 0.85 and 8.1, respectively. The modelled and measured subgrain and grain sizes, as well as fraction of LAGB and wall dislocation density for different deformation conditions, present similar orders of magnitude and non-linear tendencies with respect to temperature and strain rates. Discrepancies can be attributed to the following aspects:

- **Model assumptions:** The main limitation is the phenomenological description of the HAGB velocity and its power-law dependency uniquely on the strain rate (Equation 93). It impacts the prediction of the boundary density evolution, consequently the subgrain and grain sizes evolutions as well as the misorientation angle distribution evolution.
- **Measurements issues:** limited measurement area size impact the statistical significance of the measured values. The large prior β-grain size limits the accuracy on the determination of the fraction of HAGBs. The formation of the substructure occurs heterogeneously within the β-grain since recovery occurs preferentially in the vicinity of the prior β-HAGBs (explained in chapter 9). Thus, it can affect the subgrain size and fraction of HAGBs by having more/less formed boundaries within the measurement area.

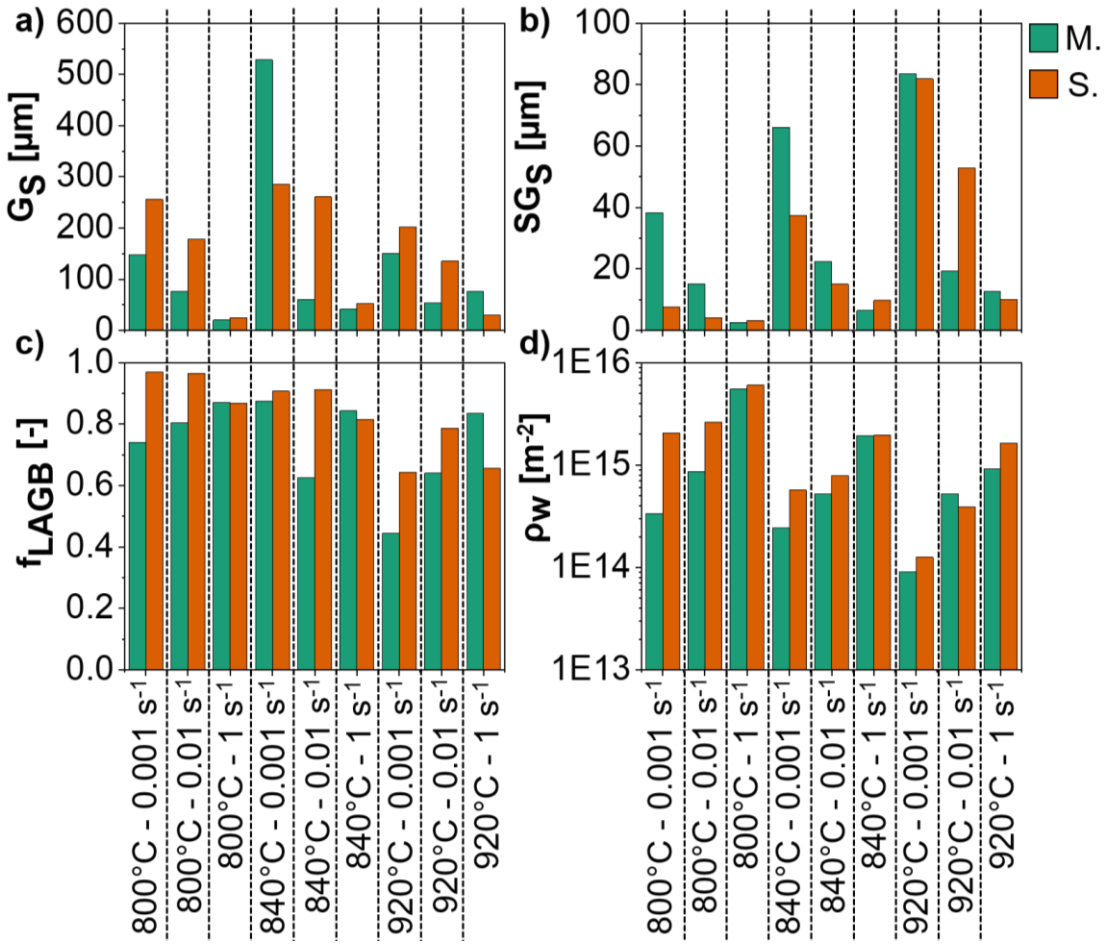

Figure 47: Comparison of measured (M.) and simulated (S.) results of the β-phase hot compressed up to 0.85 of strain: a) mean grain size; b) mean subgrain diameter; c) fraction of low angle grain boundaries; d) wall dislocation density.

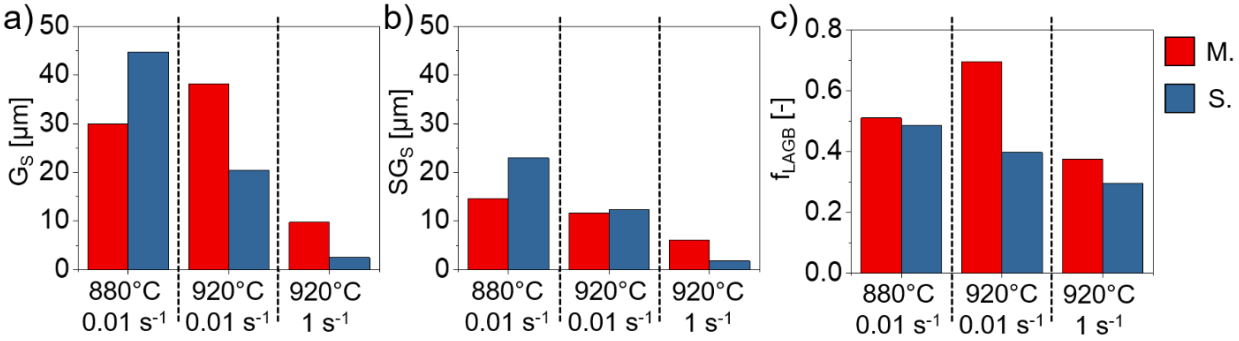

Figure 48: Comparison of measured (M.) and simulated (S.) results of the β-phase after hot torsion up to 8.1 of strain: a) mean grain size; b) mean subgrain diameter; c) fraction of low angle grain boundaries.

9.2. Discussion

The deformation of the β-phase via CDRX and the role of the α-phase are discussed.

9.2.1. Dynamic restoration mechanism: CDRX

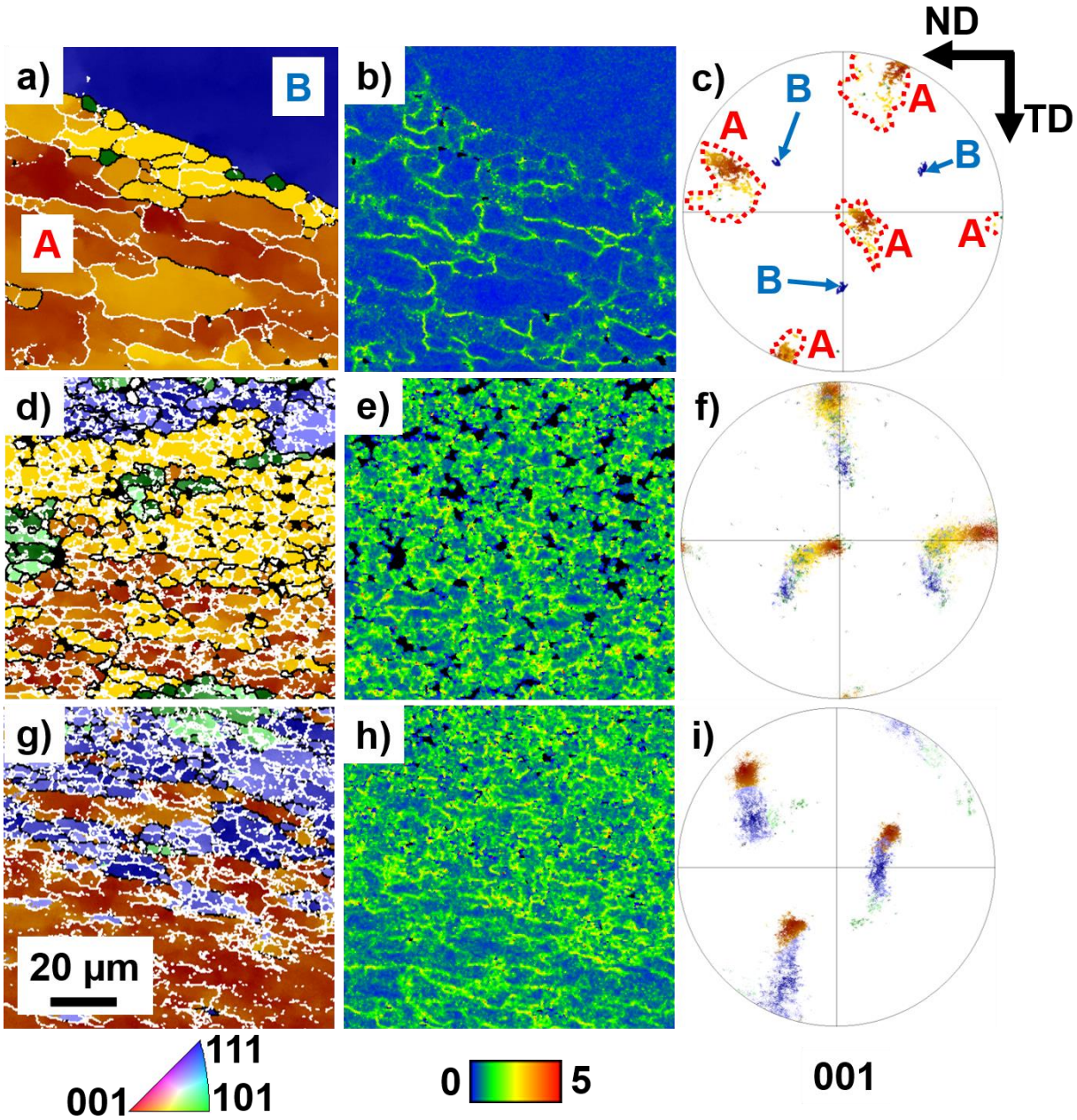

Figure 49: Typical microstructure of the deformed Ti-5553 for the "A1", "A2", and "A3" regions highlighted in Figure 41: a,d,g) IPF maps after deformation at 800°C and 0.001 s^{-1}, 800°C and 1 s^{-1}, and 840°C and 1 s^{-1}, respectively; b,e,h) KAM maps for the material deformed at 800°C with 0.001 s^{-1}, 800°C with 1 s^{-1}, and 840°C with 1 s^{-1}, respectively; c,f,i) pole figures for the material deformed at 800°C with 0.001 s^{-1}, 800°C with 1 s^{-1}, and 840°C with 1 s^{-1}, respectively. White and back indicate LAGBs and HAGBs, respectively in (a,d,g).

As shown in [141], formation of the LAGBs via DRV, the increment of the LAGB boundary misorientation angles, and eventual the occurrence of new fine grains is how CDRX manifests during hot deformation [62,190–192]. The highlighted "A1", "A2" and "A3" regions in Figure 41 is

shown with higher spatial resolution in Figure 49. The IPF maps of the hot deformed Ti-5553 at these conditions show the presence of LAGBs and HAGBs in all cases. The kernel average misorientation (KAM) maps in Figure 49(b,e,h) show a notable dependency of the strain rate. The spread in orientation within the observed grains are shown in the pole figures (PF) in Figure 49 (c,f, and i). The formation of the observed microstructure occurs via continuous rotation of the lattice. In Figure 49a, two prior β-grains are highlighted with “A” and “B”. The grain “A” with a larger surface density of LAGB and new HAGB exhibits larger misorientation spread than grain “B” (Figure 49c). The formation of the misorientation spread within a β-grain is used to accommodate the plastic deformation. Dislocations are rearranged into LAGBs, and the simultaneous increase in LAGB misorientation leads to the formation of new HAGBs. The formation of a substructure consisting of LAGBs and HAGBs (Figure 49(a,d,g)) where the subgrains experience a progressive misorientation spread (Figure 49(c,f,i)) evidences the role of CDRX as active recrystallisation mechanism for the Ti-5553 alloy.

9.2.2. Role of α-phase in the deformation

As shown in [141], the α-phase has an impact on the starting β-microstructures. Elongated prior β-grains and a fined substructure are observed in the α+β domain, and recrystallised β-grains are observed in the β-domain. A more equiaxed-like substructure, homogeneously distributed within the β-grain is observed in the α+β domain compared to the β-domain after deformation. An equiaxed-like substructure composed of LAGBs and HAGBs is observed in the α+β domain, while elongated β-grains with a heterogeneous formation of the substructure are presented for the deformed Ti-5553 in the β-domain.

The presence of the α-phase impacts the fractions recovered dislocations that are produced and recovered (Equation 62 and Equation 65, respectively), consequently increasing the amount of dislocations that takes place in CDRX (Equation 68). Higher α/β interface density increases both the formation of LAGBs and their misorientation during the iso-power load partition regime. The change in load partitioning from iso-power to iso-stress results in flow softening and a decrease of the strain rate in the α-phase, thus an increase of the strain rate in the β-phase. The increase in strain rate in the β-phase further promotes the formation of new LAGBs and the increase in their misorientation.

9.3. Summary and conclusions

A physically-based model considering CDRX and DRV as main restoration mechanisms developed as described in section 7.2 using the dislocation rate equations describe in section 7.2.6.1 is applied to predict the hot deformation of the Ti-5553. The conclusions are shown below. The innovative aspects are highlighted in bold:

a) Conclusions from the simulations:

- The model predicts an increase in wall dislocation density from a fully recrystallised microstructure and their progressive evolution into HAGBs by CDRX.
- **The fraction of HAGBs can be interpreted as recrystallisation fraction.**
- Subgrain size decreases faster at low strains, followed by a slight increase up to the steady-state value at large strains.

- **The α-phase promotes CDRX and increases the kinetics of the multiplication and recovery of dislocations.**

b) Conclusions from the experiments:

- A homogeneous nearly equiaxed substructure forms at low strain rates. Regions with a high density of LAGBs and new HAGBs in the vicinity of prior β-HAGBs are formed after deformation at high strain rates. It occurs to localisation of plastic deformation in the vicinity of prior β-HAGBs Misorientation spread is observed within β-phase and is more pronounced for high strain rates due to the lack of time for DRV promoting reorganisation of dislocation into LAGBs

c) General conclusions:

- The size of subgrains increases with increasing temperature due to higher HAGB mobility and faster CDRX.
- The formation of equiaxed-like subgrain surrounded by LAGBs and HAGBs within the β-grains evidence the role of CDRX. The increase of the fraction of HAGB is faster for higher strain rates up to a specific strain. Then, the lower the strain rate, the smaller the strain required to reach a fully recrystallised microstructure. A fully recrystallised microstructure is predicted for large strains.
- **The change from iso-power plastic strain rate between the two phases to the iso-stress regime is considered as the main reason for the flow softening in the α+β domain. The decrement in thermal stress in the α-phase plays a major role in the decrement in the overall stress.**

10. Improved predictability of the hot deformation of Ti-5553

This chapter presents a comparison between the physically-based model following Ghoniem's rate equations for the dislocation reactions [104] (described in section 7.2.6.2) and the model based on Kocks-Mecking dislocation formalism section 7.2.6.1. It corresponds to a comparison between the results and discussion published in [141] and the simulation results using the Kocks-Mecking formalism. In this chapter, this comparison is emphasised aiming to discuss the usability of both models. The first model (named "Model G" in this chapter) and the second one (named "Model KM" in this chapter) can describe DRV and are correlated to CDRX in a similar way. However, the more dislocation interactions prediction with the Model G enables the quantification of other phenomena, such as the elastic strain rate and SRV. The flow stresses of both α and β-phases are calculated using the same constitutive equations and the change in load partitioning between the α and β-phases like is described as in chapter 9. Hot compression experiments of a Ti-5553 alloy shown in chapter 9 are used for validation. The constants and parameters used in the model are given in Appendix D.

10.1. Results

The microstructure before and after deformation are presented in chapter 8.

10.1.1. Flow stress

The comparison between the measured flow curves corrected for the adiabatic heating and the simulated flow curves is shown in Figure 50 for both Model KM and Model G. A more detailed interpretation of the flow stress behaviour is present in section 9.1.2.

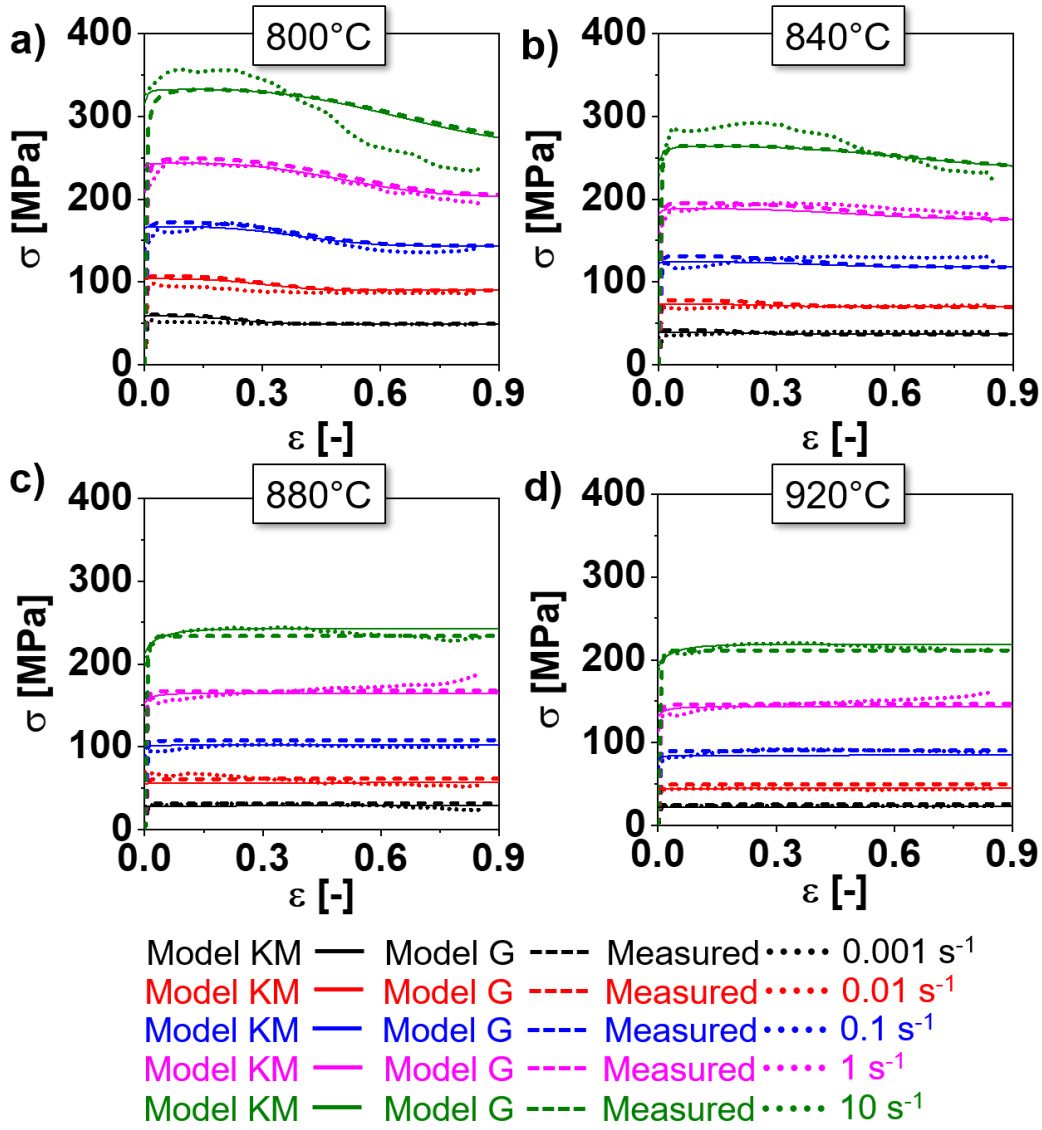

Figure 50: Comparison between the measured flow curves corrected for the adiabatic heating and the simulated flow curves for both Model KM and Model G: a) 800°C; b) 840°C; c) 880°C; and d) 920°C.

The overall differences in the flow stress evolution between the Model KM and the Model G are minor. However, differences can be large for the derivative of the flow stress with respect to the strain, is shown in Figure 51 for deformation at 920°C for the strain rate of 10 s^{-1}. The Model G predicts a notably faster work hardening at the beginning of the deformation compared to the Model KM.

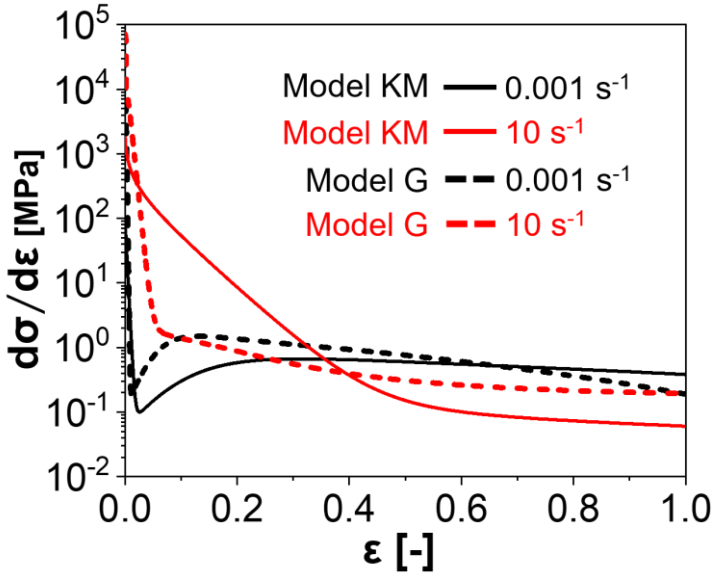

Figure 51: Derivative of the total stress with respect to the strain for the Ti-17 deformed at 970°C with the strain rates of 0.001 s^{-1} and 10 s^{-1} and for the "Model KM" and "Model G".

The mobile dislocation density is considered constant and independent on temperature and strain rate for the hot deformation modelled using the Model KM. Thus, the increase in strain rate leads to the same proportional increment in glide velocity in Model KM following Orowan's relationship, Equation 60. Model G predicts an initial near-elastic regime, where the plastic strain rate is negligible, Figure 52(c,d). With an increase in stress, mobile dislocation starts to glide once the thermal stress becomes positive. A peak in the glide velocity and a sharp increase in the plastic strain rate are predicted once the yield stress is reached. Fast multiplication of mobile dislocations follows this peak in the glide velocity. Finally, the reduction of glide velocity and stabilisation of the plastic strain rate occurs. A steady-state value of mobile dislocation density, plastic strain rate and mobile dislocation density is reached at very low strains. The sharp increase in mobile dislocation density at the beginning of deformation is responsible for the fast work-hardening predicted by the Model G (Figure 51) since the predicted mobile dislocation density is higher than immobile one in Model G (shown later in the text in Figure 54). Thus, the evolution of the flow stress shown in Figure 52(a,b) for the Model G is related to the mobile dislocation density evolution with a minor influence of the wall and immobile dislocation density.

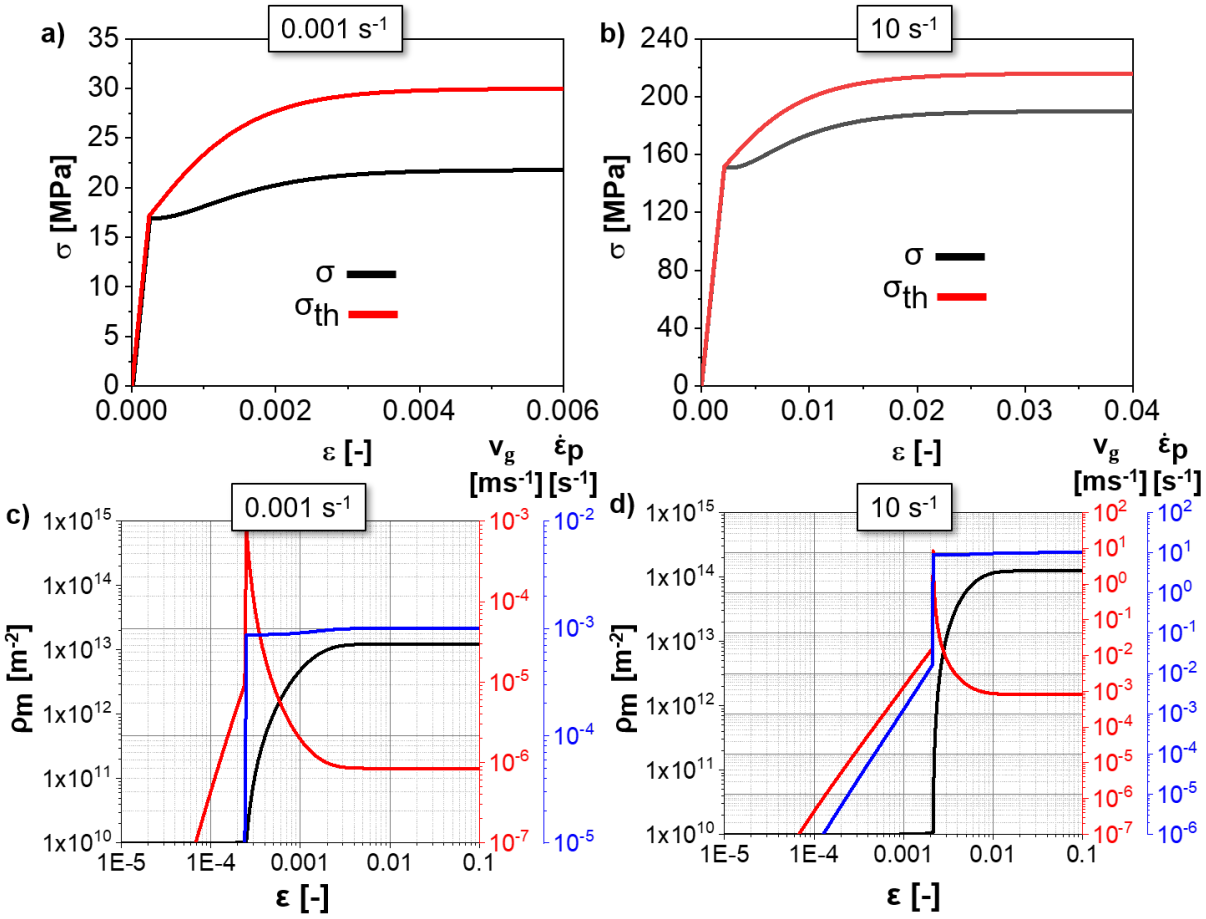

Figure 52: Evolution of the thermal and overall stress components predicted by Model G (the difference is the athermal stress) for deformation at 920°C: a) 0.001 s^{-1}, b) 10 s^{-1}. Evolutions of the mobile dislocation density, glide velocity and plastic strain rate predicted by Model G for deformation at 920°C: a) 0.001 s^{-1}, b) 10 s^{-1}.

10.1.2. Model predictions of the microstructure of β-phase

The grain and subgrain size, as well as the fraction of HAGB evolutions, are shown in Figure 53 for the Ti-5553 deformed at 920°C. For both models, a fast decrease in subgrain size and fraction of HAGBs is predicted at the beginning of deformation due to formation of LAGBs. After a specific strain, the average grain size starts to decrease due to the formation of new HAGBs, also leading to a progressive increment of the fraction of HAGBs. The grain size finally decreases with lower kinetics at larger strains reaching the subgrain size at the steady-state. The slight difference in kinetics between the Model KM and the Model G is associated with the difference in the amount of dislocations that contribute to cDRX predicted by both models. They are adjusted by the constant f_{CDRX} for Model G, while the behaviour and kinetics are given by α_{CDRX} and θ_0. However, negligible differences can be observed in the behaviour since the same cDRX rate equations are used for both models.

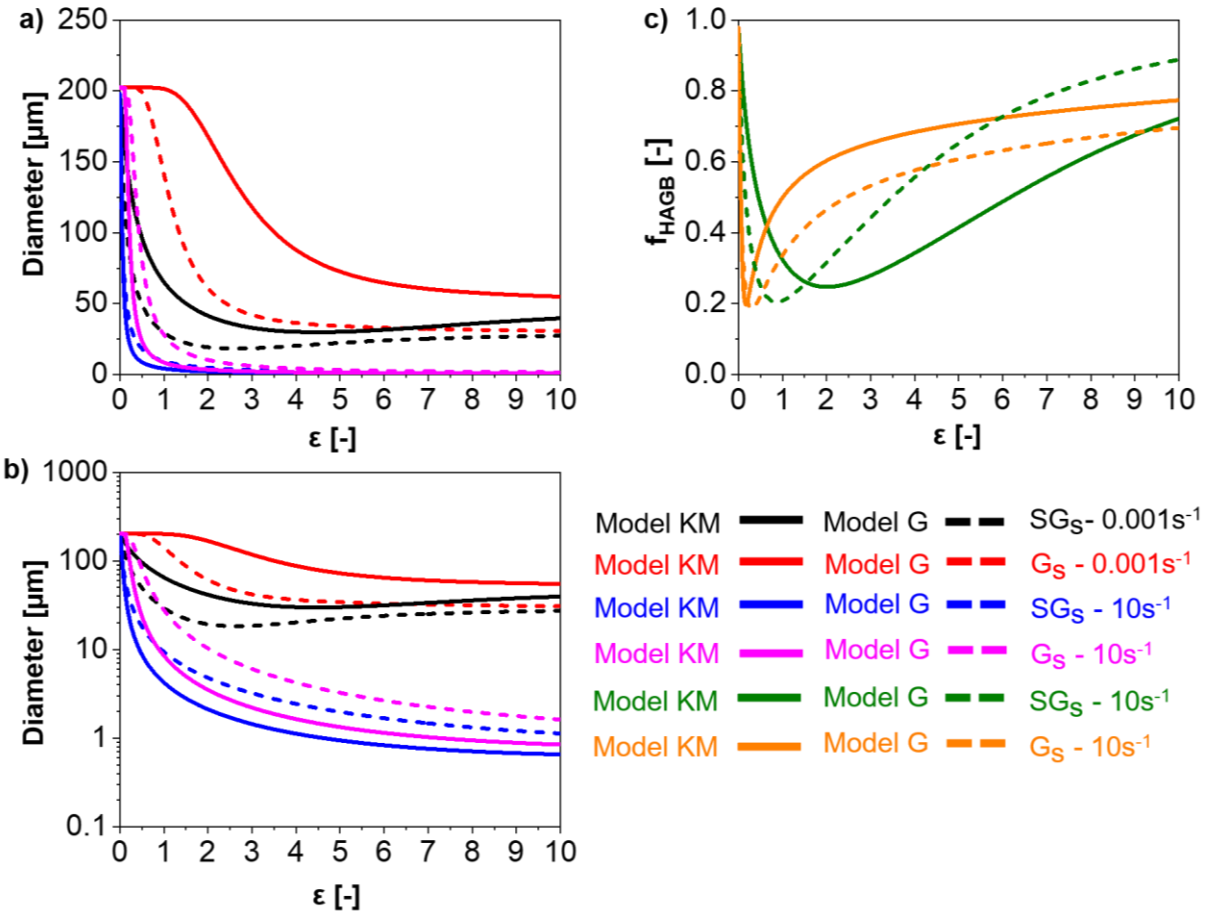

Figure 53: Predicted grain and subgrain size, as well as the fraction of HAGB, evolutions for deformation at 920°C using the Model KM and the Model G.

The evolutions of the wall and immobile dislocation densities are shown in Figure 54(a and b, respectively). The evolution of the wall dislocation density (Figure 54a) can be directly related to the fraction of HAGBs (Figure 53c) and the evolution of the grain and subgrain sizes (Figure 53(a,b)). Wall dislocations are rapidly produced due to reorganisation of immobile dislocations in the case of the Model KM and due to reorganisation of mobile and immobile dislocations via SRV and DRV in case of the Model G. Higher strain rates lead faster kinetics initially for the formation of wall dislocation due to the higher rates of DRV. A maximum wall dislocation density follows the rapid increase. It corresponds to the strain where the consumption counterbalances the production of new LAGBs. After this maximum, a progressively decrease occurs. Higher strain rates form smaller subgrains sizes. Consequently, a higher rate of dislocation is required to evolve the formed LAGBs. Thus, the higher the strain rate, the slower the wall dislocation density reach the steady-state. The fraction of HAGBs shows a fast initial decrease related to the formation of new LAGBs, followed by a valley that corresponds to the strain where the boundary misorientation distribution yields the maximum fraction of LAGBs.

The differences are more marked in the evolution of the immobile dislocation density between Model KM and Model G, Figure 54b. The Model KM predicts a rapid increase in immobile dislocation, followed by saturation. Thus, the fast production of immobile dislocations at the early stage of deformation is balanced by their annihilation via DRV. The Model G predicts a more complex behaviour for the immobile dislocation density evolution. An initial increase occurs due

to the immobilisation of mobile dislocations at LAGBs and HAGBs. The immobilisation competes with consumption of immobile dislocations via SRV due to climb, DRV and movement of HAGBs. The immobile dislocation density does not reach an apparent plateau because the subgrain size varies during deformation, so does also the immobilisation rate. It is also notable that the predicted immobile dislocation density using the Model G is smaller compared to the Model KM. The main difference is that Kocks-Mecking formalism [170] adopted in Model KM considers the production of immobile dislocations to be independent on the microstructure features. In contrast, in Model G the production rate of immobile dislocation density is dependent on the boundary density.

The mobile dislocation density is considered constant in the Model KM and independent on temperature and strain rate. The model G predicts the formation and a steady-state mobile dislocation density, Figure 52(c,d).

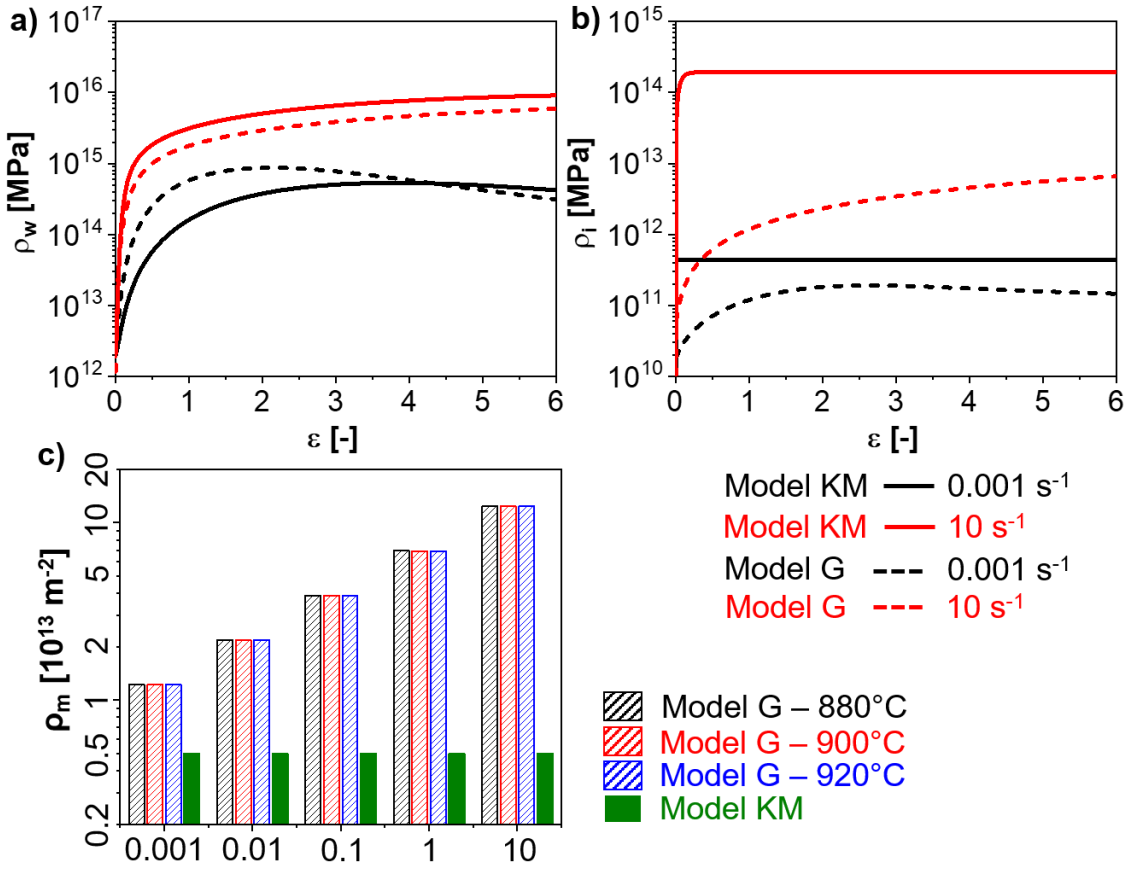

Figure 54: Simulated evolutions of a) wall dislocation density b) immobile dislocation density; c) steady-state mobile dislocation density predicted by the Model G for different strain rates and temperatures compared with the assumed invariable mobile dislocation density for the Model KM.

One notable difference between the Model KM and the Model G is the capability of describing the evolution of the mobile and immobile dislocation density due to clear physical phenomena. Figure 55 shows the evolution of the different dislocation reactions for the mobile (Figure 55(a,b)) and immobile dislocation densities (Figure 55(c,d)) for the deformation at 920°C. The production of mobile dislocations due to interactions with the existing one ($\rho_m^{3/2} v_g$) is balanced mainly by the DRV term ($\delta_{DRV} \rho_m (\rho_m + \rho_i) v_g$). A small contribution of the immobilisation rate ($\rho_m v_g / \Phi_{sg}$), SRV due to climb ($8 \rho_m v_{c_m} / \lambda_m$) and consumption of mobile dislocations due to

movement of HAGBs ($\rho_m S_v f_{HAGB} v_{HAGB}$) are also predicted. The immobilisation of mobile dislocations ($\rho_m v_g / \Phi_{sg}$) is the source of immobile dislocations, and its production is balanced by DRV ($\delta_{DRV} \rho_m \rho_i$), Figure 55(c,d). A minor contribution of the annihilation due to SRV ($8\,\rho_i v_{c_i} / \lambda_i$) and consumption of mobile dislocations due to movement of HAGBs ($\rho_i S_v f_{HAGB} v_{HAGB}$) are also predicted. A higher strain rate (Figure 55 (b,d)) yields a lower annihilation rate of dislocations via SRV compared to a lower strain rate (Figure 55(ac)) for both mobile and immobile dislocation density.

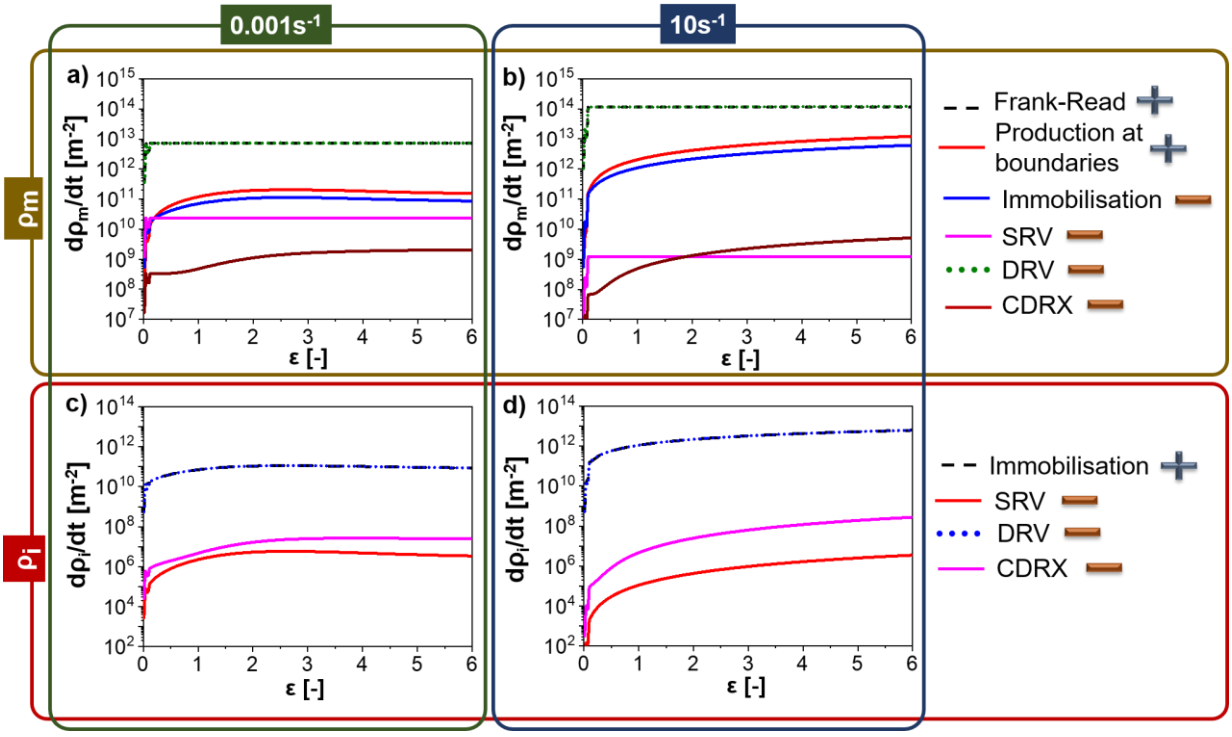

Figure 55: Evolution of the dislocation densities predicted by the Model G for deformation at 920°C and a,c) 0.001 s^{-1}; and b,d) 10 s^{-1}. a,b) mobile dislocation density reactions; c,d) immobile dislocation density reactions. The production terms are indicated with a "+" while the deduction ones with a "-".

The comparison between measured and simulated subgrain size and the fraction of HAGBs is shown in Figure 56 and Figure 57 for the hot compression and hot torsion experiments, respectively. The differences between Model KM and Model G are mainly due to the adopted values of α_{CDRX}, θ_0, f_{CDRX}. The simulated and measured values exhibit non-linear behaviours, i.e. an intricate relationship between strain, strain rate and the temperature is attained. The developed models are robust to predict the evolution of any initial microstructure up to any strain, temperature and strain rate.

The deviations are related to both modelling and measurements issues:

- **Model assumptions:** the mobile dislocation density is considered constant in the Model KM, and no term to describe its influence on the CDRX is given. This issue is overcome in the Model G but with the assumption that the mobile dislocation is adjusted to yield a constant value once a maximum value is achieved. Also, its calculation is performed, assuming constant thermal stress for a given temperature and strain rate. Another limitation is the phenomenological description of the HAGB velocity and its power-law

dependency uniquely on the strain rate (Equation 93). In the case of the Model G, the dependence of the boundary evolution on the applied strain rate is greatly influenced by the phenomenological description of the δ_{DRV} (see Appendix D).

- **Fitting parameter adjustments:** The differences between the Model KM and the Model G are mainly related to the adjustment of the fitting parameters of the model, especially the ones related to the CDRX model (see Appendix D). Thus, the error between measurement and simulation could be further minimised using a systematic and automatic fitting algorithm.
- **Measurements issues:** The formation of the substructure occurs heterogeneously within the β-grain since recovery occurs preferentially in the vicinity of the prior β-HAGBs. The large prior β-grain size limits the accuracy on the determination of the fraction of HAGBs since more/less initial β-HAGBs can be considered depending on the measurement site. The limited measurement area size impacts the statistical significance of the measured values. Thus, it can affect the subgrain size and fraction of HAGBs by having more/less formed boundaries within the measurement area.

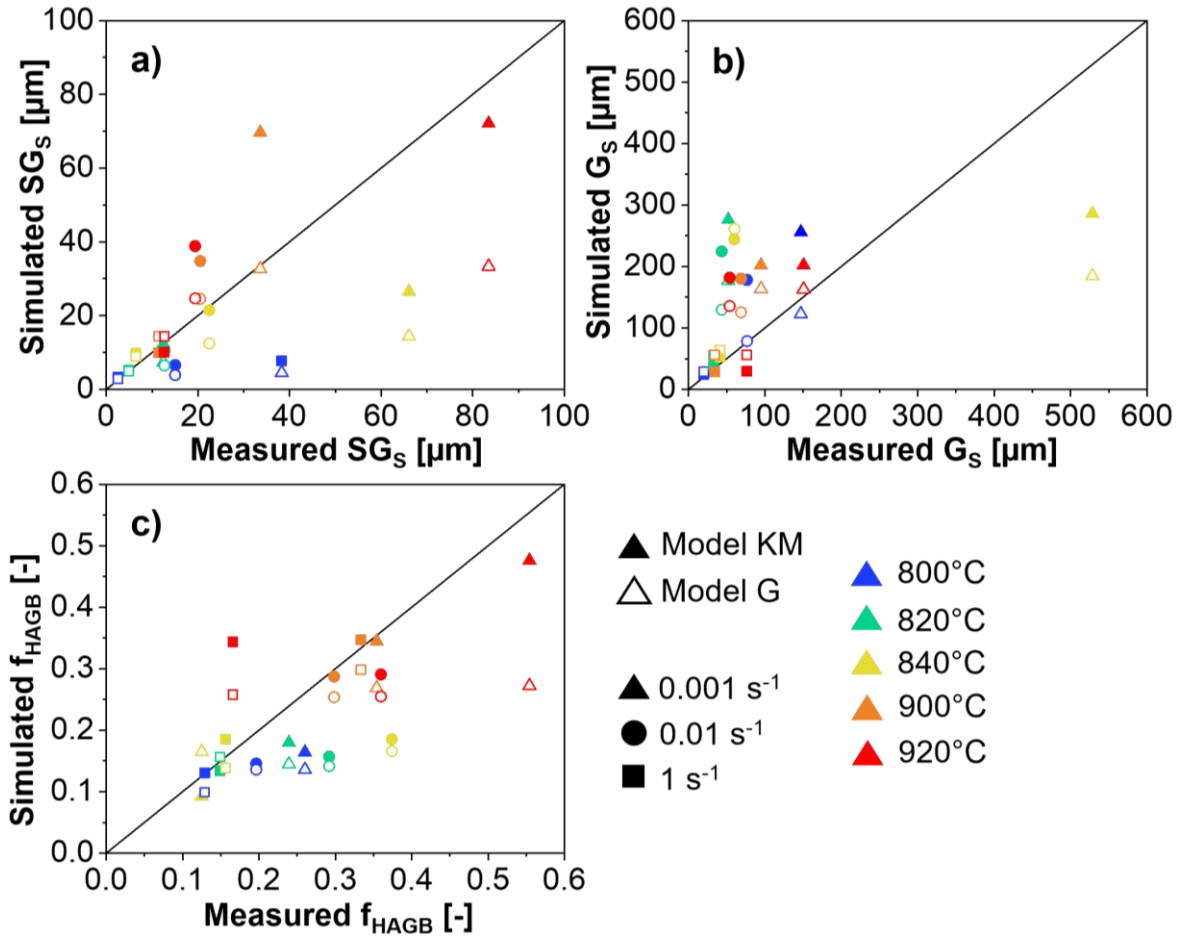

Figure 56: Measured and simulated results for the strain of 0.85 (hot compression): a) subgrain size, b) grain size, c) fraction of HAGBs.

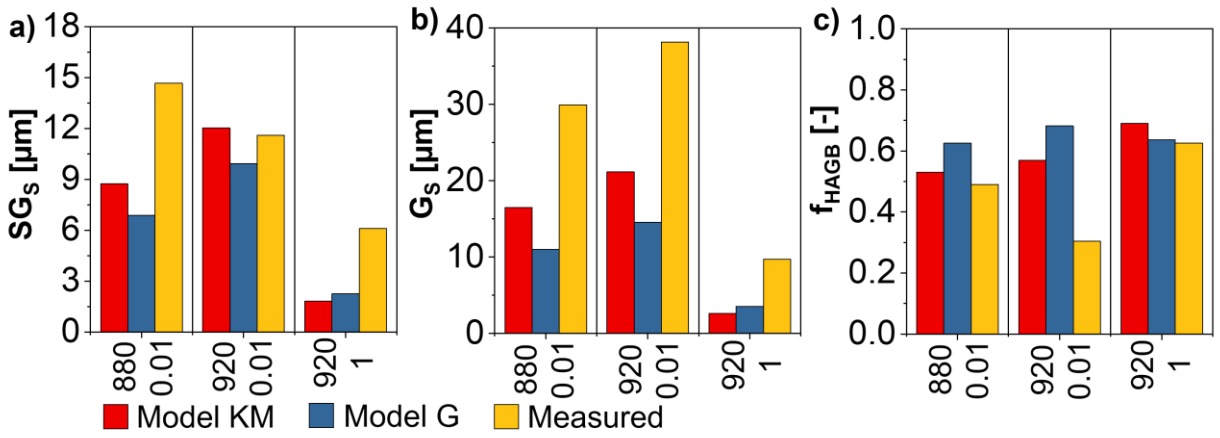

Figure 57: Measured and simulated results for the strain of 8.3 (hot torsion): a) subgrain size, b) grain size, c) fraction of HAGBs.

10.2. Discussion

The low contribution of the athermal stress in the proposed models is mainly due to the small value of Taylor constant (α = 0.1). The value of 0.1 for the Taylor constant is related to the lattice resistance due to the interaction between parallel dislocations as the main barrier for dislocation movement [193]. Different values have been proposed in the literature [193], attributed to the operating deformation and strengthening mechanisms. In the case of precipitate hardening or strong interaction with forest dislocation, the Taylor constant can acquire higher values [193]. The corollary is that thermally activated glide of dislocations is the primary attributed mechanism for plastic deformation, in agreement with the literature for the investigated strain rate and temperature ranges [194].

The Taylor factor is an essential parameter for the calculation of the glide velocity, as well as the athermal stress. The Taylor factor value changes with the crystallographic texture [195]. For simplification, the proposed model considers that the average Taylor factor is constant and independent of the deformation conditions. Despite the inherent error from this assumption, the simulated and measured flow curves of the deformed Ti-5553 are in good agreement, especially in the β-domain. A fully coupled model would require to consider the texture evolution in the Taylor factor.

Model G quantifies the amount of mobile and immobile dislocation involved in several reactions. Despite limitations on the calculation of mobile dislocation density related to the assumption related to the algorithm described in Appendix C, the Model G predicts a dependency of the mobile dislocation for the strain rate, Figure 54c. A difference of five orders of magnitude in strain rate leads to a difference in one order of magnitude, Figure 54c. This model output corroborates to the small value of Taylor constant since the thermally activated glide of dislocations is the primary mechanism for plastic deformation. It assumes that the drag of the mobile dislocations occurs by the presence of other mobile dislocations and the interspace is sufficiently large that the effect of one gliding dislocation on the neighbour one is small. Therefore, an increase in strain rate leads to faster gliding without notable multiplication of mobile dislocations.

10.3. Summary

Two physically-based models were developed to predict the flow stress and microstructure evolutions and validated for a Ti-5553 alloy. A simpler dislocation density reaction approach (Model KM) is compared to a comprehensive one (Model G). SRV, DRV and CDRX are considered as main restoration mechanisms. The evolution of mean grain size, mean subgrain size, boundary misorientation distribution, and dislocation densities of all phases can be predicted during deformation. The model can predict the evolution of any starting condition of the initial microstructure and the change in load partitioning in the α+β domain is considered the reason for the flow softening. The conclusions are shown below. The innovative aspects are highlighted in bold:

a) Conclusions from the simulations:

- **The mobile dislocation density can be estimated by the Model G for any deformation condition, while needs to be adjusted of assumed for the Model KM.**
- **The immobile dislocation density evolves together with the subgrain size for the Model G, while the Model KM predicts a fast increase followed by saturation.**
- CDRX is coupled with the dislocation reactions in the same manner for the Model KM and Model G: recovered dislocations are the source for the formation of new boundaries and increase in their misorientation.
- **The influence of the dislocation reaction approach on cDRX related variables (subgrain and grain sizes, misorientation distribution, the fraction of HAGBs) is negligible since the rate equations of the cDRX model are nearly non-independent of the mobile and immobile dislocation density reactions.**

b) General conclusions:

- **Change of load partitioning can represent the overall flow softening in the α+β domain, and this change describes the phenomena related to: decrease in dislocation density; the decrease of strain rate; and the stress of the α-phase.**

11. Hot deformation and dynamic globularisation of α-phase of the Ti-17

This chapter shows the investigations about the hot deformation behaviour of a Ti-17 alloy using hot compression tests combined by micro characterisation, in-situ synchrotron radiation diffraction, and post mortem metallography. The results of the equations for the dislocation reactions [104], as described in section 7.2 are also shown, combined with the model of dynamic globularisation of the α-platelets (section 7.2.9). The deformation in the α+β domain was investigated by hot compression experiments from 810°C to 850°C, and in the β domain from 930°C to 970°C. Strain rates between 0.001 s^{-1} to 10 s^{-1} were tested. The results of the flow stress, measured microstructure of the β-phase deformed in the β-domain, as well as the discussions that are shown here, were already published in [142]. This chapter strengths the results shown on the β-substructure formation, especially the tole of the α-phase and the deformation at high strain rates. Insights on β-microstructure evolution during hot compression using in-situ synchrotron radiation diffraction is also complementary to [142]. The model predictions that were published in [142] are also strengthened. The constants and parameters used in the model are given in Appendix E.

11.1. Methodology

The performed hot compression tests using the Gleeble® 3800 device are described in section 6.3. EBSD measurements were conducted on selected hot compressed samples. Additionally, the in-situ hot compression testing using synchrotron X-Ray diffraction was performed during hot compression, as described in section 6.4.

11.2. Results

11.2.1. Initial microstructure and α-phase morphology

The typical α-lamella are exhibited in the BSE micrographs in Figure 58(a, b and c) after holding for 15 min at 810°C, 830°C and 850°C, respectively. The α-phase area% fractions are measured after holding at 810°C, 830°C, and 850°C, resulting in 22.9 ± 1.0, 10.8 ± 1.2, and 2.5 ± 0.8, respectively [142]. A plate-like morphology of the α-phase is observed in all cases. The interconnectivity of the platelets is higher at 810°C (Figure 58a) and nearly negligible at 850°C (Figure 58c).

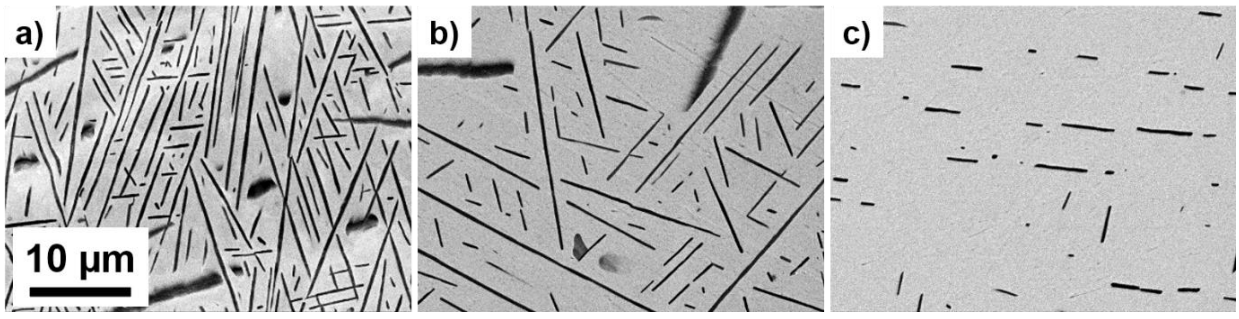

Figure 58: Backscattered electron (BSE) micrographs of the microstructure prior to deformation annealed for 15 min at: a) 810°C; b) 830°C; c) 850°C. α-phase is dark, β-phase is bright.

The typical microstructure of the β-phase prior to deformation at 810°C, 850°C, and 970°C is shown in Figure 59(a, b and c), respectively, and consists of partially recrystallised grains. Despite more recrystallised grains after holding at 970°C, the differences among the initial β-microstructure for the heat treatments at 810°C, 850°C and 970°C are minor [142].

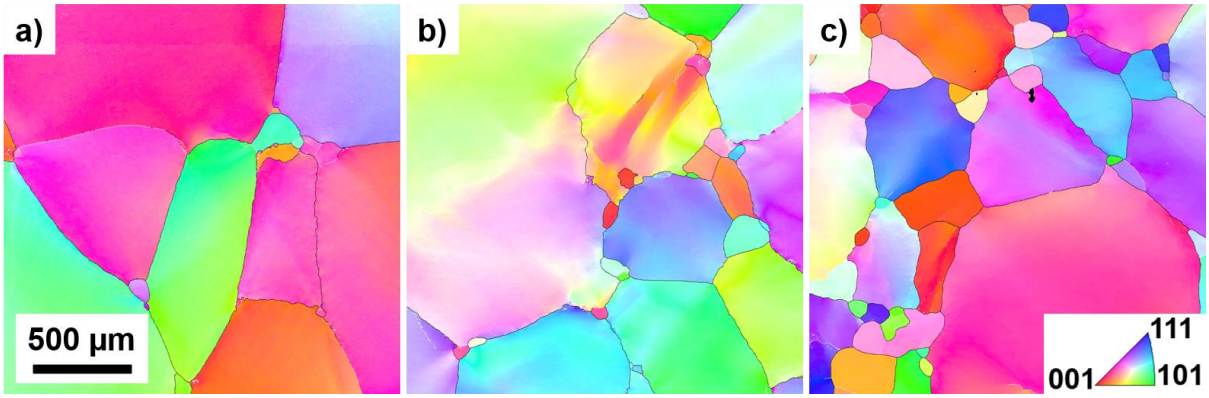

Figure 59: Inverse pole figure (IPF) maps of the β-microstructure prior to deformation for the Ti-17 annealed for 15 min at: a) 810°C; b) 850°C; c) 970°C. The α-phase is not resolved at this magnification.

11.2.2. Flow stress

Figure 60 shows the experimental and simulated flow curves at 810°C, 850°C, 930°C and 970°C. After the elastic regime, a plateau is achieved at the early stages of plastic deformation in the β-domain. Flow softening due to dynamic globularisation of the lamellar α-phase is observed in the α+β domain. The globularisation of the α-phase leads to the progressive transformation of the iso-strain load transfer regime into the iso-stress regime, causing a notable reduction of the stress withstood by the α-phase and consequently by the material. The larger volume fraction of α-phase at lower temperatures leads to a more pronounced flow softening for 810°C compared to 850°C [142].

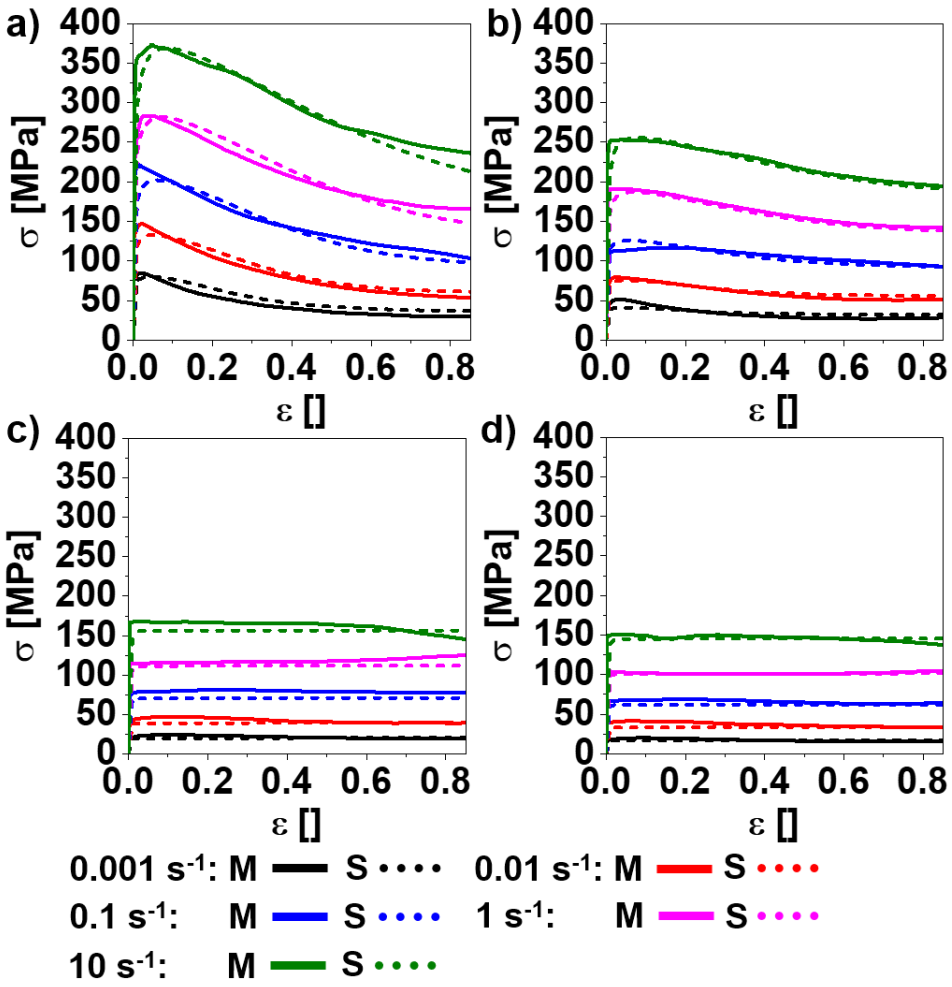

Figure 60: Measured (M) and simulated (S) flow curves: a) 810°C, b) 850°C, c) 930°C, and d) 970°C.

11.2.3. The measured microstructure of the β-phase deformed in the β-domain

Typical microstructures of the β-phase deformed in the β-domain are shown in Figure 61 for 970°C. The IPF maps (Figure 61 (a-d)), their respective grain reference orientation deviation (GROD) axis maps (Figure 61(e-h)) and KAM maps (Figure 61(k-n)) are shown for the strains of 0.25 and 0.85. The LAGBs are highlighted in white and the HAGBs in black in the IPF maps. Figure 61(a,b) reveal that LAGBs forms in a larger amount in the vicinity of the prior β-grain boundaries, while only misorientation spread is observed within the grains up to 0.25 deformation. The deformation substructure is well defined for the strain of 0.85 for 0.001 s^{-1} (Figure 61(b,f,i)), while misorientation spread within the β-grain is still pronounced for 0.1 s^{-1} (Figure 61 (d,h,n)). Although new HAGBs are formed at 0.85 strain for both strain rates, the fraction is small compared to samples deformed at 810°C [142].

The KAM maps show the organisation of the misorientation spread and the subgrain boundaries. The wave-like diffuse substructure that is observed at 0.25 strain (Figure 61m), and at 0.85 strain for 0.1 s^{-1} (Figure 61n), as highlighted by the marked areas “R1”, “R2”, and “R3”. It is attributed to the reorganisation of the dislocations into sharp walls of dislocations. Despite exhibiting a low misorientation angle, each subgrain shows a different rotation axis with respect to the parent β-grain, as shown in the GROD maps (Figure 61(e-h)) indicates that the substructure

rotates, leading to a progressive increase in boundary misorientation. Finally, the formation of a smaller substructure is evident at higher strain rates [142].

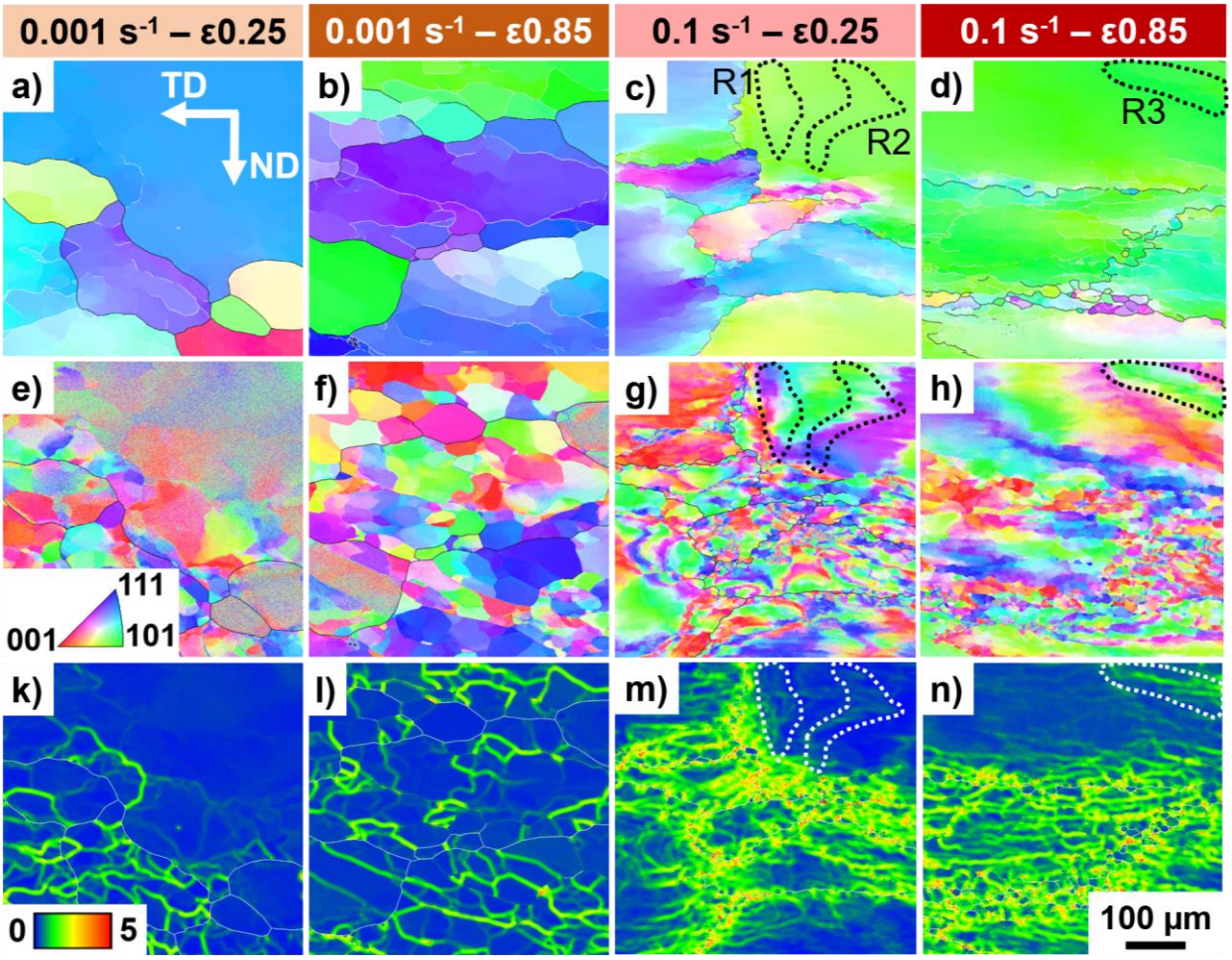

Figure 61: Inverse pole figure (IPF) maps (a-d), grain reference orientation deviation axis maps (e-h), and kernel average misorientation maps (k-n) for the deformed Ti-17 at 970°C at 0.001 s^{-1} (a,b,e,f,k,l) and 0.1 s^{-1} (c,d,g,h,m,n) up to 0.25 (a,e,k,c,g,m) and 085 (b,f,l,d,h,n) of strain, respectively. HAGBs are shown as black lines in the IPF maps and white lines in the KAM maps.

Figure 62a shows the formation of bands for the sample deformed up to 0.25 at 930°C and 10 s^{-1}. The misorientation spread within the grains “A” and “B” indicated in Figure 62b is shown in Figure 62d. The pole figure and the orientations of different regions of the band-like structure are also highlighted. Despite the formation of HAGBs in this region, the misorientation spread suggests a periodic change in the crystallographic orientation along the β-grain, forming parallel “bands” as seen in the KAM map (Figure 62c). A similar microstructural feature is observed in Figure 62(e,f).

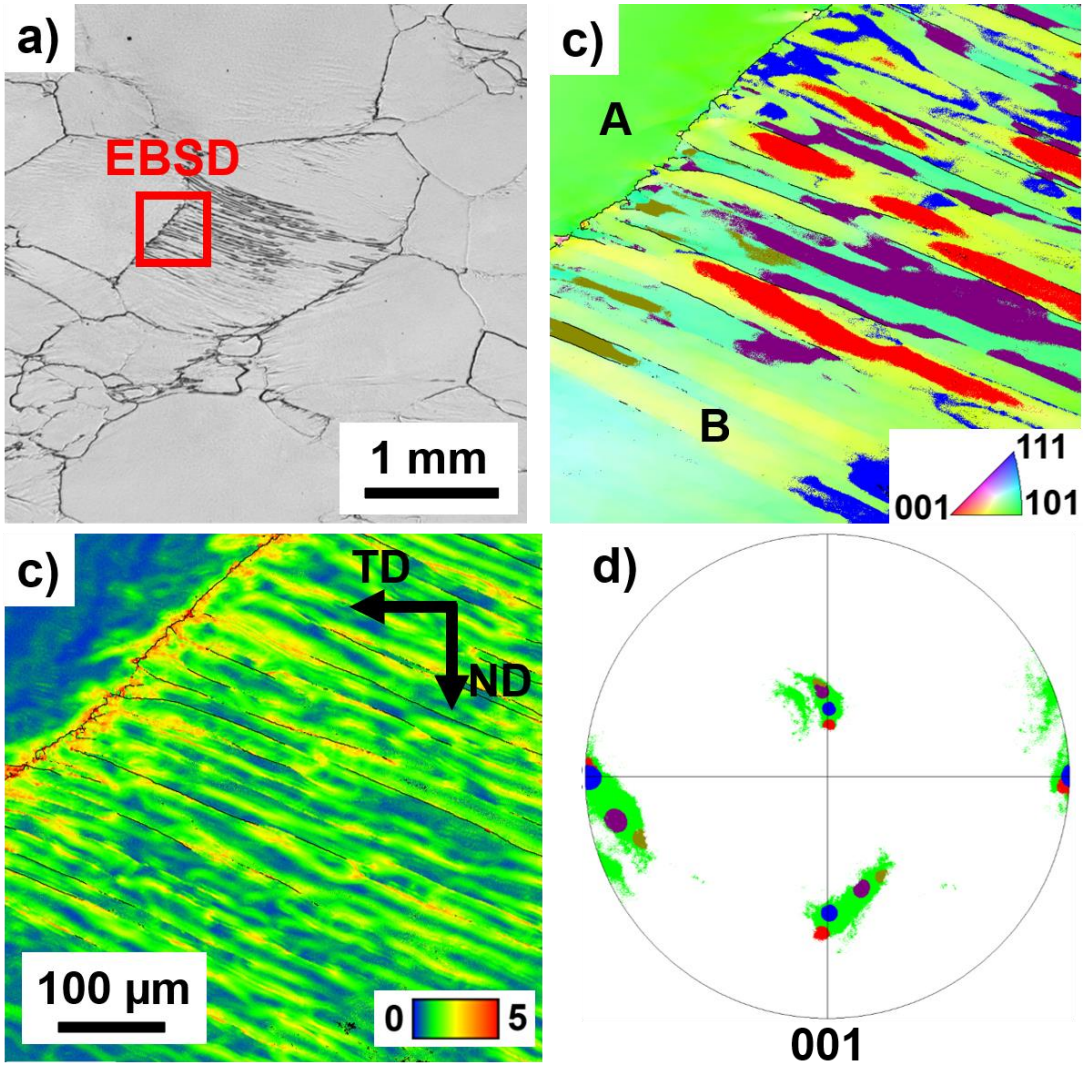

Figure 62: Microstructure of Ti-17 deformed at 930°C and 10 s^{-1} up to 0.25 of strain: a) light optical micrograph, b) Inverse pole figure map, c) kernel average misorientation map of the marked area in a). The load axis is vertical d) measured pole figure for the grains "A" and "B". Black lines indicate HAGBs.

11.2.4. Insights on β-microstructure evolution during hot compression using in-situ synchrotron radiation diffraction

The evolution of the β-phase during hot compression was investigated using synchrotron radiation diffraction during in-situ hot compression. The azimuthal-time plots for the deformation at 930°C for the strain rates of 0.001 s^{-1} and 0.01 s^{-1} are shown in Figure 63(a and b), respectively. Additionally, the in-situ hot deformation at 970°C was also performed for the strain rate of 0.001 s^{-1}, and the azimuthal-time plots are shown in Figure 63c.

Similar to the findings of Canelo-Yubero et al. in Ti-6Al-6V-2Sn [195], two main mechanisms could be distinguished: a local increase in misorientation spread highlighted by the dashed green circles, and the rotation of the crystals, highlighted by the dashed blue circles. The increase in misorientation spread occurs due to lattice rotation caused by the bending of the lattice structure, forming geometrically necessary dislocations and LAGBs [196]. Both phenomena indicate that DRV and CDRX are the major mechanisms for microstructure evolution of the β-phase, in agreement with the above-observed microstructures.

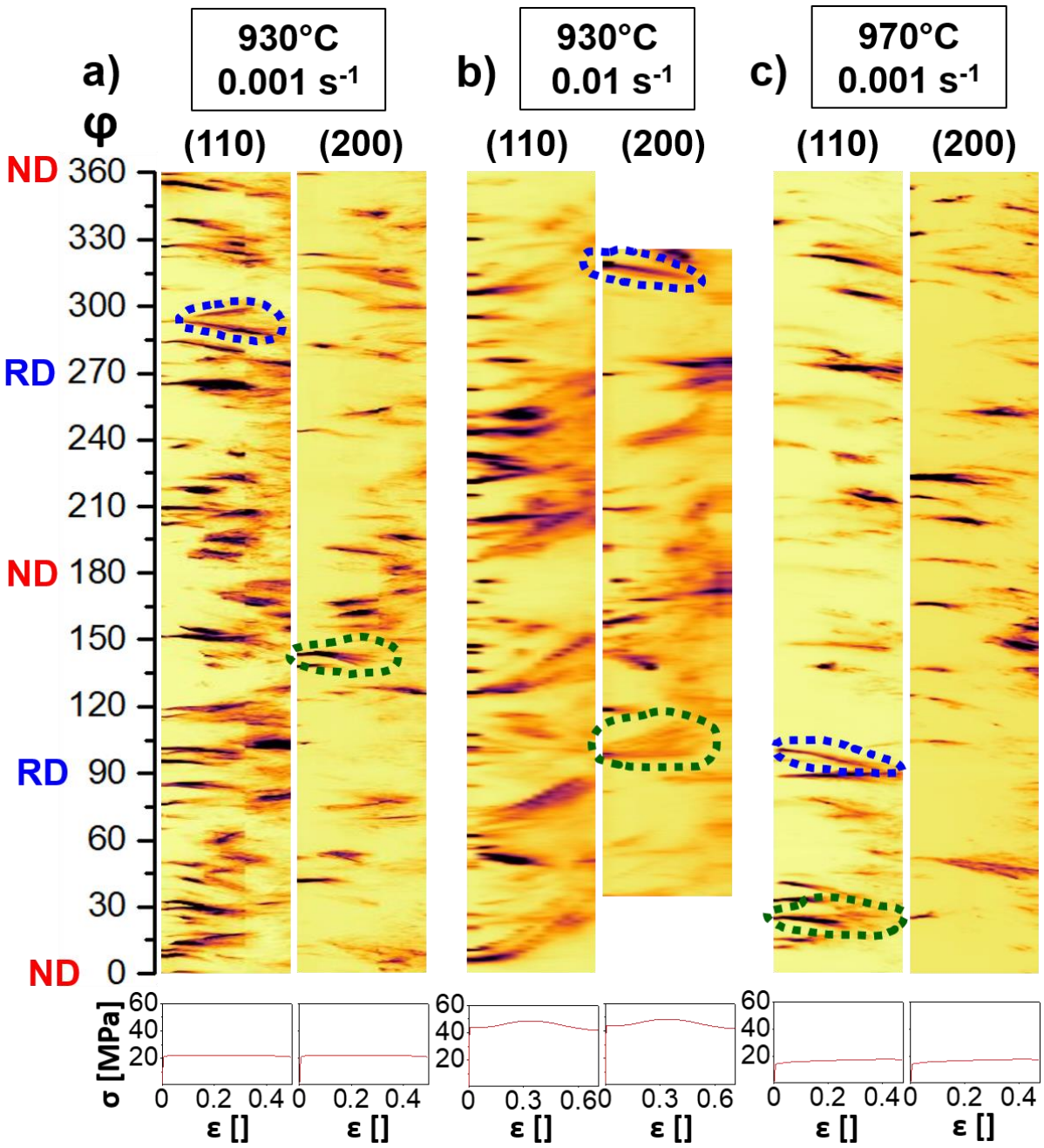

Figure 63: Azimuthal time-plots for the β-phase during deformation at: a) 930°C and 0.001 s^{-1}; b) 930°C and 0.01 s^{-1}; c) 970°C and 0.001 s^{-1}. The dashed green ellipses indicate the misorientation spread formation within the β-grains. The dashed blue ellipses indicate the subgrain rotation. ND corresponds to the load direction and TD to the radial direction.

The misorientation spread and the bending of the timelines are more pronounced at 930°C and 0.01 s^{-1} than at 930°C and 0.001 s^{-1}, suggesting a higher degree of lattice and subgrain rotation for higher strain rates, corroborate by the EBSD results, Figure 61. Furthermore, a later lattice rotation and formation of misorientation spread is observed by decreasing the strain rate. This critical strain is related to the deformation needed to form a dislocation structure within the material that is then, reorganised in sharp LAGBs for low strain rates (Figure 61(a,b,e,f,k,l)) and bands for higher strain rates (Figure 61(c,d,g,h,m,n) and Figure 62).

11.2.5. Role of the α-phase on the formation of β-substructure

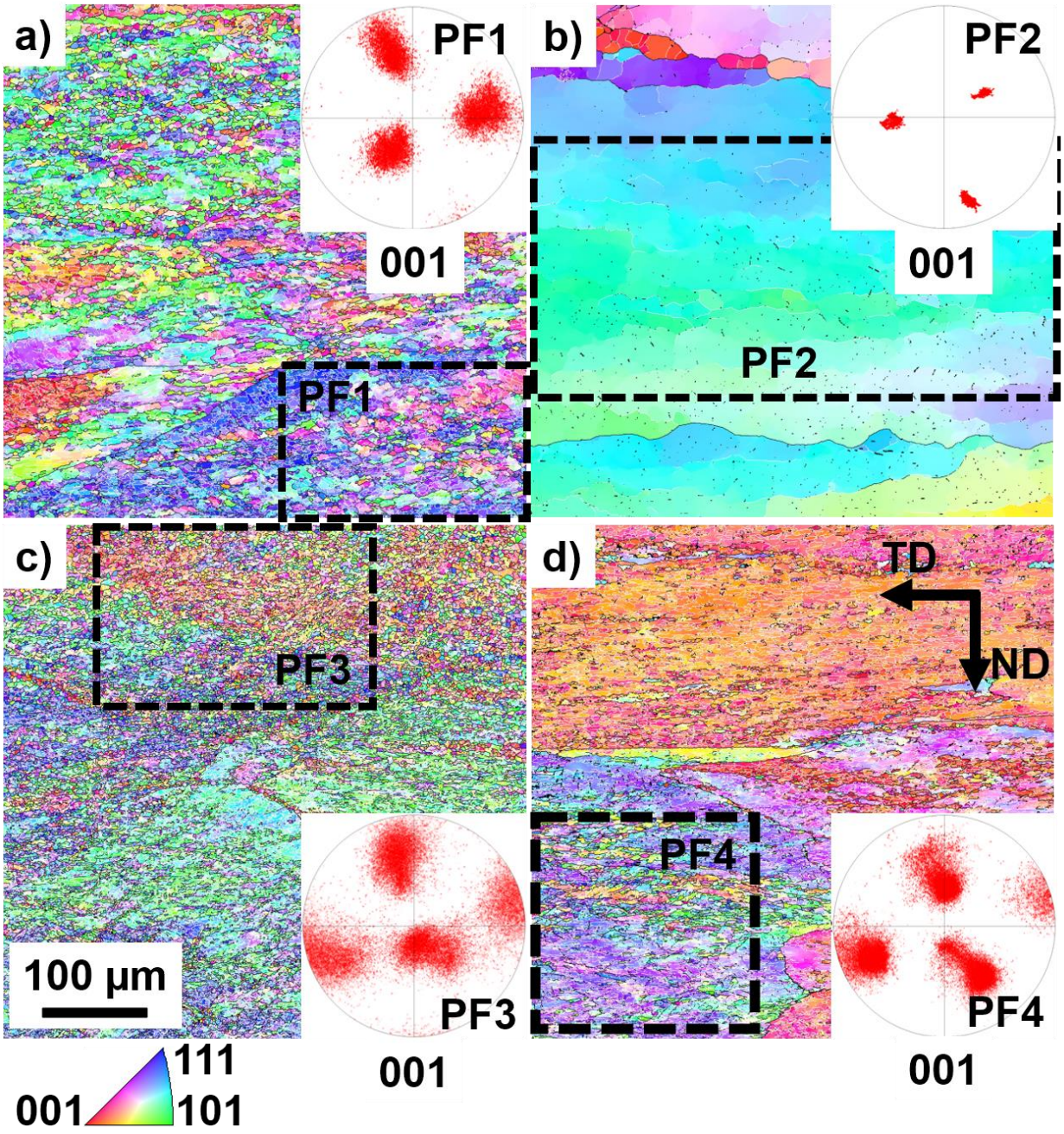

Figure 64: Inverse pole figures (IPF) maps obtained from EBSD measurements for Ti-17 deformed at: a) 810°C at 0.001 s^{-1}, b) 850°C at 0.001 s^{-1}, c) 810°C at 1 s^{-1}, d) 850°C at 1 s^{-1}. The α-phase (black spots) are embedded in the β-phase matrix. Black boundaries are HAGBs. The dashed black rectangles indicate the areas where the inserted pole figures "PF1", "PF2", "PF3" and "PF4" are measured. ND corresponds to the compression direction and TD to the transversal direction.

Figure 64 shows the typical microstructure of the β-phase after deformation up to 0.85 at 810°C (Figure 64(a,c)) and 850°C (Figure 64(b,d)) at 0.001 s^{-1} (Figure 64(a,b)) and 1 s^{-1} (Figure 64(c,d)). Fine β-substructure is observed for the temperature of 810°C for both strain rates. On the other hand, relatively large β-subgrains are observed at 850°C for 0.001s^{-1}. The dashed black rectangles indicate regions from where the inserted pole figures are calculated. In all cases, only one prior β-grain is highlighted, so the pole figure reveals the orientation spread within this grain.

A large misorientation spread is observed for the strain rate of 1 s^{-1} for both temperatures (Figure 64(c,d)). A large misorientation spread is observed for the strain rate of 0.001 s^{-1} at 810°C (Figure 64a) compared to the sample deformed at the same strain rate and 850°C (Figure 64b).

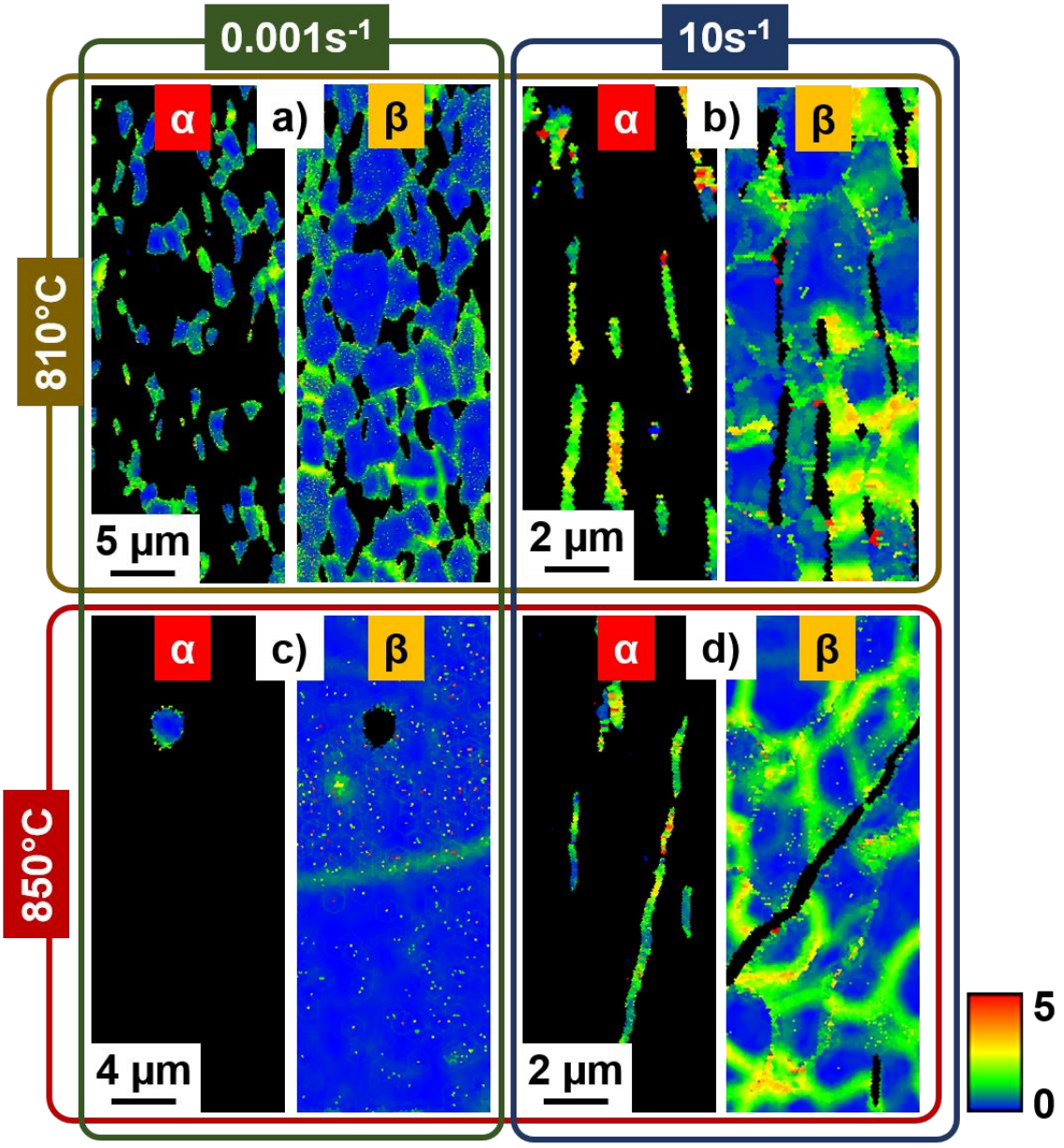

Figure 65: Inverse pole figures (IPF) (a,d,g) and kernel average misorientation (KAM) maps (b,c,e,f,h,i) of both α and β phases after deformation Ti-17 at: (a-c) 810°C at 0.001 s^{-1}, (d-f) 810°C at 10 s^{-1}, (g-i) 850°C at 10 s^{-1}.

Figure 65 shows KAM maps of both α and β phases for the Ti-17 deformed up to 0.85 at 810°C and 0.001 s^{-1} (Figure 65a) and 10 s^{-1} (Figure 65b), as well as at 850°C and 0.001 s^{-1} (Figure 65c) and 10 s^{-1} (Figure 65d). The accommodation of the plastic deformation in the α-phase occurs via rotation, as observed by Canelo-Yubero et al. [118]. Here, the KAM maps show the presence of accumulation of deformation (misorientation) near the interfaces in the α-phase and between neighbour interconnected globular grains for low strain rates (Figure 65a) as well as large misorientation values for bent-like non-globularised α-lamellas at high strain rates (Figure 65 (b,d)). The β-matrix accommodate the plastic strain via DRV followed by CDRX. The

rotation of α-phase promotes locally the β-lattice rotation, but the formed dislocations are rearranged into LAGBs instead of being accumulated at α/β interfaces.

11.2.6. Dynamic globularisation of the α-phase

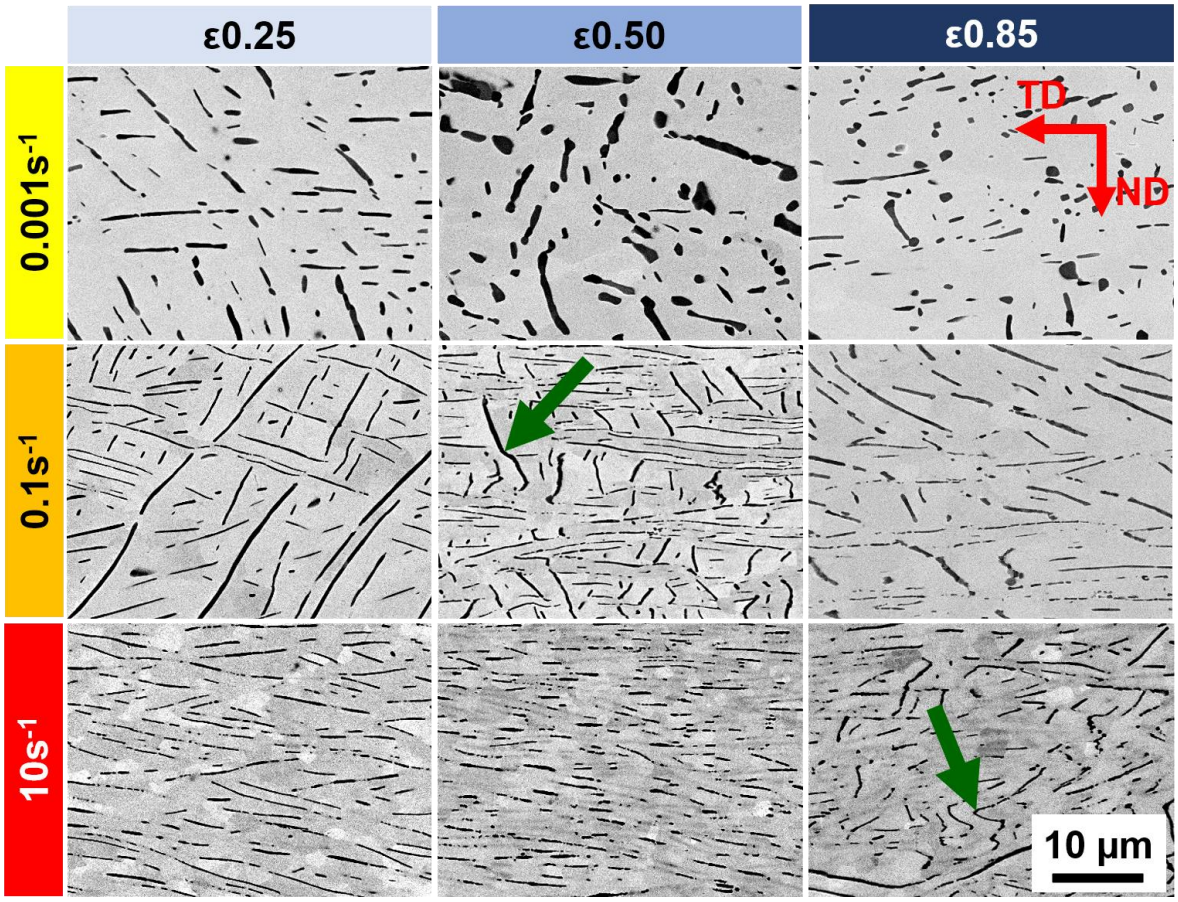

Figure 66: Backscattered electron (BSE) micrographs of the deformed Ti-17 at 830°C for the strain rates of 0.001 s^{-1}, 0.1 s^{-1} and 10 s^{-1} up to 0.25, 0.5 and 0.85 strain.

Figure 66 shows an overview of the microstructure observed after deformation at 830°C evidencing the presence of dynamic globularisation of the α-phase. The formation of isolated and relatively homogenously distributed globular-like α-phase is observed only for the strain rate of 0.001 s^{-1}. With an increase in strain, the platelets are partially transformed into globular α-phase. Moreover, the bending of the α-phase platelets is observed for the strain rates of 0.1 s^{-1} and 10 s^{-1} as indicated by the green arrows.

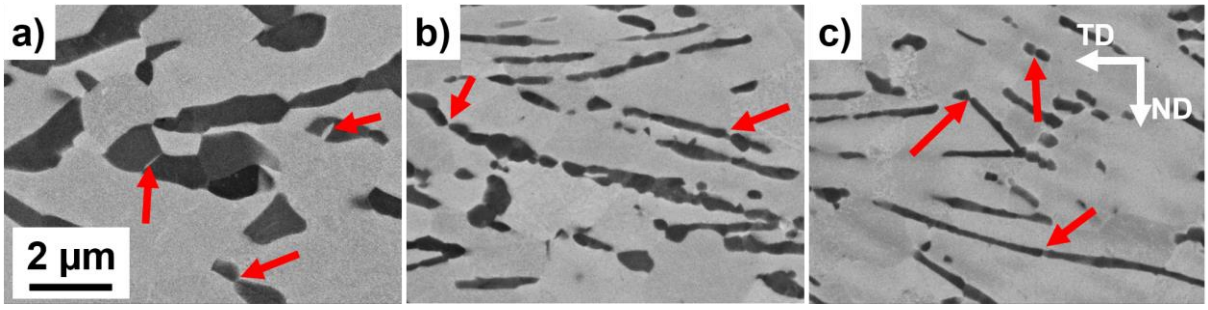

Figure 67: Detailed backscattered electron (BSE) micrographs of Ti-17 deformed at 810°C up to 0.85 strain for the strain rates of: a) 0.001 s^{-1}, b) 0.1 s^{-1}, c) 10 s^{-1}.

A detailed view of the fragmentation of the α-phase and formation of globular-like particles is shown in Figure 67. The interface between globular particles of α-phase is made by a thin layer of β-phase and is indicated by red arrows. Ti-17 deformed at 810°C for 0.001 s^{-1} (Figure 67a) shows larger α-grains, indicating coarsening.

11.2.7. Model predictions

11.2.7.1. β-phase

The simulated results for the evolutions of subgrain and grain sizes as well as the fraction of HAGBs are plotted in Figure 68(a,c) for the β-phase for the deformation in the α+β and β-domain, respectively. The investigated condition ("real") is compared to a hypothetical condition where α-phase is not present ("no α") for the deformation at 810°C in Figure 68a. A fine microstructure is achieved for both 0.001 s^{-1}, and 1 s^{-1} and a notable difference is observed between "real" and "no α", evidencing the role of α-phase in promoting cDRX and refining the microstructure in the α+β domain [142]. Despite of differences in the kinetics, the evolution behaviour of the β-phase for the Ti-17 is comparable to the one predicted for the Ti-5553 in chapters 9 and 10, i.e. a fast initial production of LAGBs followed by a progressive increment in boundary misorientation that leads to a steady-state microstructure at large strains [142]. The simulated and measured data are compared in Figure 68(e,f) for different investigated conditions. Despite the differences, especially for 850°C and 0.001 s^{-1} and 850 and 10 s^{-1}, the model depicts well the non-linear dependency of the microstructure evolution on the strain rate and temperature. The reasons for the differences are similar to the ones discussed in section 10.1.2.

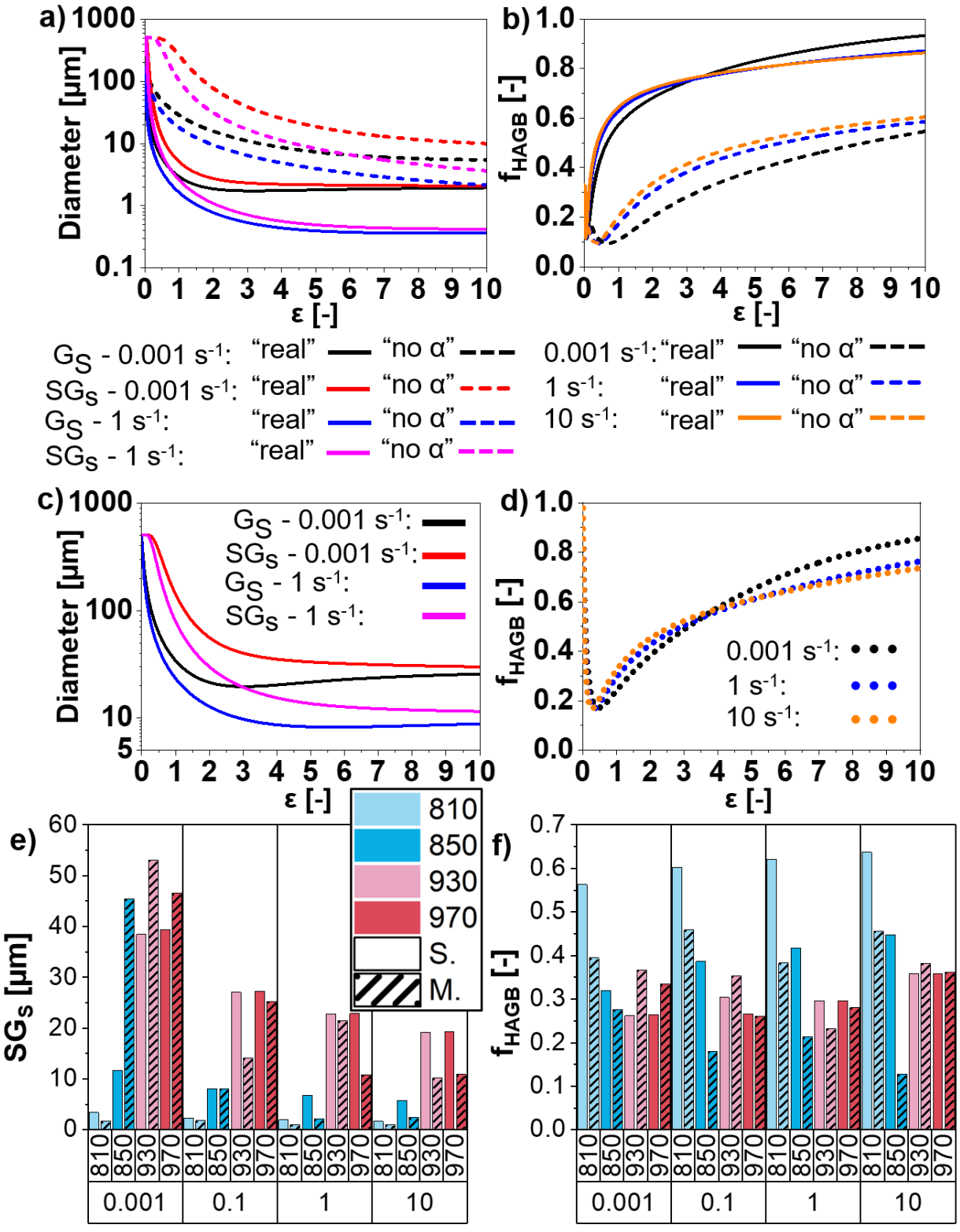

Figure 68: Simulated results for the deformation at: a,b) 810°C for the investigated condition ("real") and without the presence of α-phase ("no α") for the: a) subgrain and grain sizes; b) fraction of HAGBs; c,d) 970°C for the: c) subgrain and grain sizes; d) fraction of HAGBs. Simulated and measured results for different investigated conditions for the: e) subgrain size, f) fraction of HAGBs.

11.2.7.2. α-phase

The box-plots of the measured aspect ratio and thickness of the α-grains are compared with the predicted values in Figure 69 for the strains of 0.25 and 0.85 for the deformation at 810°C (Figure 69(a,b)) and 830°C (Figure 69(c,d)) at 0.001 s^{-1}, 0.1 s^{-1} and 10 s^{-1}. The results of deformation at 850°C exhibits similar behaviour than 830°C. The decrease in aspect ratio with the strain is pronounced for 0.001 s^{-1}. Comparable behaviour is observed for the strain rates of 0.1 s^{-1} and 10 s^{-1}. The model does not consider the decrease in thickness observed at high strain rates due to the mechanical plastic deformation. On the other hand, the increase in the α-thickness at low strain rates is slightly overestimated at 830°C. The presence of many measurement outliers and the relatively large range within 1.5IQR indicates that α-globularisation does not occur homogeneously throughout the microstructure as the model considers [142].

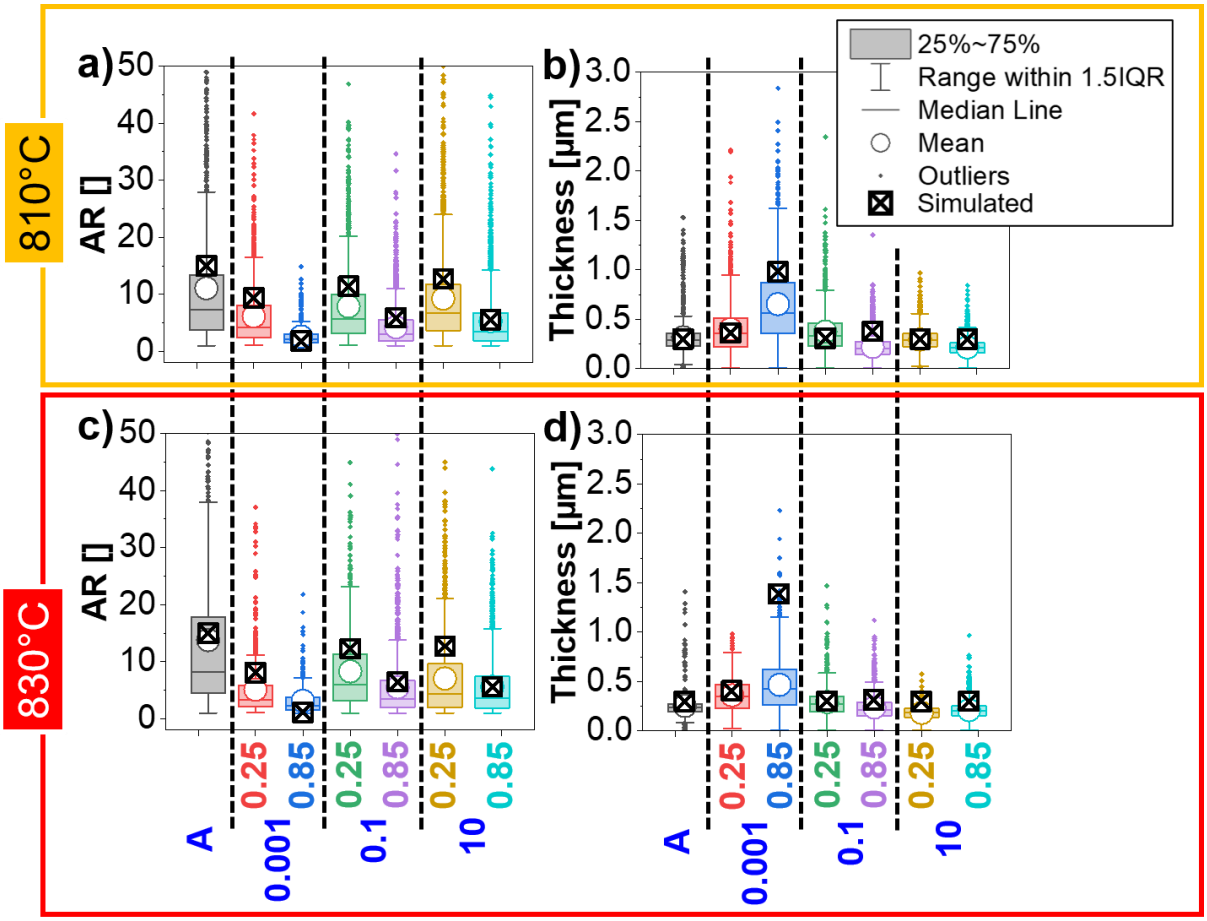

Figure 69: Measured and simulated features of α-phase for deformation at 810°C (a,b) and 830°C (c,d): a,c) aspect ratio; b,d) thickness. A indicates the annealed state before hot compression, the strain rates of 0.001 s^{-1}, 0.1 s^{-1} and 10 s^{-1} are shown for the strains of 0.25 and 0.85.

The evolution of aspect ratio is compared with measured values for interrupted tests in Figure 70a. The thickness evolution at 0.001 s^{-1} for 810°C, 830°C and 850°C is shown in Figure 70b. The initial increase at 0.25 strain is well-predicted, but the model overestimates the other values. The deviations for the predicted thickness are larger compared to the predicted aspect ratio. Figure 70(c and d) shows the measured and simulated values of aspect ratio and α-thickness, respectively.

The simulated evolution of the aspect ratio, thickness and fraction of high angle grain boundary within the α-phase is shown in Figure 71(a,b,c). An initial thickness of 0.3 µm is used as a representative thickness for the α-platelets for the investigated Ti-17. For comparison, an initial thickness of 5 µm is considered to illustrate the predictability of the model, Figure 71(d,e,f). The model predicts the formation of HAGBs within the α-platelets Figure 14(c,f) firstly as illustrated in the stages 'I', 'II' and 'V'. The formation of the α/β interfaces leads to a decrease in the aspect ratio. Additionally, the formation of the α/β interfaces leads to an increase in thickness ('II' and 'IIIB') due to α/β interfaces movement, and it occurs at lower strains by lower strain rates.

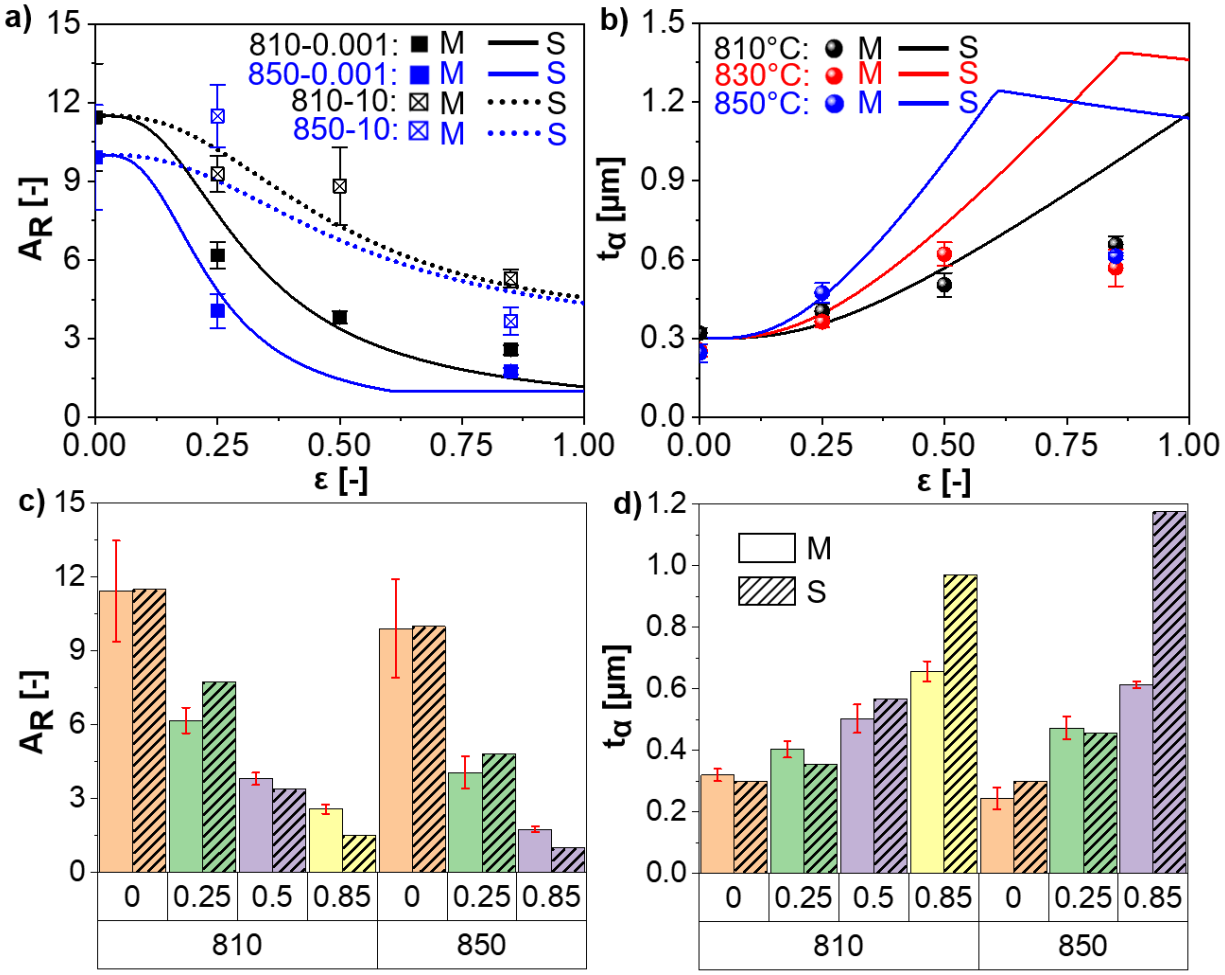

Figure 70: Comparison between measured and simulated results: a,b) aspect ratio and α-thickness evolutions, respectively; c,d) measured and simulated values of aspect ratio and α-thickness, respectively, for the strain rate of 0.001 s^{-1}.

The migration of the α/β interfaces consumes fast the formed HAGBs within α-phase for a small initial thickness of the α-platelets ('IIIA' and 'IIIB'). The globularisation fraction reaches 1 before the aspect ratio does. However, the formation of new LAGBs within α-phase and their evolution into HAGBs occurs until boundaries are not formed within α-phase [142]. If the initial thickness of α-platelet is of 5 µm, the formation of the HAGBs within α-platelet (Figure 71f) leads to its division into particles of α-phase smaller than the initial ones as illustrated in 'VI'. The aspect ratio evolves fast to 1 (Figure 71e), followed by a progressive decrease in thickness ('VII') until the steady-state is reached (Figure 71d) illustrated by 'VII'.

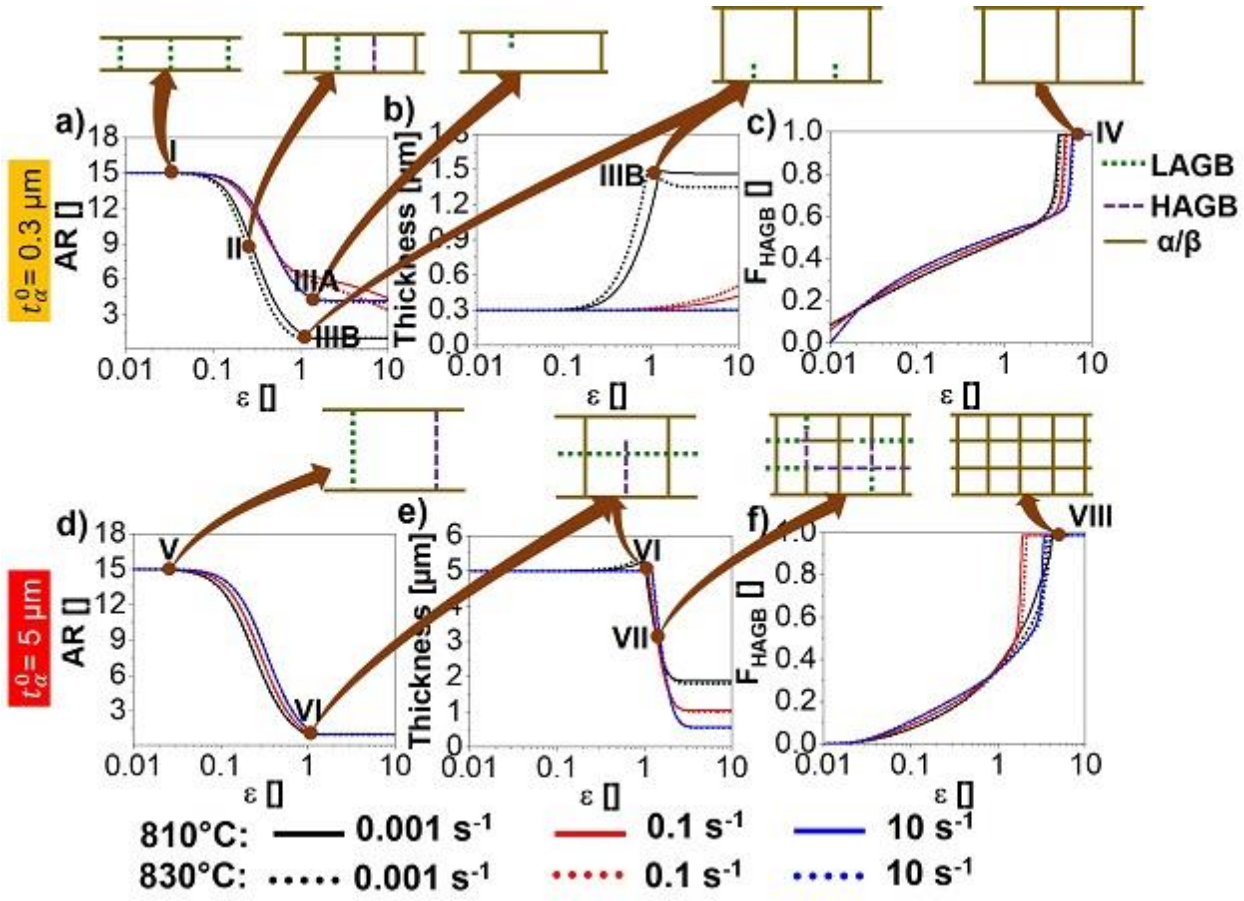

Figure 71: Simulated aspect ratio (AR) (a,d), thickness (b,e) and the fraction of HAGB in α-phase for different deformation conditions and initial thickness of α-platelet: a,b,c) 0.3 µm; d,e,f) 5 µm.

11.3. Discussion

The hot deformation of the Ti-17 with a starting lamellar microstructure was used to understand the influence of the α-phase in the stress evolution as well as in the dynamic restoration of the β-phase.

11.3.1. CDRX in the β-phase

The azimuthal-time plots (Figure 63) shows two distinct but simultaneous phenomena: subgrain rotation and misorientation spread formation [142]. Due to the lower dislocation densities achieved at lower strain rates for a given temperature and the longer time for DRV, the produced dislocations can be reorganised in sharp subgrain boundaries (Figure 61(a,b,e,f,k,l)), forming a well-established equiaxed-like substructure. On the other hand, with an increase in strain rate, the dislocation density increases, and the time for DRV decreases. Therefore, the β-phase is not able to accommodate the plastic deformation in a well-established network of LAGBs. The deformation localizes in the triple points or regions along the prior β-high angle grain boundary. This is extended to the formation of a band-like structure with large lattice rotation between band to band, leading to the formation of low and eventually new HAGBs (Figure 62). The model is limited to the mesoscopic scale. Thus, it cannot predict the localisation of deformation within the β-grains.

11.3.2. Role of the α-phase in the deformation of the β-phase

As reported in the literature, CDRX is enhanced in the β-phase deformed in the α+β domain [49]. The pole figures in Figure 64 indicate a large misorientation spread within the formed β-subgrains at large strain rates. The rotation of the α-phase [195] during dynamic globularisation increases the lattice rotation of the β-phase. The local deformation due to the rotation of the α-phase in the β-phase matrix is geometrically accommodated by the formation of new LAGBs [42], instead of a pile-up of misorientation at the α/β interfaces, as evidenced in Figure 65. This is considered in the model as an increment in the fraction of recovered dislocations that contribute to the formation of LAGBs (Equation 81).

At the lowest strain rate of 0.001 s^{-1}, the dynamic globularisation of the α-phase and the long time for DRV of the β-phase lead to the formation of a coarser and more established network of low and new HAGBs. With an increase in strain rate to 0.1 s^{-1}, the formation of isolated globular α-phase due to dynamic globularisation is limited, thus limiting the β-subgrain size to approximately the inter-lamellar spacing. With further increase in strain rate to 10 s^{-1}, the formed microstructure is smaller than the typical inter-lamellar spacing.

11.3.3. Dynamic α-globularisation

The increase in inter-diffusion due to an increase in dislocation density and pipe diffusion is indirectly present in the simplified model of the growth of the α-grains. The total globularisation of thin platelets is achieved when all the formed boundaries within the α-phase are consumed while the steady-state is reached when the aspect ratio of the formed α-particles is 1 [142] as illustrated in Figure 72. The deformation of thick α-platelets forms particles that are smaller than its initial thickness.

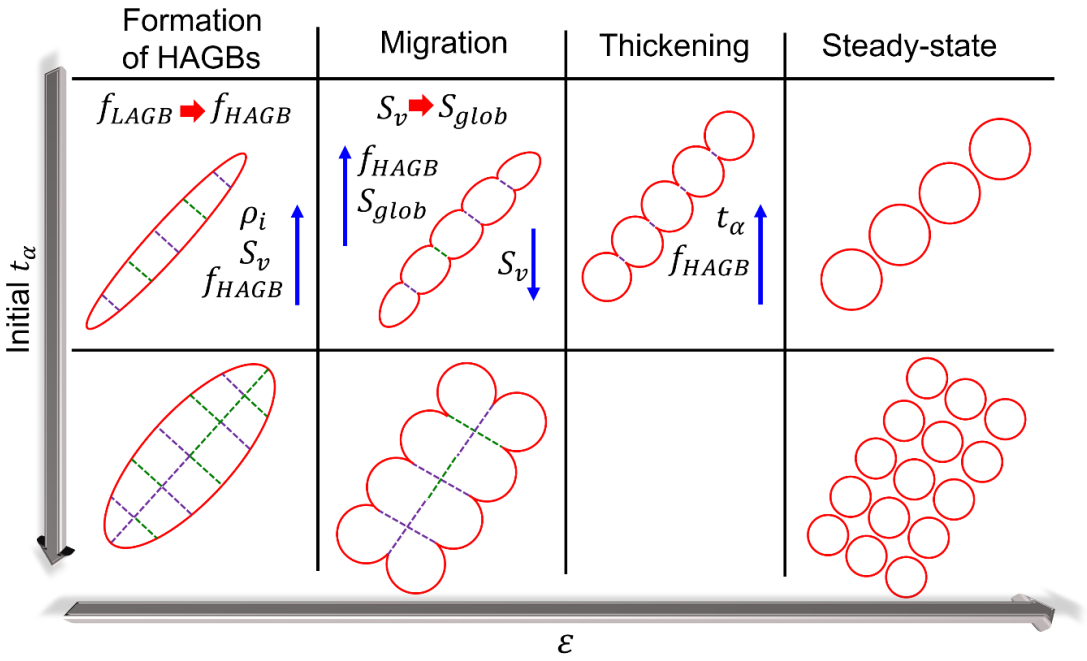

Figure 72: Evolution of the dynamic globularisation as a function of the initial thickness and strain. f_{LAGB}, f_{HAGB}, ρ_i, S_v, S_{glob}, and t_α are the fraction of LAGB, the fraction of HAGB, immobile dislocation density, boundary density, α/β interface density, and thickness of the α-phase, respectively.

11.3.4. Flow softening and load partitioning

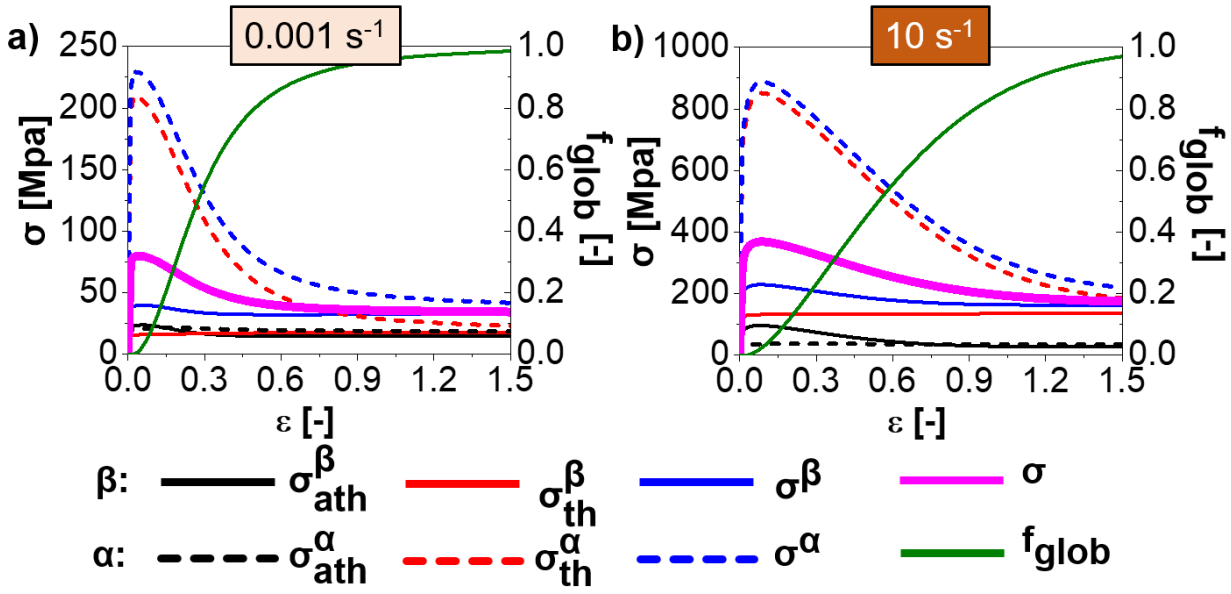

Figure 73: Simulated flow stress evolution for the Ti-17 deformed at 810°C for: a) 0.001 s^{-1}, b) 10 s^{-1}. σ^x_{ath}, σ^x_{th}, and σ^x are athermal, thermal and total stress in each phase, respectively, σ is the total stress and f_{glob} is the fraction of α-globularisation.

The flow softening observed in the α+β domain is attributed to the change in the load partitioning mechanism due to α-globularisation, as is illustrated in Figure 73. The lamellae withstand the stresses in the iso-strain regime, while a fully globularised microstructure, is under an iso-stress regime. The evolution of the thermal and athermal stresses for both phases for the strain rate of 0.001 s^{-1} (Figure 73a) and 10 s^{-1} (Figure 73b) at 810°C are shown. The fraction of globularisation is also shown for each deformation condition.

The effective strain rate and the stress of the α-phase are maximum at the beginning of the deformation, and both are minimum once the globularisation is achieved. Despite the increase in strain rate in the β-phase due to decrease of strain rate in the α-phase, the increase in the stress in the β-phase is nearly negligible in comparison to the decrease in stress in the α-phase. Thus, two main contributions for the softening behaviour can be listed [142]:

- Progressive decrease of the mobile and immobile dislocation density due to a decrease in strain rate and consumption of the formed walls of dislocation by the migration of the α/β interfaces reducing the overall athermal stress;
- A reduction of the strain rate leads to a reduction of the yield stress, and finally to a decrease in the thermal stress.

11.4. Summary

The hot compression behaviour of a Ti-17 was investigated and modelled. The complex mechanisms of dislocation reactions and the simultaneous role of DRV, CDRX, SRV and dynamic globularisation of the α-platelets as considered in the developed model, as well as dynamic globularisation of α-phase and the role of the α-morphology in the load partition. The combination of ex-situ EBSD investigations of hot compressed samples and in-situ synchrotron radiation

diffraction measurements during hot compression provide the validation of the developed model. The conclusions are shown below. The innovative aspects are highlighted in bold:

a) Conclusion from the simulations:

- **Dynamic α-globularisation can be predicted for any initial thickness and aspect ratio, and the fraction of globularisation, thickness and width of α, and the fraction of HAGBs within α-phase are calculated.**
- **Flow softening was attributed to a change in the mechanism of load transfer between α and β-phases from an iso-strain to an iso-stress condition. The dynamic globularisation of the α-phase promotes this progressive change in load transfer.**

b) Conclusions from the experiments:

- Dynamic globularisation of the α-phase is a diffusion process, and therefore more pronounced at lower strain rates and higher temperatures, resulting in thicker and more equiaxed α-phase at lower strain rates and higher temperatures.
- **α-phase increases local lattice rotation and boundary formation within the β-phase, enhancing CDRX in the β-phase in the α+β domain. Notably finer subgrains and larger fraction of HAGB are observed in the α+β domain in comparison to the β-domain for a given strain and strain rate.**
- Formation of sharp LAGBs and subgrains with negligible misorientation spread in the β-phase is only observed at low strain rates (0.001 s^{-1}). On the other hand, a band-like structure is observed at high strain rates in the β-field, due to localisation of deformation within the β-grains.

12. Mesoscale model for the static recrystallisation of Ti-17

This chapter investigates the SRX behaviour of a Ti-17 alloy using ex-situ and in-situ experiments to understand the operating mechanisms as well as to establish the recrystallisation kinetics. The results and discussions shown here were already published in [146]. This chapter strengthens the simulation results, where possible explanations for the deviation are added and the results for the dislocation densities evolution during SRX are compared to the in-situ synchrotron results.

12.1. Methodology

The microstructure of the as-deformed Ti-17 is investigated in chapter 11. Mesoscale SRX described in section 7.3 is coupled to the hot deformation model described in chapter 7.2. For simplification of the calculations, the rate equations based on the Kocks-Mecking approach described in section 7.2.6.1 were adopted for the hot deformation model. The constants and parameters used in the model are given in Appendix F.

The conditions for the performed annealing tests after hot compression using the Gleeble® device are described in section 6.5. A systematic investigation of the post-mortem annealed microstructure is performed using SEM/EBSD. Additionally, in-situ synchrotron radiation diffraction during hot compression followed by annealing was performed, as described in section 6.4.

12.2. Results

12.2.1. Static recrystallisation after isothermal treatments

The microstructures after hot deformation at 930°C and 970°C at 0.001 s^{-1} followed by annealing at each respective temperature are shown in Figure 74. The elongated and deformed β-grains are observed at 930°C up to 20 min of heat treatment. Comparable behaviour is observed for the deformation and heat treatment at 970°C. After 60 min, the isothermal heat treatment at 930°C exhibits a few large recrystallised grains. On the other hand, the deformed substructure is consumed by the formation of a recrystallised microstructure for the heat treatment at 970°C for 60 min.

The recrystallised microstructures after hot deformation at 930°C and 970°C at 0.1 s^{-1} followed by isothermal annealing are shown in the IPF maps in Figure 75. Compared to the recrystallisation behaviour after deformation at 0.001 s^{-1}, faster recrystallisation is achieved. The recrystallisation starts at prior β-grain boundaries, and the difference in recrystallisation kinetics is notable between 930°C and 970°C [146]. The presence of a near fully recrystallised microstructure is observed at 970°C after 5 min heat treatment, while it is in an intermediate stage at 930°C. A fully recrystallised microstructure is observed after 20 min at 930°C or 970°C. Slight grain coarsening is observed for 970°C after 20 min.

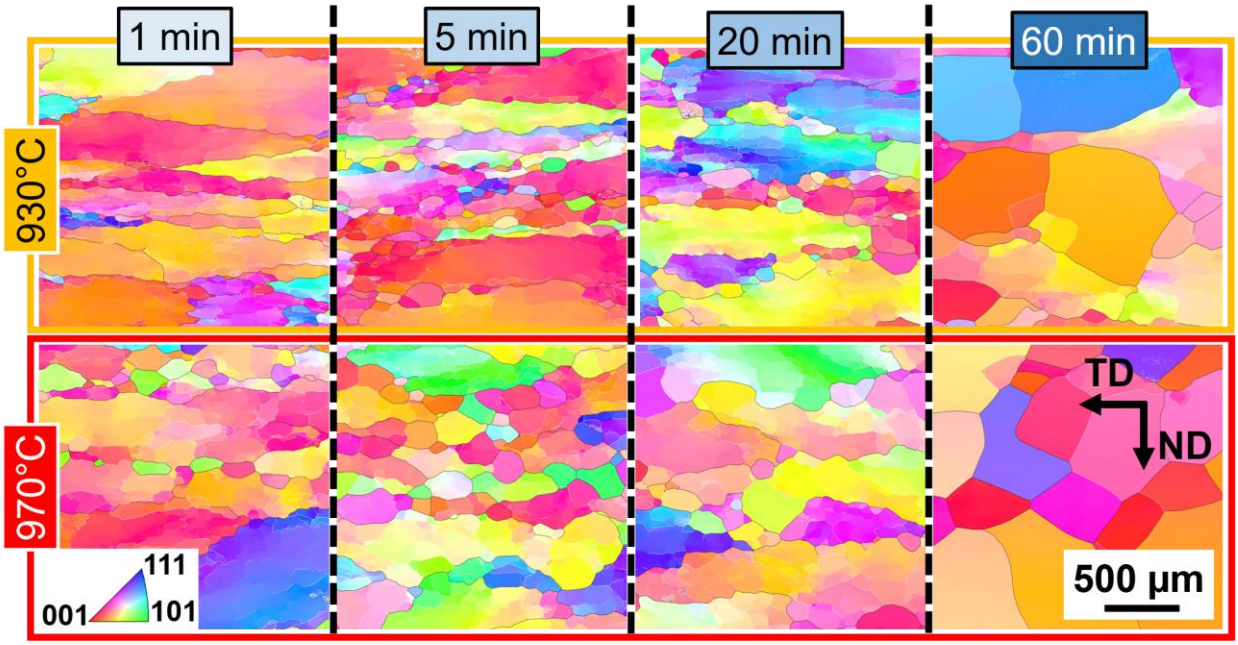

Figure 74: Inverse pole figure (IPF) maps of Ti-17 at compressed 930°C and 970°C at 0.001 s^{-1} followed by isothermal annealing at the respective deformation temperatures. The black lines indicate the HAGBs while the white ones, the LAGBs. TD and ND indicate the transversal and compression direction, respectively.

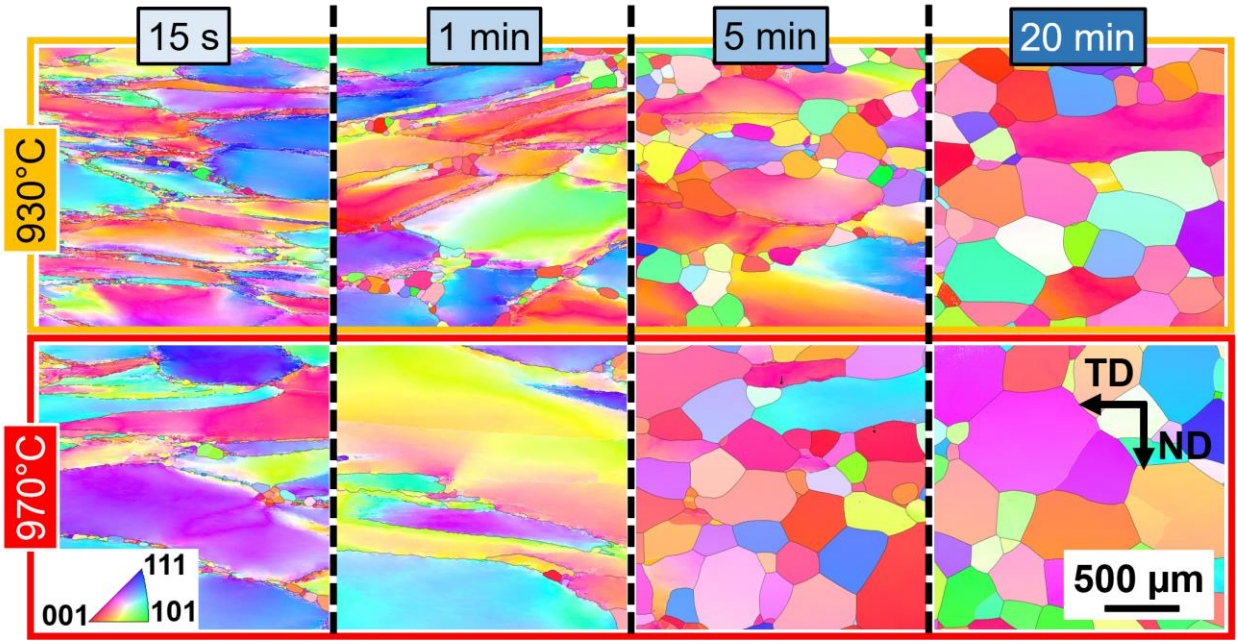

Figure 75: Inverse pole figure (IPF) maps of Ti-17 compressed at 930°C and 970°C at 0.1 s^{-1} followed by isothermal annealing at the respective deformation temperatures. The black lines indicate the HAGBs, the white ones the LAGBs.

12.2.2. Static recrystallisation during continuous cooling treatments

The microstructures of the material after hot deformation at 930°C at 0.001 s^{-1} and 0.1 s^{-1} followed by continuous cooling at 2°C/min, 5°C/min and 30°C/min and interrupted at 810°C are shown in the IPF maps in Figure 76. The recrystallised microstructure observed for the deformed Ti-17 at 0.001 s^{-1} and cooled at 2°C/min are comparable to the longer times isothermal heat treatment at 930°C after deformation at 0.001 s^{-1} in Figure 74. The recrystallisation grade is small

for the Ti-17 deformed at 0.001 s^{-1} and cooled at 30°C/min. Likewise, a few recrystallised grains are observed at 0.1 s^{-1} and cooled at 30°C/min. Thus, the faster the deformation and the higher the cooling rates, the larger the remaining stored energy [146].

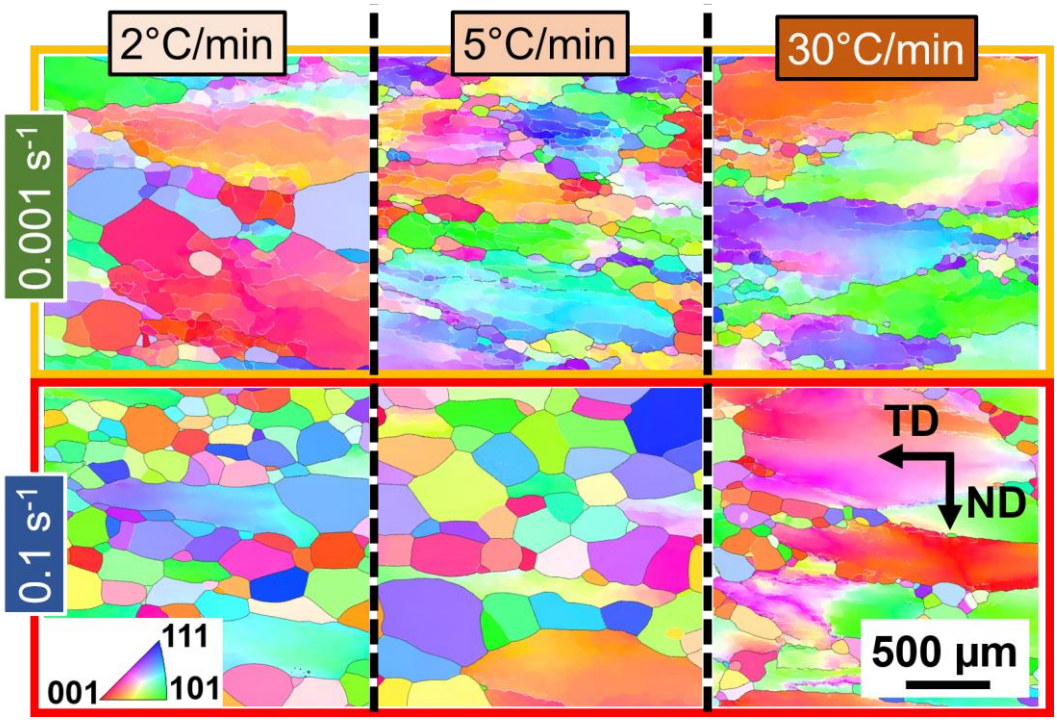

Figure 76: Inverse pole figure (IPF) maps of Ti-17 compressed at 930°C at 0.001 s^{-1} and 0.1 s^{-1} followed by continuous cooling treatments interrupted at 810°C. The black lines indicate the HAGBs, the white ones the LAGBs.

12.2.3. Insights on static recrystallisation using in-situ synchrotron radiation diffraction

Figure 77(a, b, and c) shows the results for the in-situ experiments during compression at 930°C up to 0.5 true strain at 0.001 s^{-1}, 0.1 s^{-1}, and 5 s^{-1} followed by 10 min holding at 930°C. Due to the short time of deformation in comparison to the exposure time, the deformation stage ('$\dot{\varepsilon}$') is only depicted in the time-lines in Figure 77a for 0.001 s^{-1}. A visible spreading in orientation during deformation leading to a relatively stable microstructure due to minor changes in the time-lines during holding is observed in Figure 77a for 0.001 s^{-1}. On the other hand, a progressive weakening of the time-lines is visible after deformation at 0.1 s^{-1} and 5 s^{-1} in Figure 77(b and c), respectively. The appearance of new timelines is indicated by the blue arrows, evidencing new grains nucleate during SRX for the 0.1 s^{-1} and 5 s^{-1} [146]. The blue arrows indicate the appearance of new timelines at different times. It is more pronounced up to 60 s and visible up to ~120 s. It can be correlated to the formation of the onset of SRX for the 0.1 s^{-1} and 5 s^{-1}.

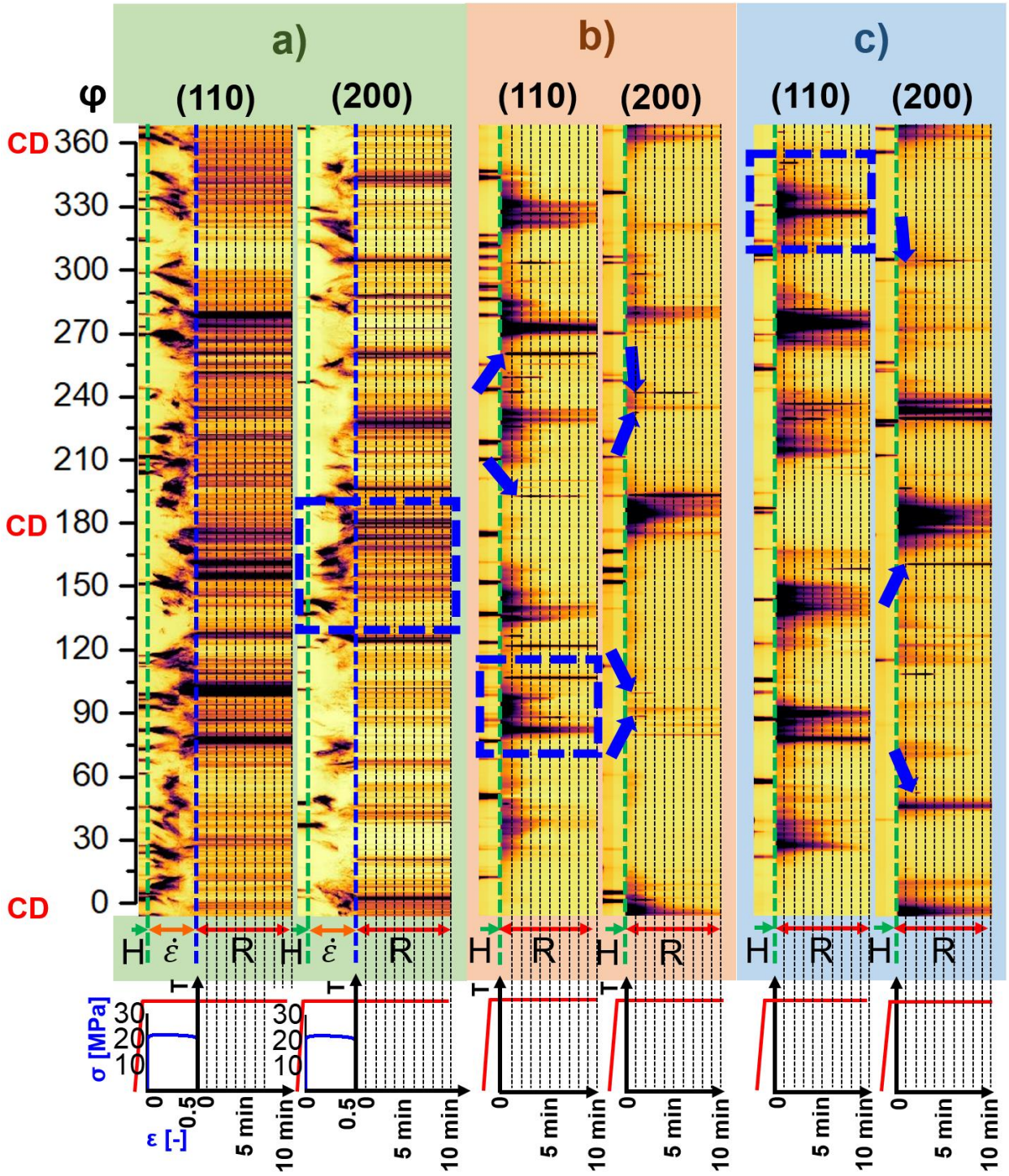

Figure 77: Azimuthal-time (AT) plots for the (110) and (200) of the in-situ synchrotron diffraction during hot compression at 930°C up to 0.5 strain for: a) 0.001 s^{-1}; b) 0.1 s^{-1}; c) 5 s^{-1}. The heating cycle, deformation, and holding are indicated by 'H', 'ε̇', and 'R', respectively. CD indicates the compression direction, and the dashed blue rectangles are shown in Figure 84. The blue arrows indicate the appearance of new grains to the illuminated volume.

Figure 78 shows the FWHM (left) and normalised interplanar distance (right) evolutions during the isothermal heat treatments for the samples deformed at 930°C with strain rates of 0.001 s^{-1} (upper) and 5 s^{-1} (bottom). The FWHM, which contains information related to the size of the coherently scattering domains and the microstrains or mean square strain $<\varepsilon^2>$, shows an

almost constant behaviour for the lower strain rate while evident variations are distinguishable for the 5 s^{-1} strain rate. Thus, SRX, in a first approach, cannot be detected for the 0.001 s^{-1} conditions for the tested holding time. Concerning the normalised interplanar distances, the 0.001 s^{-1} exhibits a constant behaviour up to the first 200 s with subsequent slight relaxation of strains, more pronounced for the plane (110). In contrast, there is a decrease of FWHM for the 5 s^{-1} strain rate during approximately the first 70 – 100 s probably as a result of both nucleation for SRX and strain relaxation [146]. It is important to remark that these evolutions must be merely seen as trends because mainly for the 5 s^{-1} strain rate, the Debye-Scherrer rings become spotty as time proceeds.

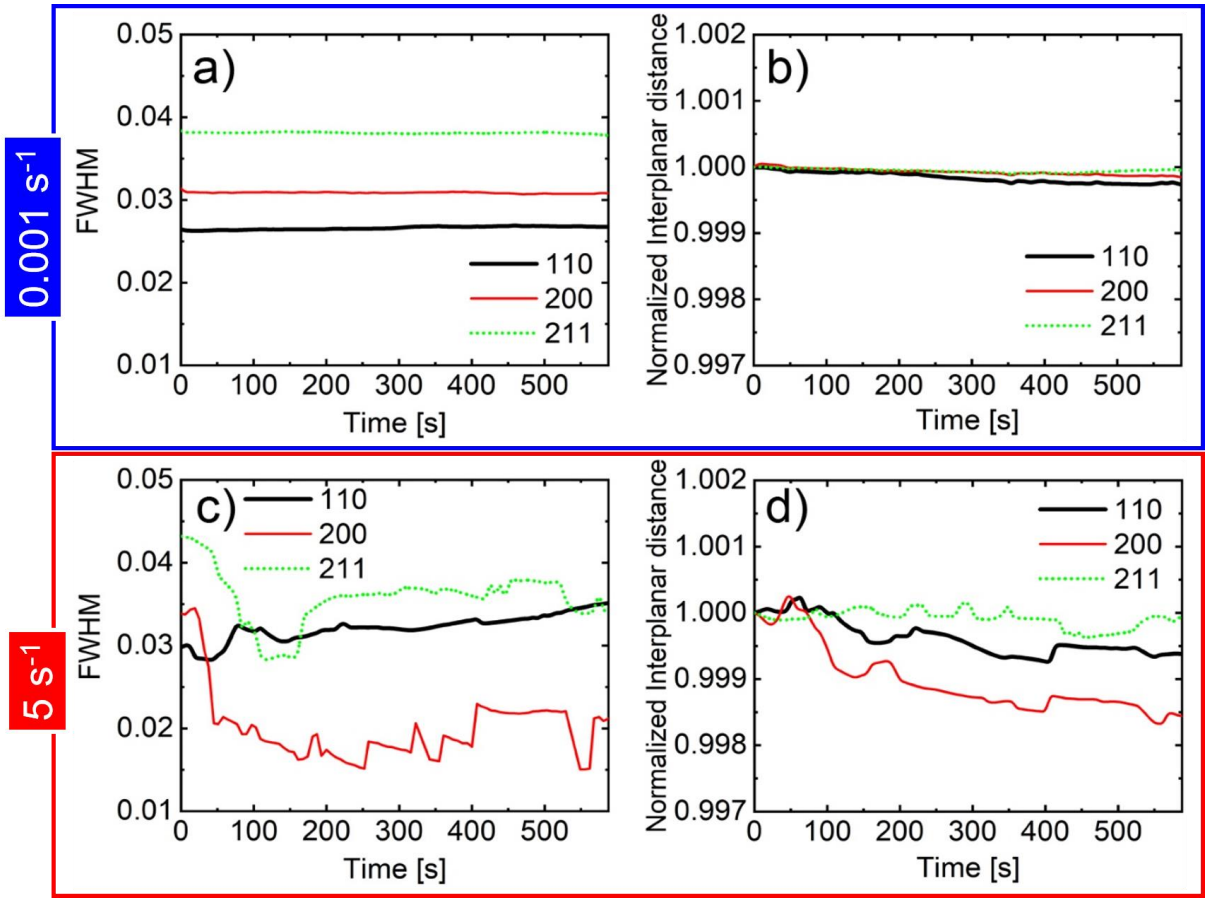

Figure 78. FWHM (left) and normalised interplanar distance (right) evolutions during the isothermal heat treatments after deformations at 0.001 s^{-1} (a and b) and 5 s^{-1} (c and d).

12.2.4. Simulation results

The measured and simulated results for the recrystallisation fraction (f_{SRX}), the SRX grain size (GS_{SRX}), the average subgrain size (SGS_{mean}) and the average grain size (GS_{mean}) are shown in Figure 79(a, b, c, and d), respectively, for the deformation for 930°C and 970°C at 0.001 s^{-1} and 0.1 s^{-1} followed by isothermal heat treatment at the same temperature. The model predicts well the recrystallisation kinetics for the isothermal heat treatments. Once the incubation time is reached, nucleation and growth are very fast, leading to a sharp increase in the recrystallisation fraction [146]. The recrystallisation kinetics is finally reduced due to the consumption of the stored energy in the form of dislocation within the β-phase. The observed inflexion of the recrystallisation curves for 0.1 s^{-1} at high recrystallisation fraction is related to the end of nucleation and decrease

in dislocation density. A slight underestimation of the simulated recrystallised grain size is observed, Figure 79b. However, the tendency with respect to the measured values is reproduced, i.e., fast initial increase leading to slower growth, and once full recrystallisation is achieved, static grain growth takes place. The overall mean subgrain and grain sizes as well predicted and exhibit a similar trend of the recrystallised grain size, Figure 79(c,d).

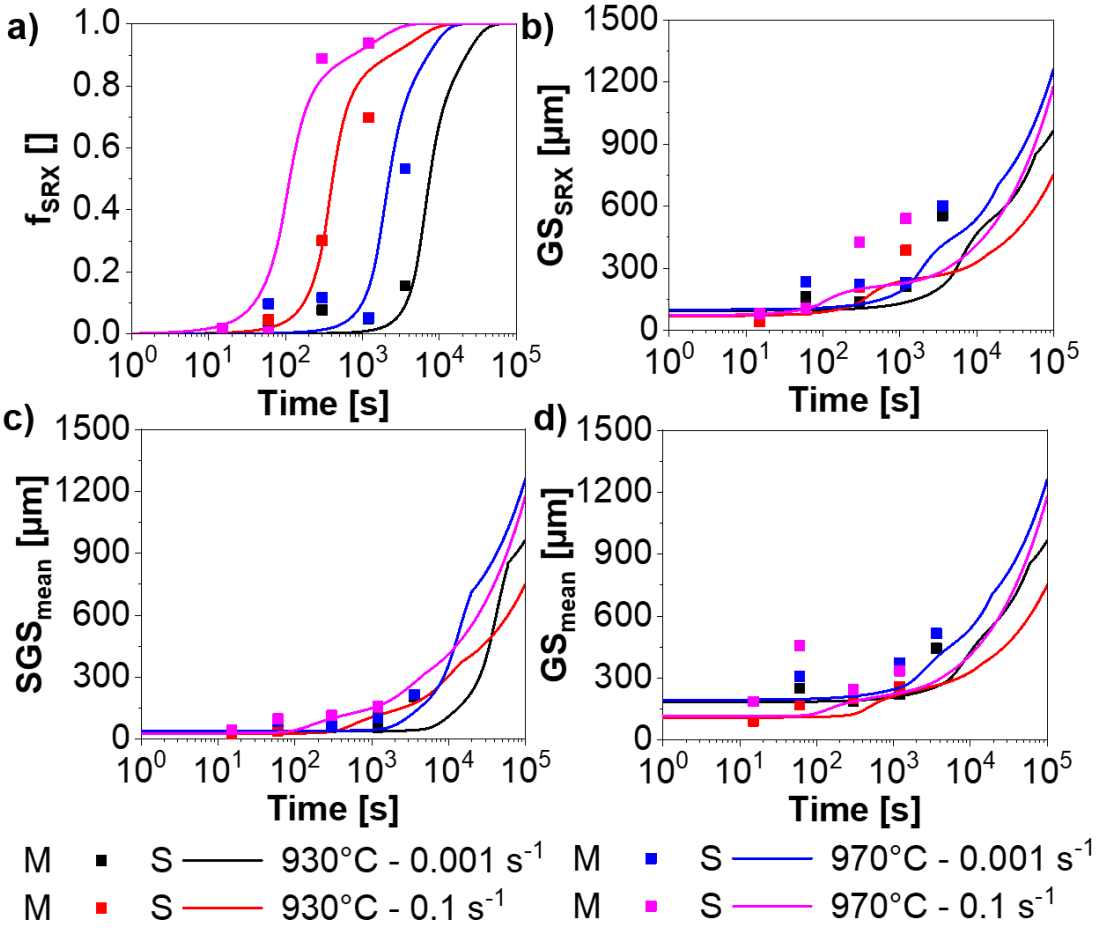

Figure 79:Simulated (S) and measured (M) results for the isothermal heat treatments: a) SRX fraction, b) mean recrystallised grain size, c) mean subgrain size, d) mean grain size.

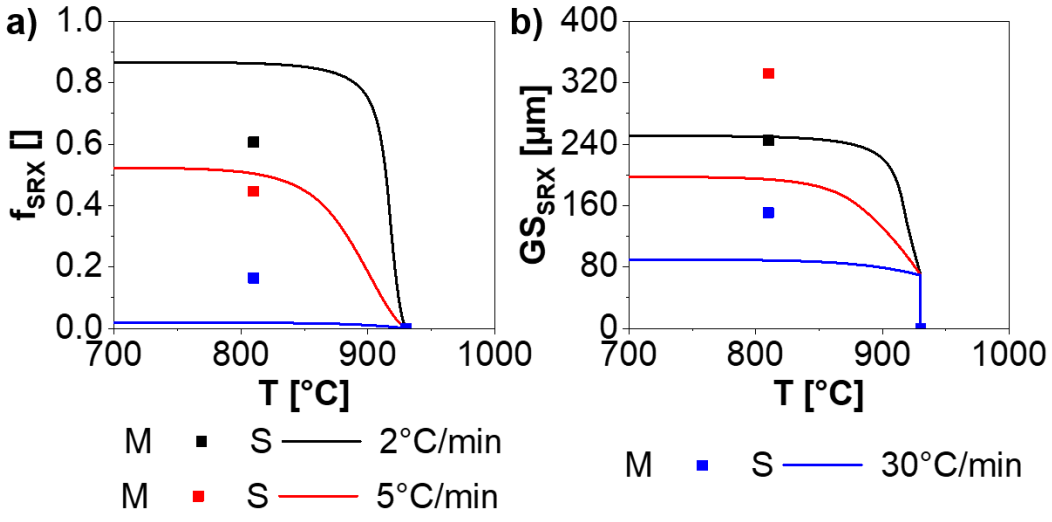

Figure 80: Simulated (S) and measured (M) results for the continuous cooling heat treatments: a) SRX fraction; b) mean recrystallised grain size.

The simulated and measured data for the continuous cooling heat treatments at 2°C, 5°C/min and 30°C/min after deformation at 970°C for 0.1 s^{-1} are shown in Figure 80. The evolution of the recrystallisation fraction is underestimated by the model at high cooling rates (30°C/min) and overestimated at slow cooling (2°C/min).

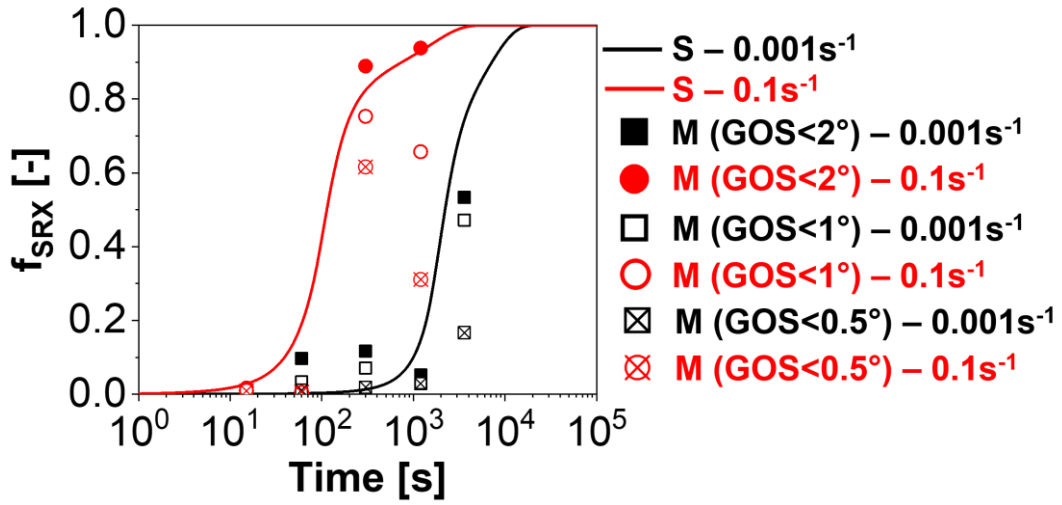

Figure 81: Simulated evolution of the fraction of recrystallisation and measured values for different maximum grain orientation spread (GOS) values defining a recrystallised grain.

The discrepancies between measured and simulated results can be attributed to:

- The relatively small measured areas compared to the initial β-grain size, resulting in low statistics. There may be a systematic error by choosing areas close to triple grain boundaries
- Both nucleation and growth of grains are dependent on the stored energy of the material and is given as a function of the dislocation density. This stored energy is adjusted with respect to the set of dislocations for the wall dislocation density (Equation 121), distributed homogeneously through the microstructure. The local experimental driving force might be higher than in the simulation leading to smaller simulated recrystallised grain sizes.
- The driving force for HAGB movement during static recrystallisation depends on several parameters that influence the difference in stored energy between neighbour grains such as the difference in normal crystallographic direction between neighbour grains [197–199] or the difference in dislocation density [200]. In the developed model, only the difference in dislocation density is considered, and the mean velocity is considered as representative for the average normal crystallographic directions.
- The maximum grain orientation spread (GOS) attributed to a recrystallised grain that is considered for the measured results is 2°. Figure 81 shows the variation of the measured fraction of recrystallisation for different maximum GOS defining a recrystallised grain.

The evolution of the internal variables of the model is shown in Figure 82 for the same conditions tested in-situ (section 11.2.2). Static recovery and consumption of the deformed β+phase by the recrystallised grains explains the sharp decrease in dislocation density [146], reaching their minimum value when full recrystallisation is achieved, Figure 82a. The velocity of the HAGBs formed during SRX (V_{SIBM}, Figure 82b) decreases with the decrease

dislocation density of the deformed material due to static recovery and consumption of the deformed region (X_{def}). On the other hand, the velocity for grain growth (V_{GG-SRX} and $V_{GG-NON\ SRX}$, Figure 82b) is nearly constant at the early stages and progressively decreases with the static grain growth after longer holding times, Figure 82b.

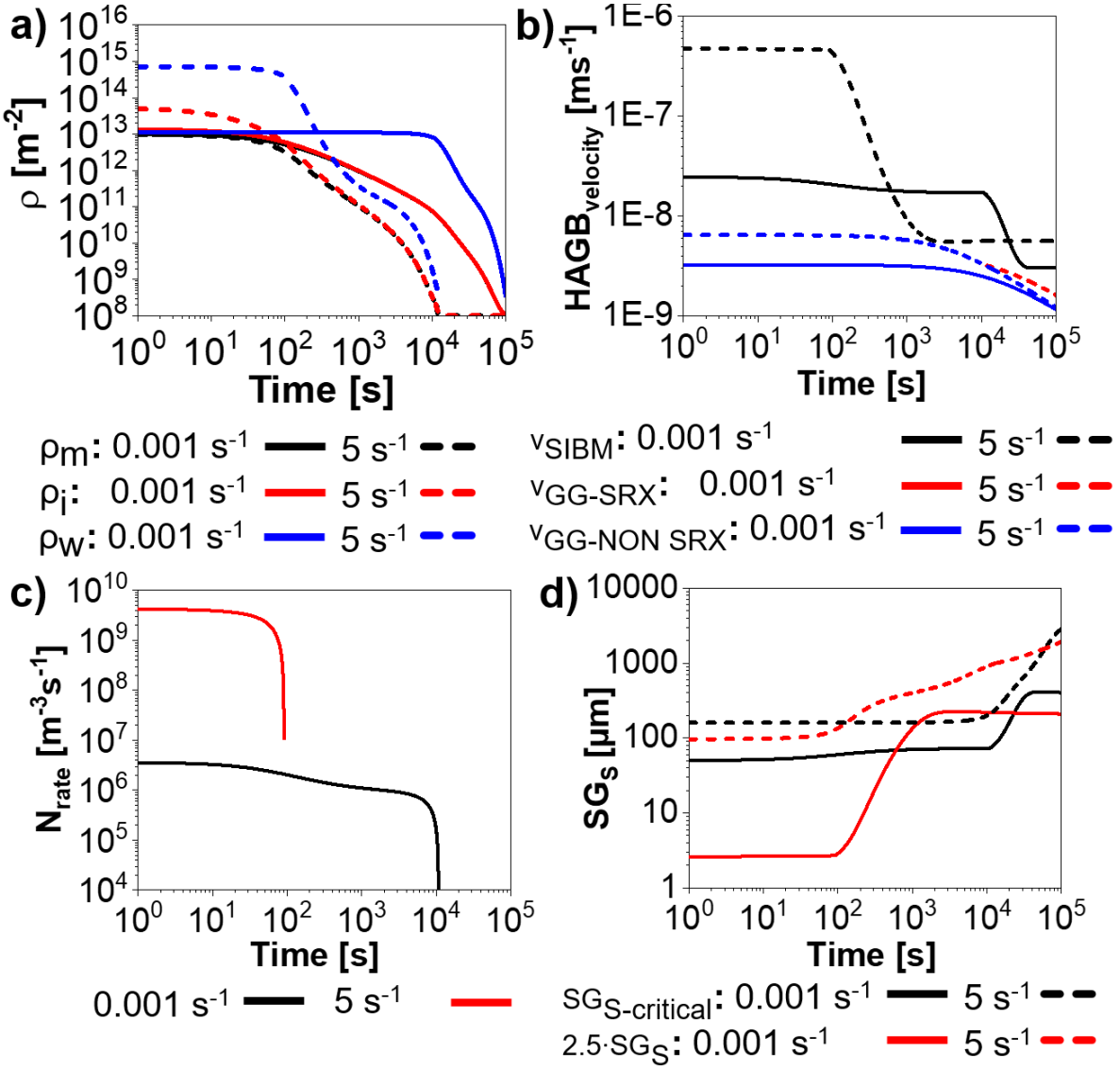

Figure 82: Simulated results for the isothermal heat treatments at 930°C after hot compression at 0.001 s^{-1} and 5 s^{-1} up to strain of 0.5: a) mobile (ρ_m), immobile (ρ_i) and wall (ρ_w) dislocation densities; b) HAGB velocity for the recrystallised grains (V_{SIBM}), static grain growth of the recrystallised grains (V_{GG-SRX}), and static grain growth of the deformed grains ($V_{GG-NON-SRX}$); c) nucleation rate; d) critical and maximum (2.5x the mean value) subgrain sizes.

The nucleation rate (Figure 82c), given by Equation 125, is maximum at the beginning of the treatment and decreased with a decrease in stored energy by consumption of the deformed region, Equation 120. Once X_{def} = 0, the nucleation is finished, and only growth of the formed grains occurs. The nucleation time of ~200 s for deformation at 930°C and 5 s^{-1} inferred in Figure 78(b,d) is well depicted in the simulations, that predict a fast consumption of dislocation after ~150 s (Figure 82a). The evolution of the critical subgrain size and the maximum subgrain size (2.5x the mean subgrain size) is shown in Figure 82d. The critical subgrain size is minimum at the

beginning of deformation and smaller than the simulated required subgrain size for nucleation [146]. Thus, the incubation time is not related the time required for subgrain coarsening until the critical subgrain size is achieved but to the low number of formed nuclei formed for the investigated conditions at the early stages of SRX. Once the number of SRX grains increases, the recrystallisation fraction becomes notable, and the stored energy for SIBM reduces notably, increasing the minimum subgrain size sharply for nucleation.

12.3. Discussion

A physically-based model to predict the hot deformation of a Ti-17 alloy is coupled with a physically-based model for the SRX behaviour using the same internal variables. Nucleation occurs via bulging of the formed subgrains during hot deformation, and its growth is driven by the stored energy due to dislocations.

12.3.1. SIBM

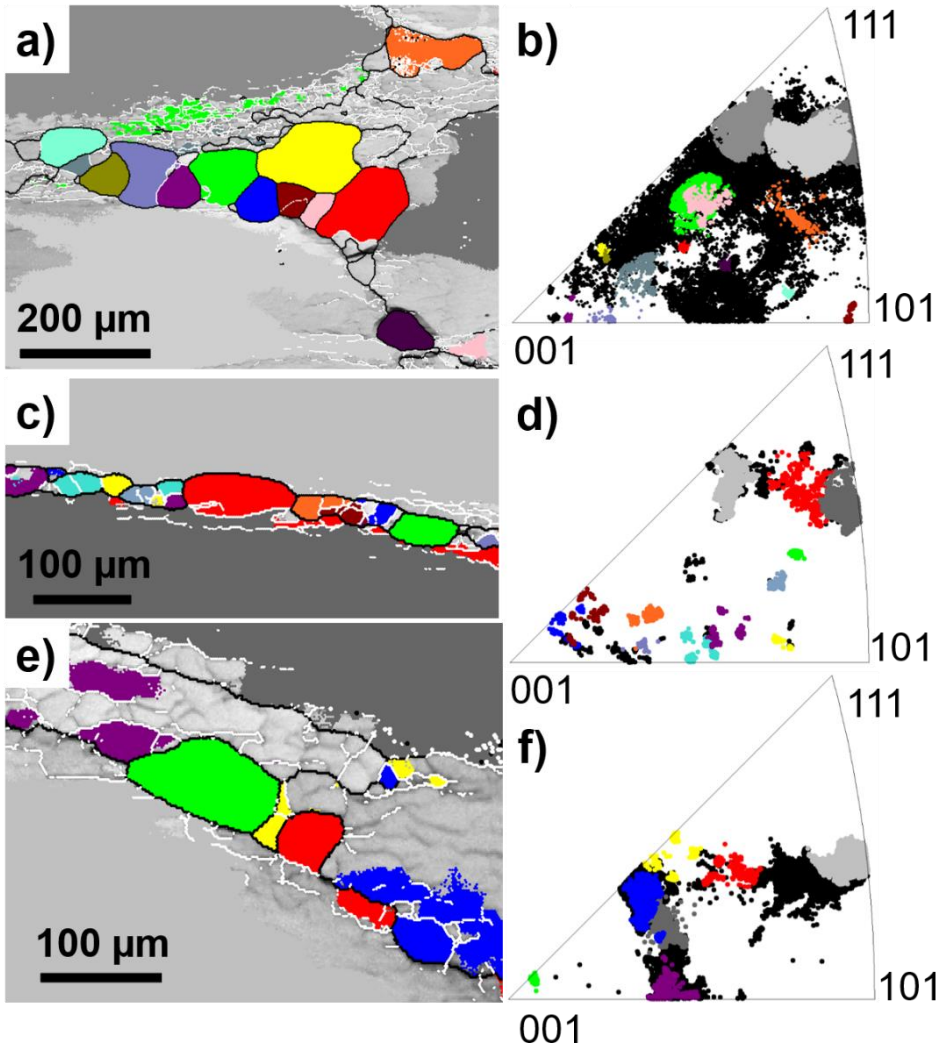

Figure 83: Highlighted maps with an image quality (IQ) background (a,c,e) and measured inverse pole figures (b,d,f) for Ti-17 isothermally heat-treated after deformation at 0.1 s^{-1}: a,b) annealing at 930°C for 1 min; c,d) annealing at 970°C for 15 s; e,f) annealing at 970°C for 1 min. The grains were highlighted with a misorientation spread of 5°. White and black boundaries indicate LAGBs and HAGBs, respectively.

DRV forms a substructure within the β-grains accompanied by continuous lattice rotation between the adjacent subgrains leading to the progressive transformation of LAGBs into HAGBs. The subgrains formed during hot deformation are the active nuclei for bulging by SIBM during SRX.

Figure 83((a,b), (c,d), and (e,f)) show grew nuclei in advanced condition after isothermal heat treatments at 930°C for 1 min, 970°C for 15 s, and 970°C for 1 min, respectively. As expected, [121] there is a large misorientation between the formed subgrain and the deformed β-grains [146]. The different highlighted subgrains indicate the ones with different boundary misorientations with respect to the deformed β-grain are observed in Figure 83(a,b), highlighted in grey as well as corresponding to the non-highlighted regions (black regions in Figure 83b). The inverse pole figures in Figure 83(b,d,f) indicate that the formed recrystallised grains belong to the dispersion in orientation spread formed due to plastic deformation in the vicinity of the prior β-HAGBs with a high orientation axis deviation with respect to the deformed parent grains.

Figure 84 shows a magnified view of the dashed blue rectangles in Figure 77. The formed timelines during deformation at 0.001 s^{-1} are not modified during holding for 10 min at 930°C, a, which it indicates the microstructure was fully preserved during the isothermal heat treatment. Eventual static recovery and subgrain growth do not cause a visible modification of the grains in the azimuthal position φ. On the other hand, the onset of SRX during isothermal treatment modifies the grain structure of the Ti-17 deformed at higher strain rates (Figure 84(b,c)). The appearance of new spots during the holding stage for the 0.1 s^{-1} and 5 s^{-1} is indicated by the blue arrows. They suggest the formation of recrystallised grains during the first seconds of the heat treatment [146]. The formation of new recrystallised grains is correlated to the existence of a nucleation rate with finite incubation time. The disappearance of some spots, indicated by the white arrows, is related to grain coarsening. Nucleation via SIBM and growth of the formed nuclei reduces misorientation of the parent microstructure. Thus, sharper regions (or bands) are progressively formed as indicated by the dashed white lines in Figure 84. Similar findings are also reported for a Ti-64 alloy [148].

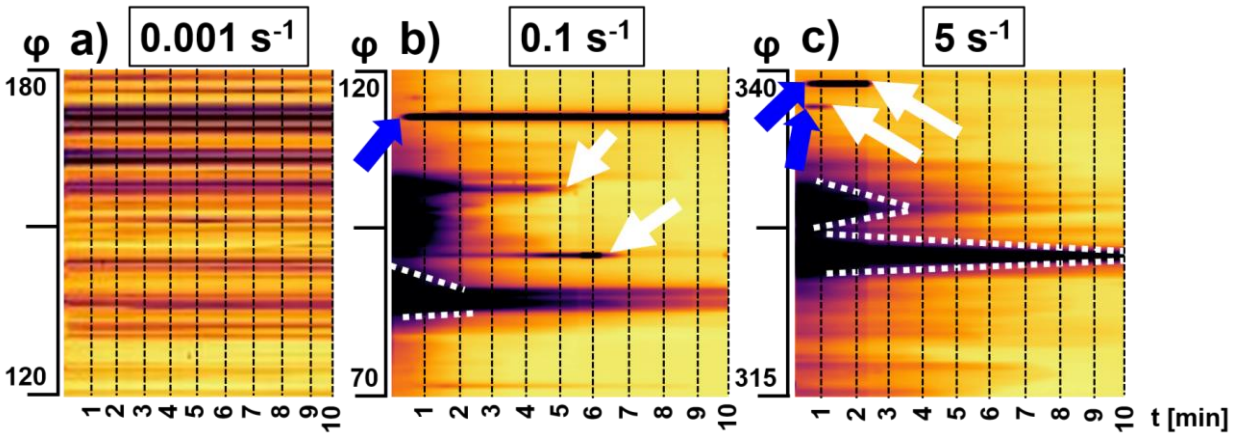

Figure 84: Highlighted areas in Figure 77 of the azimuthal-time (AT) plots of the in-situ synchrotron diffraction tests during and after compression at 930°C up to 0.5 of true strain for: a) 0.001 s^{-1}; b) 0.1 s^{-1}; c) 5 s^{-1}. The white arrows indicate the disappearance of timelines, while the dashed white lines, the decrease in orientation spread.

Despite the variation in the FWHM due to dislocation changes (mostly by decreasing the ρ_m and ρ_i, Figure 82a), the fact that no strain relaxation is observed can be ascribed to the larger population of wall dislocations that only relaxes when the nucleated grains grow up. Thus, the time of the end of nucleation is ~70-100 s as inferred from the evaluation of the normalised interplanar distances (Figure 78d). The end of nucleation is larger for higher deformation temperatures and lower strain rates.

12.3.2. Role of prior deformation condition and heterogeneous deformation of the β-phase

The main drawback of the proposed mesoscale model for microstructure evolution is the non-predictability of the heterogeneity of deformation within a β-grain and between β-grains [146]. To overcome this issue, an empirical correction of the number of aligned dislocations forming a wall of dislocations is proposed for the calculation of the wall dislocation density, Equation 122. Moreover, the nucleation is assumed to occur only in a limited volume of deformed material (X_{def}) to compensate for the heterogeneous distribution of the wall of dislocations. Figure 85 shows the kernel average misorientation (KAM) maps of the isothermal heat treatments at 930°C for the holding times of 15 s (Figure 85a), 1 min (Figure 85b), 5 min (Figure 85c), and 20 min (Figure 85d). Nucleation starts in regions with high KAM (Figure 85(a,b)) and that the recrystallised grain grows consuming the existing region with high KAM (Figure 85c). Once these regions are consumed, the stored energy for further growth decreases, slowing the recrystallisation, as shown in Figure 85d.

This issue has been addressed in the literature [121,201] as a deviation for the homogeneous nucleation. For the investigated Ti-17 alloy, the nucleation is relatively homogenous when compared to the difference in stored energy at the beginning and in a later stage of recrystallisation [146]. Therefore, the JMAK model can still be used (Equation 128) for calculation of the SRX fraction, and the corrections in nucleation rate and stored energy aim to incorporate in a simple way the effect of the heterogeneous deformation within a large β-grain. The measured Avrami exponents are shown in Table 6.

Table 6: Measured Avrami coefficients

Avrami coefficients		
	930°C	970°C
0.001 s^{-1}	0.41 ± 0.18	0.51 ± 0.16
0.1 s^{-1}	1.15 ± 0.10	1.51 ± 0.66

Low values for the Avrami exponent are related to grain boundary surface nucleation, while large values can be associated with grain corner nucleation [201]. The change in stored energy modified the nucleation mechanism. Larger strain rates provoke higher stored energy for a given strain and temperature, resulting in initial nucleation at grain edges. With the development of the recrystallised structure, the nucleation mechanism changes towards grain boundary surface nucleation.

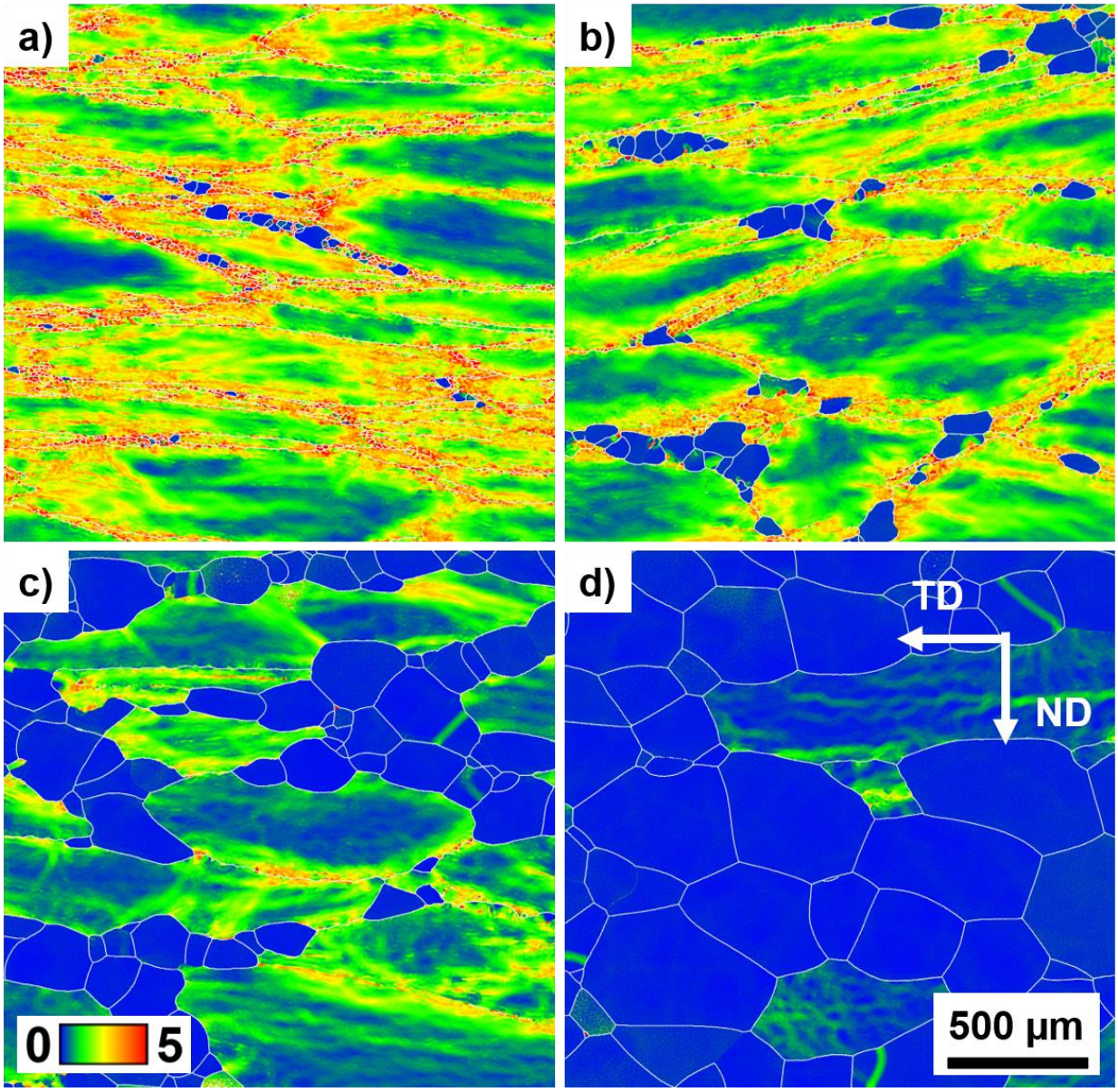

Figure 85: Kernel average misorientation (KAM) maps for Ti-17 deformed at 930°C at 0.1 s^{-1} followed by isothermal annealing at 930°C for: a) 15 s; b) 1 min; c) 5 min; d) 20 min. The white lines indicate the HAGBs.

12.4. Summary

The isothermal and continuous cooling heat treatments after the hot deformation of a Ti-17 alloy were investigated after the deformation in the β-domain. The recrystallisation kinetics was obtained by systematic ex-situ experiments. In-situ synchrotron radiation diffraction during hot compression shed lights on the recrystallisation mechanisms. A simple mesoscale model that couples the hot deformation and the SRX behaviours is proposed. The phenomena of DRV and CDRX are considered as restoration mechanisms during hot deformation. At the same time, static recovery, nucleation, and growth via strain-induced boundary migration and grain growth are regarded as restoration mechanisms during annealing. The conclusions are subdivided accordingly, and the new ones with respect to the literature are highlighted in bold:

a) Conclusions from the simulations:

- Ti-17 deformed at higher strain rates leads to higher nucleation rate and thus, to faster recrystallisation kinetics.

b) General conclusions:

- Higher strain rates produce smaller subgrains as well as higher stored energy, and the deformation within the β-grain is more heterogeneous.
- A nucleation time is needed and evidenced by the ex-situ and in-situ experiments, and the process of SRX is attributed to occur via strain induced boundary migration.
- **The stored energy reached within the tested conditions was insufficient for grain refinement due to the low nucleation rate.**

13. Discussion on the predictability of the models

This chapter aims to discuss the performance of the models even beyond the experimental validation conditions. The results obtained for each model are related to the initial microstructure and processing parameters, aiming to describe the predicted overall behaviour. These maps can be used to tailor microstructures as a function of local processing parameters and initial microstructures.

13.1. Phase transformation in Ti-6Al-4V

The phase transformation of β→α+β was modelled using the exact diffusion equations. The current model does not allow the prediction of interaction of complex supersaturation fields, nor the prediction of irregularities on the shape of the formed particles of α-phase. Despite the limitations, it is novel on the prediction for the formation of three investigated morphologies of α-phase: α_P, α_{GB}, α_{SEC}. The mean diameter of α_P, the mean thickness of α_{GB} and α_{SEC}, as well as the fraction of each morphology, are the outputs of the model. The contour maps for the evolution of the fraction of α_P, α_{GB}, α_{SEC}, as well as the diameter of α_P and the thickness of α_{GB} and α_{SEC} are shown in Figure 86 as a function of the cooling rate and the size of α_P immediately before cooling (α_P^0).

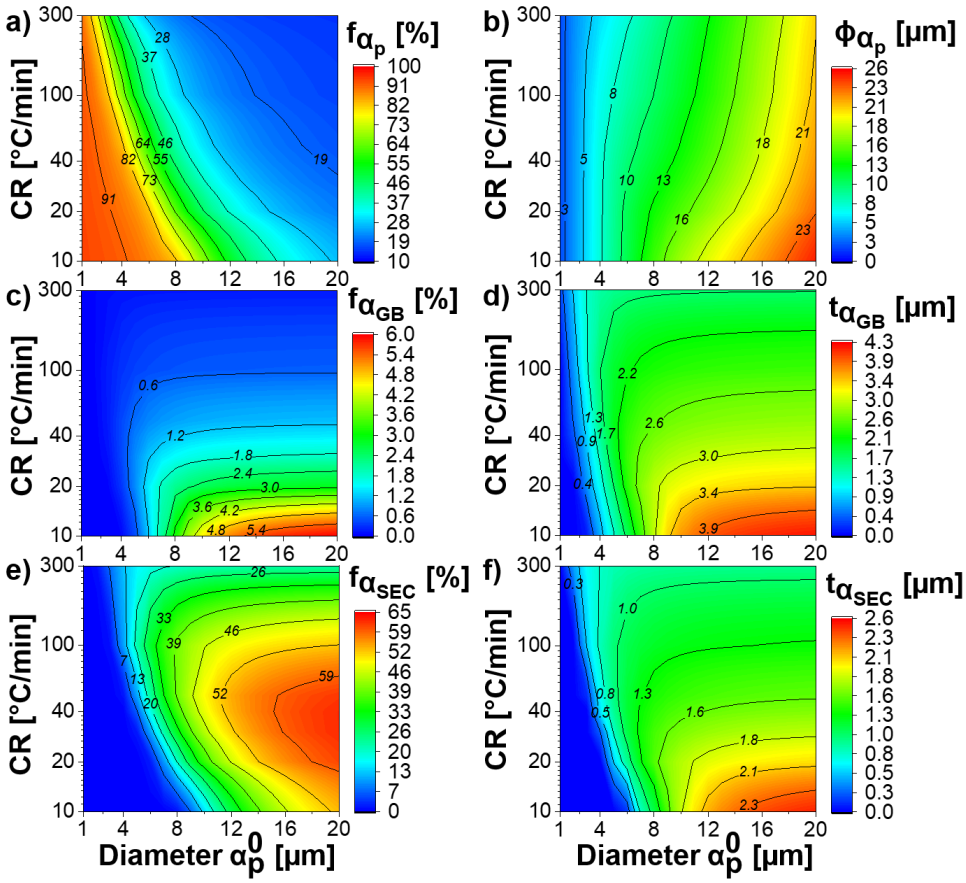

Figure 86: Contour maps for the phase transformation model for the Ti-6Al-4V as a function of the cooling rate and size of α_P immediately before cooling (α_P^0): a) fraction of α_P, b) mean diameter of α_P, c) fraction of α_{GB}, d) mean thickness of α_{GB} e) fraction of α_{SEC}, f) mean diameter of α_{SEC}.

Small sizes of α_P^0 promote the fast growth of α_P, and inhibits the formation of α_{GB} and α_{SEC}. The increment of the volume of a small sphere during diffusion occurs faster than that of a larger sphere since its growth is inversely proportional to its radius (Equation 5). The fraction of α_P is a cubic function of the radius of the α_P (Equation 9). Therefore, large α_P^0 growths slower, promoting supersaturation of V in the matrix, and the nucleation and growth of α_{SEC} and α_{GB}. Figure 86 (a,b) shows that for initial sizes of α_P smaller than ~4 μm, only growth of α_P occurs. For the cooling rate of 40°C/min, the fraction of α_P can vary from 82% up to 37% for the initial primary α-phase size of 5 μm and 9 μm, respectively. Therefore, strict microstructure control is challenging for this range of α_P. A small variation in the initial microstructure or a slight difference in cooling rate can promote the formation of a different microstructure.

Figure 86(c,d) shows that the predicted fraction of α_{GB} is larger than 3% only for cooling rates lower than 20°C/min and for initial α_P sizes larger than 10 μm. The increase in cooling rate leads to a decrease in α_{GB} thickness and fraction. This relationship is nearly independent on the initial α_P size for α_P sizes larger than 14 μm. Figure 86(e,f) shows that the predicted fraction of α_{SEC} exhibits a maximum, and its peak is a function of the initial α_P size and cooling rate. Larger initial α_P promotes the formation of a larger fraction of α_{SEC} for a given cooling rate. The cooling rate that leads to the maximum formed fraction of α_{SEC} decreases with increase in initial α_P size. The reduction in the formed fraction of α_{SEC} with an increase in cooling rate is related to the lack of time for nucleation. It leads to larger remaining β-phase. In practice, it is related to the formation of α'.

13.2. Hot deformation behaviour

A CDRX-based model for hot deformation was developed to predict the evolution of the mean microstructural features of the material, i.e. the grain size, subgrain size and fraction of HAGB. In this chapter, the model used in chapter 112 is discussed: CDRX is coupled with a model for the rate equations of dislocation reactions based on Ghoniem's rate equations (described in 7.2.6.2). The Mackenzie and Rayleigh distributions are coupled to the CDRX model to simulate a fully recrystallised and a recovered microstructure, respectively. The novel model can start with any initial microstructure and consider the already existing HAGBs and can be extrapolated up to large strains.

13.2.1. Influence of the initial microstructure

The initial β-grain size, the initial ratio between low and high angle grain boundaries and the initial thickness of α-phase are correlated to the evolution of the microstructural features. Here, the results presented in chapter 112 are extrapolated for any starting microstructure. The interpretation and discussion of the results that are shown here were already published in [141,142]. As described in those chapters, deviations between the predicted and measured microstructure are found. Small subgrain sizes can lead to deviations because the present model neglected mobility of the LAGBs. Moreover, the formation of deformation bands at high strain rates, as shown in chapters 9 and 11 will result in larger deviations the large the initial grain size. Finally, the prediction of the influence of the α-phase is strongly influenced by the mathematical approaches of the globularisation evolution on the aspect ratio ("2D" or "3D cases"), and on the empirical calculations of the α/β interface velocity and growth velocity.

13.2.1.1. Initial β-grain size

Figure 87 shows the evolution of the wall dislocation density as a function of the initial β-grain size and the strain. A maximum of wall dislocation density is reached, corresponding to the maximum product between low angle grain boundary density and low angle grain boundary average misorientation, Equation 41.

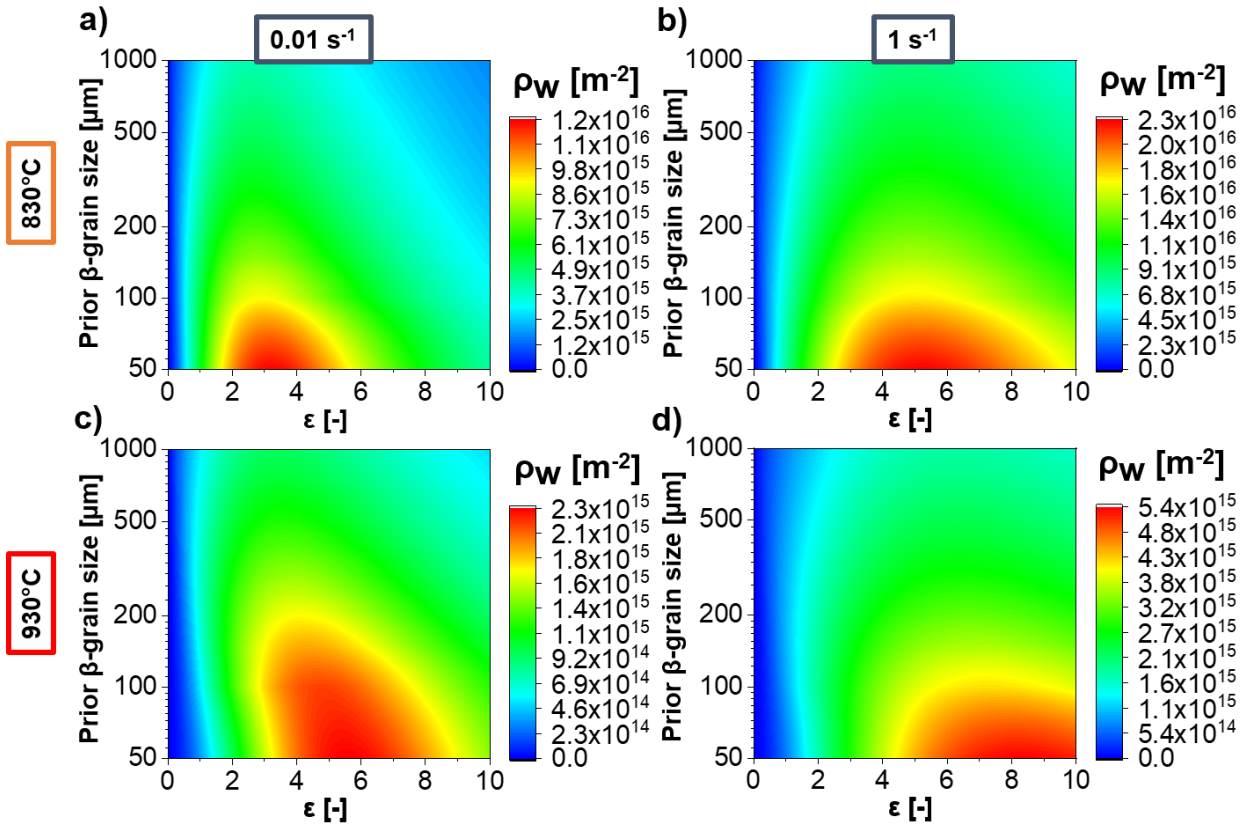

Figure 87: Contour maps for the evolution of wall dislocation density for the β-phase for the Ti-17 with a β-grain size before deformation of 500 µm for different initial β-grain sizes during deformation at: a) 830°C and 0.01 s^{-1}, b) 830°C and 1 s^{-1}, c) 930°C and 0.01 s^{-1}, d) 930°C and 1 s^{-1}.

The evolution of the fraction of HAGBs as a function of strain and initial β-grain size is shown in Figure 88. Starting from a partially recrystallised microstructure (f^0_{HAGB} = 0.35), LAGBs are formed at small strains, leading to a decrease in the fraction of HAGBs. The larger the initial grain size, the faster the increment in boundary average misorientation (Equation 85). Moreover, smaller grain sizes promote the consumption of the formed LAGBs due to the movement of HAGBs (Equation 87). Therefore, larger initial β-grain sizes lead to a fast evolution of the fraction of HAGB for a given temperature and strain rate.

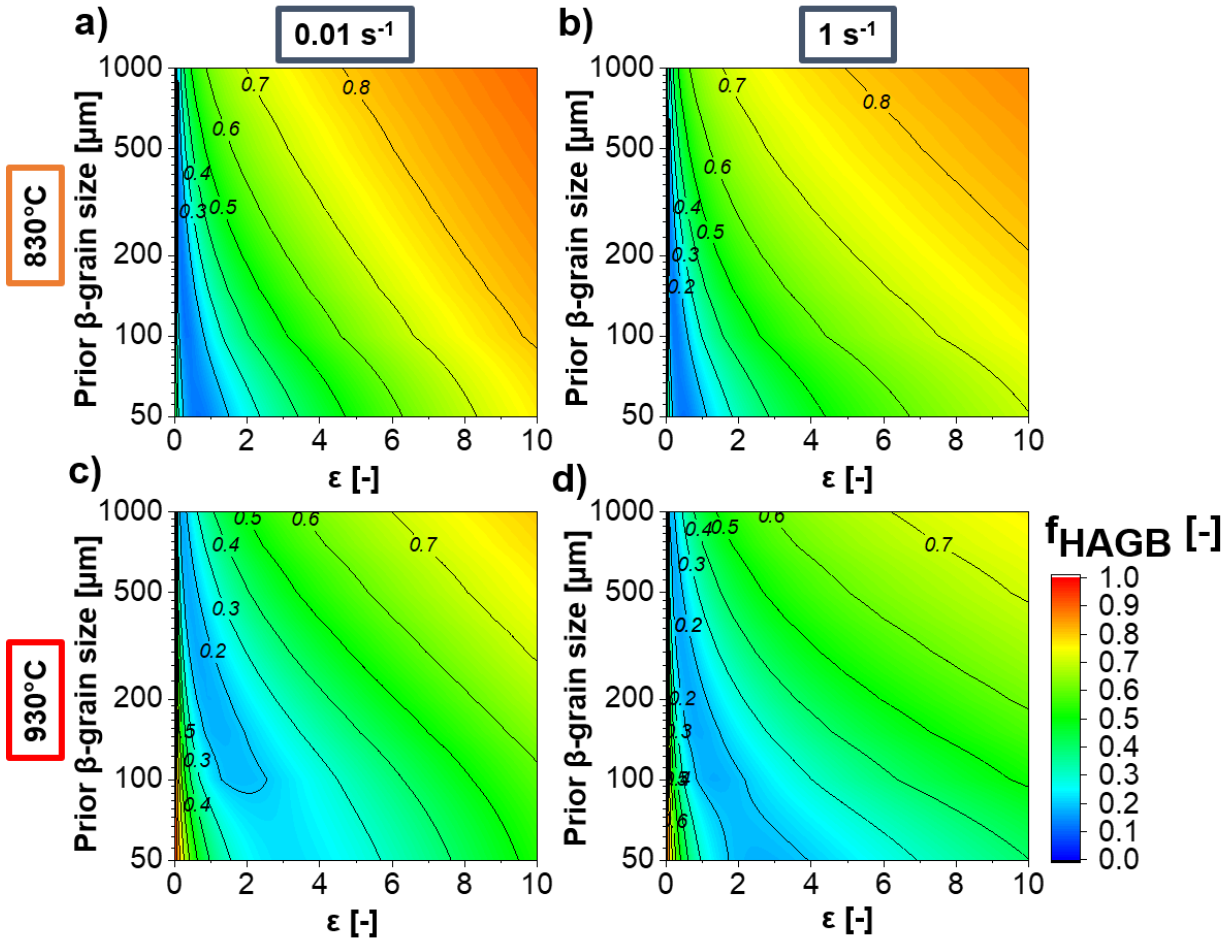

Figure 88: Contour maps for the evolution of the fraction of high angle grain boundaries of the β-phase for the Ti-17 with a β-grain size before deformation of 500 µm for different initial β-grain sizes during deformation at: a) 830°C and 0.01 s^{-1}, b) 830°C and 1 s^{-1}, c) 930°C and 0.01 s^{-1}, d) 930°C and 1 s^{-1}.

Theoretically, an infinitely large initial β-grain size leads to a rapid formation of a microstructure formed by HAGBs, as the result of the mathematical assumption that the increment of the misorientation angle of the LAGBs is proportional to the initial grain size (Equation 85). It means that the local lattice rotation would lead to a very fast increase in boundary misorientation. This, however, does not imply that the steady-state microstructure is reached instantaneously. It means that formed LAGBs evolves fast to HAGBs.

The evolution of the β-grain size as a function of the strain and initial β-grain size is shown in Figure 89. A large difference in grain size is observed between 830°C and 930°C, showing the enhancement of CDRX due to the presence of α-phase at 830°C. The microstructure evolves faster towards its steady-state, the larger the initial β-grain size and the lower the strain rate for a given temperature are. A refinement of the microstructure can occur at deformation at large strains.

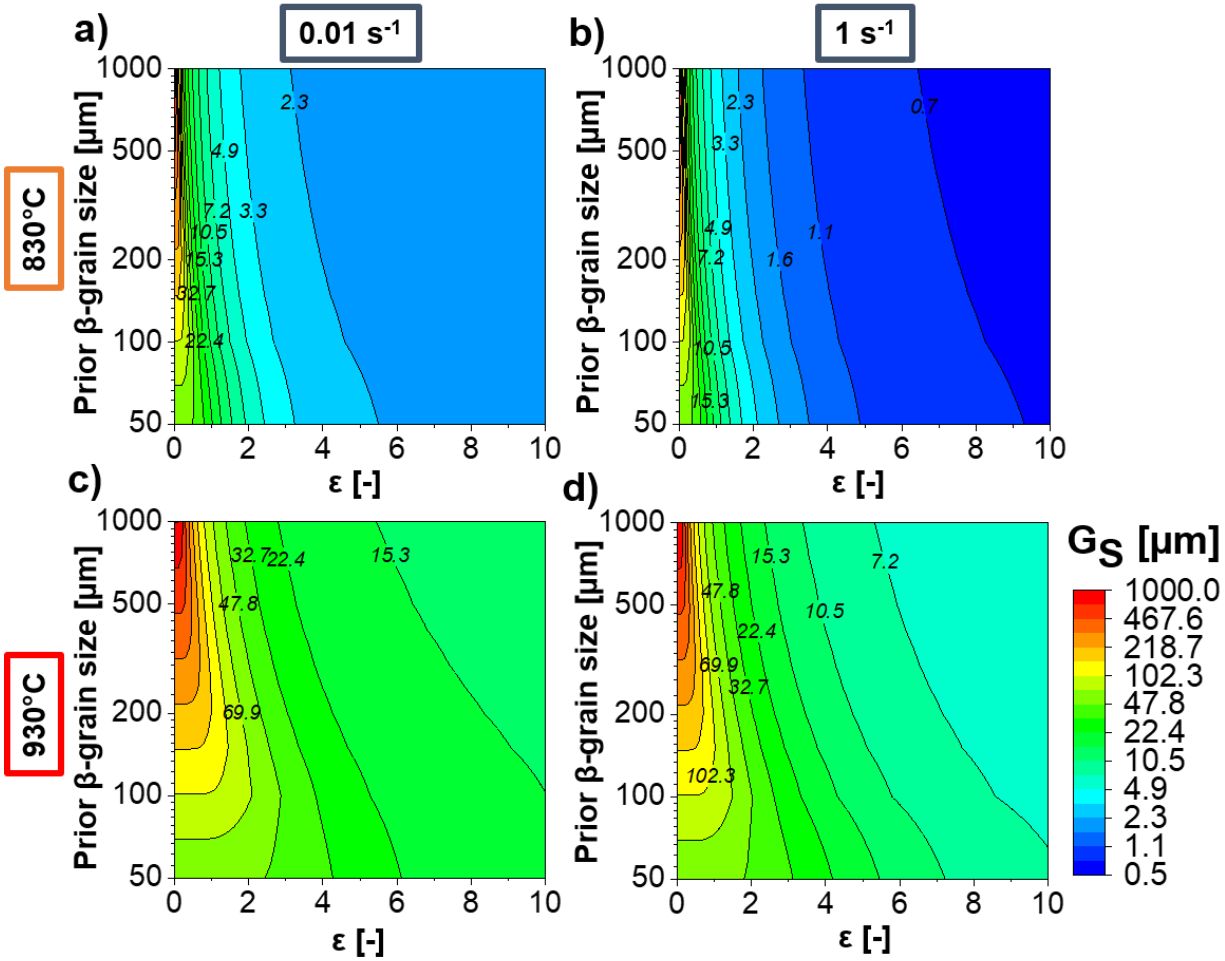

Figure 89: Contour maps for the evolution of grain size of the β-phase for the Ti-17 with a β-grain size before deformation of 500 µm for different initial β-grain sizes during deformation at: a) 830°C and 0.01 s^{-1}, b) 830°C and 1 s^{-1}, c) 930°C and 0.01 s^{-1}, d) 930°C and 1 s^{-1}.

The β-subgrain size evolution as a function of strain and initial β-grain size is shown in Figure 90. Larger initial β-grain sizes lead to the formation of larger subgrain sizes for a given strain, temperature and strain rate. Although the higher consumption of the formed LAGBs due to the movement of a larger surface density of HAGBs for smaller initial β-grain sizes, the evolution of the boundary misorientation requires more recovered dislocations to promote the same increment in boundary misorientation. That and the slowest evolution of HAGB can explain the higher wall dislocation density for smaller initial β-grain sizes that was shown in Figure 87.

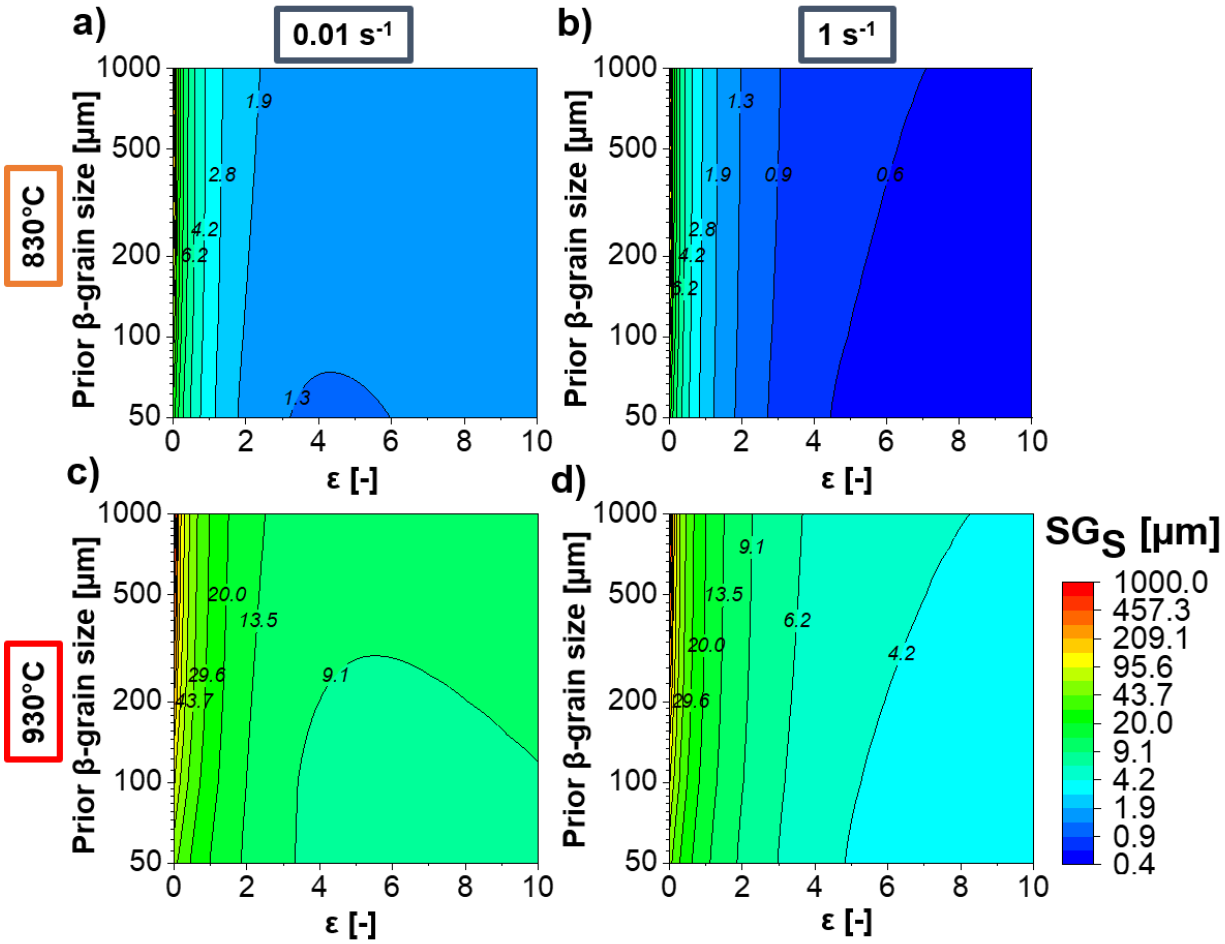

Figure 90: Contour maps for the evolution of β-subgrain size for the Ti-17 with a β-grain size before deformation of 500 µm for different initial β-grain sizes during deformation at: a) 830°C and 0.01 s^{-1}, b) 830°C and 1 s^{-1}, c) 930°C and 0.01 s^{-1}, d) 930°C and 1 s^{-1}.

Finally, the stress evolution as a function of the strain and initial β-grain size is shown in Figure 91. Note the large differences in the scales by deforming in α+β and β domains. A fast increment at early stages followed by a slight decrement due to consumption of the dislocation walls of low misorientation angle is observed up to achieving a steady-state in the β-domain (Figure 91(c,d)). A fast strengthening is followed by flow softening due to change in load partitioning mechanism in the α+β domain due to dynamic α-globularisation (Figure 91(a,b)). The flow softening is pronounced up to strains < 1. The subsequent hardening and flow softening observed for strains > 1 in the α+β domain is related to the increment of wall dislocation density and the effect of its strengthening on the overall athermal stress (Equation 48). The strengthening caused by the dislocation walls is more pronounced in the α+β domain compared to the β-domain, and it increases with a decrease in initial β-grain size.

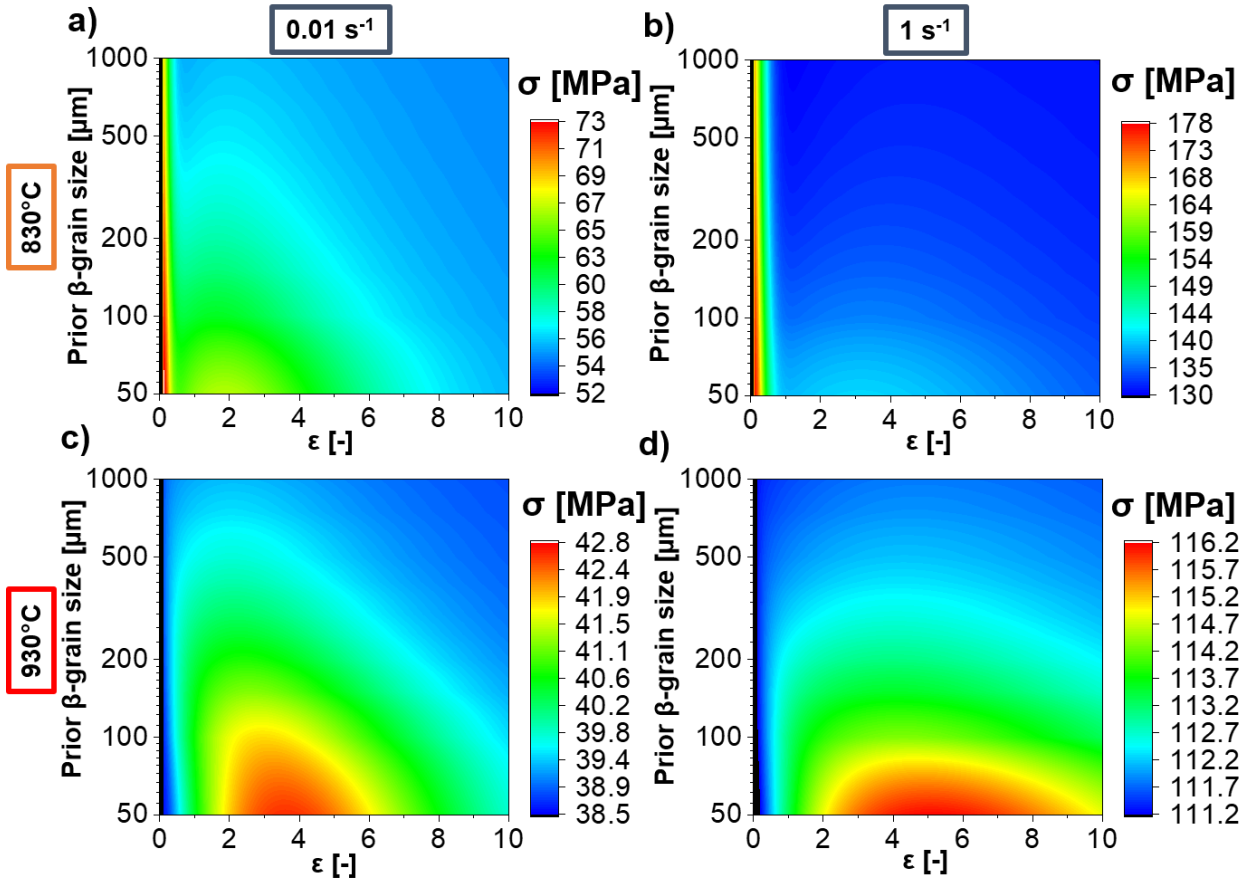

Figure 91: Contour maps for the evolution of stress for the β-phase for the Ti-17 with a β-grain size before deformation of 500 µm for different initial β-grain sizes during deformation at: a) 830°C and 0.01 s^{-1}, b) 830°C and 1 s^{-1}, c) 930°C and 0.01 s^{-1}, d) 930°C and 1 s^{-1}.

13.2.1.2. Initial β-subgrain size

The influence of the initial subgrain size is translated into the fraction between the initial surface density of HAGBs ($S^0_{v_{HAGB}}$) and the initial surface density of LAGBs ($S^0_{v_{LAGB}}$) for a fixed initial β-grain size of 500 µm and an initial LAGB average misorientation of 1°. Small subgrain size means smaller fractions $S^0_{v_{HAGB}} / S^0_{v_{LAGB}}$, while a fully static recrystallised microstructure corresponds to large $S^0_{v_{HAGB}}/S^0_{v_{LAGB}}$ values. The results are influenced by the assumption that only the mobility of the HAGBs is considered [33].

Figure 92 shows the immobile dislocation density evolution as a function of the strain and $S^0_{v_{HAGB}} / S^0_{v_{LAGB}}$. Smaller initial subgrain size leads to higher immobilisation rate of mobile dislocations, thus higher immobile dislocation density is produced. This difference is more pronounced if $S^0_{v_{HAGB}}/S^0_{v_{LAGB}} < 0.1$.

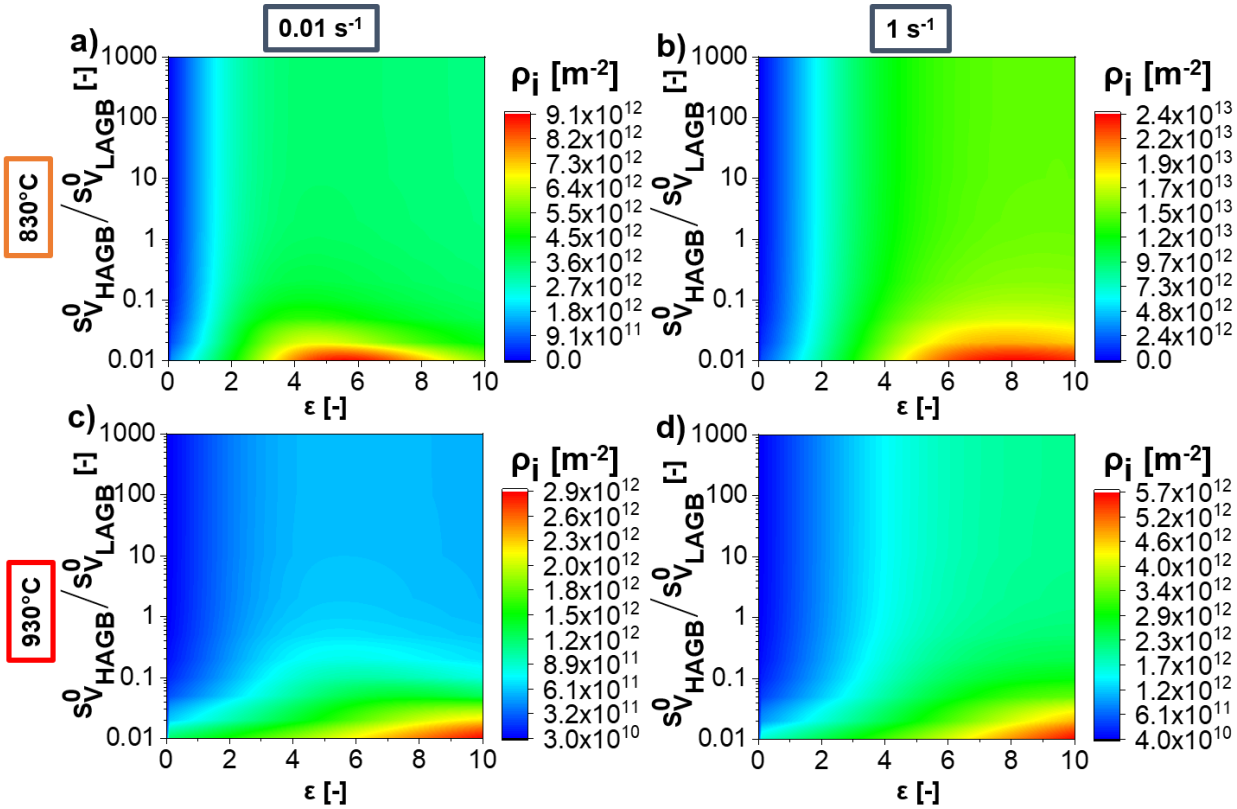

Figure 92: Contour maps for the evolution of immobile dislocation density for the β-phase for the Ti-17 with a β-grain size before deformation of 500 µm for different initial ratios between high angle grain boundaries ($S^0_{V_{HAGB}}$) and low angle grain boundaries ($S^0_{V_{LAGB}}$) during deformation at: a) 830°C and 0.01 s^{-1}, b) 830°C and 1 s^{-1}, c) 930°C and 0.01 s^{-1}, d) 930°C and 1 s^{-1}.

Figure 93 shows the evolution of the wall dislocation density as a function of the strain and $S^0_{V_{HAGB}}/S^0_{V_{LAGB}}$ for a fixed initial β-grain size. The proposed model predicts that formation of LAGBs continuously occurs, and the larger the surface density of boundaries, the slower the increase in mean boundary average misorientation angle (Equation 84). Therefore, a small initial subgrain size leads to slower evolution of the microstructure via CDRX, consequently a higher wall dislocation density.

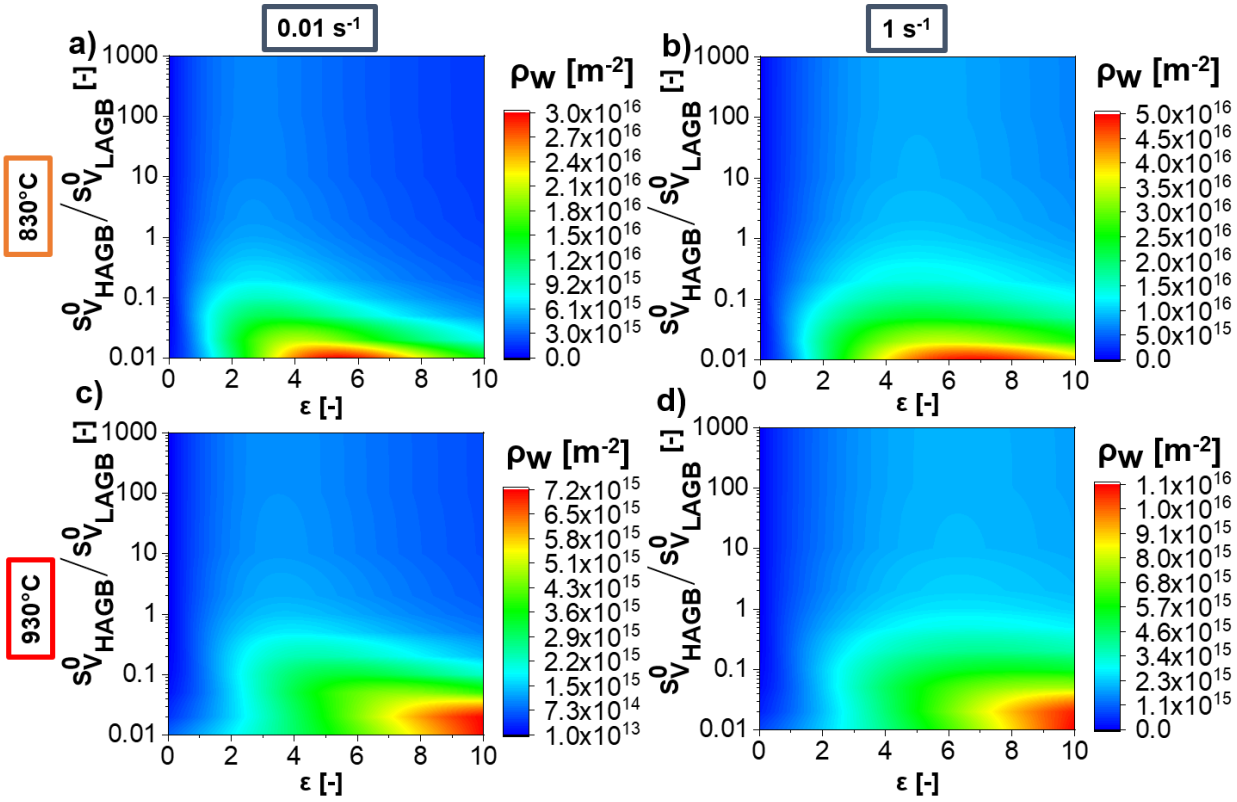

Figure 93: Contour maps for the evolution of wall dislocation density for the β-phase for the Ti-17 with a β-grain size before deformation of 500 µm for different initial ratios between high angle grain boundaries ($S^0_{v_{HAGB}}$) and low angle grain boundaries ($S^0_{v_{LAGB}}$) during deformation at: a) 830°C and 0.01 s^{-1}, b) 830°C and 1 s^{-1}, c) 930°C and 0.01 s^{-1}, d) 930°C and 1 s^{-1}.

The evolution of the fraction of HAGB as a function of strain and $S^0_{v_{HAGB}}/S^0_{v_{LAGB}}$ is shown in Figure 94. The smaller the initial subgrain size, the larger the strains required to achieve a certain fraction of HAGB. The continuous formation of new LAGBs and the slow increment of boundary misorientation for small subgrain sizes (Equation 85), leads to a retardation of CDRX. The influence of the initial subgrain size on the evolution of the microstructural features becomes negligible if the $S^0_{v_{HAGB}}/S^0_{v_{LAGB}}$ is larger than 10.

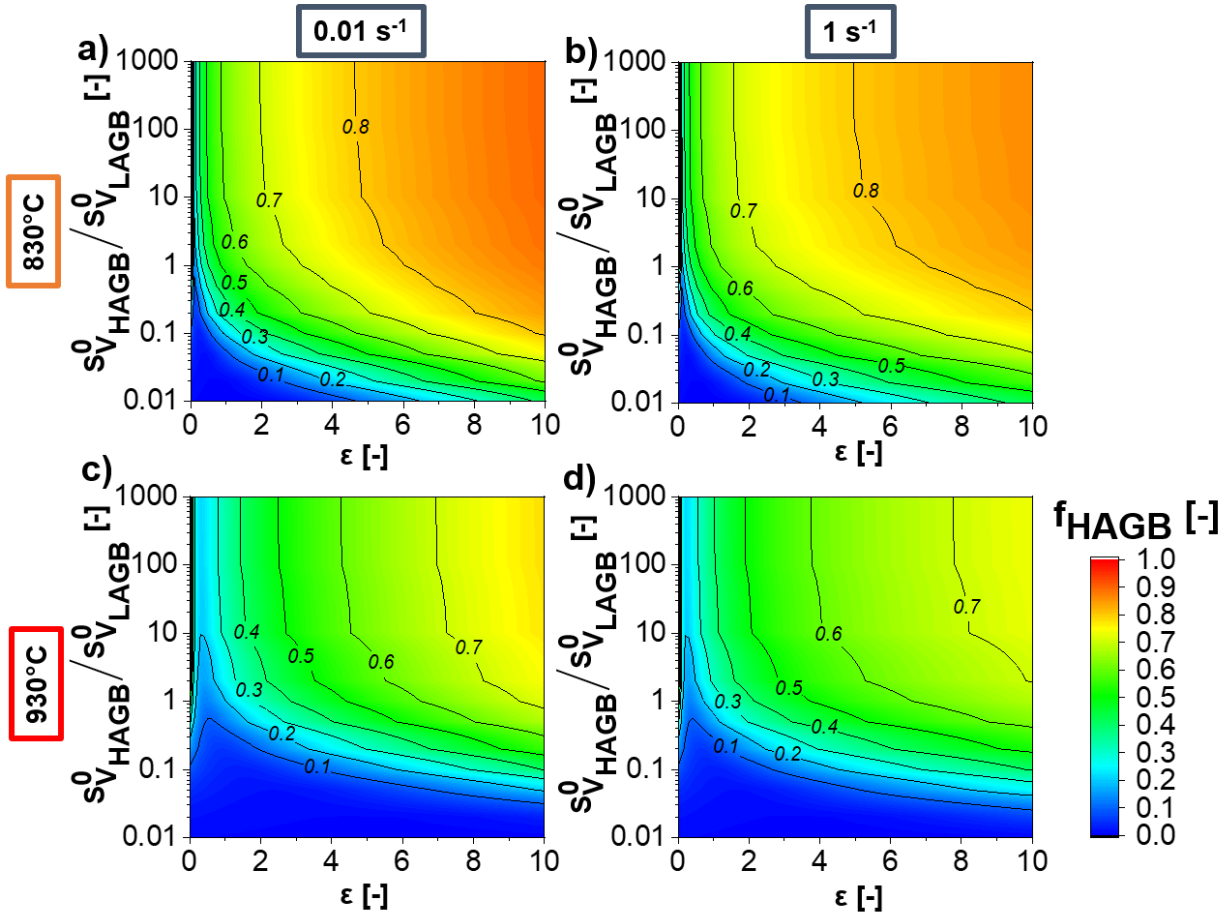

Figure 94: Contour maps for the evolution of the fraction of high angle grain boundaries the β-phase for the Ti-17 with a β-grain size before deformation of 500 µm for different initial ratios between high angle grain boundaries ($S^0_{V_{HAGB}}$) and low angle grain boundaries ($S^0_{V_{LAGB}}$) during deformation at: a) 830°C and 0.01 s^{-1}, b) 830°C and 1 s^{-1}, c) 930°C and 0.01 s^{-1}, d) 930°C and 1 s^{-1}.

The evolution of the β-grain size as a function of strain and $S^0_{V_{HAGB}}/S^0_{V_{LAGB}}$ is shown in Figure 95 for the initial β-grain size of 500 µm. Here, similar behaviour is observed as for the evolution of HAGB (Figure 94). The decrease in grain size due to the formation of new HAGBs via CDRX requires larger strains for small initial β-subgrains due to the slower increase in boundary misorientation. Grain refinement occurs at large strains and is more pronounced, the higher the strain rate and the lower the temperature are.

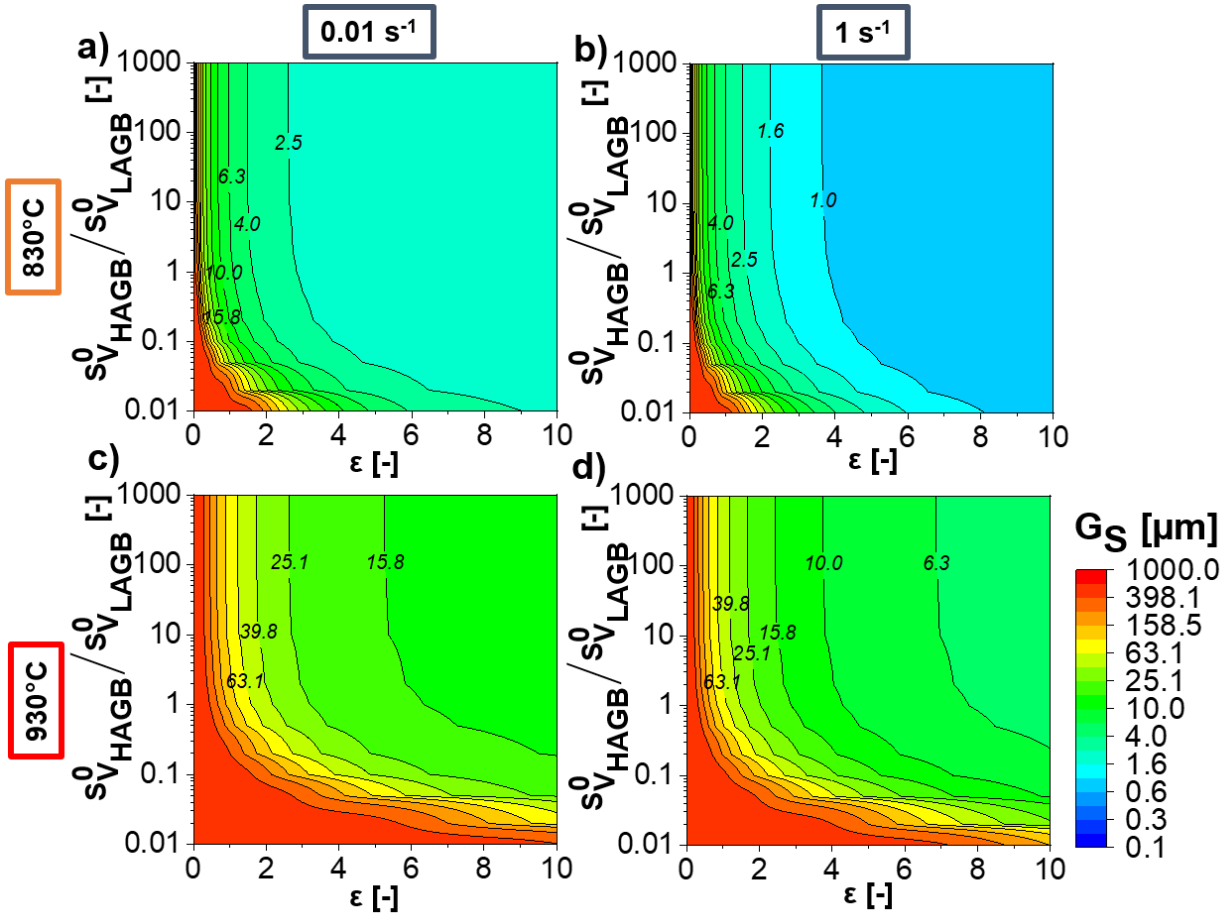

Figure 95: Contour maps for the evolution of grain size of the β-phase for the Ti-17 with a β-grain size before deformation of 500 μm for different initial ratios between high angle grain boundaries ($S^0_{V_{HAGB}}$) and low angle grain boundaries ($S^0_{V_{LAGB}}$) during deformation at: a) 830°C and 0.01 s^{-1}, b) 830°C and 1 s^{-1}, c) 930°C and 0.01 s^{-1}, d) 930°C and 1 s^{-1}.

Figure 96 shows the evolution of β-subgrain size as a function of the strain and $S^0_{V_{HAGB}}/S^0_{V_{LAGB}}$. An initial decrease in subgrain size is predicted and is more pronounced for larger $S^0_{V_{HAGB}}/S^0_{V_{LAGB}}$. The transformation of LAGBs into HAGBs and the movement of the formed HAGBs leads to a small increase of the subgrain size at large strains up to its steady-state value, i.e. the steady-state grain size.

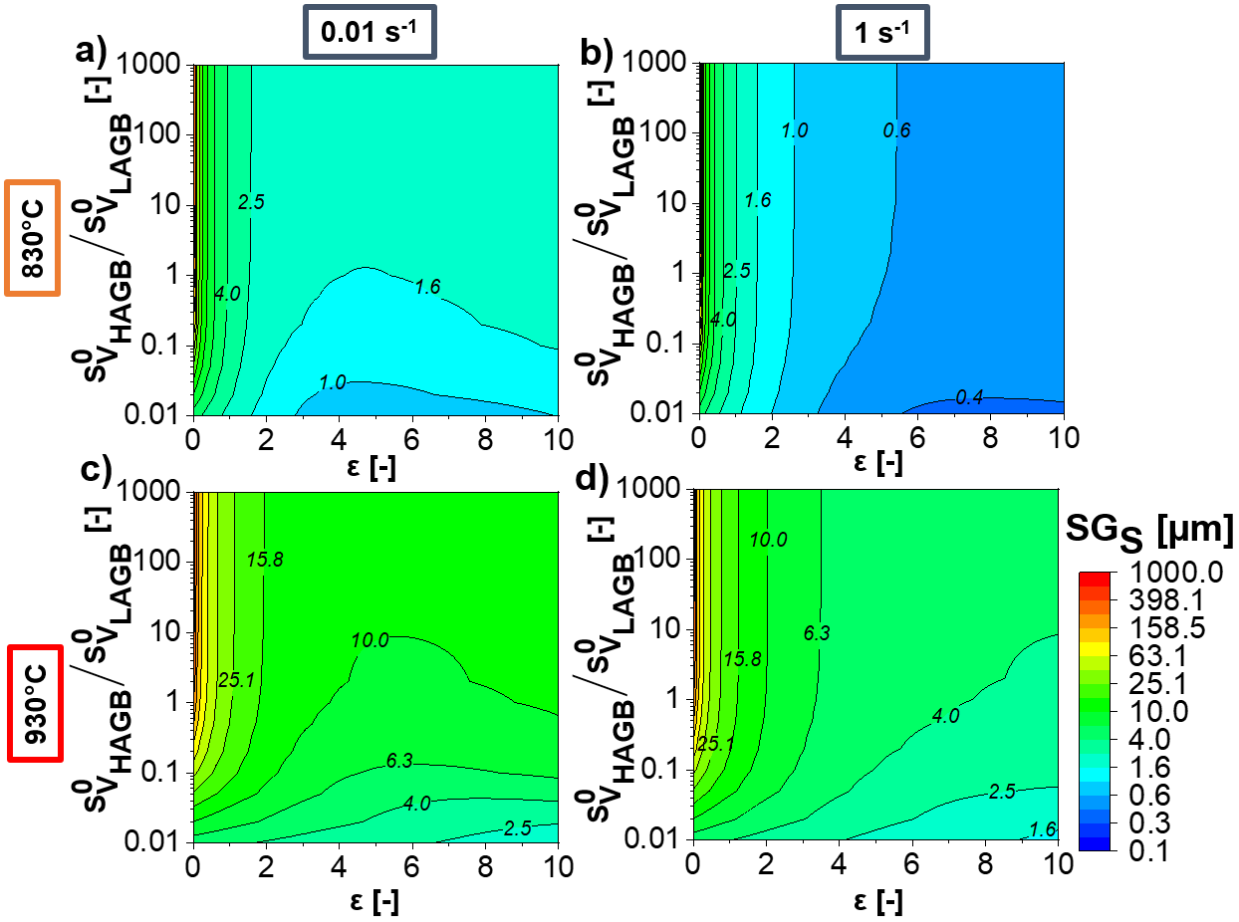

Figure 96: Contour maps for the evolution of subgrain size of the β-phase for the Ti-17 with a β-grain size before deformation of 500 µm for different initial ratios between high angle grain boundaries ($S^0_{v_{HAGB}}$) and low angle grain boundaries ($S^0_{v_{LAGB}}$) during deformation at: a) 830°C and 0.01 s^{-1}, b) 830°C and 1 s^{-1}, c) 930°C and 0.01 s^{-1}, d) 930°C and 1 s^{-1}.

The evolution of the stress in the β-phase as a function of the strain and $S^0_{v_{HAGB}}/S^0_{v_{LAGB}}$ is shown in Figure 97. A fast increase due to production of mobile dislocations is observed at the early stages. It is followed by a nearly steady-state in case of deformation in the β-domain and to flow softening in case of deformation in the α+β domain. The second increase in stress at strains > 1 is observed in the α+β domain for small values of $S^0_{v_{HAGB}}/S^0_{v_{LAGB}}$. Similarly, a peak in stress is observed in the β-domain for larger strains and small values of $S^0_{v_{HAGB}}/S^0_{v_{LAGB}}$. It corresponds to the strengthening caused by the presence of wall dislocations with small misorientation angle. Those contribute to athermal stress (Equation 45). The strengthening caused by the wall dislocation density at strains higher than 1 is negligible for higher values of $S^0_{v_{HAGB}}/S^0_{v_{LAGB}}$ (initial recrystallised microstructure).

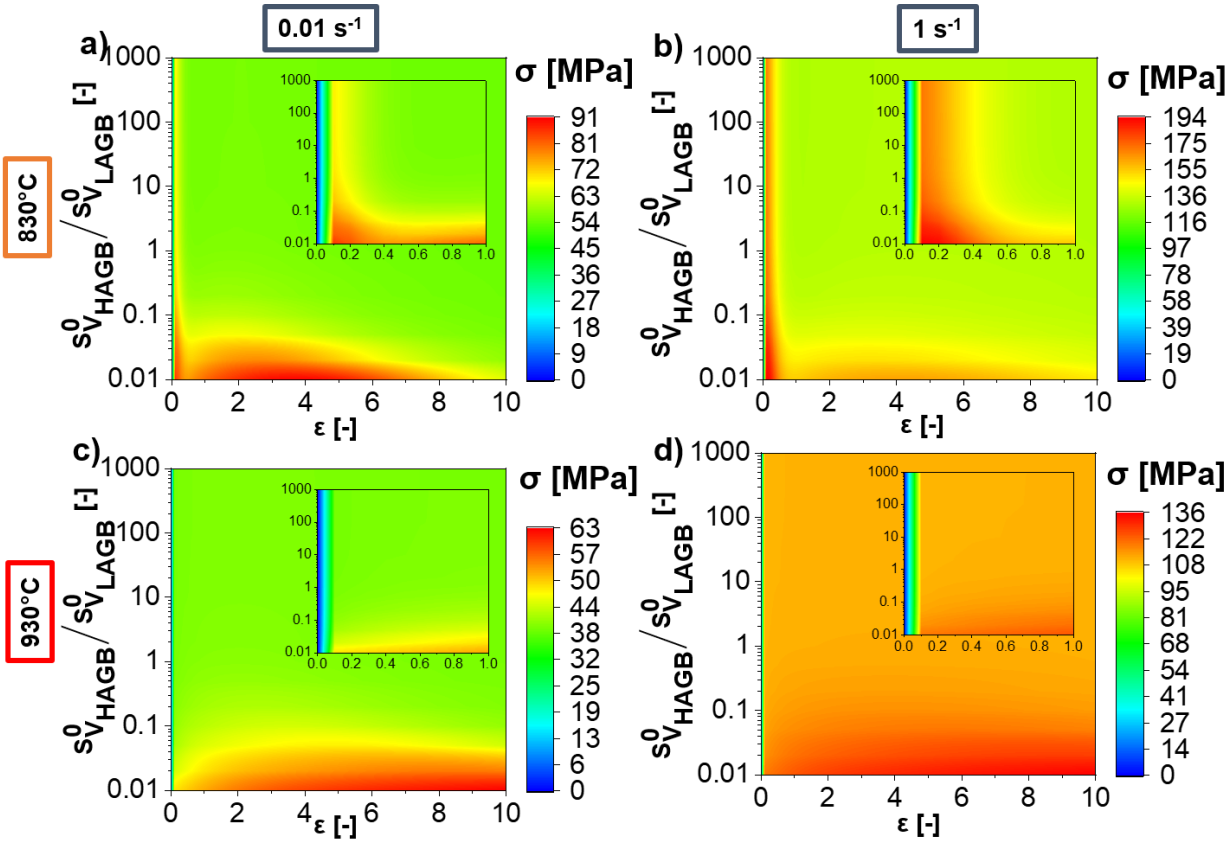

Figure 97: Contour maps for the evolution of stress for the β-phase for the Ti-17 with a β-grain size before deformation of 500 µm for different initial ratios between high angle grain boundaries ($S^0_{V_{HAGB}}$) and low angle grain boundaries ($S^0_{V_{LAGB}}$) during deformation at: a) 830°C and 0.01 s^{-1}, b) 830°C and 1 s^{-1}, c) 930°C and 0.01 s^{-1}, d) 930°C and 1 s^{-1}.

13.2.1.3. Initial α-thickness

Different initial thickness leads to different kinetics of formation of boundaries within the α-platelets and, consequently, different kinetics of α/β migration. Figure 98 shows the contour maps for the evolution of the aspect ratio of α-phase as a function of strain and the initial α-thickness. The initial aspect ratio of α-phase is considered as 15, and the initial grain size of β-phase is 500 µm. A fast decrease of aspect ratio is observed for either small or large initial thickness of α-phase. Smaller thickness leads to a larger number density of α-lamellas, and a larger amount of boundary density. Once a boundary is formed, the movement of α/β causes the separation of the lamellas into smaller particles, and the evolution of the aspect ratio is faster for smaller initial α-thickness. The increase in α-thickness leads to a progressive migration from a 2D case of dynamic globularisation into a 3D case of dynamic globularisation. Thus, the formed boundaries within α-phase lead to a division of the lamellas in particles with smaller thickness compared to the initial one.

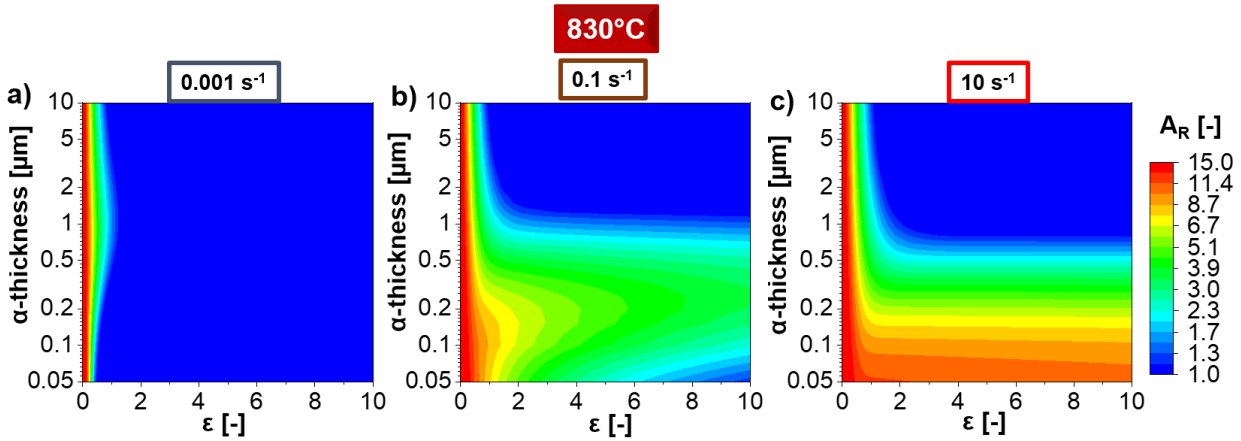

Figure 98: Contour maps for the evolution of aspect ratio of the α-particles during hot compression at 830°C for the Ti-17 with a β-grain size before deformation of 500 µm for different initial α-thickness for the strain rates of: a) 0.001 s^{-1}, b) 0.1 s^{-1}, c) 10 s^{-1}.

Larger strains are required to achieve an aspect ratio of 1 with an increase in strain rate for lower initial α-thickness. However, the impact of the strain rate on the aspect ratio evolution is not so pronounced for large initial α-thickness. The required boundary density to divide a platelet into particles of an aspect ratio of 1 decreases with increase in α-thickness. Since the growth of the particles occurs via a diffusion-based processed, higher strain rates require larger strains to achieve a similar aspect ratio.

Numerical artefacts more than the physical behaviour of the material can be highlighted:

- The increase in strain rate leads to a shift of the peak in aspect ratio to lower initial values of initial α-thickness for a given strain and temperature. The calculations change from the "2D case" to the "3D case" once the aspect ratio reaches the value of 1 and leads to the inflexion point in Figure 98.
- Once the α-particles are globularising in a "3D case", the dependency of the evolution of the aspect ratio on the strain rate is negligible. On the other hand, in the 2D case, the boundaries formed within α-phase are consumed before achieving an aspect ratio of 1.

The evolution of the immobile dislocation density in β-phase is shown in Figure 99(a,b) as a function of the strain and initial α-thickness. An empirical correlation between initial α/β boundary density and the fraction of dynamically and statically recovered dislocations that form new LAGBs or contribute to the increase in boundary misorientation is proposed, Equation 81. Therefore, finer α-platelets leads to a higher density of α/β interface density, and CDRX in β-phase occurs faster. It can be understood as the influence of the α-particle interspacing that contributes to both mobile dislocation production and mobile dislocation immobilisation as well as an increase in local lattice rotation, promoting the formation of new LAGBs and increasing their misorientation. Thus, the smaller the α-thickness, the larger the immobile dislocation density in β-phase for a given strain, strain rate and temperature. A peak in immobile dislocation density is predicted as a function of deformation, and the corresponding peak strain increases with increase in α-thickness.

The evolution of the wall dislocation density is shown in Figure 99(c,d) as a function of strain and initial α-thickness. A peak in the wall dislocation density increases with a decrease in α-thickness and is displaced at lower strains with a decrease in α-thickness since CDRX in occurs

faster in β-phase for thinner α-platelets. Higher strain rates lead to higher values of wall dislocation density, and larger strains are required to achieve the peak.

The evolution of the fraction of HAGB in the β-phase as a function of strain and initial α-thickness is shown in Figure 99(e,f). The faster CDRX in the β-phase for thinner α-platelets due to larger α/β interface density leads to a faster evolution of the fraction of HAGB in the β-phase with a decrease in α-thickness.

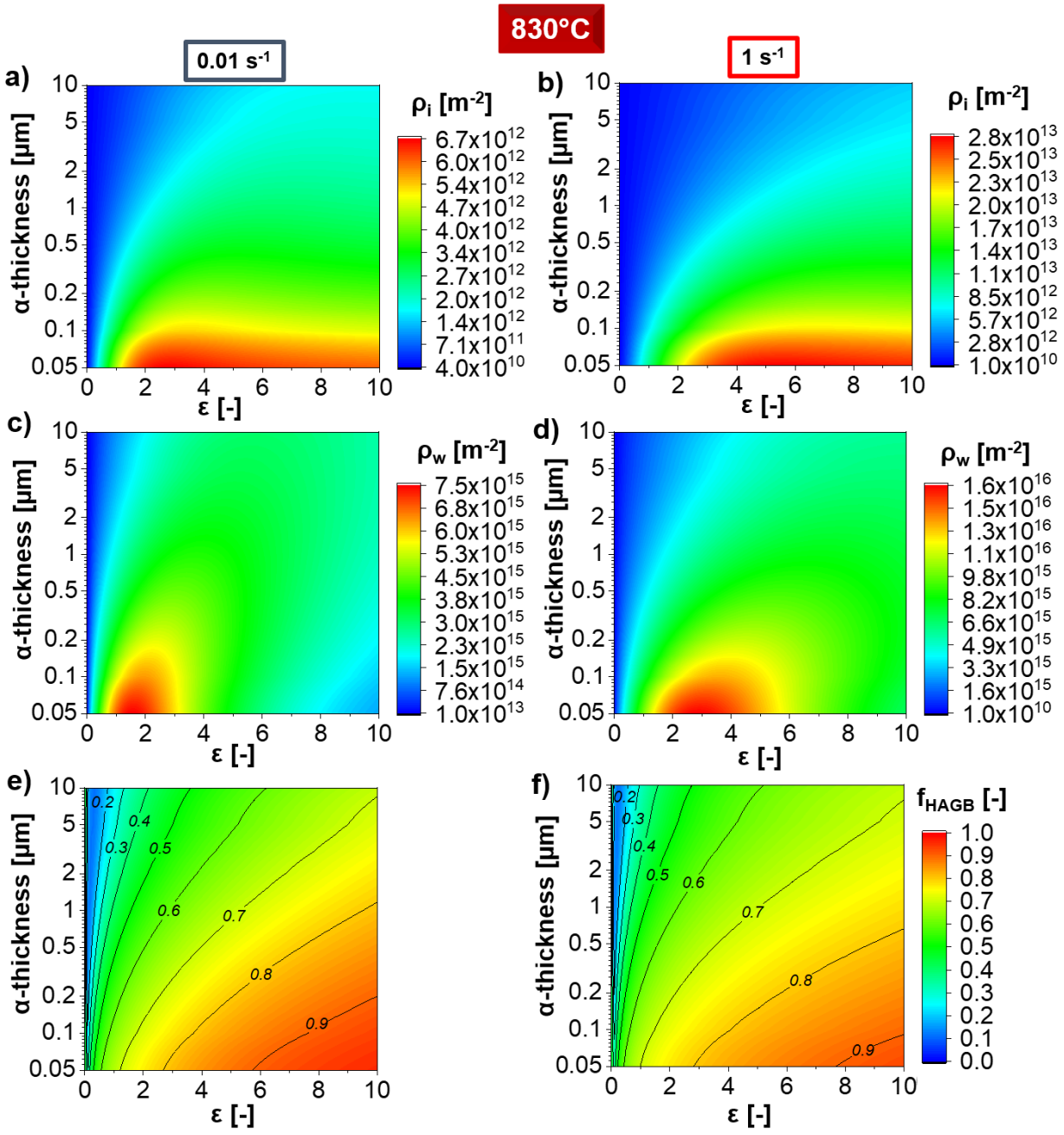

Figure 99: Contour maps for the β-phase during hot compression at 830°C for the Ti-17 with a β-grain size before deformation of 500 µm for different initial α-thickness for the strain rates of a,c,e) 0.01 s^{-1}; and b,d,f) 1 s^{-1}; and for the evolution of a,b) immobile dislocation density; c,d) wall dislocation density; e,f) fraction of HAGB.

Faster CDRX in the β-phase and faster decrease in the aspect ratio of the α-phase for thinner α-platelets is also related to the faster globularisation kinetics of the α-phase. The evolution

of the fraction of globularisation is shown in Figure 100 as a function of strain and initial α-thickness. The evolution of the aspect ratio, as described in Figure 98 exhibits notably different tendency in comparison to the evolution of the fraction of globularisation. The fraction of globularisation is achieved at low strains for the smallest thickness of α-platelet, while a large aspect ratio is predicted for the same conditions. Afterwards, the growth of the formed elongated α-particles occurs until they reach an aspect ratio of 1.

A numerical artefact more than the physical behaviour of the material can be highlighted:

- The proposed model assumes that the fraction of globularisation is related to the fraction between newly formed α/β boundaries and the total amount of boundaries in α-phase. Not necessarily an aspect ratio of 1 is achieved when the fraction of globularisation is 100%. The formation of boundaries in thicker α-plates (3D case) is accompanied by the reduction of aspect ratio, reaching the value of 1 before achieving 100% globularisation for large α-thickness.

Therefore, the proposed model can take into account the separate phenomena of formation of boundaries within α-phase, the formation of α/β boundaries that lead to separation of the α-platelets into smaller particles, and growth of the formed particles.

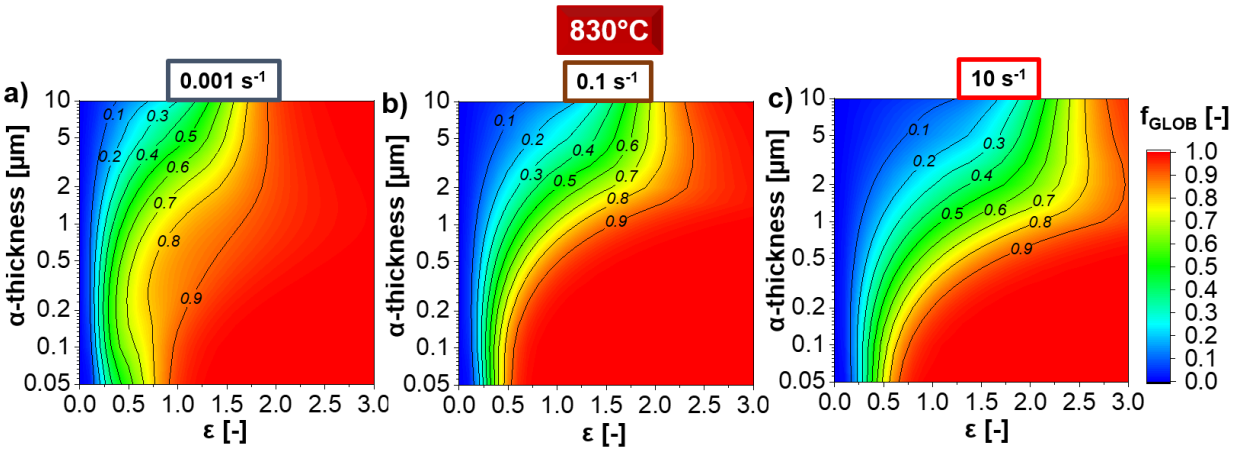

Figure 100: Contour maps for the evolution of high angle grain boundaries for the β-phase during hot compression at 830°C for the Ti-17 with a β-grain size before deformation of 500 µm for different initial α-thickness for the strain rates of: a) 0.001 s^{-1}, b) 0.1 s^{-1}, c) 10 s^{-1}.

The evolution of the grain size of the β-phase is shown in Figure 101(a,b) as a function of the strain and the initial α-thickness. Thinner initial α-platelets promote not only a faster CDRX but also the formation of a finer β-microstructure. Increasing the f_{CDRX} with an increase in α/β surface density leads to an increase in the formation of new LAGBs, thus, promoting the formation of finer grains. The β-grain size and the β-subgrain size as a function of strain and initial α-thickness show the same tendency, as shown in Figure 101(c,d).

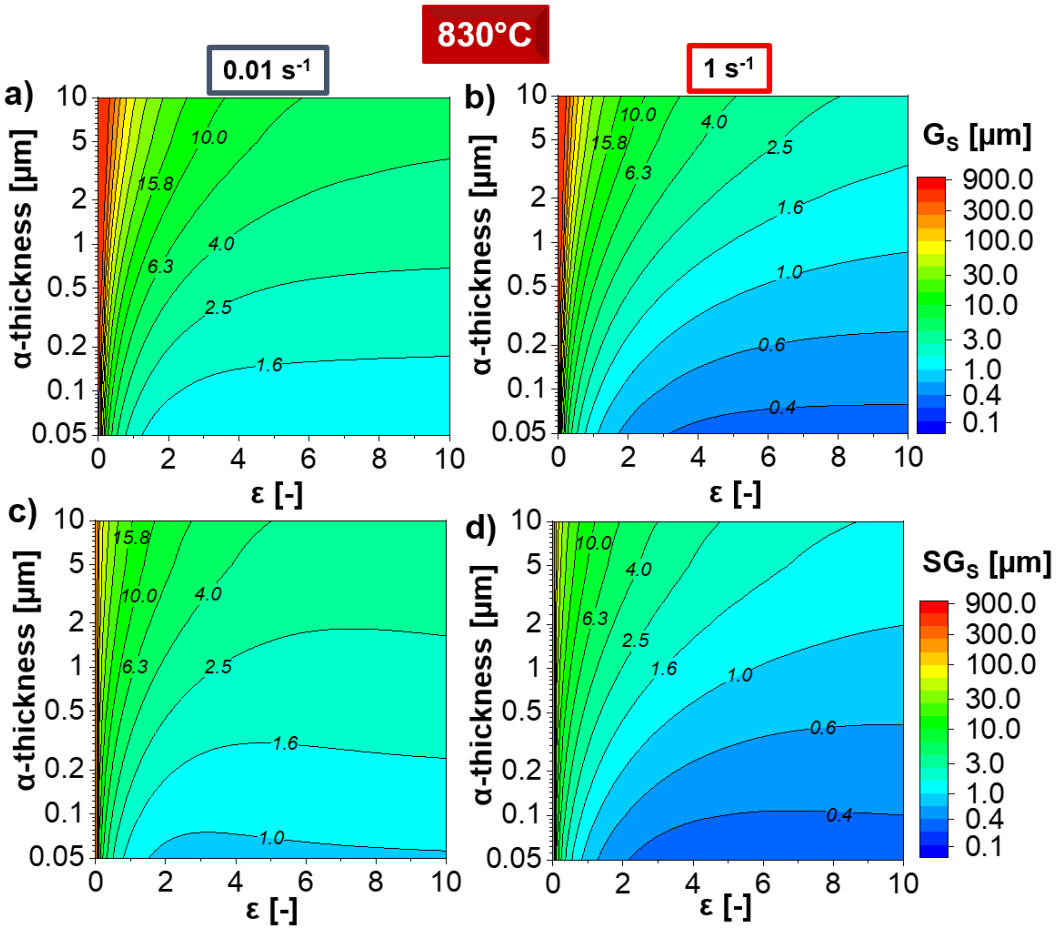

Figure 101: Contour maps for the β-phase during hot compression at 830°C for the Ti-17 with a β-grain size before deformation of 500 μm for different initial α-thickness for the strain rates of a,c) 0.01 s^{-1}; and b,d) 1 s^{-1}; and for the evolution of a,b) grain size; c,d) subgrain size.

The evolution of the overall stress as a function of strain and initial α-thickness is shown in Figure 102. The dynamic α-globularisation leads to progressive change in load partition from iso-strain into iso-stress. The slower evolution of the fraction of α-globularisation with an increase in α-thickness leads to slower kinetics of flow softening. The increase in strain rate leads to an increase in strain for the steady-state stress due to lower time for α/β migration and larger density of formed boundaries within the α-phase.

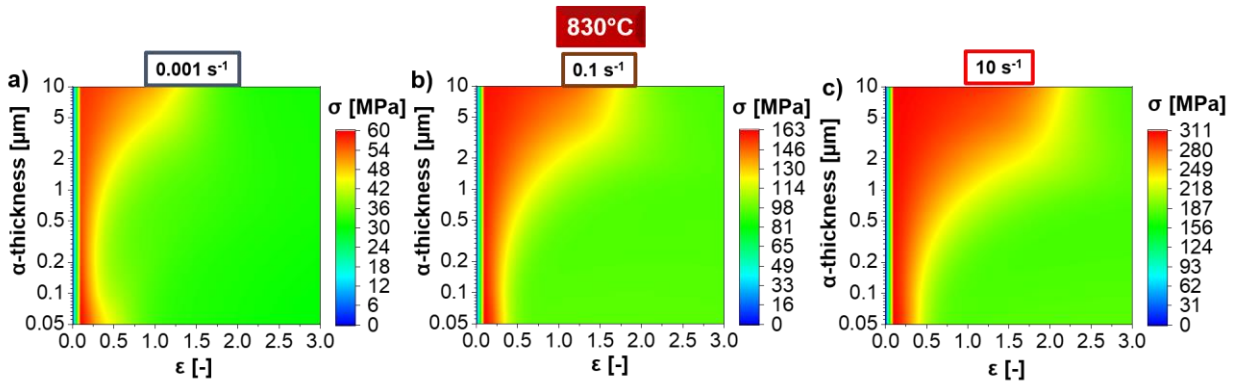

Figure 102: Contour maps for the overall stress evolution during hot compression at 830°C for the Ti-17 with a β-grain size before deformation of 500 μm for different initial α-thickness for the strain rates of: a) 0.001 s^{-1}, b) 0.1 s^{-1}, c) 10 s^{-1}.

Finally, the evolution of the thickness of the formed α-phase as a function of strain and initial α-thickness is shown in Figure 103. The model is not able to predict the separation of the α-particles. Thus, the growth is considered as a function of the climb velocity instead of a more rigorous physical description of the Ostwald-ripening effect of the formed particles. Therefore, a steady-state α-thickness is predicted instead of a progressive increase with strain. Despite the model limitations, the formation of α/β boundaries and the migration up to the formation of particles of an aspect ratio of 1 are well-described. The division of the thicker α-platelets into finer particles with lower thickness is predicted and occurs more pronouncedly up to the strain of ~2 and for initial α-thickness larger than 1.5 µm. For a lower initial thickness of α-phase, the dynamic globularisation occurs mainly in the 2D-case. Thus, the formation of new α/β boundaries followed by growth is observed. Lower strain rates lead to a lower strain required to achieve the steady-state α-thickness due to longer time for growth.

A numerical artefact more than the physical behaviour of the material can be highlighted:

- The evolution of the α-thickness is a result of the intricate relationship between the formation of α/β interface and the growth of the non-spherical particles up to a particle of an aspect ratio of 1, which is possible only in the 2D case. An inflexion point is visible for the initial α-thickness in the range between 0.5 µm to 2 µm for the strain rate of 0.001 s-1, Figure 103a. The increase in thickness up to the maximum is related to the growth due to diffusion. The maximum thickness is reached once the aspect ratio is 1. From this strain on, the decrease in thickness is related to the formation of new boundaries within the α-particles that lead to decrement in thickness. Therefore, the inflexion point observed in Figure 103a is a result of a mathematical model and cannot be directly related to a physical process.

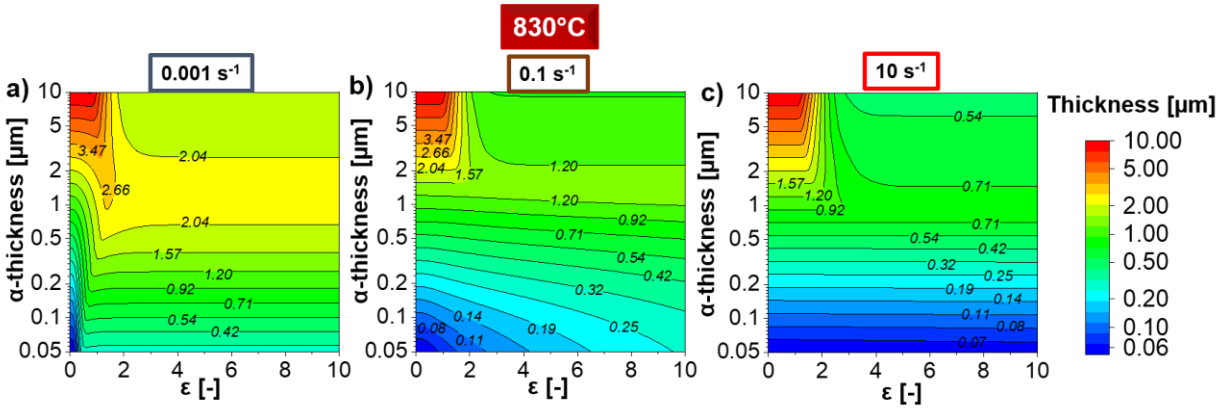

Figure 103: Contour maps for the α-thickness evolution during hot compression at 830°C for the Ti-17 with a β-grain size before deformation of 500 µm for different initial α-thickness for the strain rates of: a) 0.001 s^{-1}, b) 0.1 s^{-1}, c) 10 s^{-1}.

The initial thickness of α-phase is related to the heat treatment performed before the deformation step. As shown in chapter 8 and in section 13.1 for the continuous cooling transformation in Ti-64, thicker α-platelets are produced at lower cooling rates. Thus, depending on the initial α-thickness distribution, the dynamic globularisation of α-phase, as well as the CDRX and microstructure evolution in the β-phase, can be notably different. A more homogeneous microstructure will be obtained when the α-thickness is small.

13.3. Static recrystallisation behaviour

A mesoscale model for SRX is developed and fully coupled with the hot deformation model. The heterogeneities observed in the microstructure of the β-phase lead to the adoption of empirical correlations. However, the current model enables the prediction of the microstructure as a function of the initial microstructure after any deformation condition.

The coupled model to describe the microstructure evolution during SRX after hot deformation is discussed in this section in terms of the influence of the initial microstructure prior to deformation on the SRX behaviour. The extrapolation of the results to different values from those used in chapter 12 could result in notable deviations. However, general behaviour and overall conclusions can be drawn, showing the robustness of the coupled models developed in this work to predict the evolution of any starting microstructure for any thermo-mechanical treatment. The interpretation and discussion of the results that are shown here were already published in [146].

13.3.1. Influence of deformation before SRX

The influence of the total deformation on the evolution of the recrystallisation fraction is shown in Figure 104(a,b). The increase in stored energy due to an increase in dislocation density promotes nucleation (Equation 125) and increase the β-HAGB velocity (Equation 117). Thus, larger deformation and higher strain rates promote SRX. A decrease in wall dislocation density is predicted once the newly formed LAGBs transform in HAGBs. However, this effect occurs at strain larger than 2 at 930°C for the give strain rates.

The influence of the deformation before SRX on the mean grain size is shown in Figure 104 (c,d). The initial grain size for SRX is the final grain size predicted for hot deformation. Thus, the larger the deformation, the smaller the initial grain size for SRX and the higher stored energy. Higher stored energy promotes faster nucleation and growth rates. Considering the deformation and heat treatment temperature of 930°C, grain refinement due to larger deformations is nearly not achievable since the initial grain size is 500 µm and a minimum value of ~210 µm is predicted for the strain rate of 1 s^{-1} and strains larger than 1 when heat-treated at 930°C for ~2h.

The influence of the deformation before SRX on the statically recrystallised grain size is shown in Figure 104(e,f). Similar to the mean grain size, larger deformation leads to larger stored energy and smaller recrystallised grain sizes. Likewise, higher strain rates lead to the formation of finer recrystallised grains.

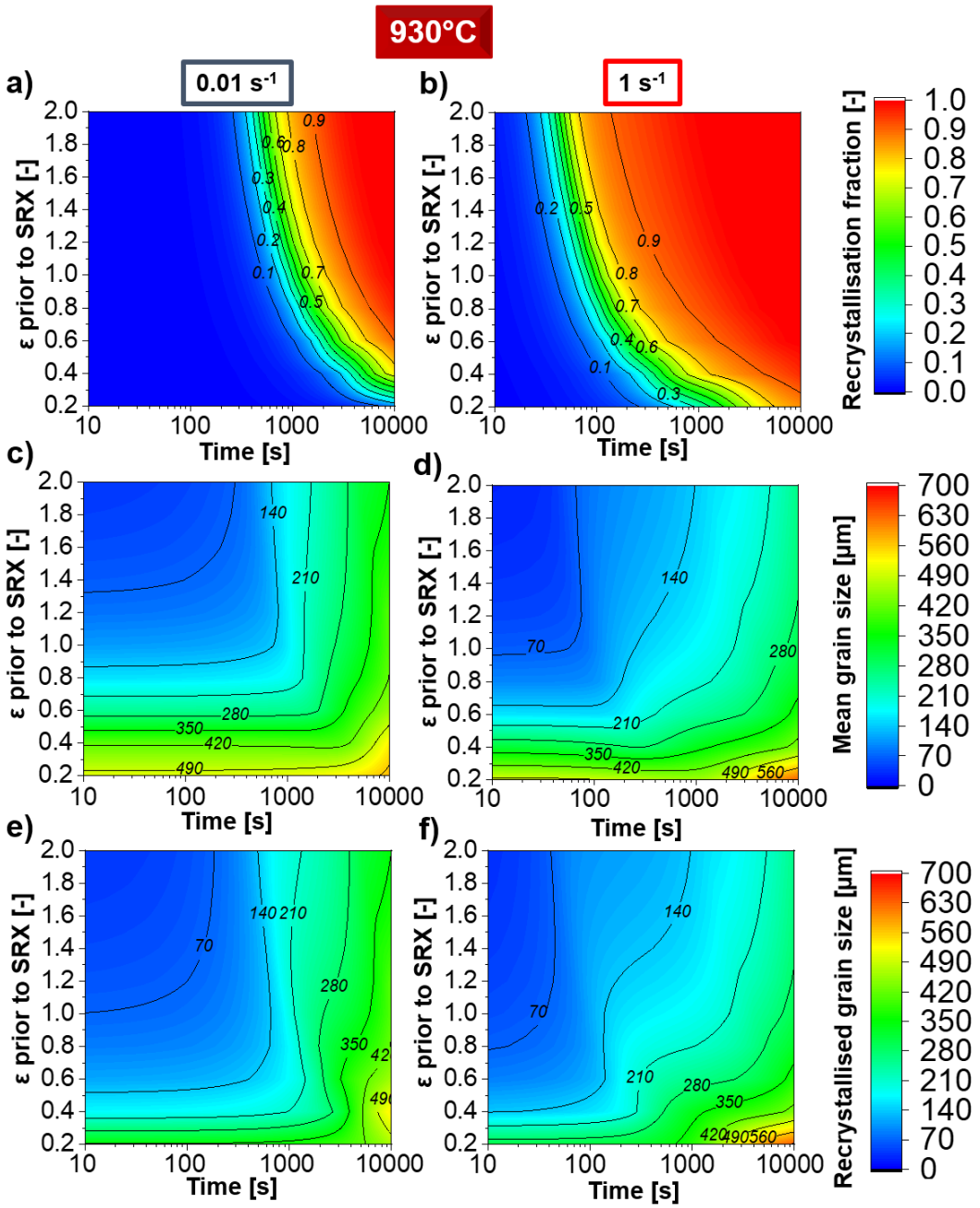

Figure 104: Contour maps for the recrystallisation fraction (a,b), mean grain size (c,d), recrystallised grain size (e,f) evolutions for the Ti-17 with a β-grain size before deformation of 500 µm for different strains of hot compression followed by annealing at 930°C for the strain rate of a,c,e) 0.01 s^{-1}; b,d,f) 1 s^{-1}.

13.3.2. Influence of β-grain size prior to deformation

The influence of the β-grain size before deformation on the SRX fraction evolution is shown in Figure 105(a,b) for the deformation and annealing temperature of 930°C. Smaller prior β-grains exhibit slower CDRX (section 13.2.1.1) due to:

- Formation of smaller subgrain.
- The larger density of HAGB surface sweeps the formed boundaries and dislocations.
- The lower wall dislocation density (Figure 87).

On the other hand, larger initial grains form faster a dynamically recrystallised microstructure via CDRX. The maximum in mean grain size for a given strain is, thus, related to a combination of insufficient formation of nuclei and their fast growth.

The influence of the β-grain size before deformation on the mean grain size formed during SRX is shown in Figure 105(c,d) for the material deformed at 930°C up to a strain of 1. It is shown in section 13.3.1 that increase in stored energy not necessarily leads to grain refinement. The higher nucleation is counterbalanced by the faster growth. Thus, the formation of small recrystallised grains is difficult to be achieved after deformation at 930°C up to strain of 1. Figure 105(c,d) shows that a peak is recrystallised grain size as a function of the β-grain size prior to deformation. It corresponds to the stored energy where the growth of the formed recrystallised grains has a more decisive influence over nucleation.

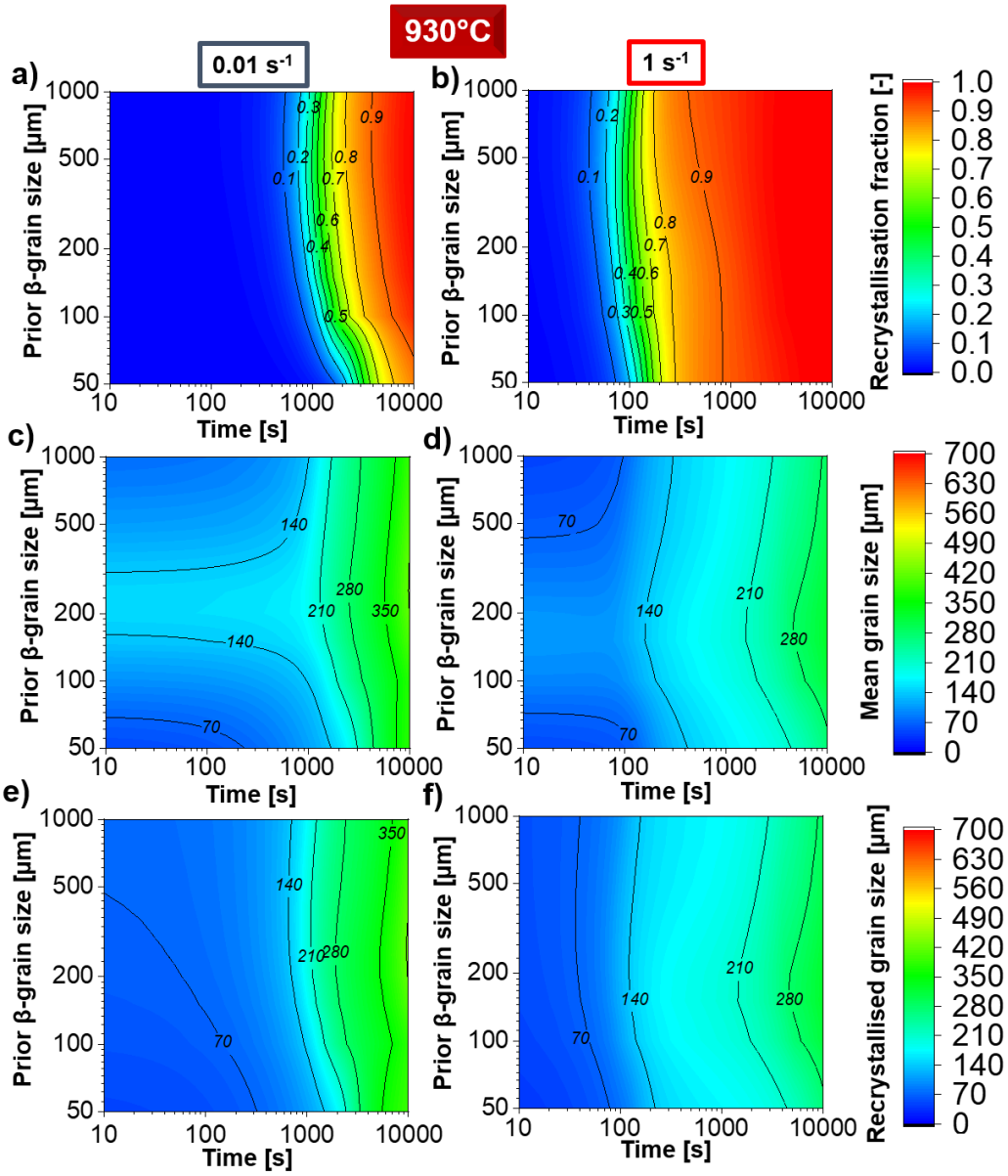

Figure 105: Contour maps for the recrystallisation fraction (a,b), mean grain size (c,d), recrystallised grain size (e,f) evolutions for the Ti-17 for different prior β-grain sizes for hot compression followed by annealing at 930°C up to 1 of strain for the strain rate of a,c,e) 0.01 s^{-1}; b,d,f) 1 s^{-1}.

Similarly to the influence of the β-grain size on the mean grain size during SRX, the effect of the β-grain size on the recrystallised grain size during SRX exhibits nearly the same tendency, Figure 105(e,f).

13.3.3. Influence of temperature

The influence of the temperature on the SRX fraction evolution is shown in Figure 106(a,b) for an initial grain size of 500 µm and up to deformation of 1. The dependency of the HAGB mobility on the temperature is given by the Arrhenius relationship.

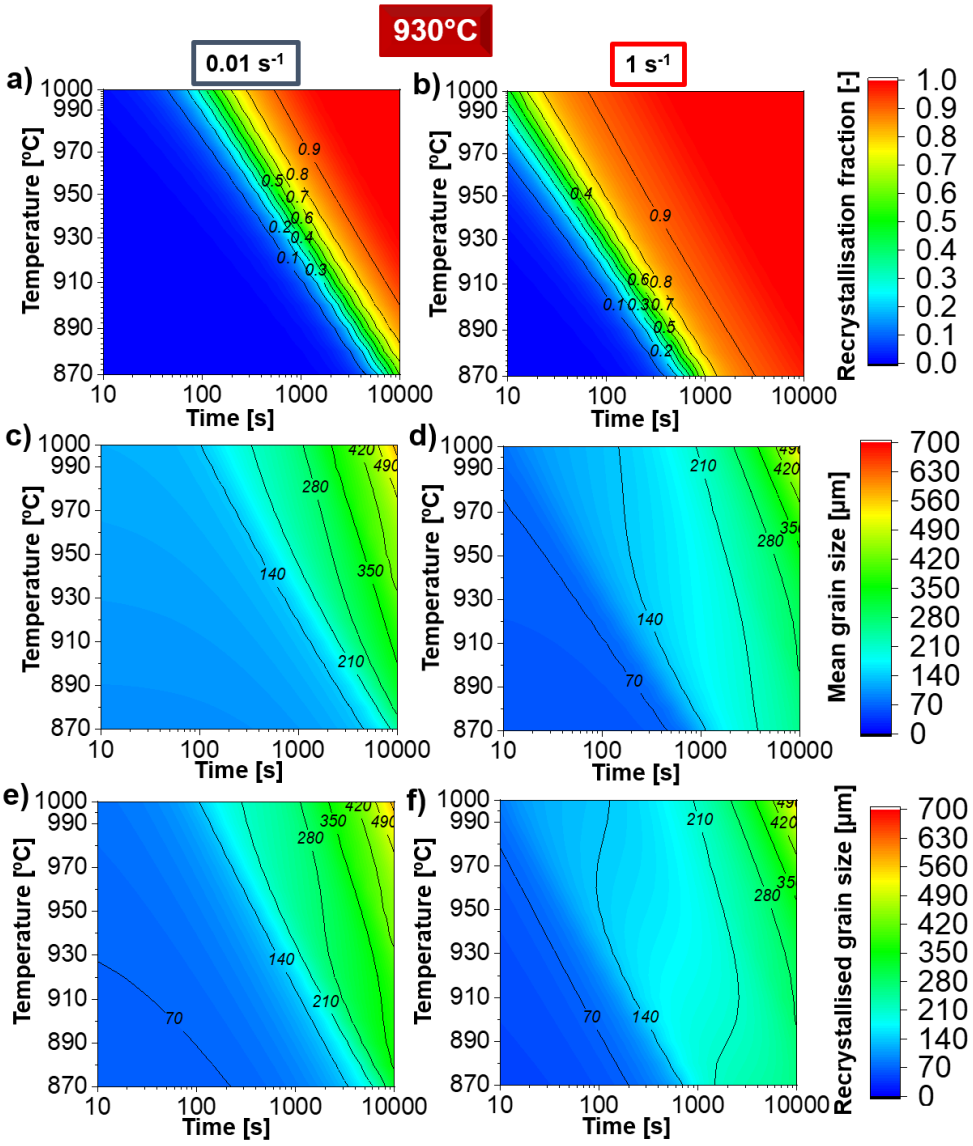

Figure 106: Contour maps for the recrystallisation fraction (a,b), mean grain size (c,d), recrystallised grain size (e,f) evolutions for the Ti-17 with a β-grain size before deformation of 500 µm for different temperatures up to 1 of strain for the strain rate of a,c,e) 0.01 s^{-1}; b,d,f) 1 s^{-1}. Hot deformation and annealing temperature are the same.

The influence of the deformation and annealing temperature on the formed mean β-grain size during SRX is shown in Figure 106(c,d). Two combined factors can explain the increase in grain size with an increase in temperature:

- Higher mobility of the HAGBs.
- Lower stored energy due to pronounced annihilation of dislocations via DRV and SRV.

For example, considering an initial grain size of 500 µm, a mean grain size of ~210 µm is predicted if the material is deformed at 870°C and 1 s^{-1} followed by annealing at the same temperature for 2 h. On the other hand, if the material is deformed at 1000°C and 0.01 s^{-1} followed by 2 h annealing also at 1000°C, the final mean grain size is predicted to be larger than 500 µm.

The influence of the temperature on the recrystallised grain size is shown in Figure 106 for an β-grain size before deformation of 500 µm, for a deformation up to the strain of 1. The iso-lines and the trends are as similar as for the mean grain size Figure 106(c,d).

14. Conclusions

Despite the complexity in terms of nucleation site localisation, supersaturation field description for the formation of the different morphologies of α-phase, the β→α transformation can be described as a competitive formation of different morphologies. The new conclusions with respect to the literature are highlighted in bold:

- Small α_P grow faster than large α_P particles and α_{GB} and α_{SEC}. A slight increase in radius for small α_P by the volumetric diffusion growth lead to higher consumption of the supersaturation of V compared to larger α_P
- **The nucleation of α_{SEC} increases with increasing cooling rate up to a limit around 300°C/min. Higher cooling rates promote the formation of α' and is related to the supersaturation of V in the β-phase**
- **Small variations in the cooling rate or the size of α_P lead to significant differences in the final fraction of the different α-morphologies**
- **Formation of α_{GB} occurs before α_{SEC}. However, its growth kinetics follows the same tendency than that of the α_{SEC}**

The hot deformation behaviour of two near-β alloys was investigated, and a physically-based model that couples the simultaneous role of SRV, DRV, CDRX, dynamic globularisation of the α-phase and load transfer is proposed. The new conclusions with respect to the literature are highlighted in bold:

- CDRX is the mechanism followed for β-phase during deformation that involves HAGB movement
- The formation of the substructure and the annihilation of the dislocations by DRV are the source mechanisms involved in the CDRX.
- **CDRX can be understood as the accommodation of the misorientation spread within the β-phase during deformation by the formation of LAGBs and its progressive increase in misorientation angle**
- CDRX does not occur homogeneously within the β-phase. Higher strain rates lead to localisation of the misorientation spread along the prior β/β boundaries
- High strain rates and a large fraction of α-phase lead to kinking and bending of the lamellas
- The formation of boundaries within α-platelets promote grooving and migration of α/β interfaces. The separation of the formed α-grains occurs due to the flow of material during plastic deformation
- **Globularisation kinetics of the α-phase is defined by the initial morphology and size of the α-platelets and the load transfer between α/β phases**
- **The rotation of α-phase with respect to the β-phase increase the misorientation spread formation in the vicinity of the α/β interfaces, accelerating CDRX of the β-phase**

Finally, the SRX behaviour of a Ti-17 alloy was investigated, and a coupled model with the hot deformation behaviour was developed. The conclusions are subdivided accordingly, and the new ones with respect to the literature are highlighted in bold:

- High strain rates produce high stores energy due to higher immobile dislocation density and finer substructure (higher wall dislocation density)
- Localisation of the deformation within the β-phase results in a heterogeneous distribution of dislocation within the β-grains. Different kinetics of strain induced boundary migration kinetics occurs: the regions near the prior β-HAGBs accumulate higher stored energy, and the nucleation is fast. Low stored energy at the centre of the β-grain leads to a decrease in the HAGB velocity of the formed recrystallised grains
- **The dependency of the velocity of HAGB on temperature is more pronounced for SRX than for CDRX.**

14.1. Novel insights from the simulations to be taken into account for microstructure design

14.1.1. Phase transformation in Ti-6Al-4V

- Strict microstructure control is probably not achievable for sizes of α_P ranging between 5 µm to 15 µm, typically observed in commercially hot deformed Ti-6Al-4V. A small variation in the initial microstructure or a slight difference in cooling rate results in the formation of different microstructures.

14.1.2. Hot deformation behaviour

- Larger initial β-grain sizes lead to a fast evolution of the fraction of HAGB for a given temperature and strain rate. However, It does not imply that the steady-state microstructure is reached instantaneously for an infinitely large β-grain size. The average boundary misorientation increases rapidly, but a reasonable strain is required for the steady-state condition.
- The strengthening caused by the dislocation walls is typically small but can be pronounced in the α+β domain compared to the β-domain due to the role of α-phase on enhancing CDRX in the β-phase. The strengthening increases with a decrease in initial β-grain size due to the slower microstructure evolution for larger initial β-grain size, respectively.
- The influence of the β-grain size on the hot deformation behaviour of the β-phase follows an opposite tendency if compared to materials where DDRX occurs instead of CDRX. In DDRX, the amount of nuclei that are formed is proportional to the surface density of HAGBs. Thus, finer starting grains leads to faster microstructure evolution in DDRX. In the case of CDRX, finer initial β-grains lead to faster annihilation of dislocations due to HAGB movement and the formation of a finer substructure. Thus, higher strains are required to achieve a steady-state condition
- The starting condition of the substructure plays a vital role in its evolution due to CDRX. The microstructure evolves faster via CDRX if the deformation occurs in a fully

recrystallised microstructure (large $S^0_{v_{HAGB}}/S^0_{v_{LAGB}}$) considering the same initial grain size and the same initial mean boundary misorientation angle

- A physically-based model is proposed to describe the globularisation of the α-phase: the separate phenomena of formation of boundaries within α-phase, the formation of α/β boundaries, and the growth of the formed α-particles
- Thinner initial α-platelets promote not only a faster CDRX but also the formation of a finer β-microstructure.

14.1.3. Static recrystallisation behaviour

- It can be concluded from the simulated results that a significative grain refinement will not be achieved with one step of deformation followed by annealing for the investigated Ti-17 alloy. A repetition of deformation at lower temperatures followed by short heat treatments at slightly higher temperature aiming to maximize the number of formed nuclei could provide a path for grain refinement and also guarantee that the final microstructure is fully statically recrystallised.

15. Outlook

15.1. Phase transformation

A simple coupled model to describe the phase transformation in Ti-6Al-4V is proposed. The model is based on the exact solution of diffusion equations. It would be interesting to compare the results with modelling approaches such as phase field that are able to predict the formation of complex shape phases in complex supersaturation field. Moreover, the formation of martensite is not implemented in the proposed model. It could be the next step to implement the massive martensitic transformations into the proposed model.

Despite the investigations being conducted only for continuous cooling, the dissolution of α-phase during heating is also an issue in the processing. A comprehensive model should be able to incorporate the dissolution, growth during isothermal or heating (Ostwald-Ripening), and formation of α-phase during cooling. An extension of this approach would be to include the transformation of α' into α-phase, an essential topic for the emerging additive manufactured components of Ti alloys. The model can also be applied to the near-β alloys and other α+β alloys despite becoming more complicated due to the presence of two types of α_{SEC}: formed inside the β-grains and from the β/β grain boundaries.

15.2. Hot deformation

The hot deformation of the near-β Ti alloys was investigated for compression. Here, several possibilities can be explored in the attempt to develop a unified and comprehensive model as well as material behaviour understanding:

- Investigate the hot tension, hot torsion behaviour and plain strain of the same near-β alloys, to better understand the effect of the dependency of the CRSS on the deformation mode. Moreover, texture evolution needs to be further investigated
- The proposed model is validated for hot compression tests, thus, lower strains. For further validation, larger strains are required, for example, using torsion experiments
- The model predicts the formation of a homogeneous microstructure. The deformation at higher strain rates deviates from this assumption. The understanding of the related factors could be extracted from crystal plasticity or discrete dislocation dynamics modelling
- Despite the physical concepts of each rate equation for the dislocation reactions, some fitting parameters are still existing in the current modelling approach. A better understanding of the material behaviour and dislocation mechanics with other approaches can enable the physical modelling of these parameters
- The role of load transfer and its dependency on the initial microstructure is clarified. However, it is still unclear the role of the back-stress. More in-depth investigations on this topic could be of interest
- The proposed model seems to be comprehensive to describe the hot deformation behaviour of Ti-alloys in general. It would be of interest to be implemented for other alloys,

especially the α+β or near α-alloys to improve the understanding of the hot deformation behaviour of the α-phase

- More sophisticated algorithms of homogenisation and optimisation can be developed to enhance the predictability of the developed model
- The fitting parameters of the developed model are currently adjusted manually. Sensitivity analysis is necessary to understand better the influence of each fitting parameter on the predictability of the models.
- A criterion and automatization of the fitting routine is necessary and could also lead to a minimisation of the error between measured and simulated values.
- The current approach needs to be further validated considering other kinetics of deformation, such as creep, stress relaxation and severe plastic deformation. The phenomena of CDRX will be not prevalent in most cases.
- Testing the coupled models for an industrial process followed by microstructural validation is needed.

15.3. Static recrystallisation

- The influence of α-phase on the microstructure evolution during heat treatments in the α+β domain is needed to understand and properly model the role of α-phase on pinning the β-HAGBs.
- The combination of hot torsion followed by static recrystallisation could lead to a better understanding of the role of the stored energy on nucleation rate and grain refinement since the heterogeneity within β-grains can be minimised and the initial β-grain size is smaller.
- Better predictions and a better understanding of the strain induced boundary migration could also be investigated using cellular automata or crystal plasticity-based models to describe further the role of heterogeneity of deformation and the mechanisms for bulging of the nuclei

16. Appendixes

Appendix A

A Matlab® routine was developed to implement the model to couple the growth of the α_p and the formation and growth of α_{GB} and α_{SEC}. The used parameters are listed in Table A. 1, and the procedure for the fitting of the model parameters is schematically shown in Figure A. 1. The parameters were adjusted manually, aiming to minimise the error between the available measured data and the simulated one. The accuracy relies on the measured data, and on the equilibrium fraction of α-phase, calculated using JMatPro® v.10.

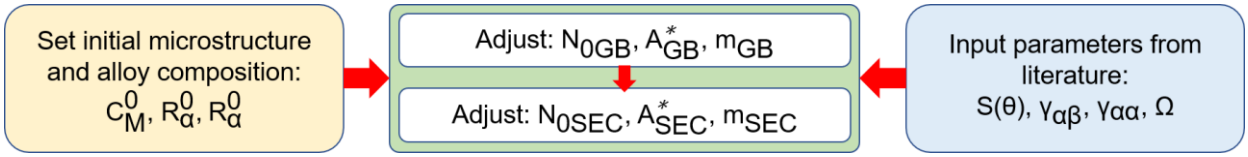

Figure A. 1: Schematic procedure for the fitting of the parameters used in the model of phase transformation in Ti-6Al-4V.

Table A. 1: List of the parameters used for the modelling of the growth of α_P and formation and growth of α_{GB} and α_{SEC}.

Description	Parameter	Value	Reference
V concentration in the alloy	C_0	4.21	Chemical composition measurement
V concentration in α-phase	C_P, $C_P^{\alpha_{GB}}$, $C_P^{\alpha_{SEC}}$	2.0	[11]
V concentration at the α/β interface	C_I	Function of temperature	Calculated with JMatPro® v.10
Pre-exponent nucleation parameter for α_{GB}	N_{0GB}	$6.9 \cdot 10^4$	Empirical from this work
Reference grain size for the nucleation of α_{GB}	GS_0	35 μm	Fitting parameter. This work
Pre-exponent nucleation parameter for α_{SEC}	N_{0SEC}	$6x10^7$	Fitting parameter. This work
Parameter for the activation energy of nucleation for α_{GB}	A^*_{GB}	$2.79x10^3$	Fitting parameter. This work
Parameter for the activation energy of nucleation for α_{SEC}	A^*_{SEC}	$8.35x10^3$	Fitting parameter. This work
Parameter for the activation energy of nucleation for sympathetic growth	A_{SYM}	$1.39x10^4$	[10]

Parameter for activation energy for nucleation at α/β interface	$A_{\alpha\beta}$	$1.27x10^{3}$	[23]
α/β interface energy	$\gamma_{\alpha\beta}$	0.10 J/m^2	[23]
α/ α interface energy	$\gamma_{\alpha\alpha}$	0.30 J/m^2	[10]
Ti atomic volume	Ω	$1.0896x10^{-5}$	[10]
Shape factor	S(θ)	0.001728	[23]
Activation energy for diffusion	Q	145.17 kJ/mol	[11]
Activity coefficient	$\frac{\partial V}{\partial C_l}\frac{C_l}{V}$	0.9	[11]
Ledge coefficient for α_{GB} growth	m_{GB}	5	Fitting parameter. This work
Ledge coefficient for α_{SEC} growth	m_{SEC}	3	Fitting parameter. This work

Appendix B

A Matlab® routine was developed to implement the hot deformation model described in section 7.2 with the rate equations described in section 7.2.6.1 for the Ti-5553 alloy. The used parameters are listed in Table B. 1, and the procedure for the fitting of the model parameters is schematically shown in Figure B. 1. The parameters were adjusted manually, aiming to minimise the error between the available measured data and the simulated one. The parameters related to the change in load partitioning ($A_{iso-\sigma}$ and n_s) depends on the morphology and distribution of the α-phase, thus on the initial microstructure. The other constants and parameters are material properties and can be considered independent on the thermomechanical history of the material. However, different solutions can be obtained for those material parameters, especially the n and θ_0. If n is selected as 2, a large value of θ_0 is adjusted, and vice-versa.

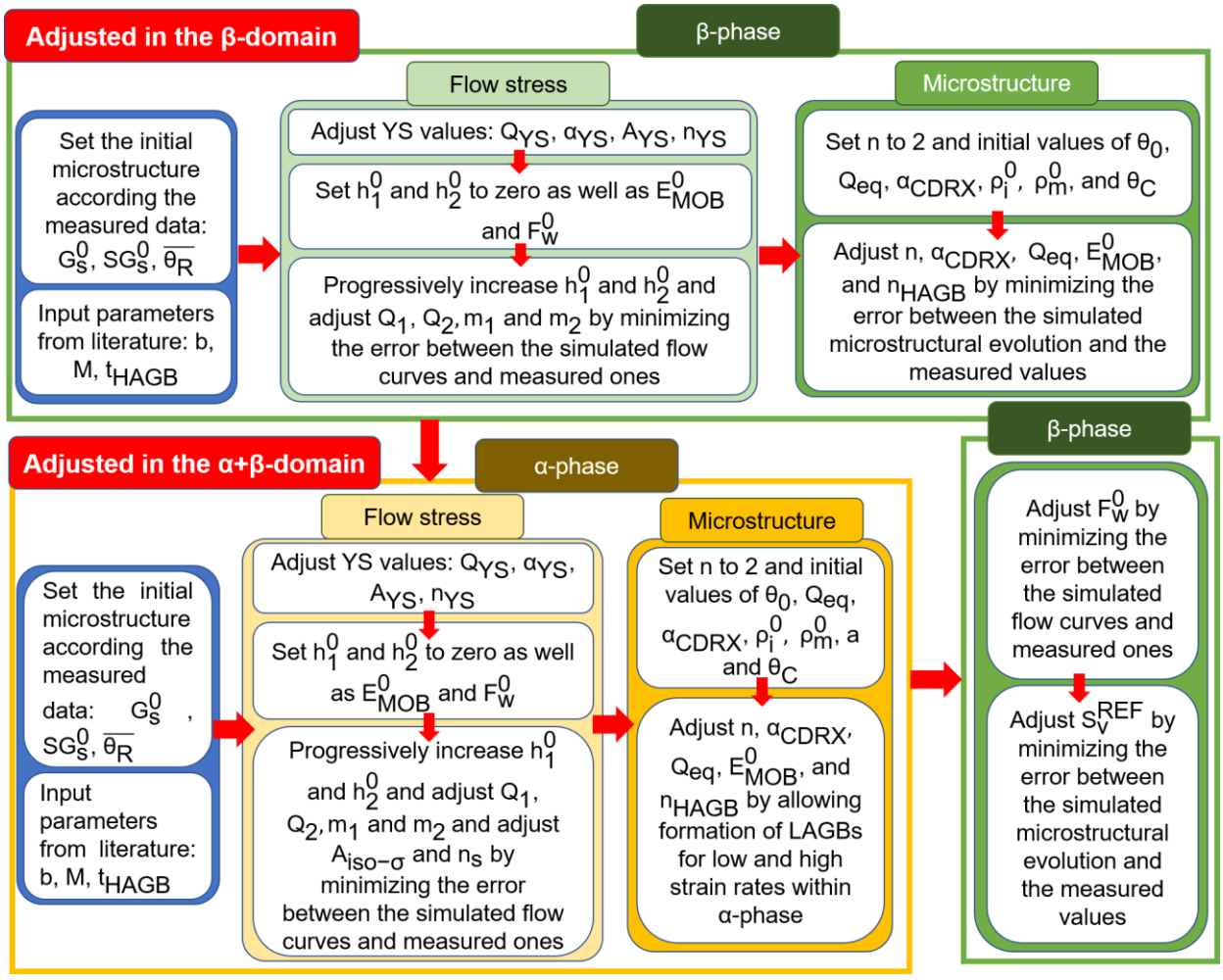

Figure B. 1: Schematic procedure for the fitting of the parameters used in the model of hot deformation applied to the Ti-5553, as discussed in chapter 9.

Table B. 1: Internal variables, parameters, constants and initialisation parameters used in the developed model for the hot deformation of the Ti-5553 alloy.

		α-phase	β-phase
Initial microstructure	G_s^0 in α+β domain [μm]	3 μm	300 μm
	G_s^0 in β domain [μm]	-	200 μm
	SG_s^0 in α+β domain [μm]	3 μm	$1.5x\lambda_{interparticle}$
	SG_s^0 in β domain [μm]	-	200μm
	$\overline{\theta_R}$ in α+β domain [°]	0.1°	4°
	$\overline{\theta_R}$ in β domain [°]	-	0.1°
Parameters fitted from a range established in the literature	α_{CDRX} [-]	0.4	0.2
	Q_{eq} [J/mol]	$1.97x10^5$	$1.97x10^5$
	n [-]	30	30
	θ_0 [°]	1	0.8
	θ_C [°]	12°	12°
	$\dot{\varepsilon}_{ref}$ [s^{-1}]	$1x10^5$	$1x10^5$
Parameters obtained from literature	b [nm]	0.295	0.286
	M [-]	5	3.05
	t_{HAGB} [m] [202]	$3.6x10^{-9}$	$3.6x10^{-9}$
Parameters obtained experimentally	Q_{YS} [J/mol]	$1.58x10^5$	$2.38x10^5$
	α_{YS} [MPa^{-1}]	$2.85x10^{-3}$	$1.16x10^{-2}$
	A_{YS} [s^{-1}]	$2.22x10^6$	$2.17x10^9$
	n_{YS} [-]	3.33	3.23
Parameters fitted	Q_1 [J/mol]	$1.2x10^4$	$1.2x10^4$
	Q_2 [J/mol]	$1.2x10^4$	$1.2x10^4$
	h_1^0 [m^{-2}]	$2x10^{16}$	$4.80x10^{16}$
	h_2^0 [-]	0.3	1.3
	E_{MOB}^0 [W/m]	$6x10^1$	$3.5x10^2$
	n_{HAGB} [-]	0.4	0.4
	F_w^0 [-]	0.03	0.03
	m_1 [-]	0.33	0.33
	m_2 [-]	0.33	0.33
	$A_{iso\text{-}stress}$ [-]	0.06	
	n_s [-]	3	

Appendix C

An algorithm is developed to limit the thermal stress to a constant value for a fixed strain rate and temperature (Equation 48 in the β-domain and Equation 58 in the α+β domain), Figure C. 1.

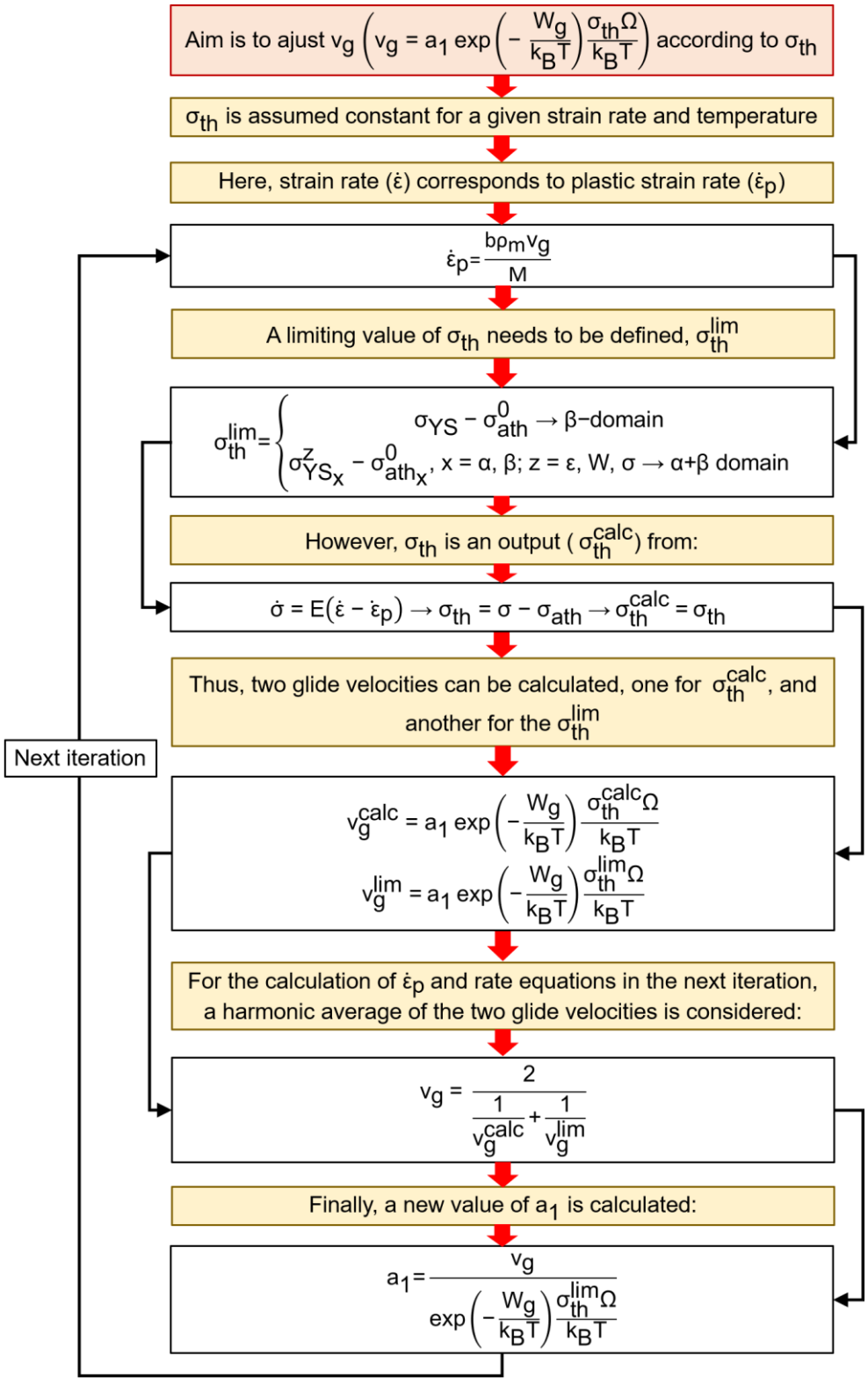

Figure C. 1: Algorithm developed to limit and link the thermal stress with the glide velocity.

Appendix D

A Matlab® routine was developed to implement the hot deformation model described in section 7.2 with the rate equations described in section 7.2.6.2 for the Ti-5553 alloy. The used parameters are listed in Table D. 1, and the procedure for the fitting of the model parameters is schematically shown in Figure D. 1. The parameters were adjusted manually, aiming to minimise the error between the available measured data and the simulated one. The parameters related to the change in load partitioning ($A_{iso-\sigma}$ and n_s) depends on the morphology and distribution of the α-phase, thus on the initial microstructure. The other constants and parameters are material properties and can be considered independent on the thermomechanical history of the material. However, different solutions can be obtained for those material parameters, especially the n and θ_0 as mentioned in

Appendix B.

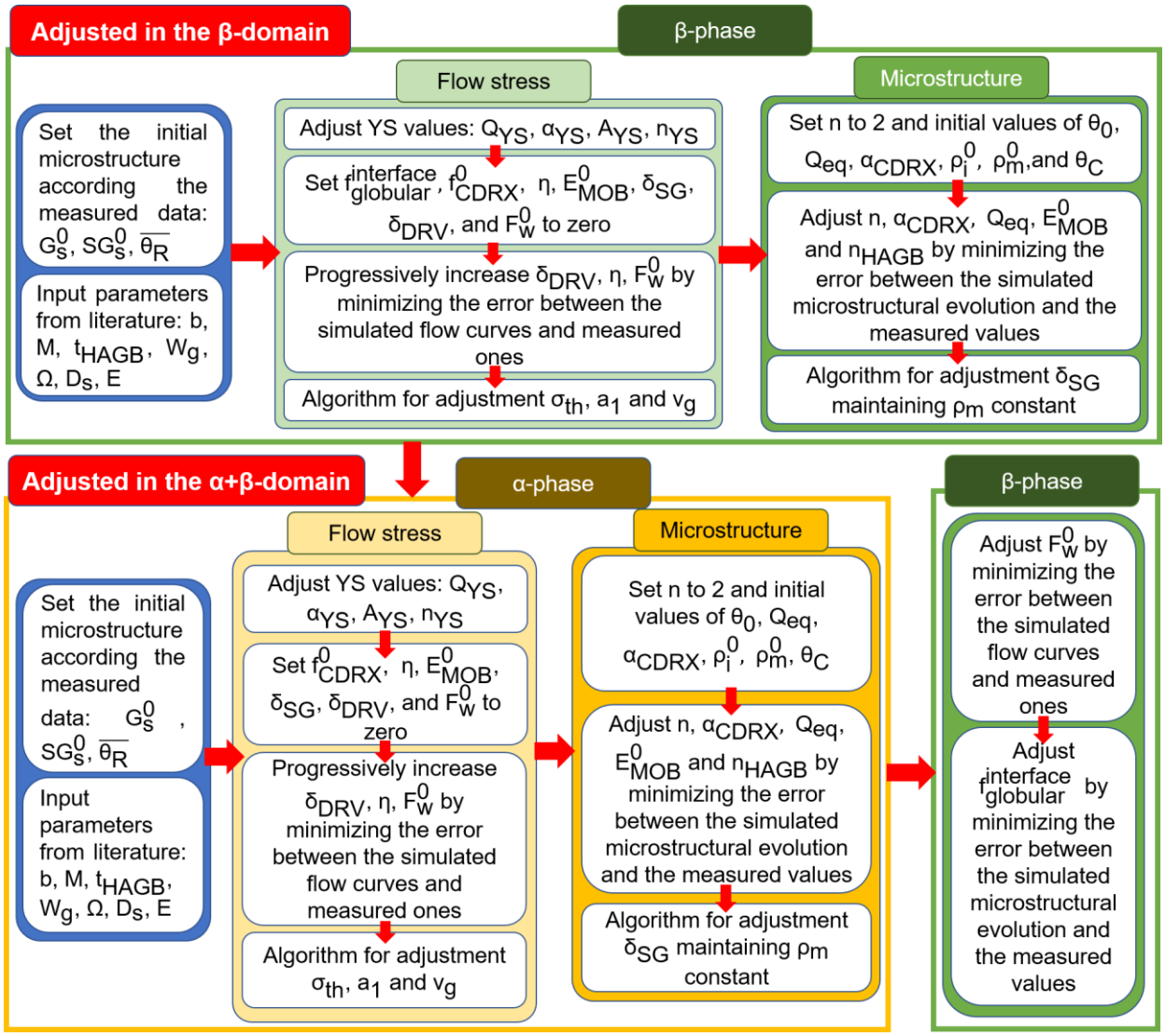

Figure D. 1: Schematic procedure for the fitting of the parameters used in the model of hot deformation applied to the Ti-5553, as discussed in chapter 10.

Table D. 1: Internal variables, parameters, constants and initialisation parameters used in the developed model for the hot deformation of the Ti-5553 alloy.

		α-phase	β-phase
Initial microstructure	G_s^0 in α+β domain [μm]	3 μm	300 μm
	G_s^0 in β domain [μm]	-	200 μm
	SG_s^0 in α+β domain [μm]	3 μm	$1.5x\lambda_{interparticle}$
	SG_s^0 in β domain [μm]	-	200μm
	$\overline{\theta_R}$ in α+β domain [°]	0.1°	4°
	$\overline{\theta_R}$ in β domain [°]	-	0.1°
Parameters fitted from a range	α_{CDRX} [-]	0.4	0.2
	Q_{eq} [J/mol]	$1.97x10^5$	$1.97x10^5$
	n [-]	30	30

established in the literature	θ_0 [°]	1	0.8
	θ_C [°]	12°	12°
	$\dot{\varepsilon}_{ref}$ [s^{-1}]	$1x10^6$	$1x10^6$
Parameters obtained from literature	b [nm]	0.295	0.286
	M [-]	5	3.05
	Ω [m3]	$1.7668x10^{-29}$	$1.7668x10^{-29}$
	t_{HAGB} [m] [202]	$3.6x10^{-9}$	$3.6x10^{-9}$
Parameters obtained experimentally	Q_{YS} [J/mol]	$1.58x10^5$	$2.38x10^5$
	α_{YS} [MPa^{-1}]	$2.85x10^{-3}$	$1.16x10^{-2}$
	A_{YS} [s^{-1}]	$2.22x10^6$	$2.17x10^9$
	n_{YS} [-]	3.33	3.23
Parameters fitted	W_g [J/mol]	$2.1x10^5$	$2.1x10^5$
	δ_{DRV} [m^{-2}]	$6.75x10^{-7}(\dot{\varepsilon}/\dot{\varepsilon}_{ref})^{-0.125}$	$5.62x10^{-7}(\dot{\varepsilon}/\dot{\varepsilon}_{ref})^{-0.125}$
	H [-]	0.002	0.002
	E^0_{MOB} [W/m]	-	60
	η_{HAGB} [-]	-	0.65
	f^0_{CDRX} [-]	0.02	0.125
	A_{REF} [-]	-	$1 x10^{10}$
	$A_{iso\text{-}stress}$ [-]	0.06	
	n_s [-]	3	

Appendix E

A Matlab® routine was developed to implement the deformation model described in section 7.2, with the rate equations described in section 7.2.6.2. The dynamic globularisation, as described in section 7.2.9, is also implemented for the hot compression behaviour of the Ti-17 alloy. The used parameters are listed in Table E. 1, and the procedure for the fitting of the model parameters is schematically shown in Figure E. 1. The parameters were adjusted manually, aiming to minimise the error between the available measured data and the simulated one. Different from the Ti-5553, here the process of change in load partitioning is correlated with the physically-based process of dynamic α-globularisation. Thus, the constants and parameters are material properties and independent on the thermomechanical history of the material. However, different solutions can be obtained for those material parameters, especially the n and θ_0 as mentioned in

Appendix B. Moreover, the adjustment of the parameters related to the dynamic α-globularisation (A_{glob} and B_{glob}) is strongly influenced by the initial aspect ratio considered for the α-platelets prior to deformation.

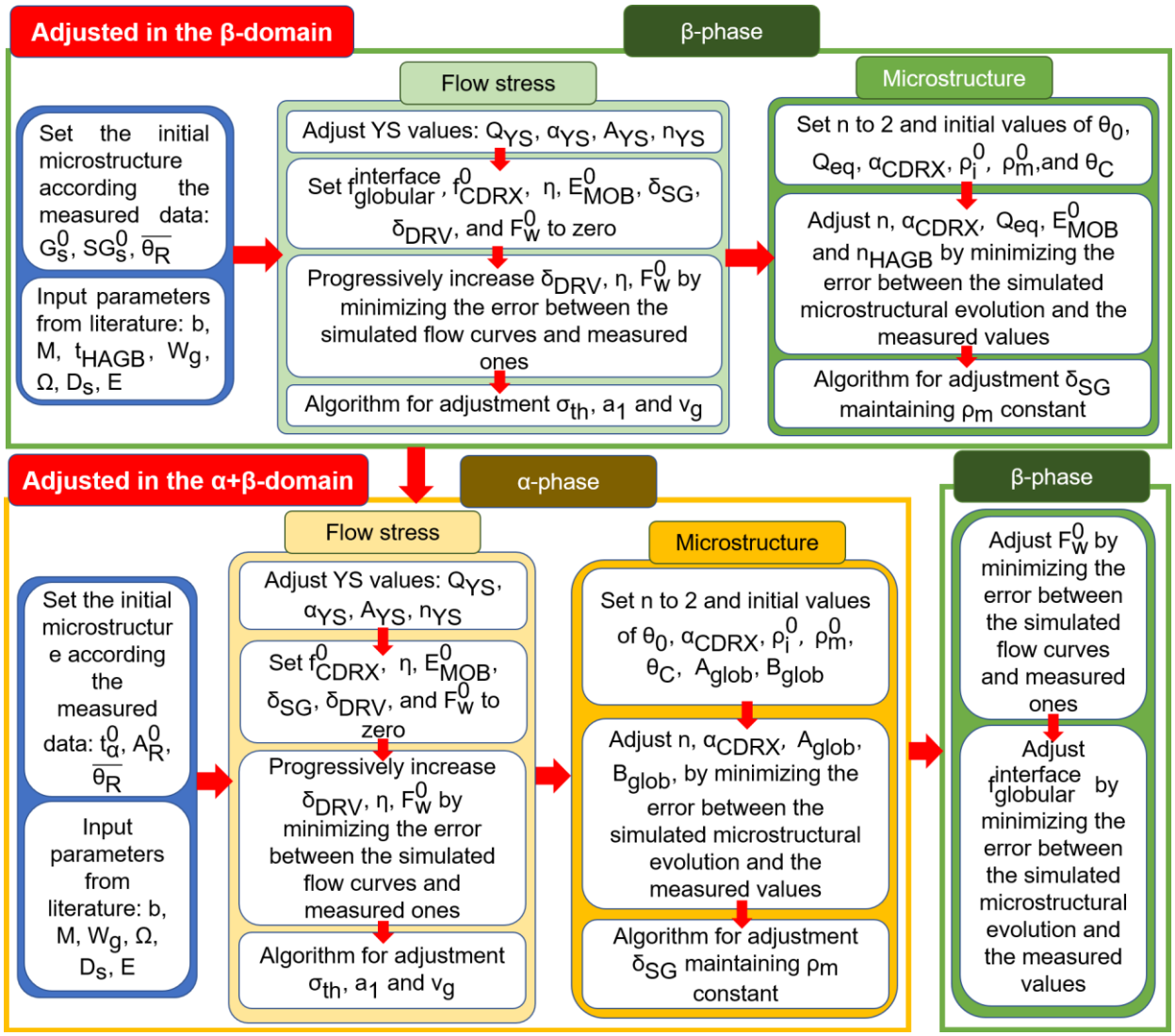

Figure E. 1: Schematic procedure for the fitting of the parameters used in the model of hot deformation applied to the Ti-17, as discussed in chapter 11.

Table E. 1: Internal variables, parameters, constants and initialisation parameters used in the developed model oh hot deformation for the Ti-17 alloy.

		α-phase	β-phase
Initial microstructure	G_s^0 in α+β domain [μm]	-	500 μm
	G_s^0 in β domain [μm]	-	500 μm
	SG_s^0 in α+β domain [μm]	-	250 μm
	SG_s^0 in β domain [μm]	-	250 μm
	t_α [μm]	0.3	-
	$\overline{\theta_R}$ in α+β domain [°]	0.4°	0.5°
	$\overline{\theta_R}$ in β domain [°]	-	0.01°

Parameters fitted from a range established in the literature	α_{CDRX} [-]	0.15	0.19
	Q_{eq} [J/mol]	$1.97x10^{5}$	$1.97x10^{5}$
	n [-]	15	30
	θ_0 [°]	0.2	0.7
	θ_C [°]	12°	12°
	$\dot{\varepsilon}_{ref}$ [s^{-1}]	$1x10^{6}$	$1x10^{6}$
Parameters obtained from literature	b [nm]	0.295	0.286
	M [-]	5	3.05
	Ω [m3]	$1.7668x10^{-29}$	$1.7668x10^{-29}$
	t_{HAGB} [m] [202]	$3.6x10^{-9}$	$3.6x10^{-9}$
Parameters obtained experimentally	Q_{YS} [J/mol]	$1.58x10^{5}$	$2.38x10^{5}$
	α_{YS} [MPa^{-1}]	$2.80x10^{-3}$	$1.85x10^{-2}$
	A_{YS} [s^{-1}]	$1.78x10^{6}$	$1.80x10^{6}$
	n_{YS} [-]	4.24	2.94
Parameters fitted	W_g [J/mol]	$2.1x10^{5}$	$2.1x10^{5}$
	δ_{DRV} [m^{-2}]	$3.20x10^{-7}(\dot{\varepsilon}/\dot{\varepsilon}_{ref})^{-0.065}$	$3.50x10^{-7}(\dot{\varepsilon}/\dot{\varepsilon}_{ref})^{-0.07756}$
	η [-]	0.002	0.002
	E^{0}_{MOB} [W/m]	-	24000
	η_{HAGB} [-]	-	0.65
	f^{0}_{CDRX} [-]	0.02	0.0075
	A_{glob} [-]	400	-
	B_{glob} [-]	0.03	

Appendix F

A Matlab® routine was developed to implement the deformation model described in section 7.2, with the rate equations described in section 7.2.6.1. The dynamic globularisation, as described in section 7.2.9, is also implemented for the hot compression behaviour of the Ti-17 alloy. The model is coupled with the mesoscale model for SRX, as described in section 7.3. The used parameters for the hot deformation are listed in Table F. 1, and the procedure for the fitting of the model parameters is schematically shown in Figure F. 1. The parameters were adjusted manually, aiming to minimise the error between the available measured data and the simulated one. Here, A_{SRX} and B_{SRX} are adjusted using the simulated deformation model. Thus, different adjustments on the hot deformation model can lead to variations on the fitting of A_{SRX} and B_{SRX}. The other constants and parameters are material properties and independent on the thermomechanical history of the material. However, different solutions can be obtained for those material parameters, especially the n and θ_0. If n is selected as 2, a large value of θ_0 is adjusted, and vice-versa.

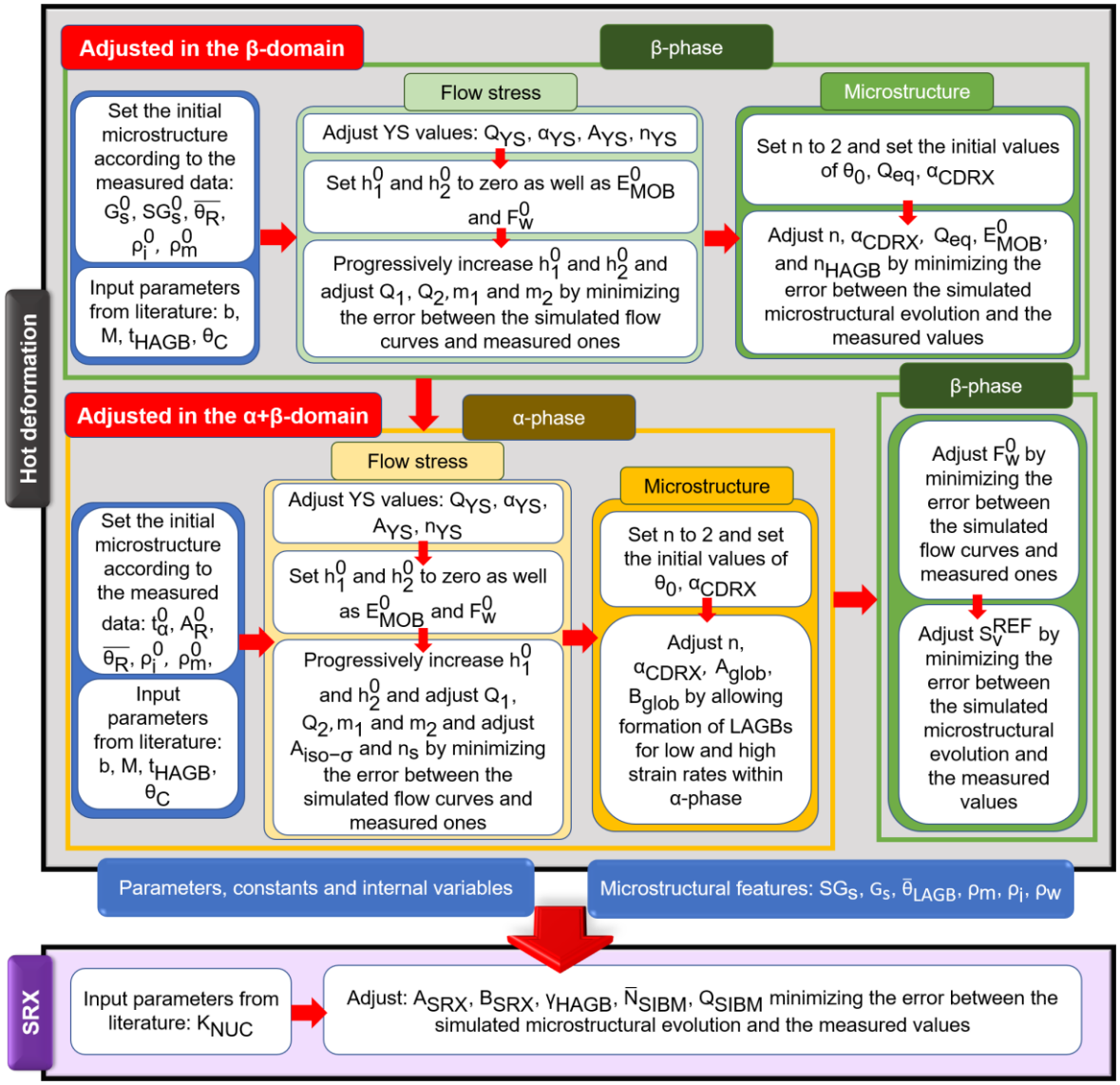

Figure F. 1: Schematic procedure for the fitting of the parameters used in the model of hot deformation followed by static recrystallisation (SRX) applied to the Ti-17, as discussed in chapter 12.

Table F. 1: Internal variables, parameters, constants and initialisation parameters used in the developed model for hot deformation of Ti-17 alloy.

		α-phase	β-phase
Initial microstructure	G_s^0 in α+β domain [μm]	-	500 μm
	G_s^0 in β domain [μm]	-	500 μm
	SG_s^0 in α+β domain [μm]	-	250 μm
	SG_s^0 in β domain [μm]	-	250 μm
	t_α [μm]	0.3	-
	$\overline{\theta_R}$ in α+β domain [°]	0.06	0.1
	$\overline{\theta_R}$ in β domain [°]	-	0.1
Parameters fitted from a range established in the literature	α_{CDRX} [-]	0.25	0.215
	Q_{eq} [J/mol]	$1.97x10^5$	$1.97x10^5$
	n [-]	15	18
	θ_0 [°]	0.8	0.8
	θ_C [°]	12°	12°
	$\dot{\varepsilon}_{ref}$ [s^{-1}]	$1x10^6$	$1x10^6$
Parameters obtained from literature	b [nm]	0.295	0.286
	M [-]	5	3.05
	Ω [m3]	$1.7668x10^{-29}$	$1.7668x10^{-29}$
	t_{HAGB} [m] [202]	$3.6x10^{-9}$	$3.6x10^{-9}$
Parameters obtained experimentally	Q_{YS} [J/mol]	$1.58x10^5$	$2.38x10^5$
	α_{YS} [MPa^{-1}]	$2.80x10^{-3}$	$1.85x10^{-2}$
	A_{YS} [s^{-1}]	$1.78x10^6$	$1.80x10^6$
	n_{YS} [-]	4.24	2.94
Parameters fitted	Q_1 [J/mol]	$1.2x10^4$	$1.2x10^4$
	Q_2 [J/mol]	$1.2x10^4$	$1.2x10^4$
	h_1^0 [m^{-2}]	$2.2x10^{16}$	$4.0x10^{14}$
	h_2^0 [-]	0.003	11
	E_{MOB}^0 [W/m]	-	$2x10^4$
	n_{HAGB} [-]	-	0.65
	F_w^0 [-]	0.01	0.01
	m_1 [-]	0.08	0.08
	m_2 [-]	0.6	0.08
	A_{glob} [-]	400	-
	B_{glob} [-]	0.003	

The additional or modified parameters for the SRX model are listed in Table A.2.

Table A.2: Internal variables, parameters, constants and initialisation parameters used in the developed model for SRX of Ti-17 alloy.

Parameters fitted from a range established in the literature	Q_{eq} [J/mol]	$4.12x10^5$
	Q_{SIBM} [J/mol]	$6.25x10^5$
	γ_{HAGB} [J/m^2]	1
Parameters obtained from the literature	t_{HAGB} [nm] [202]	1.5
Parameters fitted	$\bar{N}_{SIBM}$ [-]	$1.5x10^{21}$

Appendix G

During SRX the average subgrain size is calculated considering the average boundary density using a simple law of mixture for the recrystallised fraction (X_{SRX}) and deformed one ($1 - X_{SRX}$), Equation D. 1 to Equation D. 3.

$$\bar{S}_v = X_{SRX}\bar{S}_{v_{SIBM}} + (1 - X_{SRX})S_v \qquad \textit{Equation D. 1}$$

$$\frac{2}{\overline{SG}_s} = X_{SRX}\frac{2}{G_{SIBM}} + (1 - X_{SRX})\frac{2}{SG_s} \qquad \textit{Equation D. 2}$$

$$\overline{SG}_s = \frac{G_{SIBM}SG_s}{X_{SRX}SG_s + (1 - X_{SRX})G_{SIBM}} \qquad \textit{Equation D. 3}$$

Similarly, the average grain size is calculated considering the average HAGB density using a simple law of mixture for the recrystallised fraction (X_{SRX}) and deformed one ($1 - X_{SRX}$), Equation D. 4 to Equation D. 6

$$\bar{S}_{v_{HAGB}} = X_{SRX}\bar{S}_{v_{HAGB_{SIBM}}} + (1 - X_{SRX})S_{v_{HAGB}} \qquad \textit{Equation D. 4}$$

$$\frac{2}{\bar{G}_s} = X_{SRX}\frac{2}{G_{SIBM}} + (1 - X_{SRX})\frac{2}{G_s} \qquad \textit{Equation D. 5}$$

$$\bar{G}_s = \frac{G_{SIBM}G_s}{X_{SRX}G_s + (1 - X_{SRX})G_{SIBM}} \qquad \textit{Equation D. 6}$$

17. References

[1] G. Lütjering, J.C. Williams, Titanium, Springer Berlin Heidelberg, Berlin, Heidelberg, 2007. https://doi.org/10.1007/978-3-540-73036-1.

[2] M. Peters, J. Hemptenmacher, J. Kumpfert, C. Leyens, Structure and Properties of Titanium and Titanium Alloys, in: Titan. Titan. Alloy., John Wiley & Sons, Ltd, 2005: pp. 1–36. https://doi.org/10.1002/3527602119.ch1.

[3] H. Sibum, Titanium and Titanium Alloys – From Raw Material to Semi-finished Products, in: Titan. Titan. Alloy., John Wiley & Sons, Ltd, 2005: pp. 231–244. https://doi.org/10.1002/3527602119.ch7.

[4] G. Terlinde, T. Witulski, G. Fischer, Forging of Titanium, in: Titan. Titan. Alloy., John Wiley & Sons, Ltd, 2005: pp. 289–304. https://doi.org/10.1002/3527602119.ch11.

[5] Metallurgical Materials Science and Alloy Design - Titanium alloys, (n.d.). http://www.dierk-raabe.com/titanium-alloys/ (accessed July 2, 2017).

[6] R.I. Jaffee, H.M. Burte, Metallurgical Society of AIME., Titanium science and technology; proceedings., Plenum Press, New York, 1973.

[7] R. Pederson, Microstructure and Phase Transformation of Ti-6Al-4V, (2002) 1–62. https://doi.org/LTU-LIC-0230-SE.

[8] X. Gao, W. Zeng, S. Zhang, Q. Wang, A study of epitaxial growth behaviors of equiaxed alpha phase at different cooling rates in near alpha titanium alloy, Acta Mater. 122 (2017) 298–309. https://doi.org/10.1016/j.actamat.2016.10.012.

[9] S.L. Semiatin, S.L. Knisley, P.N. Fagin, F. Zhang, D.R. Barker, Microstructure evolution during alpha-beta heat treatment of Ti-6Al-4V, Metall. Mater. Trans. A Phys. Metall. Mater. Sci. 34 A (2003).

[10] M. Meng, X.G. Fan, H. Yang, L.G. Guo, M. Zhan, P.F. Gao, Precipitation of secondary alpha in competition with epitaxial growth of primary alpha in two-phase titanium alloys, J. Alloys Compd. 714 (2017) 294–302. https://doi.org/https://doi.org/10.1016/j.jallcom.2017.04.209.

[11] Z. Sun, X. Li, H. Wu, H. Yang, A unified growth model of the secondary grain boundary α phase in TA15 Ti-alloy, J. Alloys Compd. 689 (2016) 693–701. https://doi.org/10.1016/j.jallcom.2016.08.013.

[12] N. Kherrouba, M. Bouabdallah, R. Badji, D. Carron, M. Amir, Beta to alpha transformation kinetics and microstructure of Ti-6Al-4V alloy during continuous cooling, Mater. Chem. Phys. 181 (2016) 462–469. https://doi.org/https://doi.org/10.1016/j.matchemphys.2016.06.082.

[13] M. Enomoto, H.I. Aaronson, T. Furuhara, Thickening of grain-boundary $α$ allotriomorphs in a Ti-Cr alloy by multiple sets of ledges, Metall. Trans. A. 22 (1991) 1341–1348. https://doi.org/10.1007/BF02660667.

[14] E.S.K. Menon, H.I. Aaronson, Nucleation, growth, and overall transformation kinetics of grain boundary allotriomorphs of proeutectoid alpha in Ti-3.2 At. Pct Co and Ti-6.6 At. Pct Cr alloys, Metall. Mater. Trans. A. 17 (1986) 1703–1715. https://doi.org/10.1007/BF02817269.

[15] C. Atkinson, A mathematical method for the calculation of ledge growth kinetics, Metall. Trans. A. 22 (1991) 1211–1218. https://doi.org/10.1007/BF02660652.

[16] M. Enomoto, Computer simulation of morphological changes of grain boundary precipitates growing by the ledge mechanism, Metall. Trans. A. 22 (1991) 1235–1245. https://doi.org/10.1007/BF02660655.

[17] K.J. Song, Y.H. Wei, Z.B. Dong, X.Y. Wang, W.J. Zheng, K. Fang, Cellular Automaton

Modeling of Diffusion, Mixed and Interface Controlled Phase Transformation, J. Phase Equilibria Diffus. 36 (2015) 136–148. https://doi.org/10.1007/s11669-015-0369-3.

[18] Q. Chen, N. Ma, K. Wu, Y. Wang, Quantitative phase field modeling of diffusion-controlled precipitate growth and dissolution in Ti–Al–V, Scr. Mater. 50 (2004) 471–476. https://doi.org/https://doi.org/10.1016/j.scriptamat.2003.10.032.

[19] B. Appolaire, L. Héricher, E. Aeby-Gautier, Modelling of phase transformation kinetics in Ti alloys – Isothermal treatments, Acta Mater. 53 (2005) 3001–3011. https://doi.org/https://doi.org/10.1016/j.actamat.2005.03.014.

[20] G.W. Mei Yang Tao Liu, Wen-Juan Zhao, Dong-Sheng Xu, Quantitative Phase Field Simulation of *α* Particle Dissolution in Ti-6Al-4V Alloys Below *β* Transus Temperature, Acta Metall. Sin. Lett. 30 (n.d.) 745–752. http://www.amse.org.cn.

[21] M. Meng, H. Yang, X.G. Fan, S.L. Yan, A.M. Zhao, S. Zhu, On the modeling of diffusion-controlled growth of primary alpha in heat treatment of two-phase Ti-alloys, J. Alloys Compd. 691 (2017) 67–80. https://doi.org/10.1016/j.jallcom.2016.08.218.

[22] V. Raghavan, Solid State Phase Transformations, PHI Learning Private Limited, Delhi, 1987.

[23] I. Katzarov, S. Malinov, W. Sha, Finite element modeling of the morphology of $β$ to $α$ phase transformation in Ti-6Al-4V alloy, Metall. Mater. Trans. A. 33 (2002) 1027–1040. https://doi.org/10.1007/s11661-002-0204-4.

[24] M. Ahlers, Stacking fault energy and mechanical properties, Metall. Trans. 1 (1970) 2415–2428. https://doi.org/10.1007/BF03038369.

[25] Z.C.C. Sun, H.L.L. Wu, J. Cao, Z.K.K. Yin, Modeling of continuous dynamic recrystallization of Al-Zn-Cu-Mg alloy during hot deformation based on the internal-state-variable (ISV) method, Int. J. Plast. 106 (2018) 73–87.

[26] F.J. Humphreys, M. Hatherly, F.J. Humphreys, M. Hatherly, Chapter 13 – Hot Deformation and Dynamic Restoration, in: Recryst. Relat. Annealing Phenom., 2004: pp. 415–V. https://doi.org/10.1016/B978-008044164-1/50017-7.

[27] T. Takaki, C. Yoshimoto, A. Yamanaka, Y. Tomita, Multiscale modeling of hot-working with dynamic recrystallization by coupling microstructure evolution and macroscopic mechanical behavior, Int. J. Plast. 52 (2014) 105–116. https://doi.org/https://doi.org/10.1016/j.ijplas.2013.09.001.

[28] H. Li, C. Wu, H. Yang, Crystal plasticity modeling of the dynamic recrystallization of two-phase titanium alloys during isothermal processing, Int. J. Plast. 51 (2013) 271–291. https://doi.org/10.1016/j.ijplas.2013.05.001.

[29] W. Blum, Q. Zhu, R. Merkel, H.J. McQueen, Geometric dynamic recrystallization in hot torsion of Al-5Mg-0.6Mn (AA5083), Mater. Sci. Eng. A. (1996). https://doi.org/10.1016/0921-5093(95)09990-5.

[30] G. Zhou, Z. Li, D. Li, Y. Peng, H.S. Zurob, P. Wu, A polycrystal plasticity based discontinuous dynamic recrystallization simulation method and its application to copper, Int. J. Plast. 91 (2017) 48–76. https://doi.org/https://doi.org/10.1016/j.ijplas.2017.01.001.

[31] S. Gourdet, F. Montheillet, An experimental study of the recrystallization mechanism during hot deformation of aluminium, Mater. Sci. Eng. A. 283 (2000) 274–288. https://doi.org/10.1016/S0921-5093(00)00733-4.

[32] M.E. Kassner, S.R. Barrabes, New developments in geometric dynamic recrystallization, Mater. Sci. Eng. A. 410–411 (2005) 152–155. https://doi.org/10.1016/j.msea.2005.08.052.

[33] S. Gourdet, F. Montheillet, A model of continuous dynamic recrystallization, Acta Mater. 51 (2003) 2685–2699. https://doi.org/10.1016/S1359-6454(03)00078-8.

[34] M. Huang, Z. Li, The key role of dislocation dissociation in the plastic behaviour of single crystal nickel-based superalloy with low stacking fault energy: Three-dimensional discrete dislocation dynamics modelling, J. Mech. Phys. Solids. 61 (2013) 2454–2472. https://doi.org/https://doi.org/10.1016/j.jmps.2013.07.011.

[35] F.J. Humphreys, M. Hatherly, F.J. Humphreys, M. Hatherly, Chapter 14 – Continuous Recrystallization During and after Large Strain Deformation, in: Recryst. Relat. Annealing Phenom., 2004: pp. 451–467. https://doi.org/10.1016/B978-008044164-1/50018-9.

[36] N.E. Paton, R.G. Baggerly, J.C. Williams, Deformation and Solid Solution Strengthening of Titanium-Aluminum Single Crystals., 1976. http://www.dtic.mil/docs/citations/ADA023195 (accessed July 2, 2017).

[37] A. Momeni, S.M. Abbasi, Effect of hot working on flow behavior of Ti–6Al–4V alloy in single phase and two phase regions, Mater. Des. 31 (2010) 3599–3604. https://doi.org/10.1016/j.matdes.2010.01.060.

[38] Y. Yu, B.-Q. Xiong, S.-X. Hui, W.-J. Ye, Hot deformation behavior and globularization mechanism of Ti-6Al-4V-0.1B alloy with lamellar microstructure, Rare Met. 32 (2013) 122–128. https://doi.org/10.1007/s12598-013-0022-4.

[39] M. Jackson, N.G. Jones, D. Dye, R.J. Dashwood, Effect of initial microstructure on plastic flow behaviour during isothermal forging of Ti–10V–2Fe–3Al, 2009. https://doi.org/10.1016/j.msea.2008.09.071.

[40] R.G. Guan, Y.T. Je, Z.Y. Zhao, C.S. Lee, Effect of microstructure on deformation behavior of Ti-6Al-4V alloy during compressing process, Mater. Des. 36 (2012) 796–803. https://doi.org/10.1016/j.matdes.2011.11.057.

[41] K.X. Wang, W.D. Zeng, Y.Q. Zhao, Y.J. Lai, X.M. Zhang, Y.G. Zhou, Flow behaviour and microstructural evolution of Ti-17 alloy with lamellar microstructure during hot deformation in α+β phase field, Mater. Sci. Technol. 27 (2011) 21–28. https://doi.org/10.1179/174328409X463252.

[42] J.Z. Sun, M.Q. Li, H. Li, Interaction effect between alpha and beta phases based on dynamic recrystallization of isothermally compressed Ti-5Al-2Sn-2Zr-4Mo-4Cr with basketweave microstructure, J. Alloys Compd. 692 (2017) 403–412. https://doi.org/https://doi.org/10.1016/j.jallcom.2016.09.065.

[43] K. Wang, W. Zeng, Y. Zhao, Y. Lai, Y. Zhou, Dynamic globularization kinetics during hot working of Ti-17 alloy with initial lamellar microstructure, Mater. Sci. Eng. A. 527 (2010) 2559–2566. https://doi.org/https://doi.org/10.1016/j.msea.2010.01.034.

[44] J.-Z. Sun, M.-Q. Li, H. Li, Fragmentation of α Grains Accelerated by the Growth of β Phase in Ti–5Al–2Sn–2Zr–4Mo–4Cr during Hot Deformation, Adv. Eng. Mater. 20 (2018) 1700200. https://doi.org/10.1002/adem.201700200.

[45] L. Li, J. Luo, J.J. Yan, M.Q. Li, Dynamic globularization and restoration mechanism of Ti–5Al–2Sn–2Zr–4Mo–4Cr alloy during isothermal compression, J. Alloys Compd. 622 (2015) 174–183. https://doi.org/https://doi.org/10.1016/j.jallcom.2014.10.043.

[46] I. Weiss, S.L. Semiatin, Thermomechanical processing of beta titanium alloys—an overview, Mater. Sci. Eng. A. 243 (1998) 46–65. https://doi.org/https://doi.org/10.1016/S0921-5093(97)00783-1.

[47] T. Furuhara, B. Poorganji, H. Abe, T. Maki, Dynamic recovery and recrystallization in titanium alloys by hot deformation, JOM. 59 (2007) 64–67. https://doi.org/10.1007/s11837-007-0013-8.

[48] R. Ding, Z.X. Guo, A. Wilson, Microstructural evolution of a Ti-6Al-4V alloy during thermomechanical processing, Mater. Sci. Eng. A. 327 (2002) 233–245. https://doi.org/10.1016/S0921-5093(01)01531-3.

[49] L. Li, M.Q. Li, J. Luo, Mechanism in the β phase evolution during hot deformation of Ti–5Al–2Sn–2Zr–4Mo–4Cr with a transformed microstructure, Acta Mater. 94 (2015) 36–45. https://doi.org/10.1016/j.actamat.2015.04.045.

[50] K. Tan, J. Li, Z. Guan, J. Yang, J. Shu, The identification of dynamic recrystallization and constitutive modeling during hot deformation of Ti55511 titanium alloy, Mater. Des. 84 (2015) 204–211. https://doi.org/https://doi.org/10.1016/j.matdes.2015.06.093.

[51] X.G. Fan, H. Yang, Internal-state-variable based self-consistent constitutive modeling for hot working of two-phase titanium alloys coupling microstructure evolution, Int. J. Plast. 27 (2011) 1833–1852. https://doi.org/10.1016/J.IJPLAS.2011.05.008.

[52] B. Babu, L.-E.E. Lindgren, Dislocation density based model for plastic deformation and globularization of Ti-6Al-4V, Int. J. Plast. 50 (2013) 94–108.

[53] D.. OuYang, M.W. Fu, S.Q. Lu, Study on the dynamic recrystallization behavior of Ti-alloy Ti–10V–2Fe–3V in β processing via experiment and simulation, Mater. Sci. Eng. A. 619 (2014) 26–34. https://doi.org/10.1016/J.MSEA.2014.09.067.

[54] W. Chuan, Y. He, L.H. Wei, Modeling of discontinuous dynamic recrystallization of a near-α titanium alloy IMI834 during isothermal hot compression by combining a cellular automaton model with a crystal plasticity finite element method, Comput. Mater. Sci. 79 (2013) 944–959. https://www.sciencedirect.com/science/article/pii/S0927025613004564 (accessed July 9, 2017).

[55] Y.Q. Ning, B.C. Xie, H.Q. Liang, H. Li, X.M. Yang, H.Z. Guo, Dynamic softening behavior of TC18 titanium alloy during hot deformation, Mater. Des. 71 (2015) 68–77. https://doi.org/10.1016/J.MATDES.2015.01.009.

[56] H. Liang, H. Guo, Y. Ning, X. Peng, C. Qin, Z. Shi, Y. Nan, Dynamic recrystallization behavior of Ti–5Al–5Mo–5V–1Cr–1Fe alloy, Mater. Des. 63 (2014) 798–804.

[57] P.M. Souza, H. Beladi, R. Singh, B. Rolfe, P.D. Hodgson, Constitutive analysis of hot deformation behavior of a Ti6Al4V alloy using physical based model, Mater. Sci. Eng. A. 648 (2015) 265–273. https://doi.org/10.1016/j.msea.2015.09.055.

[58] R. Bobbili, B. Venkata Ramudu, V. Madhu, A physically-based constitutive model for hot deformation of Ti-10-2-3 alloy, J. Alloys Compd. 696 (2017) 295–303. http://www.sciencedirect.com/science/article/pii/S092583881633688X (accessed June 7, 2017).

[59] H. Li, X. Sun, H. Yang, A three-dimensional cellular automata-crystal plasticity finite element model for predicting the multiscale interaction among heterogeneous deformation, DRX microstructural evolution and mechanical responses in titanium alloys, Int. J. Plast. 87 (2016) 154–180. https://doi.org/10.1016/j.ijplas.2016.09.008.

[60] P. Gao, H. Yang, X. Fan, S. Zhu, Unified modeling of flow softening and globularization for hot working of two-phase titanium alloy with a lamellar colony microstructure, J. Alloys Compd. 600 (2014) 78–83. https://doi.org/10.1016/J.JALLCOM.2014.02.110.

[61] X.G. Fan, Y. Zhang, P.F. Gao, Z.N. Lei, M. Zhan, Deformation behavior and microstructure evolution during hot working of a coarse-grained Ti-5Al-5Mo-5V-3Cr-1Zr titanium alloy in beta phase field, Mater. Sci. Eng. A. 694 (2017) 24–32. https://doi.org/10.1016/j.msea.2017.03.095.

[62] C. Poletti, L. Germain, F. Warchomicka, M. Dikovits, S. Mitsche, Unified description of the softening behavior of beta-metastable and alpha+beta titanium alloys during hot deformation, Mater. Sci. Eng. A. 651 (2016) 280–290. https://doi.org/10.1016/j.msea.2015.10.109.

[63] H. Matsumoto, M. Kitamura, Y. Li, Y. Koizumi, A. Chiba, Hot forging characteristic of Ti–5Al–5V–5Mo–3Cr alloy with single metastable β microstructure, Mater. Sci. Eng. A. 611 (2014)

337–344. https://doi.org/10.1016/j.msea.2014.06.006.

[64] M. Dikovits, C. Poletti, F. Warchomicka, Deformation Mechanisms in the Near-β Titanium Alloy Ti-55531, Metall. Mater. Trans. A. 45 (2014) 1586–1596. https://doi.org/10.1007/s11661-013-2073-4.

[65] F. Warchomicka, C. Poletti, M. Stockinger, Study of the hot deformation behaviour in Ti–5Al–5Mo–5V–3Cr–1Zr, Mater. Sci. Eng. A. 528 (2011) 8277–8285. https://doi.org/10.1016/j.msea.2011.07.068.

[66] J.C. Fanning, Properties of TIMETAL 555 (Ti-5Al-5Mo-5V-3Cr-0.6Fe), in: J. Mater. Eng. Perform., 2005: pp. 788–791. https://doi.org/10.1361/105994905X75628.

[67] G. Welsch, R. Boyer, E. Collings, Materials properties handbook: titanium alloys, ASM international, 1993. https://books.google.at/books?hl=de&lr=&id=x3rToHWOcD8C&oi=fnd&pg=PR3&dq=Roger+R,+Collings+EW,+Welsch+G+(1993)+Materials+properties+handbook:+titanium+alloys.+ASM+International,+Materials+Par&ots=x5C5SHgjiY&sig=Y4FBxIwHlYjkRMZBxqSlHKp05Bw (accessed June 16, 2017).

[68] M. Ninomi, S. Akiyama, M. Ikeda, M. Hagiwara, K. Maruyama The, Phase Transformations in Ti-5Al-5Mo-5V-3Cr-0.5Fe, Japan Institute of Metals, 2007.

[69] J.D.C. Teixeira, B. Appolaire, E. Aeby-Gautier, S. Denis, G. Cailletaud, N. Späth, Transformation kinetics and microstructures of Ti17 titanium alloy during continuous cooling, Mater. Sci. Eng. A. 448 (2007) 135–145. https://doi.org/https://doi.org/10.1016/j.msea.2006.10.024.

[70] J. Luo, L. Li, M. Li, Deformation behavior of Ti–5Al–2Sn–2Zr–4Mo–4Cr alloy with two initial microstructures during hot working, Trans. Nonferrous Met. Soc. China. 26 (2016) 414–422. https://doi.org/https://doi.org/10.1016/S1003-6326(16)64130-4.

[71] H. Matsumoto, D. Naito, K. Miyoshi, K. Yamanaka, A. Chiba, Y. Yamabe-Mitarai, Forging property, processing map, and mesoscale microstructural evolution modeling of a Ti-17 alloy with a lamellar (α+β) starting microstructure, Sci. Technol. Adv. Mater. 18 (2017) 893–904. https://doi.org/10.1080/14686996.2017.1386530.

[72] J.-H. Zheng, J. Lin, J. Lee, R. Pan, C. Li, C.M. Davies, A novel constitutive model for multi-step stress relaxation ageing of a pre-strained 7xxx series alloy, Int. J. Plast. 106 (2018) 31–47. https://doi.org/https://doi.org/10.1016/j.ijplas.2018.02.008.

[73] D.-L. Wu, F.-Z. Xuan, S.-J. Guo, P. Zhao, Uniaxial mean stress relaxation of 9–12% Cr steel at high temperature: Experiments and viscoplastic constitutive modeling, Int. J. Plast. 77 (2016) 156–173. https://doi.org/https://doi.org/10.1016/j.ijplas.2015.10.001.

[74] A.S. Khan, S. Yu, H. Liu, Deformation induced anisotropic responses of Ti–6Al–4V alloy Part II: A strain rate and temperature dependent anisotropic yield criterion, Int. J. Plast. 38 (2012) 14–26. https://doi.org/10.1016/j.ijplas.2012.03.013.

[75] A.S. Khan, R. Kazmi, B. Farrokh, M. Zupan, Effect of oxygen content and microstructure on the thermo-mechanical response of three Ti–6Al–4V alloys: Experiments and modeling over a wide range of strain-rates and temperatures, Int. J. Plast. 23 (2007) 1105–1125. https://doi.org/https://doi.org/10.1016/j.ijplas.2006.10.007.

[76] G.M. Castelluccio, D.L. McDowell, Mesoscale cyclic crystal plasticity with dislocation substructures, Int. J. Plast. 98 (2017) 1–26. https://doi.org/https://doi.org/10.1016/j.ijplas.2017.06.002.

[77] H.M. Mourad, C.A. Bronkhorst, V. Livescu, J.N. Plohr, E.K. Cerreta, Modeling and simulation framework for dynamic strain localization in elasto-viscoplastic metallic materials subject to large deformations, Int. J. Plast. 88 (2017) 1–26. https://doi.org/https://doi.org/10.1016/j.ijplas.2016.09.009.

[78] Y.C. Lin, D.-X. Wen, M.-S. Chen, X.-M. Chen, A novel unified dislocation density-based model for hot deformation behavior of a nickel-based superalloy under dynamic recrystallization conditions, Appl. Phys. A. 122 (2016) 805. https://doi.org/10.1007/s00339-016-0333-z.

[79] F. Jiang, S. Takaki, T. Masumura, R. Uemori, H. Zhang, T. Tsuchiyama, Nonadditive strengthening functions for cold-worked cubic metals: Experiments and constitutive modeling, Int. J. Plast. 129 (2020) 102700. https://doi.org/https://doi.org/10.1016/j.ijplas.2020.102700.

[80] C.Y. Gao, L.C. Zhang, Constitutive modelling of plasticity of fcc metals under extremely high strain rates, Int. J. Plast. 32–33 (2012) 121–133. https://doi.org/https://doi.org/10.1016/j.ijplas.2011.12.001.

[81] A. He, G. Xie, X. Yang, X. Wang, H. Zhang, A physically-based constitutive model for a nitrogen alloyed ultralow carbon stainless steel, Comput. Mater. Sci. 98 (2015) 64–69. https://doi.org/10.1016/j.commatsci.2014.10.044.

[82] R. Neumann, T. Böhlke, Hashin–Shtrikman type mean field model for the two-scale simulation of the thermomechanical processing of steel, Int. J. Plast. 77 (2016) 1–29. https://doi.org/https://doi.org/10.1016/j.ijplas.2015.09.003.

[83] N. Haghdadi, D. Martin, P. Hodgson, Physically-based constitutive modelling of hot deformation behavior in a LDX 2101 duplex stainless steel, Mater. Des. 106 (2016) 420–427. https://doi.org/10.1016/j.matdes.2016.05.118.

[84] Y.C. Lin, X.-M. Chen, D.-X. Wen, M.-S. Chen, A physically-based constitutive model for a typical nickel-based superalloy, Comput. Mater. Sci. 83 (2014) 282–289. https://doi.org/10.1016/j.commatsci.2013.11.003.

[85] J. Blaizot, T. Chaise, D. Nélias, M. Perez, S. Cazottes, P. Chaudet, Constitutive model for nickel alloy 690 (Inconel 690) at various strain rates and temperatures, Int. J. Plast. 80 (2016) 139–153. https://doi.org/https://doi.org/10.1016/j.ijplas.2015.08.010.

[86] G. Ji, Q. Li, L. Li, A physical-based constitutive relation to predict flow stress for Cu–0.4Mg alloy during hot working, Mater. Sci. Eng. A. 615 (2014) 247–254. https://doi.org/10.1016/j.msea.2014.07.082.

[87] G. Ji, Q. Li, K. Ding, L. Yang, L. Li, A physically-based constitutive model for high temperature deformation of Cu-0.36Cr-0.03Zr alloy, J. Alloys Compd. 648 (2015) 397–407. https://doi.org/10.1016/j.jallcom.2015.06.264.

[88] L. Cheng, X. Xue, B. Tang, H. Kou, J. Li, Flow characteristics and constitutive modeling for elevated temperature deformation of a high Nb containing TiAl alloy, Intermetallics. 49 (2014) 23–28. https://doi.org/10.1016/j.intermet.2014.01.007.

[89] M. Hiratani, H.M. Zbib, M.A. Khaleel, Modeling of thermally activated dislocation glide and plastic flow through local obstacles, Int. J. Plast. 19 (2003) 1271–1296. https://doi.org/10.1016/S0749-6419(02)00016-5.

[90] Z.C. Sun, H. Yang, G.J. Han, X.G. Fan, A numerical model based on internal-state-variable method for the microstructure evolution during hot-working process of TA15 titanium alloy, Mater. Sci. Eng. A. 527 (2010) 3464–3471. https://doi.org/https://doi.org/10.1016/j.msea.2010.02.009.

[91] W. Peng, W. Zeng, Q. Wang, H. Yu, Comparative study on constitutive relationship of as-cast Ti60 titanium alloy during hot deformation based on Arrhenius-type and artificial neural network models, Mater. Des. 51 (2013) 95–104. https://doi.org/https://doi.org/10.1016/j.matdes.2013.04.009.

[92] U.F. Kocks, A statistical theory of flow stress and work-hardening, Philos. Mag. 13 (1966) 541–566. https://doi.org/10.1080/14786436608212647.

[93] Y. Bergström, A dislocation model for the stress-strain behaviour of polycrystalline α-Fe with special emphasis on the variation of the densities of mobile and immobile dislocations, Mater. Sci. Eng. 5 (1970) 193–200. https://doi.org/10.1016/0025-5416(70)90081-9.

[94] Y. Bergstrom, W. Roberts, The dynamical strain ageing of α-iron: Effects of strain rate and nitrogen content in the jerky-flow region, Acta Metall. 21 (1973) 741–745. https://doi.org/10.1016/0001-6160(73)90038-2.

[95] W. Roberts, Y. Bergström, The stress-strain behaviour of single crystals and polycrystals of face-centered cubic metals-a new dislocation treatment, Acta Metall. 21 (1973) 457–469. https://doi.org/10.1016/0001-6160(73)90203-4.

[96] H. Mecking, Y. Estrin, The effect of vacancy generation on plastic deformation, Scr. Metall. 14 (1980) 815–819. https://doi.org/10.1016/0036-9748(80)90295-1.

[97] Y. Bergström, The plastic deformation of metals - a dislocation model and its applicability, Rev. Powder Metall. Phys. Ceram. 2/3 (1983) 79–265.

[98] Y. Estrin, L.S. Tóth, A. Molinari, Y. Bréchet, A dislocation-based model for all hardening stages in large strain deformation, Acta Mater. 46 (1998) 5509–5522. https://doi.org/10.1016/S1359-6454(98)00196-7.

[99] X. Feaugas, On the origin of the tensile flow stress in the stainless steel AISI 316L at 300 K: back stress and effective stress, Acta Mater. 47 (1999) 3617–3632. https://doi.org/10.1016/S1359-6454(99)00222-0.

[100] X. Feaugas, C. Gaudin, Different levels of plastic strain incompatibility during cyclic loading: in terms of dislocation density and distribution, Mater. Sci. Eng. A. 309–310 (2001) 382–385. https://doi.org/10.1016/S0921-5093(00)01730-5.

[101] F. Barlat, J.J. Gracio, M.-G. Lee, E.F. Rauch, G. Vincze, An alternative to kinematic hardening in classical plasticity, Int. J. Plast. 27 (2011) 1309–1327. https://doi.org/10.1016/j.ijplas.2011.03.003.

[102] A. Arsenlis, D.M. Parks, R. Becker, V. V Bulatov, On the evolution of crystallographic dislocation density in non-homogeneously deforming crystals, J. Mech. Phys. Solids. 52 (2004) 1213–1246. https://doi.org/10.1016/j.jmps.2003.12.007.

[103] K.S. Cheong, E.P. Busso, A. Arsenlis, A study of microstructural length scale effects on the behaviour of FCC polycrystals using strain gradient concepts, Int. J. Plast. 21 (2005) 1797–1814. https://doi.org/10.1016/j.ijplas.2004.11.001.

[104] N.M. Ghoniem, J.R. Matthews, R.J. Amodeo, Dislocation model for creep in engineering materials, Res Mech. 29 (1990) 197–219.

[105] S. Nemat-Nasser, W.G. Guo, J.Y. Cheng, Mechanical properties and deformation mechanisms of a commercially pure titanium, Acta Mater. 47 (1999) 3705–3720. https://doi.org/10.1016/S1359-6454(99)00203-7.

[106] R.C. Picu, A. Majorell, Mechanical behavior of Ti–6Al–4V at high and moderate temperatures—Part II: constitutive modeling, Mater. Sci. Eng. A. 326 (2002) 306–316. https://doi.org/10.1016/S0921-5093(01)01508-8.

[107] C.Y. Gao, L.C. Zhang, H.X. Yan, A new constitutive model for HCP metals, Mater. Sci. Eng. A. 528 (2011) 4445–4452. https://doi.org/10.1016/j.msea.2011.02.053.

[108] R.G. Stringfellow, D.M. Parks, A self-consistent model of isotropic viscoplastic behavior in multiphase materials, Int. J. Plast. 7 (1991) 529–547. https://doi.org/10.1016/0749-6419(91)90043-X.

[109] P.M. Suquet, Overall potentials and extremal surfaces of power law or ideally plastic composites, J. Mech. Phys. Solids. 41 (1993) 981–1002. https://doi.org/10.1016/0022-5096(93)90051-G.

[110] L. Briottet, J.J. Jonas, F. Montheillet, A mechanical interpretation of the activation energy of high temperature deformation in two phase materials, Acta Mater. 44 (1996) 1665–1672. https://doi.org/10.1016/1359-6454(95)00257-X.

[111] X.G. Fan, X.Q. Jiang, X. Zeng, Y.G. Shi, P.F. Gao, M. Zhan, Modeling the anisotropy of hot plastic deformation of two-phase titanium alloys with a colony microstructure, Int. J. Plast. 104 (2018) 173–195. https://doi.org/https://doi.org/10.1016/j.ijplas.2018.02.010.

[112] Z. Ji, H. Yang, H. Li, Predicting the effects of microstructural features on strain localization of a two-phase titanium alloy, Mater. Des. 87 (2015) 171–180. https://doi.org/https://doi.org/10.1016/j.matdes.2015.07.128.

[113] G.I. Taylor, Plastic strain in metals, J. Inst. Met. 62 (1938) 307–324.

[114] G. Sachs, Plasticity problems in metals, Trans. Faraday Soc. 24 (1928) 84–92.

[115] F. Montheillet, G. Damamme, Simple Flow Rules for Modeling the Behaviour of Inhomogeneous Viscoplastic Materials, Adv. Eng. Mater. 7 (2005) 852–858. https://doi.org/10.1002/adem.200500100.

[116] L. Wang, X.G. Fan, M. Zhan, X.Q. Jiang, X. Zeng, Y.F. Liang, H.J. Zheng, A.M. Zhao, The heterogeneous globularization related to crystal and geometrical orientation of two-phase titanium alloys with a colony microstructure, Mater. Des. 186 (2020) 108338. https://doi.org/https://doi.org/10.1016/j.matdes.2019.108338.

[117] J. Luo, P. Ye, W.C. Han, M.Q. Li, Collaborative behavior in α lamellae and β phase evolution and its effect on the globularization of TC17 alloy, Mater. Des. 146 (2018) 152–162. https://doi.org/https://doi.org/10.1016/j.matdes.2018.03.020.

[118] D. Canelo-Yubero, G. Requena, F. Sket, C. Poletti, F. Warchomicka, J. Daniels, N. Schell, A. Stark, Load partition and microstructural evolution during in situ hot deformation of Ti–6Al–6V–2Sn alloys, Mater. Sci. Eng. A. 657 (2016) 244–258. https://doi.org/https://doi.org/10.1016/j.msea.2016.01.059.

[119] Y. Zhu, X. Wu, Perspective on hetero-deformation induced (HDI) hardening and back stress, Mater. Res. Lett. 7 (2019) 393–398. https://doi.org/10.1080/21663831.2019.1616331.

[120] X.L. Liu, Q.Q. Xue, W. Wang, L.L. Zhou, P. Jiang, H.S. Ma, F.P. Yuan, Y.G. Wei, X.L. Wu, Back-stress-induced strengthening and strain hardening in dual-phase steel, Materialia. 7 (2019) 100376. https://doi.org/10.1016/J.MTLA.2019.100376.

[121] F.J. Humphreys, M. Hatherly, F.J. Humphreys, M. Hatherly, Chapter 7 – Recrystallization of Single-Phase Alloys, in: Recryst. Relat. Annealing Phenom., 2004: pp. 215–IV. https://doi.org/10.1016/B978-008044164-1/50011-6.

[122] A.L. Pilchak, G.A. Sargent, S.L. Semiatin, Early Stages of Microstructure and Texture Evolution during Beta Annealing of Ti-6Al-4V, Metall. Mater. Trans. A. 49 (2018) 908–919. https://doi.org/10.1007/s11661-017-4444-8.

[123] S. Huang, Y. Ma, S. Zhang, S.S. Youssef, J. Qiu, H. Wang, B.Y. Zong, J. Lei, R. Yang, Nonuniform Recrystallization and Growth Behavior of β Grains Dominated by Grain Misorientation and Interfacial Energy in Metastable β Titanium Alloy, Metall. Mater. Trans. A. 49 (2018) 6390–6400. https://doi.org/10.1007/s11661-018-4933-4.

[124] M. Sen, S. Suman, M. Kumar, T. Banerjee, A. Bhattacharjee, S.K. Kar, Thermo-mechanical processing window for β phase recrystallization inTi-5Al-5Mo-5V-3Cr alloy, Mater. Charact. 146 (2018) 55–70. https://doi.org/https://doi.org/10.1016/j.matchar.2018.09.038.

[125] M. Allan, M. Thomas, J. Brooks, P. Blackwell, β Recrystallisation Characteristics of α + β Titanium Alloys for Aerospace Applications, in: Proc. 13th World Conf. Titan., John Wiley & Sons, Ltd, 2016: pp. 203–208. https://doi.org/10.1002/9781119296126.ch30.

[126] M. Semblanet, F. Montheillet, D. Piot, C. Desrayaud, A. Bénéteau, Y. Millet, Kinetics of

Recrystallization and Grain Growth in Ti-17 Alloy, in: L. Zhou, H. Chang, Y. Lu, D. Xu (Eds.), Proc. 12th World Conf. Titan., Science Press, Beijing, 2012: pp. 573–576.

[127] L.A. Elagina, A.I. Gordienko, O.P. Evmenov, V.V. Ivashko, Methods of Refining Coarse-Grained Structures of Titanium Alloys, in: J.C. Williams, A.F. Belov (Eds.), Titan. Titan. Alloy. Sci. Technol. Asp., Plenum Press, New York, 1982: pp. 1789–1798.

[128] A. Krumphals, M. Stockinger, F. Warchomicka, C. Sommitsch, Evolution of Beta Grain Size During Beta Phase Processing of Ti-6Al-4V, in: L. Zhou, H. Chang, Y. Lu, D. Xu (Eds.), Proc. 12th World Conf. Titan., Science Press, Beijing, 2012: pp. 493–496.

[129] N. Côme-Dingremont, E. Gautier, A. Simon, Grain growth of TA6V beta phase after thermomechanical treatments, in: F.H. Froes, I.L. Caplan (Eds.), Titan. '92 Sci. Technol., TMS, Warrendale, PA, 1993: pp. 667–674. https://cdn.ymaws.com/titanium.org/resource/resmgr/ZZ-WCTP1992-VOL1/1992_Vol.1-3-D-Grain_Growth_.pdf.

[130] J.M. Kempf, E. Gautier, A. Simon, J.F. Uginet, A. Gavart, Effect of thermomechanical treatments on TA6Zr5D beta, in: F.H. Froes, C. I.L. (Eds.), Titan. '92 Sci. Technol., TMS, Warrendale, PA, 1993: pp. 627–634. https://cdn.ymaws.com/titanium.org/resource/resmgr/ZZ-WCTP1992-VOL1/1992_Vol.1-3-B-Effect_of_The.pdf.

[131] Florence Chaussy Mraizika, Evolutions microstructurales en compression à chaud des alliages de titane BETACEZ et 6246 et influence du forgeage sur la transformation β → α, Institut National Polytechnique de Grenoble, Grenoble, France, 1996. https://www.theses.fr/1996INPG4206.

[132] R.D. Doherty, D.A. Hughes, F.J. Humphreys, J.J. Jonas, D.J. Jensen, M.E. Kassner, W.E. King, T.R. McNelley, H.J. McQueen, A.D. Rollett, Current issues in recrystallization: a review, Mater. Sci. Eng. A. 238 (1997) 219–274. https://doi.org/https://doi.org/10.1016/S0921-5093(97)00424-3.

[133] C. Zheng, N. Xiao, D. Li, Y. Li, Mesoscopic modeling of austenite static recrystallization in a low carbon steel using a coupled simulation method, Comput. Mater. Sci. 45 (2009) 568–575. https://doi.org/10.1016/j.commatsci.2008.11.021.

[134] F.J. Humphreys, A unified theory of recovery, recrystallization and grain growth, based on the stability and growth of cellular microstructures—I. The basic model, Acta Mater. 45 (1997) 4231–4240. https://doi.org/10.1016/S1359-6454(97)00070-0.

[135] F.J. Humphreys, A unified theory of recovery, recrystallization and grain growth, based on the stability and growth of cellular microstructures—II. The effect of second-phase particles, Acta Mater. 45 (1997) 5031–5039. https://doi.org/https://doi.org/10.1016/S1359-6454(97)00173-0.

[136] M.K. Rehman, H.S. Zurob, A Novel Approach to Model Static Recrystallization of Austenite During Hot Rolling of Nb Microalloyed Steel. Part I: Precipitate-Free Case, Metall. Mater. Trans. A. 44 (2013) 1862–1871. https://doi.org/10.1007/s11661-012-1526-5.

[137] P. Homporová, Thermal history of alpha morphology in titanium alloy Ti-6Al-4V, Vienna University of Technology, 2011.

[138] N.G. Jones, R.J. Dashwood, D. Dye, M. Jackson, Thermomechanical processing of Ti–5Al–5Mo–5V–3Cr, Mater. Sci. Eng. A. 490 (2008) 369–377. https://doi.org/10.1016/j.msea.2008.01.055.

[139] N.G. Jones, R.J. Dashwood, D. Dye, M. Jackson, The Flow Behavior and Microstructural Evolution of Ti-5Al-5Mo-5V-3Cr during Subtransus Isothermal Forging, Metall. Mater. Trans. A. 40 (2009) 1944–1954. https://doi.org/10.1007/s11661-009-9866-5.

[140] R.H. Buzolin, D. Weiß, A. Krumphals, M. Lasnik, M.C. Poletti, Modelling the Competitive

Growth of Primary, Allotriomorphic, and Secondary Alpha in Ti-6Al-4V, Metall. Mater. Trans. A. (2020). https://doi.org/10.1007/s11661-020-05810-4.

[141] R.H. Buzolin, M. Lasnik, A. Krumphals, M.C. Poletti, A dislocation-based model for the microstructure evolution and the flow stress of a Ti5553 alloy, Int. J. Plast. 136 (2021). https://doi.org/10.1016/j.ijplas.2020.102862.

[142] R.H. Buzolin, M. Lasnik, A. Krumphals, M.C. Poletti, Hot deformation and dynamic α-globularization of a Ti-17 alloy: Consistent physical model, Mater. Des. 197 (2021) 109266. https://doi.org/https://doi.org/10.1016/j.matdes.2020.109266.

[143] A.S. Khan, R. Liang, Behaviors of three BCC metal over a wide range of strain rates and temperatures: Experiments and modeling, Int. J. Plast. 15 (1999) 1089–1109. https://doi.org/10.1016/S0749-6419(99)00030-3.

[144] R.L. Goetz, S.L. Semiatin, The adiabatic correction factor for deformation heating during the uniaxial compression test, J. Mater. Eng. Perform. 10 (2001) 710–717. https://doi.org/10.1361/105994901770344593.

[145] B. Song, S. Dong, B. Zhang, H. Liao, C. Coddet, Effects of processing parameters on microstructure and mechanical property of selective laser melted Ti6Al4V, Mater. Des. 35 (2012) 120–125. https://doi.org/10.1016/j.matdes.2011.09.051.

[146] R.H. Buzolin, D. Canelo-Yubero, F. Warchomicka, M. Lasnik, A. Krumphals, M.C. Poletti, Refinement of the Ti-17 microstructure after hot deformation: Coupled mesoscale model, Mater. Sci. Eng. A. (2020) 140268. https://doi.org/https://doi.org/10.1016/j.msea.2020.140268.

[147] D. Tolnai, G. Szakács, G. Requena, A. Stark, N. Schell, K.U. Kainer, N. Hort, Study of the solidification of AS alloys combining in situ synchrotron diffraction and differential scanning calorimetry, in: Mater. Sci. Forum, Trans Tech Publications Ltd, 2013: pp. 286–290. https://doi.org/10.4028/www.scientific.net/MSF.765.286.

[148] F. Warchomicka, D. Canelo-Yubero, E. Zehetner, G. Requena, A. Stark, C. Poletti, In-Situ Synchrotron X-Ray Diffraction of Ti-6Al-4V During Thermomechanical Treatment in the Beta Field, Metals (Basel). 9 (2019) 862. https://doi.org/10.3390/met9080862.

[149] K.-D. Liss, T. Schmoelzer, K. Yan, M. Reid, M. Peel, R. Dippenaar, H. Clemens, In situ study of dynamic recrystallization and hot deformation behavior of a multiphase titanium aluminide alloy, J. Appl. Phys. 106 (2009) 113526. https://doi.org/10.1063/1.3266177.

[150] The GIMP Team, GIMP - GNU Image Manipulation Program, (n.d.). https://www.gimp.org/ (accessed August 20, 2019).

[151] ImageJ, (n.d.). https://imagej.nih.gov/ij/ (accessed August 20, 2019).

[152] J. Tiley, T. Searles, E. Lee, S. Kar, R. Banerjee, J.C. Russ, H.L. Fraser, Quantification of microstructural features in α/β titanium alloys, Mater. Sci. Eng. A. (2004). https://doi.org/10.1016/j.msea.2003.12.008.

[153] U. Zwicker, Titan und Titanlegierungen, Springer Berlin Heidelberg, Berlin, Heidelberg, 1974. https://doi.org/10.1007/978-3-642-80587-5.

[154] M. Villa, J.W. Brooks, R.P. Turner, H. Wang, F. Boitout, R.M. Ward, Microstructural Modeling of the α + β Phase in Ti-6Al-4V: A Diffusion-Based Approach, Metall. Mater. Trans. B. 50 (2019) 2898–2911. https://doi.org/10.1007/s11663-019-01675-0.

[155] R. Shi, Y. Wang, Variant selection during α precipitation in Ti–6Al–4V under the influence of local stress – A simulation study, Acta Mater. 61 (2013) 6006–6024. https://doi.org/https://doi.org/10.1016/j.actamat.2013.06.042.

[156] D.S. Wilkinson, Mass Transport in Solids and Fluids, Cambridge University Press, 2000. https://doi.org/10.1017/CBO9781139171267.

[157] J.W. (John W. Christian, The theory of transformations in metals and alloys : an advanced textbook in physical metallurgy, Pergamon Press, 1975. https://books.google.co.jp/books/about/The_Theory_of_Transformations_in_Metals.html?id=R5JTAAAAMAAJ&redir_esc=y (accessed August 20, 2019).

[158] R.D. DOHERTY, CHAPTER 15 - DIFFUSIVE PHASE TRANSFORMATIONS IN THE SOLID STATE, in: R.W. CAHN, P. HAASEN† (Eds.), Phys. Metall. (Fourth Ed., Fourth Edi, North-Holland, Oxford, 1996: pp. 1363–1505. https://doi.org/https://doi.org/10.1016/B978-044489875-3/50020-X.

[159] A. Deschamps, Y. Brechet, Influence of predeformation and ageing of an Al–Zn–Mg alloy—II. Modeling of precipitation kinetics and yield stress, Acta Mater. 47 (1998) 293–305. https://doi.org/https://doi.org/10.1016/S1359-6454(98)00296-1.

[160] P. Shanthraj, M.A. Zikry, Dislocation density evolution and interactions in crystalline materials, Acta Mater. 59 (2011) 7695–7702. https://doi.org/https://doi.org/10.1016/j.actamat.2011.08.041.

[161] B.L. Hansen, I.J. Beyerlein, C.A. Bronkhorst, E.K. Cerreta, D. Dennis-Koller, A dislocation-based multi-rate single crystal plasticity model, Int. J. Plast. 44 (2013) 129–146. https://doi.org/10.1016/j.ijplas.2012.12.006.

[162] A. Ma, F. Roters, D. Raabe, A dislocation density based constitutive model for crystal plasticity FEM including geometrically necessary dislocations, Acta Mater. 54 (2006) 2169–2179. https://doi.org/10.1016/j.actamat.2006.01.005.

[163] Y. Aoyagi, R. Kobayashi, Y. Kaji, K. Shizawa, Modeling and simulation on ultrafine-graining based on multiscale crystal plasticity considering dislocation patterning, Int. J. Plast. 47 (2013) 13–28. https://doi.org/https://doi.org/10.1016/j.ijplas.2012.12.007.

[164] L. Yan, J. Shen, Z. Li, J. Li, X. Yan, Microstructure evolution of Al-Zn-Mg-Cu-Zr alloy during hot deformation, Rare Met. 29 (2010) 426–432. https://doi.org/10.1007/s12598-010-0143-y.

[165] J.K. Mason, C.A. Schuh, The generalized Mackenzie distribution: Disorientation angle distributions for arbitrary textures, Acta Mater. 57 (2009) 4186–4197. https://doi.org/10.1016/J.ACTAMAT.2009.05.016.

[166] D.G. Brandon, The structure of high-angle grain boundaries, Acta Metall. 14 (1966) 1479–1484. https://doi.org/https://doi.org/10.1016/0001-6160(66)90168-4.

[167] M. Winning, A.D. Rollett, Transition between low and high angle grain boundaries, Acta Mater. 53 (2005) 2901–2907. https://doi.org/https://doi.org/10.1016/j.actamat.2005.03.005.

[168] P.M. Souza, H. Beladi, R.P. Singh, P.D. Hodgson, B. Rolfe, An Analysis on the Constitutive Models for Forging of Ti6Al4V Alloy Considering the Softening Behavior, J. Mater. Eng. Perform. 27 (2018) 3545–3558. https://doi.org/10.1007/s11665-018-3402-y.

[169] S.. Semiatin, T.. Bieler, The effect of alpha platelet thickness on plastic flow during hot working of TI–6Al–4V with a transformed microstructure, Acta Mater. 49 (2001) 3565–3573. https://doi.org/10.1016/S1359-6454(01)00236-1.

[170] H. Mecking, U.F. Kocks, Kinetics of flow and strain-hardening, Acta Metall. 29 (1981) 1865–1875. https://doi.org/10.1016/0001-6160(81)90112-7.

[171] U. Köhler, C. Herzig, On the Anomalous Self-Diffusion in B.C.C. Titanium, Phys. Status Solidi. 144 (1987) 243–251. https://doi.org/10.1002/pssb.2221440122.

[172] B. Sonderegger, E. Kozeschnik, Particle strengthening in fcc crystals with prolate and oblate precipitates, Scr. Mater. 66 (2012) 52–55. https://doi.org/https://doi.org/10.1016/j.scriptamat.2011.10.003.

[173] F.J. Humphreys, M. Hatherly, F.J. Humphreys, M. Hatherly, Chapter 5 – The Mobility and

Migration of Boundaries, in: Recryst. Relat. Annealing Phenom., 2004: pp. 121–167. https://doi.org/10.1016/B978-008044164-1/50009-8.

[174] J. Xu, W. Zeng, Z. Jia, X. Sun, J. Zhou, Static globularization kinetics for Ti-17 alloy with initial lamellar microstructure, J. Alloys Compd. 603 (2014) 239–247. https://doi.org/https://doi.org/10.1016/j.jallcom.2014.03.082.

[175] S.L. Semiatin, M.W. Corbett, P.N. Fagin, G.A. Salishchev, C.S. Lee, Dynamic-coarsening behavior of an α/β titanium alloy, Metall. Mater. Trans. A. 37 (2006) 1125–1136. https://doi.org/10.1007/s11661-006-1091-x.

[176] S.P. Marsh, M.E. Glicksman, Ostwald ripening in non-spherical morphologies, Mater. Sci. Eng. A. 238 (1997) 140–147. https://doi.org/https://doi.org/10.1016/S0921-5093(97)00440-1.

[177] R. Sandsttröm, Subgrain growth occurring by boundary migration, Acta Metall. 25 (1977) 905–911. https://doi.org/https://doi.org/10.1016/0001-6160(77)90177-8.

[178] F.J. Humphreys, M. Hatherly, F.J. Humphreys, M. Hatherly, Chapter 4 – The Structure and Energy of Grain Boundaries, in: Recryst. Relat. Annealing Phenom., 2004: pp. 91–119. https://doi.org/10.1016/B978-008044164-1/50008-6.

[179] J.H. Gittus, Theoretical value of the ratio (K) of cell diameter to dislocation spacing for a material undergoing dislocation-creep, Philos. Mag. A J. Theor. Exp. Appl. Phys. 35 (1977) 293–300. https://doi.org/10.1080/14786437708237054.

[180] J.H. Gittus, Theoretical relationship between free energy and dislocation cell diameter during creep, Philos. Mag. A. 39 (1979) 829–832. https://doi.org/10.1080/01418617908239311.

[181] W.T. Read, W. Shockley, Dislocation Models of Crystal Grain Boundaries, Phys. Rev. 78 (1950) 275–289. https://doi.org/10.1103/PhysRev.78.275.

[182] J.M. Burgers, Geometrical considerations concerning the structural irregularities to be assumed in a crystal, Proc. Phys. Soc. 52 (1940) 23–33. https://doi.org/10.1088/0959-5309/52/1/304.

[183] F.J. Humphreys, M. Hatherly, F.J. Humphreys, M. Hatherly, Chapter 11 – Grain Growth Following Recrystallization, in: Recryst. Relat. Annealing Phenom., 2004: pp. 333–378. https://doi.org/10.1016/B978-008044164-1/50015-3.

[184] W. Rae, Thermo-metallo-mechanical modelling of heat treatment induced residual stress in Ti–6Al–4V alloy, Mater. Sci. Technol. 35 (2019) 747–766. https://doi.org/10.1080/02670836.2019.1591031.

[185] J. Sieniawski, W. Ziaja, K. Kubiak, M. Motyka, Microstructure and mechanical properties of high strength two-phase titanium alloys, in: J. Sieniawski, Z. Waldemar (Eds.), Titan. Alloy. Prop. Control, InTech, Rijeka, Croatia, Croatia, n.d.: pp. 69–80. https://doi.org/http://dx.doi.org/10.5772/49999.

[186] S.M. Abbasi, A. Momeni, Y.C. Lin, H.R. Jafarian, Dynamic softening mechanism in Ti-13V-11Cr-3Al beta Ti alloy during hot compressive deformation, Mater. Sci. Eng. A. 665 (2016) 154–160. http://linkinghub.elsevier.com/retrieve/pii/S0921509316304233 (accessed June 7, 2017).

[187] Y. Zhu, W. Zeng, F. Feng, Y. Sun, Y. Han, Y. Zhou, Characterization of hot deformation behavior of as-cast TC21 titanium alloy using processing map, Mater. Sci. Eng. A. 528 (2011) 1757–1763. https://www.sciencedirect.com/science/article/pii/S092150931001302X (accessed June 7, 2017).

[188] J.K. Fan, H.C. Kou, M.J. Lai, B. Tang, H. Chang, J.S. Li, Characterization of hot deformation behavior of a new near beta titanium alloy: Ti-7333, Mater. Des. 49 (2013) 945–952. https://www.sciencedirect.com/science/article/pii/S0261306913001556 (accessed June 7,

2017).

[189] X.G. Fan, Y. Zhang, H.J. Zheng, Z.Q. Zhang, P.F. Gao, M. Zhan, Pre-processing related recrystallization behavior in β annealing of a near-β Ti-5Al-5Mo-5V-3Cr-1Zr titanium alloy, Mater. Charact. 137 (2018) 151–161. https://doi.org/https://doi.org/10.1016/j.matchar.2018.01.026.

[190] H. Asgharzadeh, A. Simchi, H.S. Kim, Dynamic restoration and microstructural evolution during hot deformation of a P/M Al6063 alloy, Mater. Sci. Eng. A. 542 (2012) 56–63. https://doi.org/https://doi.org/10.1016/j.msea.2012.02.031.

[191] H. Hallberg, M. Wallin, M. Ristinmaa, Simulation of discontinuous dynamic recrystallization in pure Cu using a probabilistic cellular automaton, Comput. Mater. Sci. 49 (2010) 25–34. https://doi.org/10.1016/j.commatsci.2010.04.012.

[192] M.R. Rokni, A. Zarei-Hanzaki, A.A. Roostaei, H.R. Abedi, An investigation into the hot deformation characteristics of 7075 aluminum alloy, Mater. Des. 32 (2011) 2339–2344. https://doi.org/https://doi.org/10.1016/j.matdes.2010.12.047.

[193] H. Mughrabi, The α-factor in the Taylor flow-stress law in monotonic, cyclic and quasi-stationary deformations: Dependence on slip mode, dislocation arrangement and density, Curr. Opin. Solid State Mater. Sci. 20 (2016) 411–420. https://doi.org/10.1016/J.COSSMS.2016.07.001.

[194] A. Shahba, S. Ghosh, Crystal plasticity FE modeling of Ti alloys for a range of strain-rates. Part I: A unified constitutive model and flow rule, Int. J. Plast. 87 (2016) 48–68. https://doi.org/10.1016/j.ijplas.2016.09.002.

[195] D. Canelo-Yubero, C. Poletti, F. Warchomicka, J. Daniels, G. Requena, Load partition and microstructural evolution during hot deformation of Ti-6Al-6V-2Sn matrix composites, and possible strengthening mechanisms, J. Alloys Compd. 764 (2018) 937–946. https://doi.org/https://doi.org/10.1016/j.jallcom.2018.06.097.

[196] K.-D. Liss, K. Yan, Thermo-mechanical processing in a synchrotron beam, Mater. Sci. Eng. A. 528 (2010) 11–27. https://doi.org/https://doi.org/10.1016/j.msea.2010.06.017.

[197] Z. Zhang, Y. Zhang, O. V Mishin, N. Tao, W. Pantleon, D. Juul Jensen, Microstructural Analysis of Orientation-Dependent Recovery and Recrystallization in a Modified 9Cr-1Mo Steel Deformed by Compression at a High Strain Rate, Metall. Mater. Trans. A. 47 (2016) 4682–4693. https://doi.org/10.1007/s11661-016-3626-0.

[198] S. Van Boxel, S. Schmidt, W. Ludwig, Y. Zhang, D.J. Jensen, W. Pantleon, Direct Observation of Grain Boundary Migration during Recrystallization within the Bulk of a Moderately Deformed Aluminium Single Crystal, Mater. Trans. 55 (2014) 128–136. https://doi.org/10.2320/matertrans.M2013227.

[199] Y.B. Zhang, D.J. Jensen, Boundary migration during recrystallization: experimental observations, {IOP} Conf. Ser. Mater. Sci. Eng. 89 (2015) 12015. https://doi.org/10.1088/1757-899x/89/1/012015.

[200] F.J. Humphreys, M. Hatherly, Recrystallization and related annealing phenomena, Elsevier, 2004. http://www.sciencedirect.com/science/book/9780080441641 (accessed June 7, 2017).

[201] J.W. Cahn, The kinetics of grain boundary nucleated reactions, Acta Metall. 4 (1956) 449–459. https://doi.org/https://doi.org/10.1016/0001-6160(56)90041-4.

[202] Landolt-Börnstein, Group III condensed matter, Springer-Verlag, Berlin, 1990.